Fall 2017

Designing high performance overall water splitting electrocatalysts from non-precious metal selenides

Abdurazag T. Swesi

Department: Chemistry

DESIGNING HIGH PERFORMANCE OVERALL WATER SPLITTING ELECTROCATALYSTS FROM NON-PRECIOUS METAL SELENIDES

By

ABDURAZAG TAHER SWESI

A DISSERTATION

Presented to the Faculty of the Graduate School of the

MISSOURI UNIVERSITY OF SCIENCE AND TECHNOLOGY

In Partial Fulfillment of the Requirements for the Degree

DOCTOR OF PHILOSOPHY

in

CHEMISTRY

2017

Approved by

Dr. Manashi Nath, Advisor

Dr. Amitava Choudhury

Dr. Jeffrey Winiarz

Dr. Risheng Wang

Dr. Xinhua Liang

PUBLICATION DISSERTATION OPTION

This dissertation consists of the following six articles which have been published and one manuscript will be submitted for publication as follows:

Paper I, found on pages 71-110, is published in Energy & Enviromental Science.

Paper II included in pages 111-133, is published in Journal of Material Research.

Paper III, found on pages 134-180, is published in Scientific Reports.

Paper IV, found on pages 181-229, is published in ACS Applied Materials & Interfaces.

Paper V, found on pages 230-249, is published in Chemical Communications.

The pages 250-263 are from the manuscript under preparation (Paper VI) intended for the submission in ACS Nano Letters.

ABSTRACT

The energy production has been depending mostly on fossil fuel which will be depleted someday in the near future. Aspects such as the loss of energy resources and destruction of the environment have motivated researchers for pursuing transition away from fossil fuels to renewable solar–fuels. Therefore, in order to meet the continuous increasing demand for energy, the hydrogen, with the largest energy density stored in it, can then efficiently be used in fuel cells without concern of contaminants. Water splitting reaction to generate H_2 and O_2 is one promising method of converting solar energy into fuels. The major challenge with this technology is the sluggish anodic reaction, oxygen evolution reaction (OER), in combination with the harsh conditions require special catalyst materials to mediate and expedite the reaction process. Mixed precious iridium-ruthenium oxides have been investigated as promising electrocatalysts for the OER. Lately first row transition metal chalcogenides have experienced an improving attention for hydrogen evolution reaction (HER). Over the course of the past two and half years, we have designed, synthesized and evaluated a series of heterogeneous water splitting catalysts based on non-precious transition metal selenides. Facile fabrication protocol of first-row transition metal selenides has been accomplished efficiently. These first-row transition metal selenides have not been widely invesigated for OER till now. Therefore, their potential for electrocatalytic water splitting has not been fully explored, and much remains to be done here. The aim of this thesis was mainly to study the water splitting in particular OER with different electrocatalysts, and to investigate how the composition and structure of these catalysts influenced their catalytic performance.

ACKNOWLEDGEMENTS

I wish to thank my Graduate Advisor, Dr. Manashi Nath for her support, precious advice, helpful discussions and for giving me this opportunity to work in her research group.

I also wish to thank my committee members, Dr. Amitava Choudhury, Dr. Jeffrey Winiarz, Dr. Risheng Wang and Dr. Xinhua Liang.

I'm very grateful to my all lab mates.

Words are not enough to express my gratitude towards my friend Dr. Jahangir Masud for his invaluable assistance throughout this nice journey. Working with him was a learning experience and it gave me an opportunity to understand the critical aspects of electrochemistry.

My deepest appreciation to all of those who supported me throughout this journey.

My Children, "Mahmoud & Mena", If I had to choose between loving you and breathing….I would use my last breath to tell you…. I love you.

Last, but not least, I am eternally grateful to my mother for her inspiration, love and motivation, which had seen me through this thesis; though she had been a few thousand miles away from where I studied. On March 26th 2017, I said my final goodbye to my beautiful Mom….Rest in peace Mom.

Thank you GOD….Thank you to all my FRIENDS!!!

TABLE OF CONTENTS

Page

PAPER

LIST OF ILLUSTRATIONS

PAPER III

PAPER IV

SECTION

LIST OF TABLES

1. INTRODUCTION TO CATALYST IN ENERGY RESEARCH

1.1. ENERGY AND ENERGY STORAGE

It is well-known that fossil fuels face the threat of depletion and highly stimulate global climate change. There is hence a great demand for clean and sustainable alternative energy sources.[1-4] It has been predicted that by the middle of the current century annual energy consumption will jump to more than double than what it was at the turn of the new millennium and about triple by end of this century (Figure1.1).[1-4] Due to absence of alternatives, the ecology of the earth will possibly be troubled to a distressing level over the upcoming few decades.

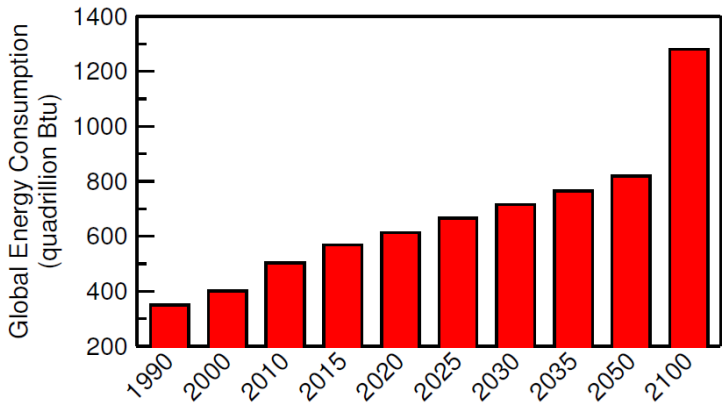

Figure 1.1. Global energy consumption for the twenty first century.[5,6]

Alternatively, hydrogen with a big amount of energy stored in it, has been considered as a clean fuel and an ideal candidate to substitute fossil fuels in the future.[7,8] However, the low availability of pure hydrogen gas is a critical challenge. There is a great global demand for hydrogen gas rising at a very fast rate (10% per year) for many industrial

applications.[9,10] Although, hydrogen could be generated by fossil fuels, the H_2 gas formed using this process still suffers from low purity and high cost.[11]

Electrochemistry offers the potential to address these issues through the electrolysis of water. However, tremendous electrical energy (237.2 kJ mol^{-1}) and thermal energy (48.6 kJ mol^{-1}) are required for water electrolysis to take place.[12] Apparently this large energy has hindered the development of water electrolysis technologies. Solar energy has long been known as an important source for renewable energy. Renewable energy could be stored in the form of chemical bonds using a technology such as electrochemical water splitting. Approximately about 128,000 ZJ (10^{21}J) of solar radiation strikes the Earth every year.[13] The electricity generated from solar cells can be utilized to produce hydrogen through water electrolysis and store the energy in a chemical form. The obtained hydrogen can then be further used to operate fuel cells generating electricity. The combination of solar cells, electrolyzers and fuel cells is a highly desired for renewable energy system based on electrochemical energy conversion and storage, which absolutely allow us to avoid relying on fossil fuels and avoid relieving carbon dioxide emission.[14-16]

Hydrogen can be stored or transported in large quantities and used as a fuel when the energy is needed for electricity or as a fuel for transportation. The only by product that accompanies the combustion or electrolysis in a fuel cell of hydrogen is pure water free of greenhouse gases. The hydrogen-energy cycle was coined as hydrogen economy and is illustrated in Figure 1.2.[17]

So hydrogen fuel becomes a significant part of future energy systems if it is produced by a cheap and sufficient means.[19-22] Hydrogen evolution only requires catalysts

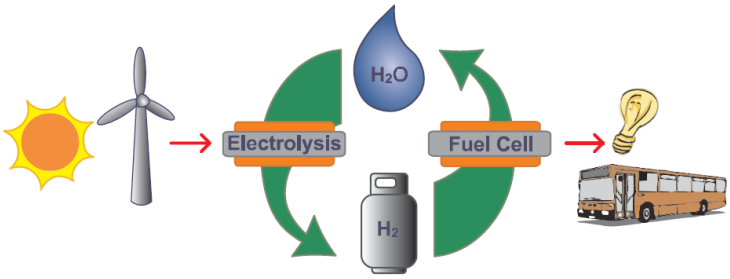

Figure 1.2. The hydrogen economy. Renewable energy is utilized for hydrogen production through water electrolysis. The produced hydrogen will then be used in fuel cells.[18]

to mediate the reaction with significant low energy consumption. This H_2 gas can then be used in a fuel cell with negligible voltage losses to provide electricity when production from the renewable source is absent or insufficient.

1.2. FUEL CELLS AND ELECTROLYSIS

1.2.1. Fuel Cells. Fuel cell is a device that converts chemical fuel directly into electricity through a chemical reaction. The most common fuel used in fuel cell is hydrogen. The foundations for fuel cells dates back to 1801 when Humphry Davy discovered several new metals such as potassium and sodium in the electrolysis research.[23,24] Christian Friedrich Schönbein designed the fuel cell after thirty seven years.[25] Later Welsh chemical-physicist William Robert Grove demonstrated the electricity production during an electochemical reaction of oxygen with hydrogen in the first crude fuel cell. The first alkaline fuel cell was obtained by British engineer Francis Bacon in 1932 with a 5 kW stationary fuel cell. This stationary fuel cell had been modified by W. Thomas Grubb in General Electric Company. Thomas introduced ion-exchange membrane as electrolyte and deposited platinum on the membrane as a catalyst.[26,27] This Grubb fuel cell was used in McDonnell Aircraft in Project Gemini, a space mission leaded by NASA. In

the space mission leaded by NASA, an alkali fuel cell providing 1.5 KW energy was used. Besides electricity, this fuel cell can provide drinking water due to the hydrogen reaction. Later during space shuttle, NASA succeeded to invent a 12 KW alkali fuel cell. Figure 1.3. illustrates alkaline fuel cells. The hydrogen fuel is injected to the anode to be oxidized to produce water and electrons. At the cathode, oxygen is reduced to produce hydroxyl ions to be transferred to the anode and the electrons flow through external circuit.

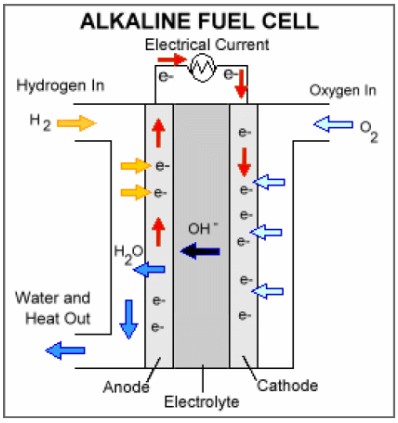

Figure 1.3. Typical alkaline fuel cell.

1.2.2. Electrolysis of Water. Electrocatalysis can be simply defined as the ability to accelerate the rate of an electrochemical process at an electrode material. Fundamentals of electrochemistry that are used throughout this study in experimental synthesis and electrochemical measurement analysis will be discussed in the introduction. Historically, water electrolysis has started since the first industrial revolution (1800), when Nicholson and Carlisle discovered the ability of electrolytical water splitting. By the beginning of the twenty century, tremendous industrial water electrolysis units were introduce in duty. The first large water electrolysis plant was established in 1939 with a capacity of 10,000 Nm^3

H_2/h. A decade after, the first pressurized industrial electrolyzer was introduced into duty by Zdansky/Lonza. In 1972 the first solid oxide electrolyte system was built by General Electric. Later in 1978 the first advanced alkaline systems was developed in industry. In current days, the developmental history ends up with the era proton exchange membranes as usable for water electrolysis units and fuel cells.[28]

1.3. THEORY OF WATER ELECTROLYSIS

Simply, the electrolysis of water is a well-known principle of producing oxygen and hydrogen gas. Figure 1.4 depicts a simple electrochemical cell. The main part of an electrolysis unit is the electrochemical cell. The cell is filled with the electrolyte solution and has two electrodes linked with an external power supply.

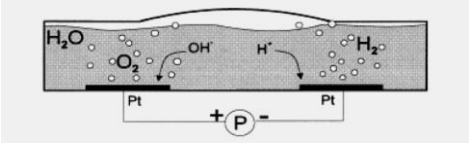

Figure 1.4. Sketch of an electrochemical cell.[29]

At a specific voltage between electrodes, the cathode starts producing hydrogen gas and the anode produces oxygen gas. The amount of gases produced is directly proportional to the current that passes through the electrochemical cell. The reaction is normally conducted in either acidic or alkaline media. In the acid, oxygen and hydrogen gas can be generated at noble metal electrodes by the electrolysis of water:

Oxidation at anode: $2H_2O \rightarrow O_2 + 4H^+ + 4e^-$ $E_a^o = (1.23 - 0.059 \times pH)$ V vs. RHE (1.1)

Reduction at cathode: $4H^+ + 4e^- \rightarrow 2H_2$ $E_c^o = (0.0 - 0.059 \times pH)$ V vs. RHE (1.2)

While in the alkaline solution, the hydroxide anions move to the anode to lose electrons while there is no hydrogen ion involved in this process.

Oxidation at anode: $4OH^- \rightarrow O_2 + 2H_2O + 4e^-$

Reduction at cathode: $4H_2O + 4e^- \rightarrow 2H_2 + 4OH^-$

Where, E_a^o and E_c^o are the thermodynamic potentials (under standard conditions) of water splitting. As can be seen above, the thermodynamic potential is dependent on pH by shifting 59 mV for each pH unit increase using Nernst Equation (Equation 1.3). To eliminate the impact of pH, reversible hydrogen electrode (RHE) was introduced.

$$E_{(RHE)} = E_{(Ag/AgCl)} + 0.197\ V + 0.059\ pH \quad (1.3)$$

No side reactions might be detected from water electrolysis to yield undesired byproducts. The net balance is:

$$2H_2O \rightarrow (4e^-) \rightarrow O_2 + 2H_2 \quad (1.4)$$

The minimum cell voltage to initiate electrolysis, $E°_{cell}$, can be described under standard conditions (P, T constant) by the following Equation.

$$E°_{cell} = -\Delta G°/nF \quad (1.5)$$

Where ΔG^o is the change in the Gibbs, n is the number of transferred electrons and F is Farady constant. ΔA^o free energy (Helmholtz) can be used instead of ΔG^o because the electrochemical cell is a closed system and no change in volume. The Helmholtz energy barrier needs some electron potentials and cell voltage required becomes as given below.

$$E°_{cell} = -\Delta A°/nF \quad (1.6)$$

$$\Delta A^o = \Delta H^o - TR\Delta n - T\Delta S^o \quad (1.7)$$

The standard reaction enthalpy is, ΔH^o= 285.8 (kJ/mol), Δn= 1.5, $\Delta S^o(H_2)$= 130.6, $\Delta S^o(O_2)$= 205.1, $\Delta S^o(H_2O)$ (l)= 70 J/mol K.

ΔS^{o}_{tot}= 130.6 + ½ 205.1 - 70= 163.14 J/mol K.

ΔA^{o} = 233.1 (kJ/mol).

So, the minimum necessary cell voltage (E_{cell}) is= 1.21 V.

$$\Delta G^{o} = \Delta H^{o} - T\Delta S^{o} \quad (1.8)$$

ΔG^{o} = 237.2 kJ/mol (standard conditions, 1 bar, 25 ^{o}C).

And ΔG^{o} for this reaction could be calculated through the formation of enthalpy change and entropy change.

$\Delta G_{reaction}=\Delta H_r - T\Delta S_r$

ΔH_r is 571.66 KJ/mol and ΔS_r is 326.686 J/mole. Then $\Delta G_{reaction}$ becomes 474.3075 KJ/mol.

And the cell voltage:

$E^{o}_{cell} = -\Delta G^{o}/nF$ = 1.23 V.

In reality, the efficiency of an electrochemical cell is given by:

$$\varepsilon_{real} = -\Delta H_r/n\Delta E_{elec} \quad (1.9)$$

Where ΔE_{elec} is the voltage to operate the electrochemical cell at a certain current (I):

$$\Delta E_{elec} = \Delta A + IR + \Sigma\eta \quad (1.10)$$

Where IR is the ohmic resistance in the cell including electrolyte, electrodes, external circuit resistance and membrane material; $\Sigma\eta$ is the sum of the overpotentials (activation energy at both electrodes). During water electrolysis, the energy required for each mole is shown in Figure 1.5.

As can be seen, with increasing the current density the activation overpotential increases. Efficient electrode materials, such as platinum could lower the energy barrier.

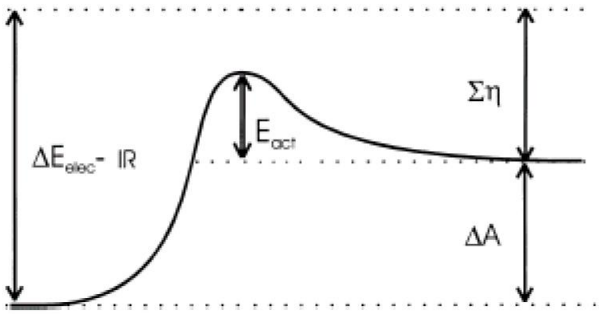

Figure 1.5. Energies involved in a reaction.[29]

For water electrolysis, under ideal reversible conditions, the maximum theoretical efficiency with respect to the electrical energy source would be ε_{max}= 120%. Therefore, heat would have to flow into the cell from the surroundings. However, under ideal reversible conditions ($\Delta S = 0$, $\Sigma\eta = 0$, so $\Delta G = \Delta H$), the cell temperature remains constant and the value of standard thermodynamic potential becomes as below:

$$E_{tn} = \Delta H / nF = 1.48 \text{ V} \quad (1.11)$$

This is named as the thermoneutral potential. Under maintained temperature, the cell takes heat in below 1.48 V, and produces heat at potentials above this value. Ideally, the overpotential η should be minimized to improve the efficiency and to reduce the heat. However, in most cases, at low overpotential the reaction occurs at slow rate. Increasing the surface areas of electrodes is amongst the best ways to increase the amount of current with minimizing overpotential.[29]

1.4. HYDROGEN PRODUCTION THROUGH WATER ELECTROLYSIS

Although the water electrolysis was first developed in acidic media, the operation in alkaline media is still preferred due controllable corrosion issues and plants can be built by cheaper construction materials compared to acidic electrolysis technology. Other

several methods for hydrogen production, such as steam electrolysis and proton exchange membrane electrolysis, have been progressed recently. Another method to generate hydrogen as byproduct from chloralkali production is well established.

1.4.1. Alkaline Electrolysis. Electrolysis of water in alkaline media is a mature technology for hydrogen generation that has been used in commercial applications. Typically the water electrolysis system consists of an anode and a cathode, separated by a membrane and flooded in alkaline solution (20 – 30% KOH). The overall reaction consists of two half reactions; the oxygen evolution reaction (OER) takes place at the anode and hydrogen evolution reaction (HER) takes place at the cathode. The membrane is used here to allow the flow of H_2O and OH^- species between the two electrodes and to block gasses generated from re-mixing (Figure 1.6).[30]

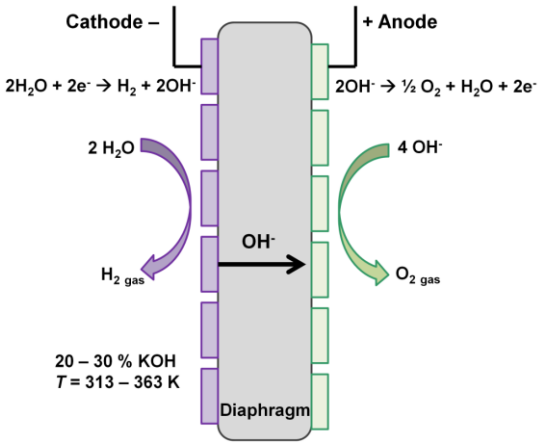

Figure 1.6. A representative of an alkaline water electrolyzer.

In recent days, cells and plants have been developed to allow operation temperatures up to 150 ^oC and at high pressure (30 bar). The new electrolyzerses in the cells contains of the porous cathode, anode and a diaphragm in between both electrodes.

This cell produces current densities up to 10 kA/m^2, which is three times more efficient than that of conventional low-pressure alkaline electrolysis plants. The cell efficiency was observed at 80%.[28]

Several important parameters have to be considered when assessing an applicable electrode material for alkaline electrolysis: (i) electrocatalytic efficiency; (ii) durability; (iii) scalability; and (iv) cost.[31] Ni-based electrodes have been used in commercial alkaline electrolyzers due to the activity of Ni as a water electrolysis catalyst,[31,32] the stability of Ni in alkaline media,[31,33] and the relatively low cost of Ni-based materials.

1.4.2. Proton Exchange Membrane Water Electrolysis. The proton exchange membrane (PEM) water electrolysis was first proposed by General Electric for fuel cell. PEM is polymer electrolyte membrane and is based on the use of a polymeric proton exchange membrane as solid electrolyte. Over the years from 1976 to 1989, the ABB, Swiss company, developed the proton exchange membrane electrolyser technology. The polymer electrolyte technology offers several advantages over the alkaline one such as: (i) better safety since no caustic electrolyte is circulated in the cell stack; (ii) the membrane materials demonstrated high durability at high differential pressure without damage and were efficient to prevent gases from mixing; and (iii) the current density was relatively high.[34]

The electrolysis cell is made of highly porous titanium and activated by a mixed noble metal oxide catalyst. Pure water is fed to the anode. The membrane allows the transfer of hydrated protons from the anode to the cathode side. The cathode is made of porous graphite with Pt. Recent designs, oxide-based electrocatalystes have been used.

A Swiss company, in 1987, installed the first commercial scale PEM electrolyzer at Stellram SA. The capacity of the produced hydrogen was up to 20 Nm^3/h at a pressure of 1-2 bar. The plant is built of 120 cells of 20 x 20 cm^2 active area each, grouped into four sets of 30 cells, and electrically connected in series. One side of each individual cell is composed of a sheet of Nafion^{TM} 117 coated by a thin layer of Pt as a cathode. In ultrapure water, all membranes were hydrated in an autoclave at 130 ^oC for two hours before the catalyst was applied. The membranes, after cooling down, were subjected to 1 M HCl for 30 min and rinsed in deionized water. The anode catalyst a Ru/Ir mixed oxide as a PTFE-bonded powder to the surface of a porous Ti, which consisted of a graphite-PTFE composite bonded to a brass wire. The temperature distribution over each set was maintained through water circulation over the anode manifolds. Online instrumentation was used to monitor the purity of the gases. The plant generated a current of 400 A (i.e. 10 kA/m^2), at 80 ^oC at cell voltages of 1.75 V. In 1990 the plant was shut down completely because the hydrogen concentration in the oxygen had exceeded the safety limit (3%).

The second design of PEM water electrolysis was by Solar Wasserstoff Bayern (SWB) which is slightly different from the Stellram plant. The thickness of the bipolar plates of the cell stacks was reduced. All 120 cells were in one stack consisting of three sets of 40 cells each. The applied pressure was the same as in the Stellram/ATEL plant. The Ir/Ru oxide material was used as a catalyst for both cathode and anode.[35]

1.4.3. Steam Electrolysis. Steam electrolysis technology offers the highest energy efficiency compared to alkaline and proton exchange membrane electrolysis. The main advantage of the steam electrolyzers is that a substantial part of the energy needed is added as heat, which is much cheaper than electric energy. The high temperature increases the

reaction kinetics, reducing the energy loss, thus increasing the overall efficiency of the cell. Typical high temperature electrolyzer achieves electrical efficiency of 92% while low temperature electrolyzers reach electrical efficiency of 85%. Ceramics as electrolyte (ZrO_2 stabilized by Y_2O_3, MgO or CaO) was conducted with high temperature. The fluid steam was heated up to 200 ^oC before entered into the cell. The fluid was further heated to 800-1000 ^oC and entered on the cathode side. After the steam was split into hydrogen gas and oxygen ions, through the ceramic material, the oxygen ions were transported to the anode, where they were oxidized to form oxygen gas. However, this high temperature system still suffers from the high cost. Usually the gas entered to the cathode side is a mixture of steam and hydrogen. The gas supplied to the anode is air. The open-circuit voltage of the system at zero current is 0.8 to 0.9 V which depending on the hydrogen/steam ratio and on the temperature. This voltage is high for water electrolysis. In order to pump oxygen from the steam side to the air side a voltage that opposes and is higher than the open circuit voltage must be applied for efficient water electrolysis. In addition, the oxygen coming from the decomposition of water into the air stream at the anode side is a waste. Air stream at the anode side is also contaminated by the oxygen coming from the decomposition of water.

A new approach named Natural-Gas-Assisted-Steam Electrolysis (NGASE) has been targeted to develop the steam electrolysis technology using natural gas to reduce the large chemical potential of the electrolyzer cell. In order to reduce the electricity consumption, the air in the anode side is replaced with natural gas. This technology has been under development attempting to scale water electrolysis units up.[36]

2. THE OER; MECHANISTIC CONCEPTS AND CATALYST DESIGN

2.1. OXYGEN ELECTRODE ELECTROCHEMISTRY

The OER, with the advantages of being benign in terms of impact on the environment and human health, is one of the most important technological reactions in electrochemistry taking place at the anode of water electrolyzers. The OER in acidic media involves four electrons per mole of O_2 as can be seen below:

$$2H_2O \rightarrow O_{2\,(g)} + 4H^+ + 4e^- \qquad (2.1)$$

So, any progress in the area of development of new or better electrocatalysts involved in the performance improvement of the anode has been welcomed. This development is highly demanding because the reaction mechanism and the oxygen evolution rate depend strongly on the electrode material. Generation of hydrogen and oxygen at cathode and anode, respectively, at a high specific rate requires a voltage of 1.23 V. Understanding the reaction mechanism at different materials could provide a close insight for energy saving purposes.

Knowledge of the fundamentals of oxygen evolution reaction (OER, $4\ OH^-\ (aq) \rightarrow O_2\ (g) + 2\ H_2O\ (l) + 4e^-$) and oxygen reduction reaction (ORR, $O_2 + 4H^+ + 4e^- \rightarrow 2H_2O$) in emerging energy generation and storage technologies is crucial. The efficiency of water electrolysis is limited by the large anodic overpotential of the OER. Whereas the HER proceeds at just a minimum potentials close to its standard thermodynamic potential.[37] The overpotential of water splitting could be divided to cathodic overpotential (η_c) and anodic overpotential (η_a). Apparently the OER has really sluggish kinetics requiring a large overpotential to generate O_2 even though it is supported by precious catalysts. The slow

kinetics of the OER complicate the electrolysis of water and the related devices from being commercialized.[38] In addition, there will always be ohmic voltage drops arise between the electrodes when current is flowing in the electrolyte which could affect the overall performance of the cell. Ohmic loss increases linearly with the applied current, according to Ohm's law.

$$\Delta V_{ohm} = IR_{ohm} \quad (2.2)$$

The ohmic resistance of the electrolyte proportional to the distance between the electrodes (l) as well as the surface area of the electrodes (A) and inversely proportional to the electrolyte conductivity (κ) as showing below:

$$R_{ohm} = lA/\kappa \quad (2.3)$$

The ohmic drop is an issue of cell engineering, whereas overpotential depends on the selection of electrode materials and is an issue for electrocatalysis. The ohmic losses cannot totally be avoided but of course can significantly be reduced by placing the reference electrode and the working electrode as close as possible. High conductivity of the electrolyte will also reduce the electrolyte resistance. However, it is essential to correct for the ohmic losses. So, the total cell voltage (E_{cell}) required to stimulate the water electrolysis is the sum of the ohmic losses, the overpotentials and the thermodynamic potential of water. It is desirable to keep the overpotentials and the ohmic drop as low as possible.

$$E_{cell} = E^o + |\eta_c| + \eta_a + \eta_{iR} \quad (2.4)$$

Obviously, in order to efficiently scale up the process there are many challenges to overcome. Among those challenges is the high overpotentel at anodic reaction (OER). Modifying the electrode material could significantly increase the reaction rate through

reducing the anodic overpotential. An efficient catalyst should minimize the energy barrier for the reaction, and the catalyst should not be degraded in the water electrolysis reaction. The electrochemical reaction occurs on electrode/electrolyte interfaces with the electron conducting electrode. So the main task of the catalyst is to maximize the current density at a fixed potential and minimize the overpotential at a fixed current density.[39] Thus, different materials and operating conditions of the electrolyzer is expected to enhance the overall performance of process. It is therefore well believed that by choice of catalyst material, appropriate engineering and device design, the parameters η_a, η_c and η_{iR} can significantly be reduced and strongly influence the process efficiency. In particular, by developing the electrocatalytic material used for anodes, great improvements in efficiency should be anticipated.[40,41] For an ideal water splitting device, it should well be designed with low cost, high catalytic activity, and stability to corrosion. Basically, OER catalysts suffer from stability in acidic media, whereas HER catalysts sometimes are inactive or even unstable in strong basic electrolytes.

According to the literature, there is a trade-off between technical and economic issues and thus difficult to compromise between them. Ir and Ru-based materials and Pt−carbon materials have been proven to be state-of-the-art for OER and HER, respectively. However, Ir and Ru-based materials still show a considerable OER overpotential when compared to the overpotential required by the best catalysts for HER. In addition, scarcity and high cost of these materials hinder their utilization in water splitting industries to achieve low cost hydrogen resource and thus limit their use. Although tremendous efforts have been devoted to develop high-performance catalysts using non-noble metals and to offer a compromise solution,[42] till date no working water electrolyzer

can reach the minimum thermodynamic potential of 1.23 V.[43] Developing bifunctional catalysts for overall water-splitting (OER and HER) in the same electrolyte to simplify the system and reduce the costs becomes important yet challenging.

2.2. THERMODYNAMICS OF THE OER

Water splitting involves two half reactions; hydrogen and oxygen evolutions as seen in Equation 2.5.

$$2H_2O_{(l)} + \text{Energy} \rightarrow 2H_{2(g)} + O_{2\ (g)} \qquad (2.5)$$

The energy required to promote the water splitting reaction can be obtained from any renewable energy sources making it a desirable energy conversion technology (Figure 2.1). Wind turbines or photovoltaics,[7,44] coupling with water electrolyzers, are amongst the most attractive options to drive the water splitting reaction. Light-driven water splitting[45-47] is an alternative method to provide a local energy. In this method, semiconductor materials are incorporated into the electrode design to harvest solar energy.

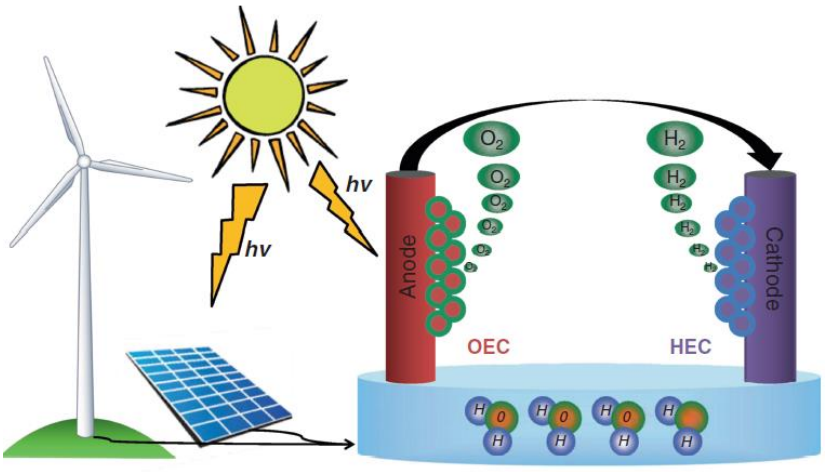

Figure 2.1. Water splitting of water via electrolysis, utilizing electricity derived from renewable sources, and photoelectrolysis. Oxygen evolution catalysts (OEC) are located on the anode and hydrogen evolution catalysts (HEC) are located on the cathode.[47]

For water electrolysis, the voltage depends on several factors such as the kinetics of the water splitting reactions and the design of the system.

$$E_{op} = E^o + \eta_a + \eta_c + \eta_\Omega \quad (2.6)$$

Where η_a and η_c are the overpotentials required for the OER at the anode and the HER at the cathode, and η_Ω is an additional overpotential needed to compensate for resistance losses within the device.[48] The efficiency of the electrolyzer unit could be evaluated through the deviation of E_{op} from E^o. Ideally, η_a and η_c would be close to zero and E_{op} should depend only on η_Ω. The η_Ω could be minimized through efficient design of the electrolyzer unit. However, this is never the case and kinetic limitations still exist and usually there are total efficiency losses at up to 85 %.[49] The thermodynamics of this reaction can be obtained through a straightforward deriving. The electrochemical potential, μ_i, must be defined first. The electrochemical potential is defined as following:

$$\mu_i = RT\lambda_i \quad (2.7)$$

Where λ is the activity of the charged species *i*.

The reaction can be written differently. The electrochemical potentials of the species at each electrode is used, where the two half reactions take place.

$$2H_2O \rightarrow O_2 + 4H^+ + 4e^- \quad (2.8)$$

Electrochemical potential becomes

$$2\mu_{H2O} = \mu O_2 + 4\mu_{H+} + 4\mu^{\alpha'}_{e-} \quad (2.9)$$

$$2H^+ + 4e^- \rightarrow 2H_2 \quad (2.10)$$

Electrochemical potential becomes

$$2\mu_{H+} + 4\mu^{\alpha}_{e-} = 2\mu_{H2} \quad (2.11)$$

Merging Equations (2.9 and 2.11) leads to

$$(\mu^{\alpha}_{e-} - \mu^{\alpha'}_{e-}) = [(1/2)\mu_{H2} + (½)\mu O_2 - (½)\mu_{H2O}] \quad (2.12)$$

The difference in electrochemical potential of the electrons at electrodes is equal to the sum of the chemical potentials of the product gases minus the chemical potential of water. Assuming this reaction is performed in standard conditions (25 °C and 1 atm), therefore, the chemical potential of both gases is zero. Since the standard chemical potential of water is -237 kJ/mol, this leads to new relationship.

$$F\mathit{E}^{\circ} = (\mu^{\alpha}_{e-} - \mu^{\alpha'}_{e-}) = - ½(\mu_{H2O}) \quad (2.13)$$

Where F is the Faraday constant (96.485 coulombs/mol e^-). Now E° is equal to 1.23 V, which is the standard thermodynamic potential for water splitting.

2.3. ELECTROCHEMICAL KINETICS

Electrochemical reactions are taking place when an electrical potential, is applied. For the water oxidation case, when the applied potential exceeds the standard thermodynamic potential, E° (1.23 V), the reaction is spontaneous (exothermic) and typically follows Butler-Volmer kinetics (Equation 2.8), with the current increasing drastically with increasing the potential.

$$i = i_o \left[e^{(\alpha a \eta_s F/RT)} - e^{(\alpha c \eta_s F/RT)}\right] \quad (2.14)$$

Where i_o is the exchange current density, α_a and α_c, are charge transfer coefficients at anode and cathode, (material dependent) and η_s is the overpotential. At high overpotentials,

$$\eta_{s=} E_{app} - \mathit{E}_o \quad (2.15)$$

$$i = i_o * e^{(\alpha_a \eta_s F/RT)} \quad (2.16)$$

This is when oxygen evolution reaction takes place at high overpotential regime. Taking the logarithm of both sides of Equation 2.16 could give a linear relationship between the log of current and the overpotential.

$$log\ i/\ i^{o} = 2.3 * (\alpha_a F/RT) * \eta_s \quad (2.17)$$

$$\text{Or } \eta_s = a + b\ log\ (i) \quad (2.18)$$

Equation 2.18 is known as Tafel Equation and *b* is Tafel slope. The Tafel slope relates directly to the amount of overpotential needed to raise the current. A close look shows that a small Tafel slope is indicative of a better active electrode. The Tafel slope also provide information about the activity, reaction mechanism and the nature of the rate determining step of the reaction.[50] This type of analysis can only be applied with sluggish kinetics where there is no significant contribution from the reverse reaction.[51] The OER is a perfect example to demonstrate this behavior.

The Tafel slope must be measured at potential region just beyond the onset of OER. The onset potential can be determined with the consideration of the effects of pH and the choice of reference electrode. The standard value of thermodynamic potential (1.23 V vs. normal hydrogen electrode, NHE) is defined at pH of 0.

A simple demonstration for a sample calculation of the conversion is below (Equation 2.19). An Ag/AgCl reference electrode, 0.197 V vs. NHE, in 0.1 M KOH (pH = 12.8) is used here.

$$E^{o} = 1.23 - 0.179V - 0.059\ (v/pH) * 12.8 = 0.278\ v\ vs,\ RHE \quad (2.19)$$

Due to capacitive charging of the double layer, we must avoid non-faradaic regime and either steady-state constant potential experiments or slow scan cyclic voltammetry experiments are required as can be seen below.

Figure 2.2. shows a slow scan cyclic voltammetry measurement which is conducted from ~ 0 to 0.4V of overpotential. During the forward scan the current is classified into three regions. The first current at 0 to ~ 0.28V is attributed to double layer charging. The electrode surface oxidation is observed at the second region (~ 0.28 to 0.34V), and the last region (η > 0.34V) is where OER takes place and the current increases exponentially with increases of η which is the Tafel region. Next, at the OER region, plotting the logarithm of the current density versus the overpotential should lead to a linear relationship, shown in Figure 2.3. In this case, the Tafel slope is 38 mV/decade for this electrode.

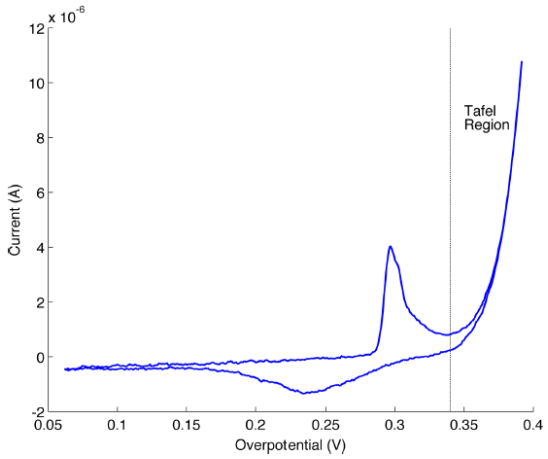

Figure 2.2. Cyclic voltammogram. The Tafel region is highlighted by the exponential relationship between potential and current.

The exchange current density, i_0, can be determined by extrapolating the Tafel plot at the equilibrium potential (η = 0 V). Extracting the Tafel slope and exchange current density, polarization curves (current density vs. potential) of the OER can be plotted for the system, thus avoiding contributions from other sources of current. The plotted curves can then be used for performance comparison for a set of electrodes.

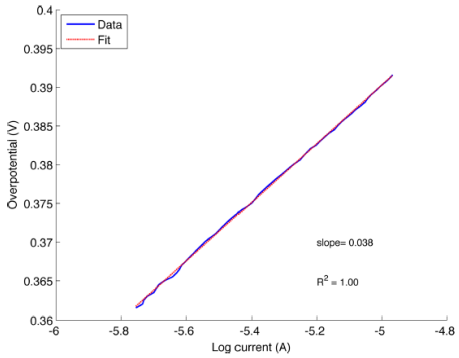

Figure 2.3. Tafel slope is the plot of the logarithm of the current vs overpotential.

2.4. A PLAUSIBLE MECHANISM FOR OER

The OER mechanisms are not yet fully understood. Since the reactions are complex, they require high overvpotentials (usually at least 0.4 V). As mentioned above, OER is the most difficult reaction in an electrochemical cell, so that the cell voltage is governed by that of the anodic reaction and is typically a demanding step, since requires 4 proton-coupled electron transfers and O–O bond formation (Figure 2.4).[52] In each step, an accumulation of the energy barrier is produced and thus leads to the sluggish kinetics of OER with large overpotential.

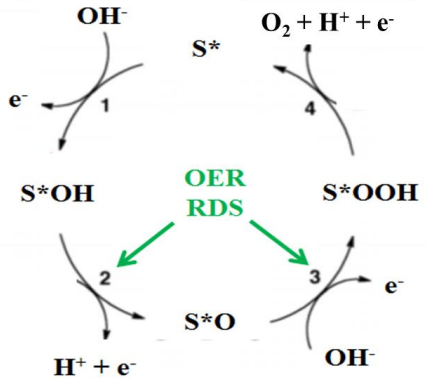

Figure 2.4. A Proposed OER mechanism.

Where S* refers to the catalytically active site in the anodic catalyst. From the proposed mechanism above (Figure 2.4), the reaction is initiated by the attachment of the hydroxyl group to S* which can be facilitated by local oxidation of the metal center. Since the hydroxyl and the oxide groups adhere to the surface at the initiation of the process, so the metal oxides, hydroxides and oxyhydroxides could form the most active catalyst. Therefore, any factor that can modify the oxidation potential of the catalytically active surface site, should affect the catalytic activity. Among the best ways to change the oxidation potential of the metal site is by replacing the ligand which adjusts the chemical potential.

2.5. ELECTROCHEMICAL ACTIVITY EVALUATION

In order to compare the OER activity, the system is modeled as was described above. Another method to evaluate activities of electrodes by measuring the generated current at a constant potential (chronoamperometry) as can be seen in Figure 2.5. Then plotting the time versus currents as a function of the applied potential leads to a steady-state polarization curve, which allows for activity comparisons for several electrode systems (Figure 2.5).

In some cases, it is beneficial to set a current instead of the potential. It is desired to use this method when the total amount of evolved gas is under investigation. Theoretically, the maximum amount of evolved O_2 is directly proportional to the current (Equation 2.20).

$$1mA=[(1/1000)Coulombs/s]*[(1\ mol\ e^-)/(96845Coulombs)]*[(1mol\ O_2)]/(4mol\ e^-) \quad (2.20)$$

$$=(2.6\ nmol)/s$$

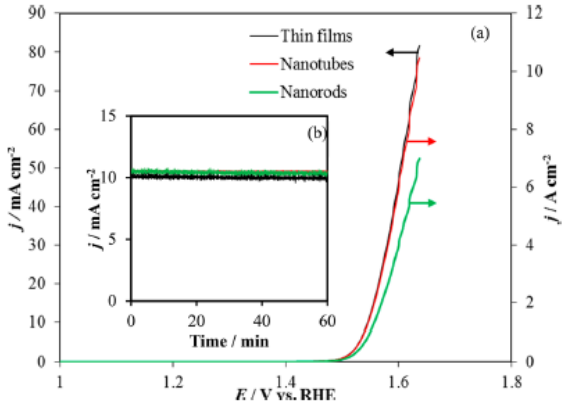

Figure 2.5. (a) Linear sweep voltammetry (LSV), where the current at a working electrode is measured while the potential between the working electrode and a reference electrode is swept linearly in time. (b) Chronoamperometry is in which the potential of the working electrode is stepped and the resulting current from faradaic processes occurring at the electrode is monitored as a function of time.

Using fluorescent oxygen probe to measure the rate of O_2 generation and gas chromatography to quantify the evolved O_2 gas and to compare to the theoretical value (i.e. the coulombic efficiency of the process).

2.6. DESCRIPTOR FOR THE OER CATALYST

The OER is divided into four paths based on number of electrons being involved in this reaction.[53] The asterisk (*) symbol stands for the catalyst active site during these four paths of the OER. Density functional calculations were applied in this method.[54-56] The following Equations show the four steps and their free energy change.

$$H_2O\ (l) + * \leftrightharpoons HO^* + H^+ + e^- \quad (2.21)$$

$$\Delta G_1 = \Delta G_{HO^*} - \Delta G_{H2O(l)} - eU + Kb\ T \ln a_{H+} \quad (2.22)$$

$$HO^* \leftrightharpoons O^* + H+ + e^- \quad (2.23)$$

$$\Delta G_2 = \Delta G_{O^*} - \Delta G_{HO^*} - eU + Kb\ T \ln a_{H+} \quad (2.24)$$

$$O^* + H_2O\ (l) \leftrightharpoons HOO^* + H^+ + e^- \quad (2.25)$$

$$\Delta G_3 = \Delta G_{HOO^*} - \Delta G_{O^*} - eU + Kb\ T \ln a_{H^+} \quad (2.26)$$

$$HOO^* \leftrightharpoons * + O_2 + H^+ + e^- \quad (2.27)$$

$$\Delta G4 = \Delta GO_2 - \Delta GHOO^* - eU + Kb\ T \ln aH+ \quad (2.28)$$

The total free energy change during the OER can be explained in the following Equation.

$$G_{OER} = \max (G_1, G_2, G_3, G_4) \quad (2.29)$$

The theoretical overpotential, at the standard condition, can be calculated as well.

$$\eta_{OER} = (G_{OER}/e) - 1.23V \quad (2.30)$$

The free energy diagram for the whole OER could be deduced if the overpotential for each step is known. Ideally, the free energy of each step should be same in order to have the lowest overpotential for OER which leads to the minimum energy loss and thus the free energy of OER should be 1.23 eV (Figure 2.6. a). Whereas, free energy diagrams for some metal oxides are different from that for the ideal catalyst (Figure 2.6. b-d).

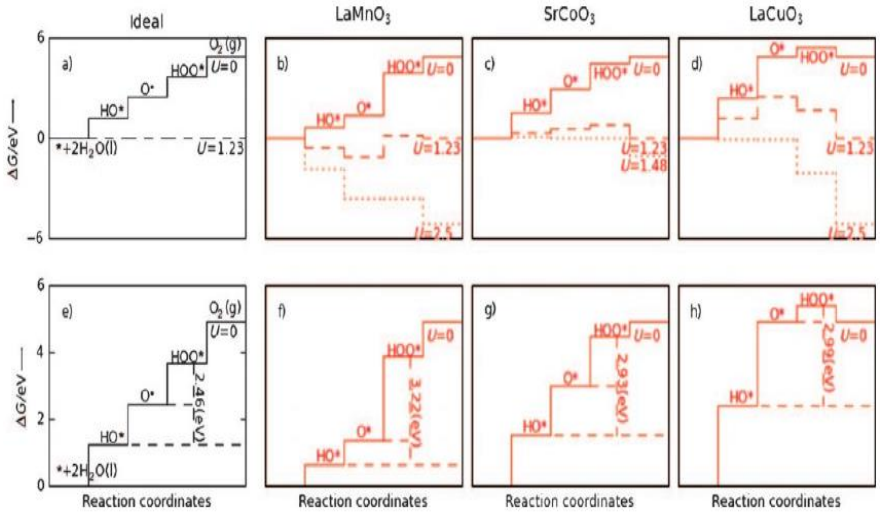

Figure 2.6. Free energy diagram for the ideal and metal oxide catalysts.

There is an interesting phenomenon happened to the free energy difference between HOO* and HO*. For both HO* and HOO*, the bindings are related to each other by constant free energy of about 3.2eV due to the preferential of these two species to bind at the same sites and the similarity of structures. The O* adsorption energy plays a key role in overpotentail of the each oxide surface. Either step 2 or step 3 is the potential determining step.

$$G_{OER} = \max [\Delta G^{0}_{2}, \Delta G^{0}_{3}] = \max [(\Delta G^{0}_{O*} - \Delta G^{0}_{HO*}), (\Delta G^{0}_{HOO*} - \Delta G^{0}_{O*})] \quad (2.31)$$

$$G_{OER} \approx [(\Delta G^{0}_{O*} - \Delta G^{0}_{HO*}), 3.2\text{eV} - (\Delta G^{0}_{O*} - \Delta G^{0}_{HO*})] \quad (2.32)$$

The free energy difference could be described as the descriptor of the OER activity. So the theoretical overpotential is determined as can be seen in the following Equation.

$$\eta_{OER} = \{\max[(\Delta G^{0}_{O*} - \Delta G^{0}_{HO*}), 3.2\text{eV} - (\Delta G^{0}_{O*} - \Delta G^{0}_{HO*})]/e\} - 1.23\text{V} \quad (2.33)$$

The free energy difference between O* and HO* is the descriptor.

2.7. VOLCANO PLOT FOR THE OER CATALYSTS

Developing a concept for the relationship between the adsorption energy behaviors and the fundamental properties of the catalytic material is important. Knowledge of the ability of the surface to form bonds is essential since the activation energies for intermediate surface reactions are strongly correlated with adsorption energies.[57] A close insight into the nature of OER, adsorption and desorption intermediates during the reaction are proven. In other words, the reaction involves bonds formation and bonds breakage between the reaction intermediates and the electrode surface. Therefore, designing the bond strength between active sites and adsorbed intermediates could influence the activation energy for the electrochemical reaction. The adsorption of intermediates at a surface is

equivalent to oxidation of the active site to a higher valence state. In order to mediate the adsorption and desorption of the catalyst surface, the catalyst should be able to change rapidly between lower and higher oxidation states. This can be quantified by the enthalpy of formation (ΔH_{f0}) from a lower to a higher oxidation state in the material.[58] Plotting the electrocatalytic activity as a function of ΔH_{f0} for different materials results volcano relations (Figure 2.7). As can be seen from the plot, the materials possess intermediate enthalpies display the highest catalytic activities. The catalytic activity on the vertical axis is typically represented as the negative of the overpotential or the current at a given overpotential. To the left side of the peak are materials with a small tendency to be oxidized to a higher valence state, minimizing the adsorption of the intermediates and thus results in higher overpotentials. Whereas the materials to the right are oxidized easily, binding intermediates too strongly due to very high ΔH_{f0} and hinders desorption of the products, thus becoming catalytically inactive. At the top of the peak RuO_2 and IrO_2 are found which

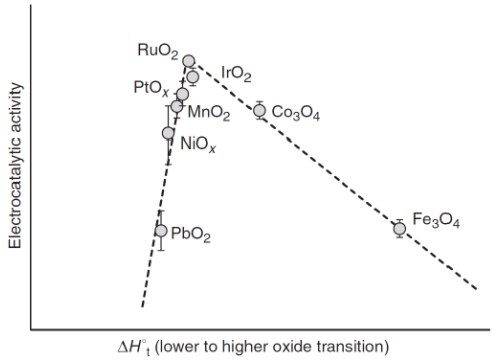

Figure 2.7. Volcano plot of the electrocatalytic activity for the OER against ΔH_{f0} of lower to higher oxide transition for different materials.[58]

demonstrates the high activity of these materials for the OER in acidic media.[59-61] Designing efficient OER catalysts is not straightforward task because of the following

reasons[62-64]: (1) thermodynamic potential for the oxidation of water should be slightly below oxidation potential of the designed catalyst; (2) for less-energy intermediates, coupling of the catalyst oxidation should simultaneously take place with proton transfer, followed by fast O−O bond formation; (3) a high rate of catalytic reaction; (4) the catalyst is not susceptible to oxidative damage at OER potentials and (5) the catalyst should operate at extreme conditions. To date, catalysts meeting all these requirements have not yet been achieved. Bockris and Otagawa,[65] on the study of the OER on perovskite oxides, have attempted to correlate the number of d-electrons of the transition metal M(III) cations with the experimental catalytic activities. It was observed that a linear increase in OER activity could be obtained with increasing d-occupancy (Figure 2.8.). The bond strength is inversely proportional to the number of d-electrons. Molecular orbital diagrams for the bonding of an OH to an M(III)O_5 complex in an octahedral geometry was constructed. They showed that the d-orbital electrons of the transition metal occupy antibonding orbitals when involved in OH bonding. With the increasing number of d-electrons in anti-bonding orbitals, the bond strength decreases.

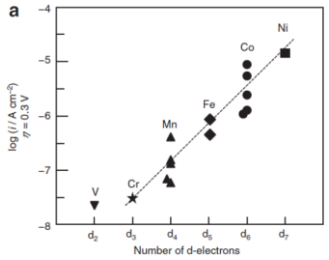

Figure 2.8. OER current density at an overpotential of 0.3 V for a series of perovskites versus the number of d-electrons of the transition metal cations.[65]

The electronic structure of the materials directly influences the catalytic properties. Concepts of orbital occupancy and electron counting have been adopted to sought a

molecular level understanding of OER activity.[66] Shao-Horn et al.[66] proposed that the occupancy of a single set of molecular orbitals is an essential activity descriptor for perovskite type oxides. The octahedral splitting of the d-orbitals in M atoms results in a low energy triplet with t_{2g} symmetry and a high energy doublet with e_g symmetry. In addition, the filling of the M of e_g-orbital was demonstrated to be more descriptor for catalysis than the total number of d-electrons because e_g orbitals participate in σ-bonding with OH species[68] to therefore form stronger overlaps with the oxygenated adsorbates. The group of Shao-Horn[66] experimentally proved that intrinsic OER activity can be optimized by achieving the near-unity occupancy of the e_g orbital of metal ion along with increasing the covalency of metal-site oxygen. Thus, the occupancy of the e_g-orbital at M can greatly influence the binding of the OER intermediates, and consequently enhance the OER activity. Figure 2.9. shows that the e_g-occupancy is a good descriptor of OER activity for a set of perovskite oxides. The oxygen bonding strength is more complex and the free energy difference should be used to design a suitable catalyst.

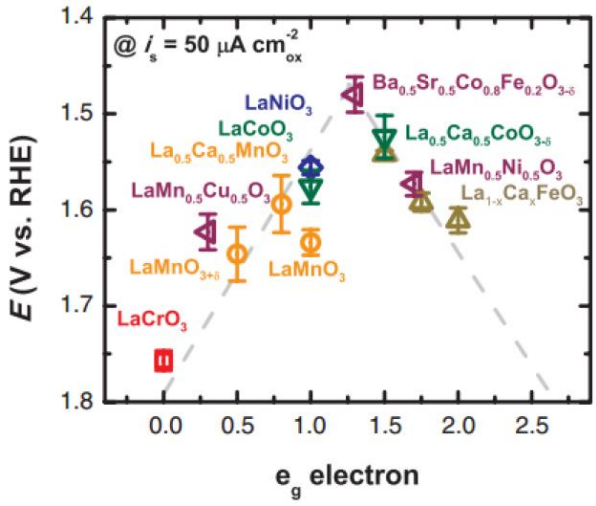

Figure 2.9. Relationship between the OER catalytic activities and the occupancy of the e_g-electrons of the transition metal oxide.[69]

Figure 2.9. revealed that the rate determining step (RDS) in the left side is deprotonation of the oxyhydroxide, whereas O-O bond formation could be the RDS for the right side of the plot. This relationship could be described as volcano shape and similar to that obtained in the Rossimeisl's study. The highest OER active material should be observed at the peak of the volcano which is $Ba_{0.5}Sr_{0.5}Co_{0.8}Fe_{0.2}O_{3-\delta}$ (BSCF) in this investigation. The BSCF exhibits the highest OER activity among the others due to the near optimal e_g-occupancy. The great challenge in OER catalysis is to establish a way to modify oxide surfaces and hence design limitations can be overcome.

2.8. TAILORING ACTIVITY

Tailoring OER catalysts atom-by-atom[70] needs enough knowledge of the factors determining catalytic activity. Nevertheless, OER catalyst design is not as easy process as it seems. Possible OER catalysts must not only highly active, but should also be electronically conductive and with long term stability under the harsh operating conditions.[71] Therefore, identification of the catalytically active species on the catalytic surface is a significant challenge in electrocatalyst development.

2.8.1. Catalyst Synergy. Systems of a multi-component catalyst are in the core of the most promising approaches of research for OER catalyst enhancement. Various mixed oxides and dopants have been targeted with a view towards gaining synergistic effects. The beneficial incorporation of Fe impurities in Ni hydroxides on the OER activity has been reported over 25 years ago.[72-74] Ni–Fe based oxide catalysts, since then, have been showing promising OER activities in alkaline media.[75-81] For instance, $Ni_{0.9}Fe_{0.1}OOH$ exhibited an OER turnover frequency greater ten folds higher than that of the state of the art IrO_x

catalysts.[82] Similarly, the presence of gold was found to have a drastic increase in the activity of manganese,[83-85] cobalt[86,87] and nickel[88] based oxides towards OER. Impurity doping in semiconductor electrodes has also shown enhancement in activity. For example, doping Ni/Co in hematite[89] and doping Mn/Mo in rutile TiO_2[90] have shown significant improvements in the activity. Also, state-of-the-art ruthenium oxide based catalysts display great increases in OER activity when mixed with Co or Ni.[91]

Halck et al.[92] proposed a model to describe the enhanced OER activity of Co and Ni for modified RuO_2. The proposed model was conducted based on an associative reaction pathway (Equations. (2.34-2.37).

$$M + H_2O \xrightarrow{\Delta G1} MOH + H^+ + e^- \quad (2.34)$$

$$MOH \xrightarrow{\Delta G2} MO + H^+ + e^- \quad (2.35)$$

$$M + H_2O \xrightarrow{\Delta G3} MOOH + H^+ + e^- \quad (2.36)$$

$$MOOH \xrightarrow{\Delta G4} M + O_2 + H^+ + e^- \quad (2.37)$$

Where ΔG is the Gibbs free reaction energy for each step of the reaction. It was suggested that the MOOH intermediate is stabilized through localized hydrogen bonding or full proton transfer (Figure 2.10). In case of rutile type oxide catalysts, the OER is believed to occur on the surface of coordinately unsaturated (CUS) sites because these sites provide reactive "atop" positions to form strongly adsorbed intermediates.[92] In the hydrogen acceptor model, the heterovalent Ni/Co cations modify the local CUS site architecture. The inactive oxygen bridge positions could be activated because of the presence of the nearby Ni or Co. So, the bridging O adsorbs the hydrogen from the MOH and MOOH intermediates or at least accepts strong hydrogen bond.

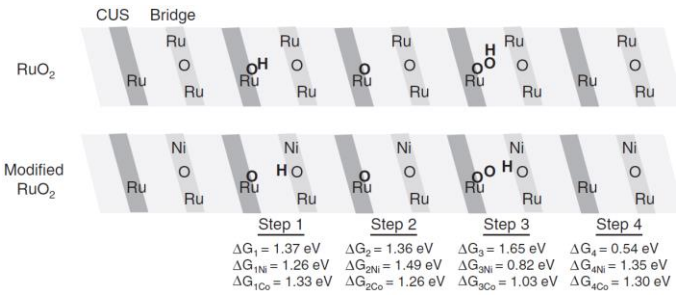

Figure 2.10. The reaction mechanism for the OER on conventional rutile RuO_2 and Ni/Co modified RuO_2 illustrating the role of the two binding sites. The dark grey row represents the CUS sites and the lighter grey the bridge sites. Adsorbed intermediates are represented in bold font.[92]

Figure 2.10. shows that the free energy changes are lowered for step 1 and step 3 on the Ni and Co modified RuO_2 compared to those on pure RuO_2. So no longer needs to apply the universal scaling relation between the binding energies of the MOH and MOOH intermediates and the OER can proceed at low potentials which close to the reversible potential. The largest reaction energies for the Ni and Co modified RuO_2 were found to come from step 2 potential-determining at 1.49 eV (overpotentials of ca. 0.26 V) and from step 1 potential-determining 1.33 eV (overpotentials of ca. 0.1 V), respectively. This observation was confirmed experimentally through a series of $Ru_xNi_{1-x}O_2$. $Ru_xCo_{1-x}O_2$ catalysts show better performance than the pure RuO_2 catalyst.[92] Clearly the catalytic properties of a material can be tuned by varying the hydrogen acceptor. In 2014, Halck et al.[92] were successful to extend this analysis to model the beneficial interaction of Au with Mn and Co. Improvements in OER activity were highlighted when Au is added to Mn or Co catalysts. El-Deab et al.[83] and Mohammad et al.[84] studied the OER electrocatalytic activity of γ-MnOOH deposited on different conducting substrates including Au, Pt and glassy carbon. It was found the overpotential was reduced by more than 200 mV when a manganese oxide was anchored on Au substrate. Gorlin et al. proved that the OER turnover

frequency of MnOx nanoparticles was increased to about 20-fold when they are co-deposited with Au nanoparticles.[87] Similarly, incorporation of Au nanoparticles to mesoporous Co_3Se_4 has been found to enhance the OER activity.[87] Au=O functionalities on the gold nanoparticles/substrates was found to lower the energy of the MOOH intermediate. The theoretical analysis, along with the experimental observations, predicted the inclusion of gold hydrogen acceptor lower the thermodynamic overpotential for some Mn and Co based catalysts by ca. 0.1–0.3 V.[83,84,87]

An alternative interpretation of the origin of such catalytic enhancement has been provided by Busch et al.[93-96] It was arguing that the catalytic performance can be improved if the transition metal oxides are mixed with opposite reactivity. The catalytic performance of a series of homo-(bi)nuclear transition metal catalysts was evaluated considering the oxidation of two MOH hydroxyl groups to form two MO oxo groups and the μ-peroxo bond formation between the MO groups. The transition metal shows a significant effect on the stabilities of the MO intermediates. Two distinct kinds of compounds were screened depending on the degree of single bond character in the M=O bond of the MO intermediate.[93,95] Figure 2.13 depicts the Fe–Fe and Co–Co reaction energy diagrams and the classification of the energetics for these two kinds of compounds. For the Co–Co, Mn–Mn and Ni–Ni catalysts, the MO moieties contain some radical character and their formation is endothermic requiring an overpotential of approximately 0.5 eV relative to a tyrosine reference potential.[93,94] Consequently, the following O–O bond formation becomes strongly exothermic (- 0.75 eV). On the other hand, for the Fe-Fe, Cr-Cr and V-V catalysts the M=O bonds are stable resulting that the two MOH oxidation steps are exothermic. This high stability leads to strongly endothermic of an O–O bond formation

step (0.75 eV). In both two cases, a significant overpotential is required for the reaction. These findings inspired Busch et al.[95] to propose a hetero-nuclear Fe-Co catalyst as an effort to overcome the shortcomings of the individual homonuclear catalysts. Figure 2.11 shows that this catalyst can follow two pathways, Fe=O or Co=O formation. The inertness of Fe=O was compensated by the reactivity of the Co=O because the di-hydroxo species displays a negligible overpotential (0.11 eV) and the μ-peroxo formation step is slightly exothermic by -0.14 eV.

In another study, the OER performance of Fe_3O_4 based catalysts was found to be improved by combining with Mn and Co oxides.[77,96-99] Therefore, mixing oxides from significant different reactivities may tune the relative energies of important intermediates, resulting to lower OER reaction barriers.

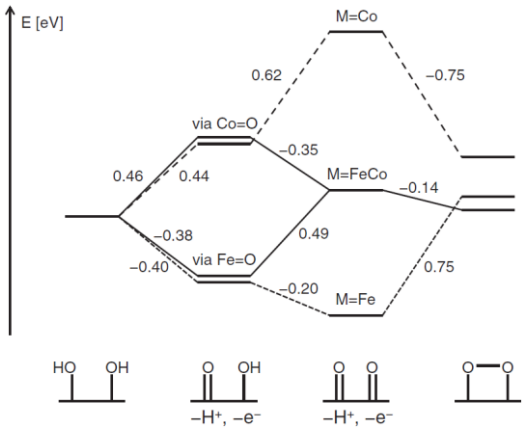

Figure 2.11. The reaction energetics for hydroxide oxidation and μ-peroxo bridge formation at the homo-binuclear Fe (short dash) and Co (long dash) sites and hetero-binuclear FeCo (solid lines) sites showing the step-by-step dehydrogenation processes.[93,94]

Several authors have also attributed the enhancement of catalytic performance to changes in the local electronic properties of the active sites. Yeo and Bell[100,101] investigated the OER activity of Co and Ni oxides synthesized on different substrates. Their study

showed that the OER activity of a submonolayer of cobalt oxide increasing with increasing electronegativity of the substrate (CoO_x/Au > CoO_x/Pt > CoO_x/Pd > CoO_x/Cu > CoO_x/Co).[100] Similarly, a monolayer of nickel oxide deposited on Au was found to exhibit better OER catalytic activity comparing to that deposited on a Pd substrate.[101] The activity in all cases increases with the increase of electronegativities and could be attributed to the partial electron transfer from the metal oxide to the more electronegative metal substrate. The extraordinary synergy in Ni–Fe based catalysts was investigated by Trotochaud et al.[106] The Fe in these catalysts is usually found in the +3 oxidation state.[101-103] However, at potentials for active oxygen evolution, *V*–pH (Pourbaix) diagrams predict that Fe in stable Fe^{3+} and Fe^{4+}.[106,107] Partial-charge transfer can therefore occur between the Ni and Fe centers. Corrigan et al.[111] through in situ Mossbauer spectroscopy proved the partial electron transfer away from Fe^{3+} centers when Ni^{3+} centers were further oxidized to Ni^{4+}.

In addition, the Fe content of the film has been shown to affect the potential of the Ni^{2+}/Ni^{3+} redox couple.[80,102] The presence of Fe effectively suppresses the oxidation of Ni^{2+}.[102] Trotochaud et al. suggested that partial electron transfer between the Ni and Fe centers facilitates the formation of Ni^{3+} or Ni^{4+} species with more oxidizing power and hence, better OER activity.[102] In this way, tailoring the electronegativities of the component metals represents an experimentally facile approach to catalyst optimization.

2.8.2. Activity–Stability Relations. The requirement of long-term stability under harsh operational conditions for an OER catalyst is required and widely recognized.[77,99,108] Even if it could be produced economically, the frequent replacement of electrode materials has to compromise between the stability of materials and their activities for the OER. Although the relationship was addressed in the volcano relations, the most active catalyst

is still neither too reactive nor too stable and an obvious understanding of the atomic scale stability of electrode materials during the OER is lacking.

Markovic's group studied the links between the activity and stability of monometallic and bimetallic oxides.[71,109,110] The OER activity of these oxides was examined at an overpotential to drive a current density of 5 mA cm^{-2}. The stability of each catalyst was determined by the concentration of corresponding metal ions in solution following each OER experiment. The OER activity and stability trends obtained for some monometallic oxides in acidic media can be seen in Figure 2.12. The structural effects of the oxides were studied on different morphologies of these catalysts. For each catalyst, a crystalline thermally prepared oxide (TC) and a highly defective amorphous electrochemically prepared oxide (EC) were investigated.

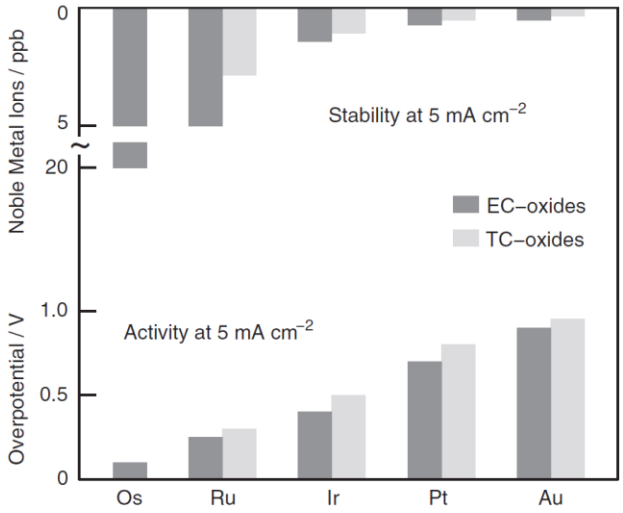

Figure 2.12. Relationships between activity and stability for the oxygen evolution reaction on monometallic oxides. Stability: the concentration of dissolved metal ions in the electrolyte solution following OER.[110]

Figure 2.12. showed that the OER activity of both morphologies increased with increasing the oxophilicity of the metal following the order Os>>Ru>Ir>Pt>Au. It was seen

that there is a trade-off between the activity and the stability of the oxides. Os was observed to be more active than Ru but was extremely unstable. Furthermore, higher activity has been observed from all amorphous oxides but less stability than the crystalline oxides. Higher density of defects in the EC-oxides may play a significant role in the relationships between activity and stability.[111]

It has also been noted similar trends for a range of polycrystalline and single crystalline oxides.[71,111] In all these oxide cases, the most defective surfaces were the most active but least stable. This study stated that the inverse relationship between activity and stability is a general observation in OER electrocatalysis. Therefore, the nature of the oxide and the density of surface defects could control the activity and stability of electrodes.[109] It has been believed that such relationship is attributed to a potential induced transformation from a stable low-valence oxide into an unstable higher-valence oxide. For the case of both Ru and Ir, the onset dissolution for polycrystalline surfaces is always accompanied by the onset of OER.[111]

In-situ analysis, using X-ray near edge structure (XANES), shows that these processes occur when a change in the average metal oxidation state from n=4 to n>4 takes place. The extent to which this transition occurred reveals the activity and stability trends. Polycrystalline Ru showed a faster oxidation rate than polycrystalline Ir, which in a good agreement with its higher activity and lower stability. The active sites or defects sites are identified as locations on the catalyst surface where the transition from the stable n=4 state to the unstable n>4 state is facilitated, and to which how variations in the oxidation state of surface atoms could govern the stability and induce activity of these oxides.[109,111]

The intrinsic activity and stability of oxide materials are linked and could provide an interpretation for OER catalyst optimization. The activity and stability for the OER should be balanced in which the dissolution rate is neither too fast nor too slow.[111,112] Reier et al.[113] studied the activity of Ru as bulk and nanoparticle catalysts in acidic media. Similar activities were reported for these catalysts but the Ru nanoparticles were highly corroded at the applied OER potentials and lost their activity. A decomposition mechanism for polycrystalline Au has been investigated through performing online mass spectrometry analysis of the oxygen evolved.[114] The study, using ^{18}O labelling of the oxide, showed that the very first oxygen evolved was $^{18}O_2$, indicating that the initial oxygen evolution process was accompanied by decomposition of the surface oxide. The Markovic group has developed a new synthesis approach to inhibit the decomposition and hence improve stability.[112,115,116] The synthesis strategy was based on thermal annealing of $Ru_{0.5}Ir_{0.5}$ alloys and nanoparticles show Ir rich which is more stable.[112] This forms an interconnected surface domain and therefore significantly enhanced the stability of the catalyst without compromising its OER activity. Tuning the surface composition of mixed oxide catalysts offers a viable strategy to enhance the catalyst activity and stability.

2.8.3. The Active Site. It has been accepted that surface reactions take place usually at active sites.[117-119] The heterogeneous reactions do not occur over the entire catalytic surface but only at specific catalytically active surface sites. In the case of metal and metal oxide surfaces, the active sites are believed to be as surface defects in the lattice structure. Somorjai[120] found that, for the same material, catalytic processes is more rapid at defects than on terraces.[121] Also it was pointed out that the most thermodynamically stable oxygen adsorption sites on Au are those with the multi-fold coordination. Moreover, Nowicka et

al.[122] have shown that treatment of Au with hydroxyl radicals can knockout the active sites on Au, suggesting that surface defects are places of partially filled d-orbitals which could stabilize free radical intermediates. Apparently, the surface reactivity might be controlled through low lattice coordination at atomic level. However, well understood of the specific nature of these sites is still to be investigated. Understanding details about what occurs at these sites at the microscopic level is a great challenge in OER catalyst design.

Burke and Lyons have provided a simple description of OER catalysis.[123-128] They stressed that the specific nature of the active site can be visualized if a close insight is paid to the underlying surface redox chemistry of the catalyst. Metal oxide surfaces, in aqueous solution, possess a hydrophilic character resulting that the surface oxy groups become hydrated or hydroxylated.[129,130] This hydration in case of compact crystalline oxides occurs on coordinately unsaturated (CUS) surface defect sites. Whereas, the hydration can permeate into deeper layers in the case of porous oxide materials. For anodically synthesized hydrous oxide films it appears that the metal oxides share a common surface–electrolyte interface, with only a difference in the magnitude of hydration/hydroxylation, as can be seen in Figure 2.13.[131] An examination of redox behavior of these hydrated surface species could be afforded through insight into the structure. For instance, negative shifts for *super-Nernstian* V-pH have been reported for the redox transitions of several transition metal oxide surfaces including Ni,[132-134] Fe,[131,135,136] Au,[129] Rh,[137] Ir[138] and Ru.[124,139] The negative shifts imply that the oxidized state of these oxides relatively gains a net negative charge. The formation of anionic oxide originates from the oxidation of the metal cations or hydrolysis reactions,[131] and can be equivalently regarded in terms of the adsorption of excess hydroxyl ions, proton loss from coordinated water molecules or the

formation of hydroxyl surface complexes. The adsorption of OH^- ions, H^+ loss from coordinated H_2O molecules or the formation of hydroxyl surface complexes are all equivalent.[140]

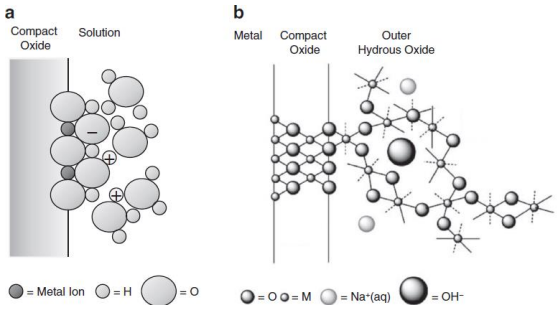

Figure 2.13. Oxide–solution interface for (a) compact thermally prepared oxides such as RuO_2 and (b) anodically prepared hydrous oxides.[141]

The structure for the hydrated surface species has been generalized in the following formula: $[M(z)O_m(OH)_n\ (OH_2)_y]^{p-}$ where p= 2m + n - z and z is the oxidation state of the metal M. This formula should be applied to any oxide known to acquire a net negative charge in aqueous solution. The electrocatalytic activity of the oxide films can be attributed to the formation of complex anionic surface clusters, with octahedrally coordinated metal complexes (surfaquo group). It has been important to emphasize that the surface stoichiometry is predominantly unknown and depends on the nature of the metal cation and its stable coordination states.[124] Lyons and Burke proposed that for thermally prepared Ru based oxides the OER takes place at Ru surfaquo groups. The following reaction illustrates the mechanism:

$$(\text{-O-})_2RuO^-(OH)_3 + OH^- \leftrightarrow (\text{-O-})_2RuO.O^- + (OH)_2 + H_2O + e^- \quad (2.38)$$

$$(\text{-O-})_2RuO.O^- \rightarrow (\text{-O-})_2RuO_2(OH)_2 + e^- \quad (2.39)$$

$$(\text{-O-})_2RuO_2(OH)_2 \leftrightarrow (\text{-O-})_2RuO_2 + 2H^+ + O_2 + 2e^- \quad (2.40)$$

$$(\text{-O-})_2RuO_2 + OH^- + H_2O \leftrightarrow (\text{-O-})_2RuO^- (OH)_3 \quad (2.41)$$

Here, two bridging oxygen species (-O-) link the surfaquo groups to the oxide surface. The rate-determining step is the second electron transfer which was shown to be in a good agreement with the observed electrokinetic data: b=60 mV dec^{-1} and reaction order, $m OH^-$= 1. Surfaquo groups have been known to involve as the OER catalytic centers on some thermal oxides,[124,131,142] passive oxide[143,149] and hydrous oxide surfaces.[125,133,134,145] For the hydrous Fe oxides, the pH dependence of the OER has been observed to reflect the surface redox processes, as shown in the inset of Figure 2.14[136,137] The OER onset potential for hydrous oxide redox transition A3 exhibited a -3 mV/pH super-Nernstian shift instead of -59 mV/pH unit. Therefore, the surfaquo groups on the hydrous layer could participate in oxygen evolution activity.

The outlined mechanism (Figure 2.14) was demonstrated to be a consistent with the kinetic data for several hydrous Fe oxide catalysts.[136,137] The Fe (V) oxo catalysis [146] which is analogous to those depicted for various homogeneous catalyst systems[93,147,148] shows a lack of a significant contribution to double-layer charging with increasing hydrous layer thickness indicating the absence of an oxide–solution interface.[132] The increase of hydrous layer thickness leads to better electrocatalytic currents,[125,129,140] revealing an increased concentration of active sites. The hydrous oxide film may consists of linked surfaquo groups arranged in a three dimensional structure and each surfaquo group could be an active site,[124] estimated the coverage of surfaquo group on RuO_2 about 30 %. The catalytic properties of thermally prepared RuO_2 films are more likely to originate from the oxidation state of surface atoms.[149]

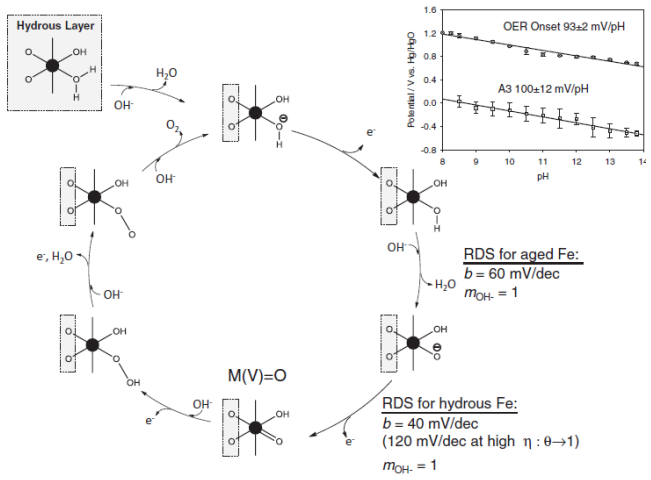

Figure 2.14. The mechanism for oxygen evolution at hydrous Fe oxides in alkaline media. The inset shows the pH dependence of the OER onset potential and the hydrous oxide redox potential A3 associated with an Fe(II)/Fe(III) transition.[128]

The group of Nocera has investigated the mechanistic behavior of several oxygen evolution catalysts through combination of electro-kinetic studies with spectroscopic analysis[150-155] X-ray absorption spectroscopy (XAS) characterization of electrodeposited Co oxides demonstrated presence of molecular cobaltate clusters (MCC) with edge-sharing CoO_6 octahedra (Figure 2.15).[152]

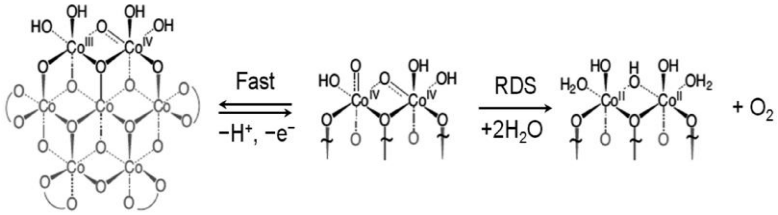

Figure 2.15. Reaction pathway for the OER at CoPi films. The structure of the MCC is shown on the left.[156]

Utilizing oxygen isotope labels, it has been suggested that the actual active sites for oxygen evolution catalysis were indeed solvent exposed Co centers at the edges of these MCCs. In addition, X-ray absorption near-edge spectroscopy[152] studies indicaede that that

the resting state of the catalyst at potentials of active oxygen evolution was a mixed valent Co(III)/Co(IV) (Figure 2.15). Similar mixed valent catalytic resting states have been observed for electrodeposited Mn,[154] Ni oxides[157] and Ni–Fe mixed oxides.[102] The proposed OER mechanism at the Co based catalysts suggested the oxidation of hydroxylated surface Co(III)–OH to Co(IV)–O followed by a chemical rate determining step of a slow O_2 evolution,[156] which is in a good agreement with the experimentally observed 60 mV dec^{-1} Tafel slope and reaction order m_{H^+}= -1.

The study of the amorphization of metal oxide surfaces has been conducted by several research groups. The presence of an amorphous oxide–solution interface might the key concept in the surfaquo group description of the oxide surface. For instance, the surface structure of lithium ion battery materials has significantly been changed during oxygen evolution.[157] The crystallinity of surface structure of $LiCoPO_4$ materials was faded with potential cycling under oxygen evolution conditions as transmission electron microscopy (TEM) revealed. At neutral pH, it was evidenced that structural changes are correlated with an increase in OER current density. Coupling energy dispersive X-ray (EDX) spectroscopy with TEM illustrated that phosphorous leaching from the layer with potential cycling led to change in surface structure. In particular, the amorphous compositional structure of the activated $LiCoPO_4$ was similar to CoPi film. The similarity suggesting the increased activity is due to the formation of hydrated molecular domains at the oxide–solution interface. The structural changes have also been seen for perovskite catalysts. The structural changes of a series of $SrCo_{0.8}Fe_{0.2}O_{3-\delta}$ (BSCF) were also shown to quickly undergo amorphization of their surface at OER potentials.[159] Reduction of surface concentrations of Ba^{2+} and Sr^{2+} ions and increased OER current densities help the structural

changes. Low activity of some perovskites has been attributed to lack of similar structural changes, indicating that these structural changes play a significant role in the catalytic activity. For a complete description of OER catalysis, understanding the chemical and structural properties of the surface oxide phase is required. Certainly, knowledge of how these changes influence the OER activity is important for designing active catalysts.

2.9. APPROACHES TO THE ACHIEVEMENT OF LOW OVERPOTENTIAL

The ideal catalyst enables a rapid transfer of electrons and bond formation/breaking and hence minimizing the overpotentials. However, so far, no electrode materials have been known to facilitate such multi-electron transfer in a mutual step. The closest approach to this ideal catalyst is by allowing all electron transfers to occur rapidly at very near to the thermodynamic potential. That improved catalyst systems should meet the requirements of the following Equation:

$$E^o \leq (E^o_1 + E^o_2 + E^o_1 + \ldots.. + E^o_n)/n \qquad (2.42)$$

The potential of the overall reaction, E^o, must equal the average of all associative potentials over the course of the transformation (E^o_1, E^o_2,…., and E^o_n, where n is the total number of electrons transferred). In addition, narrowing disparity between the potentials leads to minimum overpotentials.

$$E^o_{high} - E^o_{low} \alpha \eta \qquad (2.43)$$

Narrowing the voltage range over which a series electrochemical reactions takes place has been termed potential leveling.[159,160] OER monometallic systems[161-167] have been known as poor electrocatalysts corresponding to their extended nanocrystalline oxides.[168-170] This could be rationalized to the capacity of active sites in these oxide systems are more

delocalize accumulated charge and hold sufficient charge localization to perform better activity. A fundamental gap in knowledge the correlation between domain size, active site density, and reactivity remains unexplored. These issues are still disparity for developing catalysts with higher intrinsic activities.

3. ELECTROCATALYSTS FOR THE OXYGEN EVOLUTION REACTION (OER)

Over couple of decades, improvements on the use and exploitation of transition-metal based materials, for the catalysis of water splitting have drawn interest of many research groups. Although most excellent outcomes of catalytic activity towards the water splitting were obtained by using precious metals, materials of first-row transition-metal were also researched in water electrolysis. First-row transition-metal oxides (or hydroxides), especially Co- and Ni-based materials, perovskite oxides, layer structure type family, metal pnictides (nitrides and phosphides), organometallics and recently transition metal chalcogenides have been researched for developing efficient water splitting catalysts in alkaline conditions due to their unique electronic properties and variety chemical compositions.[171-180]

3.1. OXIDE ELECTROCATALYSTS FOR OER

3.1.1. Ru and Ir Oxides. In the rutile oxides RuO_2 and IrO_2, the Ru and Ir are in the middle of octahedral site and oxygen in the corners. Octahedrons link together through sharing the oxygens as Figure 3.1. (a) shows. The RuO_2 and IrO_2 are commonly known as benchmark electrocatalysts for OER in both acidic and alkaline media.[181,182] The OER performances of these oxides have been found to be greatly influenced by the preparation method (Figure 3.1.(b)). IrO_2 film exhibited high OER activity and can drive a current density of 0.1 J_{geo} mA cm^{-2} at overpotential of 0.275 V,[183] while the RuO_2 nanoparticles delivered only 0.01 J_{geo} mA cm^{-2} at the same overpotential. IrO_2 was observed to possess higher stability than RuO_2. At high anodic potential, the RuO_2 decomposes during OER.[184]

The decomposition mechanisms were proposed for both RuO_2 and IrO_2. First, RuO_2 transforms into the $RuO_2(OH)_2$ and deprotonates under an anodic potential into $(Ru^{8+})O_4$.[185,186] The RuO_4 is not stable in electrolyte which would be dissolved into solution with color change, thus leading to the decay of the catalytic performance. A similar mechanism for IrO_2 has been proposed as well. Under high anodic potential, a high oxidation state $(Ir^{6+})O_3$ is formed and thus will be dissolved in the electrolyte.[186]

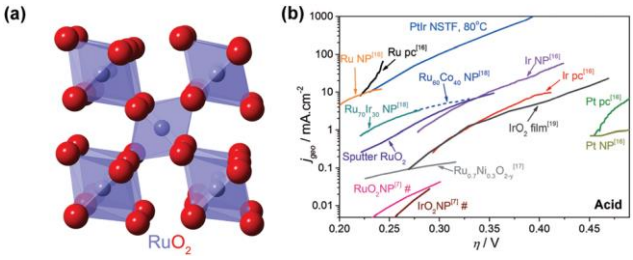

Figure 3.1. (a) Crystal structure of RuO_2. (b) OER performance of Ru and Ir based electrocatalysts in acid electrolyte.[182]

Many studies have concluded that the OER performance of IrO_2 is slightly less but more stable than that of RuO_2. This concern of stability of RuO_2 has been investigated through doping a bimetallic oxide system ($Ru_xIr_{1-x}O_2$).[187-190] This proposed system was found to be very effective and a small amount of Ir was incorporated into the sample, which could significantly inhibit the deterioration without losing much OER performance. Another way to improve their stability is by synthesizing a core–shell structure (IrO_2@RuO_2). The core–shell conformation increases the stability (1000th cycling with 96.7% remaining) and can also lower the overpotential (~ 300 mV).[191]

3.1.2. Perovskite Family. A perovskite is material with a formula $^{(XII)}A^{2+(VI)}B^{4+}X^{2-}{}_3$, where A is alkaline- and/or rare-earth metal and B is a transition metal and with same type of crystal structure as calcium titanium oxide ($CaTiO_3$). The B cation lays in the center

of the octahedron and these octahedrons connect together by sharing the corners to make the backbone for the molecule (Figure 3.2.(a)). The A cation fills the open space and to complete the structure. The oxidation state of the transition metal varies in some cases between 3+, 4+ or a mixture of both based on the oxidation state of A. The desired oxidation state of transition metal can be obtained by doping different amount of A.

Systematic studies of the perovskite for OER have been carried out and interesting results were reported. The group of Matsumoto[192] has illustrated a comprehensive study on $La_{1-x}Sr_xFe_{1-y}Co_yO_3$ and pointed out that the OER activity increases with increasing the amount of x and y. The activity was attributed to the band distribution of the d orbital character along with the higher oxidation state of the Co ion. Therefore, the OER electrocatalytic activity was linked to the electrons in the d band of the perovskite. They proved that the rate of reaction in the first and third steps is mediated as the σ* band width increased in the proposed OER mechanism path. In addition, the higher oxidation state of Co also expedite the reaction in the second step.[192] Bockris and Otagawa also screened the OER activity of perovskite compounds,[193] and the OER activity was found to follow a trend of Ni > Co > Fe > Mn > Cr for samples containing different transition metals. The Tafel slopes of the samples also followed the same trend. The Tafel slopes might also change under high potential conditions (e.g., from 70 mV dec^{-1} to 130 mV dec^{-1} for $LaCoO_3$), which revealed that the rate determining steps are changed at different regime of potentials. The study suggested that the strength of B–OH bonding influences the OER activity of the perovskite, in which the B–OH bond strength was decreased from Ni to Fe samples and further reinforced with the experimental results.[194]

Suntivich et al.[195] have reported that perovskites containing different transition metals correlated the applied potentials to number of the electrons in e_g. It was concluded that two directions have been drawn to design a good OER catalyst based on data obtained; the number of electrons in e_g should be close to unity and increased covalency interactions between the metal oxygen atoms in the oxide electrocatalysts.

Lee et al.[196] have observed phase transformations between $BaNiO_3$ and $BaNi_{0.83}O_{2.5}$ samples, which resulted in a fact that the e_g electrons were close to unity for $BaNi_{0.83}O_{2.5}$ and was zero for $BaNiO_3$ and to further explain the superior OER activity of $BaNi_{0.83}O_{2.5}$. $[Fe^{4+}O_6]$ exhibited a good OER activity which was attributed to a fact that the molecular orbital has only one electron in the e_g orbital (Figure 3.2.(b)).[197]

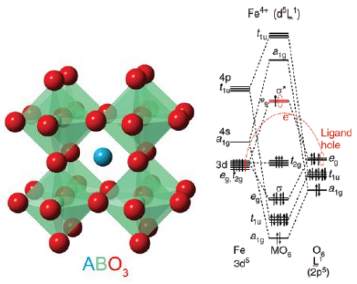

Figure 3.2. (a) Crystal structure of a perovskite (ABO_3). (b) Schematic molecular orbitals for $[Fe^{4+}O_6]$.[197]

The authors have proposed that increasing the amount of Fe^{4+} through oxygen vacancies in $La_{1-x}FeO_{3-\delta}$ may enhance the OER activity. Perovskites, $SrFeO_3$ and $CaFeO_3$ displayed very good OER activities, but low stability. The study demonstrated that substituting Sr and Ca by Cu stabilizes Fe^{4+} via covalent bonding interaction during OER.[197] The $CaCu_3Fe_4O_{12}$ catalyst showed excellent stability for OER. Zhu et al.,[198] also suggested that incorporation of Fe^{4+} in the sample could enhance OER activity. The

excellent OER activity of $La_{1-x}FeO_{3-\delta}$ compared to that of $LaFeO_3$ was attributed to the increasing Fe^{4+} population through oxygen vacancies in $La_{1-x}FeO_{3-\delta}$.

3.1.3. Spinel Family. The spinel has long been known to have a general formula $A'B'_2O_4$ where A' and B' atoms are elements from group 2, group 13 and first-row transition metals. The structure of spinel is illustrated in Figure 3.3.(a). Two crystallographic sites are in the structure of spinel including octahedral (O_h) and tetrahedral (T_d) sites. The existence of these two sites in the structure leads to two types of spinel including $(A^{2+}{}_{Td})(B^{3+}{}_{Oh})_2O_4$ and an inverse spinel of $(A^{2+}{}_{Oh})(B^{3+}{}_{Td})(B^{3+}{}_{Oh})O_4$. According to crystal field theory, the transition metals can adopt tetrahedral and octahedral coordinations, which leads to a different d-band splitting (Td: e_gt_{2g}; Oh: $t_{2g}e_g$).[200] Spinels have a good electrical conductivity with high stability in alkaline solution under high anodic potential, indicating that they act as promising OER electrocatalysts. Most spinel oxides have been used for OER are iron and cobalt based materials with other transition/alkaline metals dopants including Mn, Ni, Cu, Zn and Li.[200-203]

Li et al.[202] have studied a family of the ferrite system and reported a trend for OER electrocatalytic activities of $CoFe_2O_4 > CuFe_2O_4 > NiFe_2O_4 > MnFe_2O_4$. Incorporation of Ni in $Ni_xFe_{3-x}O_4$ ferrite compounds could improve their OER performance.[204,205] In addition, introduction of Ni, Cu and Li in a $M_xCo_{3-x}O_4$ system enhanced drastically their OER activities. However, introduction of Mn case,[200,206] in cobalt-based spinels would inhibit their OER activity. This phenomenon could be attributed to the harmful of the Jahn–Teller distortion.[207] It has been suggested that the $Mn_{3-x}Co_xO_4$ ($0 \leq x \leq 1$) performs better activities with reducing the incorporated Mn.[207] It has been observed that spinel bimetallic oxides have exhibited better OER activities comparing to monometallic spinel

oxides. For instance, replacing Co^{2+} with Zn^{2+} or Co^{3+} with Al^{3+} to form $ZnCo_2O_4$ and $CoAl_2O_4$ samples would shed light on a systematic study for the roles of Co^{2+} ions and Co^{3+} ions during OER.[202] The observations proposed that Co^{2+} ions and Co^{3+} ions act differently for OER activity in the Co_3O_4 system and revealed that the divalent Co^{2+} ruled the OER activity (Figure 3.3.(b)).[202] For this reason, the presence of Co^{2+} in $CoAl_2O_4$ display OER activity similar to that of Co_3O_4 (with presence of Co^{2+}) and outperform the performance of that of $ZnCo_2O_4$ (with the presence of Co^{3+}) (Figure 3.3.(c)).[202] These studies reveal that incorporating certain metal ions in spinel bimetallic oxides could modify the electronic structure of materials and hence optimize the binding between the intermediates and reactants during OER.

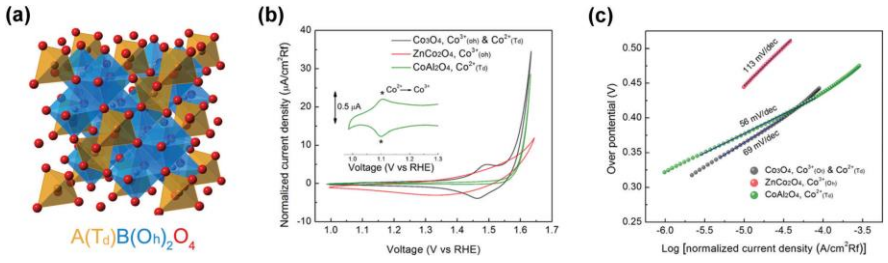

Figure 3.3. (a) Crystal structure of spinel (AB_2O_4). (b) Cyclic voltammetry (CV) curves of Co_3O_4, $ZnCo_2O_4$ and $CoAl_2O_4$. (c) Tafel slopes for Co_3O_4, $ZnCo_2O_4$, and $CoAl_2O_4$.[202]

The interaction between substrates and catalysts has been suggested to be as a promising pathway for enhancing electrocatalytic performance of OER. Switzer group[208] reported that electrodeposition of Co_3O_4 film on an Au substrate (100) leads to Co_3O_4 grown along the (111) orientation. Chen et al.[209] suggested that oriented Co_3O_4 with a (111) could expose Co ions to the electrolyte and thereby improve OER activity. In addition to Au substrate, the dispersion of spinel electrocatalysts onto carbon-based substrates shows improvement in OER activities. Al-Mamun et al.[210] have shown that the electrocatalytic

performance of the $CoCr_2O_4$ sample on carbon nanosheets was superior to that of RuO_2. Ma et al.[211] also reported a similar result that the hybrid Co_3O_4–carbon porous nanowire arrays (Co_3O_4 C-NA) exhibited an outstanding OER activity. In addition, the catalytic activity of Co_3O_4 C-NA outperformed that of physically mixed Co_3O_4 nanowire arrays with carbon. It was strongly suggested that the better catalytic performance of Co_3O_4 C-NA might be attributed to the good interaction (synergistic effect) between Co_3O_4 and carbon.

Due to low electric conductivities of oxide electrocatalysts, the multicomponent composites have become important key for the synergistic effect.[212] The composited electrocatalysts with large electroactive surface areas, mediate efficiently electron-transfer within the structure and to have a strong interaction between catalysts and substrates.[213] Accordingly, the strategy of multicomponent composite can benefit not only for oxide electrocatalysts but also for other electrocatalysts including metal chalcogenides, metal pnictides and organometallics. The phase transformations in spinel compounds during OER are another important issue. Subsequently, several groups have suggested that a structural transformation occurs on spinel metal oxide to generate a metal oxyhydroxide on the catalyst surface.[214,215] This observation allowed designing layer structure-type oxide systems toward OER.

3.1.4. Layer Structure Type Family. Basically the layer structure compounds possess good electric conductivity. Layer structure metal hydroxides ($M(OH)_2$; M = transition metals) and metal oxyhydroxides (MOOH) have shown very high electrocatalytic activity toward OER. The crystal structure can be described as a layered-stacking conformation with proton in between layers. The transition metals are situated in

the middle of the octahedron and oxygen anions on the corners as [MO_6] subunits and these subunits are connecting together via edges building 2-D layers (Figure 3.4.(a)).

Layer structure-type oxides have been classified as layered double hydroxides (LDH). Typically this family is often cobalt- and nickel-based compounds because of their high activity toward OER. These LDH compounds have been extensively studied and demonstrated to show powerful catalytic efficiencies for OER with performance closer to that of precious metal oxides. A systematic study of 3d transition-metals (Ni, Co, Fe, Mn) hydr(oxy)oxide for OER activity has been carried out,[217] and was found that the activity followed the same trend (Ni > Co > Fe > Mn) as observed in perovskite systems.[193]

According to Sabatier principle, the excellent OER activity for the NiOOH sample could be attributed to the maximum bonding strength between Ni and OH. Regardless of the above observation, Corrigan[217] has proposed that the presence of Fe impurities (1 ppm) in the unpurified electrolyte enhances the OER activity of NiOOH with increasing Fe content. Trotochaud et al. have also investigated the influence of Fe ions in NiOOH.[218] It was concluded that the electrocatalytic activity of NiOOH for OER was affected by the presence of Fe ions (Figure 3.4.(b)). As the Fe content reached 25% in the $Ni_{1-x}Fe_xOOH$, the overpotential was significantly dropped by a value of 200 mV. This improvement, however, cannot be explained solely by the slight increase in conductivity but due to co-participation with Fe. It was also demonstrated that the improvement in the $Ni(OH)_2$ and NiOOH system could be attributed to the phase transformation behavior during charge/discharge in alkaline solution. The β-(Ni^{2+})(OH^-)$_2$ loses a proton (H^+) to form β-(Ni^{3+})(OOH^{3-}), as shown in Figure 3.4.(c).[219] Similarly, the α-$Ni(OH)_2$ would tolerate an

aging effect and transform into γ-$Ni(OH)_2$ in alkaline solution. β-NiOOH (dehydrated) also underwent transformation into γ-NiOOH (hydrated) under long-term overcharging.

Several investigations suggested that the OER activity of $Ni(OH)_2$ increases in unpurified KOH while decreases in a purified KOH electrolyte.[218,219] The improvement during the OER has been commonly attributed to the phase transformation of α-$Ni(OH)_2$ to β-$Ni(OH)_2$ (so-called aging effect). However, Trotochaud et al. and Klaus et al.[218,219] have indicated that increasing OER activities of $Ni(OH)_2$ and NiOOH systems were mostly due to the existence of Fe impurities in the system. The $Ni_{1-x}Fe_xOOH$ catalyst has exhibited great potential for OER. Song and Hu synthesized single-layer nanosheets (NS) of NiFe LDH material through exfoliation method.[220] NiFe-NS showed a comparable OER performance to precious metal oxides such as RuO_2 and IrO_2 (Figure 3.4.(d)) with an overpotential of ~ 300 mV and a Tafel slope of ~ 40 mV dec^{-1}.

The group of Grätzel reported NiFe layered double hydroxide (LDH) as bifunctional electrocatalyst for overall water to approach a step closer to practical application.[221] This bifunctional catalyst delivers a 10 mA cm^{-2} current density at a cell voltage of 1.7 V in alkaline medium.

Long et al.[222] have studied the OER activity of FeNi LDH by creating graphene oxide (GO) and reduced graphene oxide (rGO) layers between metal oxide layers to form an individual alternated stacking conformation. These hybrid catalysts, FeNi–GO LDH and FeNi–rGO LDH, have shown remarkable high OER activities with overpotentials of 210 mV and 195 mV, respectively. Fe doping in the CoOOH LDH system has also shown a similar effect and revealed that could improve its OER activity.[223] Introduction of other elements such as Mn and Cr, in NiOOH was also found to enhance OER activity.[224]

Recently, Zhang et al. included W and Fe in β-CoOOH system utilizing sol-gel method to optimize the OER catalytic performance.[225] Addition of Fe and W in gelled-FeCoW LDH could modify the adsorption energy of Co–OH to acquire an appropriate energy state and therefore reduce the overpotential to 190 mV for OER.

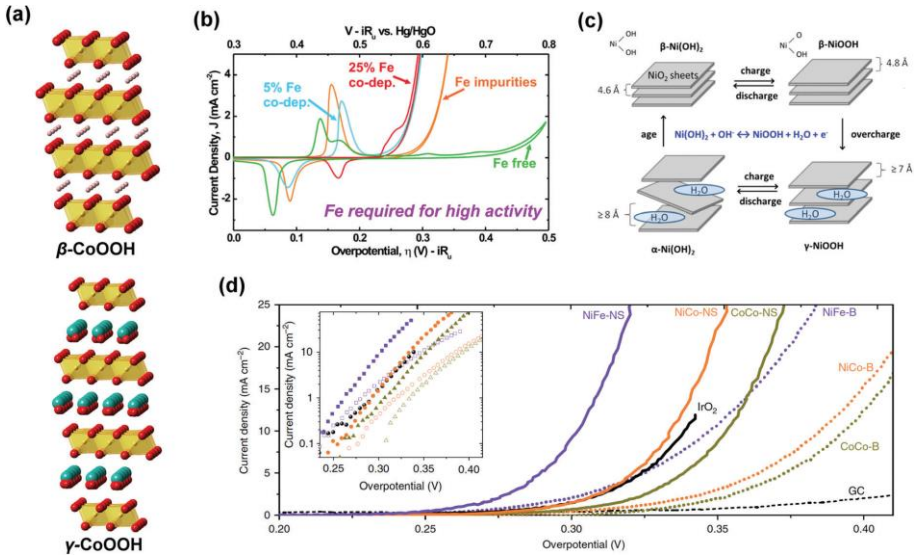

Figure 3.4. (a) Crystal structures of LDH b-CoOOH and g-CoOOH. (b) Cyclic voltammetry measurements for different Fe content in $Ni_{1-x}Fe_xOOH$ and measurements for NiOOH in purified and non-purified electrolytes.[218] (c) Schematic illustration of Bode scheme.[219] (d) OER performance of exfoliated NiFe-, NiCo and CoCo-NS (nanosheet) and non-exfoliated NiFe-, NiCo and CoCo-B (bulk). [220]

Since Fe was observed to act as the active site in both Co(Fe)OOH and Ni(Fe)OOH, the γ-FeOOH was also expected to show some OER electrocatalytic activity.[223,226] However, pure γ-FeOOH showed very poor OER electrocatalytic activity at low applied potential,[227,228] whereas the OER activity dramatically increased at overpotential above 450 mV. This improvement in OER activity under high anodic potential might be attributed to the enhancement of the electronic conductivity of γ-FeOOH. Although the excellent performance of γ-FeOOH at high anodic potential, the long-term durability decreased due

to the formation of FeO_4^{2-} which would dissolve in the electrolyte.[227,228] The intrinsic poor electronic conductivity of γ-FeOOH could be another reason for the inferior OER activity. Hybridization of FeOOH with CeO_2 to establish a heterolayered nanotube conformation on the nickel foam substrate could overcome these drawbacks and to improve the long-term durability as well as the overpotential of OER.[229]

Another layer structure type family, $LiMO_2$ (M = Co and Ni) materials were also studied for OER activity. The structure of the $LiMO_2$ is similar to that of their oxyhydroxides (i.e., β-CoOOH and β-NiOOH) except only the proton (H^+) was replaced by Li^+. The doping of Fe in $LiNi_{1-x}M_xO_2$ (M = Mn, Fe, Co) compounds was also observed to increase OER catalytic performance.[230] A similar observation was also suggested for a delithiatized $LiCoO_2$ system. The delithiatized $LiCoO_2$ samples was prepared electrochemically through a tuning route.[231] The OER activity was improved on the delithiated samples when compared to un-treated ones. Furthermore, a higher oxidation state of Co may perform higher OER activity due to the enhancement of the O adsorption to facilitate the interaction with OH^- to form oxyhydroxide (OOH) intermediate (rate-determining step) on the surface of the catalyst.[231] In addition to enhancing the intrinsic activity of an electocatalyst, lower overpotentials might be achieved through creating multiple layer catalyst films where active sites can be assembled on top of one another (Figure 3.5). This approach of course generates more active site density per unit area and electrons, protons, counter-ions, substrate molecules, and product species should be delivered in a very short period of time to and from each active site with sufficient relieves the turnover frequency (TOF) load for each active site. All species including quickness that entire active sites can be utilized efficiently. While slow intra-film transport could lead to

a low catalytic current density failing to reach its top value due to poor utilization of all catalyst materials. Catalysts with charge transport are highly desirable, since this ensures facile assembly of such multilayer catalysts, and does not need any additional process besides catalyst synthesis.

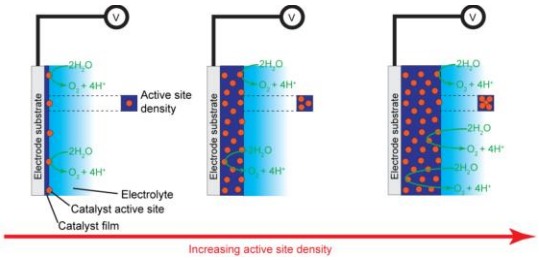

Figure 3.5. Paradigms for electrocatalysis. Lower overpotentials for a desired current density can be achieved by increasing the intrinsic activity of catalyst active sites.

3.1.5. Other Oxides. It is worth mentioning that the OER activity of electrocatalysts can be optimized through doping an appropriate amount of transition metals in these electrocatalysts. Merrill and Dougherty assessed a series of transition metal (Mn – Cu) oxide as electrocatalysts for water splitting.[232] They found that Ni-Fe oxide mixture exhibited the optimum catalysis among all other screened catalysts. It was concluded that the catalytic properties of these catalysts can be influenced through changing the preparation parameters.

In an amorphous system, 21 amorphous compounds were synthesized with various stoichiometry ratios including Fe, Co and Ni (a-$Fe_{100-y-z}Co_yNi_zO_x$) and OER activities were evaluated (Figure 3.6.(a)).[233] Among all samples, the a-$Fe_{40}Ni_{60}O_x$ showed the highest electrocatalytic kinetics for OER, while further increasing the amount of Fe was found to inhibit the OER activity. Incorporation of Fe in a-CoO_x was observed to have also a similar effect of that of a-NiO_x. However, doping of Co into binary a-$Fe_{40}Ni_{60}O_x$ to form ternary

a-$Fe_{39}Ni_{39}Co_{22}O_x$ was counterproductive toward the OER activity.[233] The doping effects of Fe, Co and Ni in a given oxide system (spinel and layer structure type family) seem to be universal and can be extended to other systems. A replacement of Fe with Mn, Co and Ni in a $LiFePO_4$-based material was studied as an electrocatalyst for OER.[194] The doping strategy was noted to have a similar influence on the $Li(FeM)PO_4$ (M= Mn, Co and Ni) system. $Li(FeNi)PO_4$ displayed the best OER performance among compounds and insertion of Co further enhanced the OER activity. Delithiatization of $LiMO_2$ (M = Co and Ni),[231] led to higher oxidation state of the transition metal which promoted the OER activity of the De-$Li(NiFe)PO_4$ sample ($\eta \sim 270$ mV at 10 mA cm^{-2}). These metal oxides commonly exhibited very low activity in neutral electrolyte while very few catalysts are active in neutral media (pH ~ 7).[234-239] In situ formation of CoPi during OER in phosphate buffer solution has been reported.[234,240] The CoPi exhibited an overpotential of 410 mV at a current density of 1 mA cm^{-2} with a long-term stability due to its self-healing property.[234] The promising results of CoPi have drawn great attention owing to its properties such as crystal structure, composition and mechanism toward OER. The local structure of CoPi was analyzed utilizing *in situ* X-ray absorption spectroscopy (XAS).[241,242] Kanan et al.[242] have proposed structural models for CoPi and suggested that the model is consisting of edge-sharing [CoO_6] theme in molecular dimension which is similar to that observed in CoOOH.[242] It was noted that as the applied potential exceeds 1.25 V vs. RHE the oxidation state of Co was elevated above 3+. The same phenomenon has also been observed in CoPi by McAlpin et al. through ex-situ electron paramagnetic resonance (ex-EPR) measurement and the oxidation state of Co further increases to reach Co^{4+} in CoPi clarifying that the rest state is a combination of Co^{3+} and Co^{4+} during OER.[152] A close insight into the OER

mechanism with regards to the CoPi system (Figure 3.6.(b))[243] has drawn several key conclusions such as: (1) phosphate buffer electrolyte serves as a proton acceptor, but the proton transfer step is not the turnover-limiting step; (2) Tafel slope of CoPi shows a value of 60 mV dec^{-1} revealing that the reaction undergoes an one electron/proton step and follows the turnover-limiting chemical step (formation of O–O bond to produce O_2).

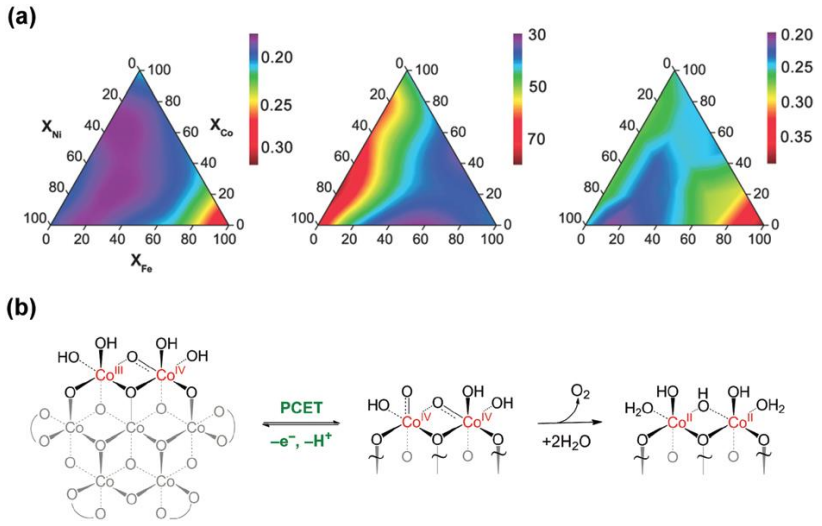

Figure 3.6. (a) Contour plots for onset overpotential (η) (left), Tafel slopes (middle) and overpotential (η) at 0.5 mA cm^{-2} (right) for reported 21 metal oxide films.[233] (b) Proposed OER mechanism for CoPi.[243]

Interestingly most of the Co_3O_4 and Co-based hydroxide/oxydroxides show a similar value of Tafel slopes (60 mV dec^{-1}), which suggests the mechanisms of these electrocatalysts for OER are similar. Subsequently, considerable studies regarding catalysts containing transition metals such as Mn, Fe and Ni have been investigated in neutral solution (pH ~ 7).[237,238,244] The mechanisms for these transitional metal-based oxides appear to be different from each other depending on the media. For instance, an electrodeposited δ-MnO_2 was applied for OER activity in electrolytes with a pH range from

3 to 13.[239] According to in situ UV-vis spectra, an absorption peak at 510 nm during water oxidation was observed which could be attributed to Mn^{3+} surface intermediates. In acidic solution, the formed Mn^{3+} ions were unstable and undergo a self-disproportionation reaction to generate Mn^{2+} and Mn^{4+}. Mn^{2+} would dissolve in electrolyte before producing Mn^{3+}, which could be the reason for its instability. In alkaline media (pH > 9), the self-disproportionation reaction is suppressed because of a higher stability of Mn^{3+} to generate higher population of Mn^{3+}, thus leading to a better OER electrocatalytic activity of δ-MnO_2.[239] The OER activity of MnO_x–Pi was reported as pH dependent and suggested different mechanisms in acidic and alkaline media. Two mechanisms were proposed to compete with each other in neutral media.[237] The rate-limiting step under hard acidic environment was the deprotonation of OH^- to bridge between two Mn^{4+} ions. This step was kinetically slow in acid environment with a very high Tafel slope (653 mV dec^{-1}). On the other hand, in hard alkaline conditions, the Tafel slope was lowered to a value of 60 mV dec^{-1}. The relative small rate-limiting step indicates the chemical step (most likely O_2 evolution) became the predominant step and followed by one electron/proton transfer reaction. Other electrocatalyst systems such as Bi_2WO_6,[236] Mn_5O_8[235] and $Co(PO_3)_2$,[152,245] with well-defined stoichiometries have shown superior OER activity to Co–Pi in a neutral system.

A Ni–borate (Ni–Bi) system has also been reported[238,246,247] and exhibited superior electrocatalytic kinetics of OER (Tafel slopes in neutral; 30 mV dec^{-1} for Ni–Bi, 60 mV dec^{-1} for Co–Pi and 120 mV dec^{-1} for MnO_x–Pi). The structure of pristine Ni–Bi film resembled β-NiOOH and transformed to a short-range δ-NiOOH like structure during OER (higher oxidation state of Ni and less Jahn–Teller distortion).[246] The Tafel slopes were

observed at 30 mV dec^{-1} for non-anodized Ni–Bi (β-NiOOH like structure) and at 100 mV dec^{-1} for anodized Ni–Bi (δ-NiOOH like structure). The phase of Ni–Bi transformed δ -NiOOH like exhibited a considerable OER activity comparing to β-NiOOH like structure.

3.2. NON-OXIDE ELECTROCATALYSTS FOR OER

3.2.1. Metal Chalcogenides. Transition metal oxides are known to possess wide bandgap and classify as insulating, whereas transition metal chalcogenides with narrower bandgap could be considered as a semiconducting and some of them due to zero bandgap are metals.[248-258] very wide bandgap (3.5 eV) was estimated for NiO but much smaller bandgaps of NiS_2 and $NiSe_2$ (0.35 eV and 0.0 eV, respectively) were observed.[248,249] Due to decreasing electronegativity from O to Te, the valence band edge is expected to rise higher in energy and show a higher degree of covalency. These movements in the orbital energy levels will affect the alignment of these orbitals with respect to the water oxidation and reduction energy levels. This in turn will affect the charge transfer between the catalyst and water because the valence and conduction band edges of the catalyst are just above the energy levels of water oxidation-reduction.[251,252] Perfect alignment and closeness of the orbitals could result better charge transfer at the catalyst-electrolyte interface and hence improve significantly the water oxidation-reduction.

Metal oxides have shown outstanding electrocatalytic abilities for OER, and the intrinsic electroconductivity of the materials would be increased from oxides to other chalcogenides (sulfide, selenides or telluride). Cobalt- and nickel-based compounds have been known as the most active metal chalcogenides for the water-splitting reaction. Compounds such as AB, AB_2, A_9S_8, Ni_3B_2, A_3S_4 (A = Co and Ni, B = S, Se and Te) have

originally been utilized for HER due to their excellent electroconductivities with no corrosion in both acid and alkaline electrolyte.[261-276] Bifunctional materials to perform the overall water splitting reaction in the same electrolyte have rarely been inspected.[261-276] The coordination of the transition metals are generally octahedral except A_9S_8, Ni_3B_2 and A_3S_4,[259,270,272-274] which they are tetrahedral coordination. The $[AB_6]$ possesses octahedral coordination connecting to each other through a B–B bond $[B_2]^{2-}$ in AB_2, which results in oxidation state +2 for Co and Ni in these compounds instead of +4. The chalcogenides generally show robust properties and in some cases outperform OER activities of metal oxides. Commonly these chalcogenide compounds exhibit overpotentials of 200 - 300 mV to drive a current density of 10 mA cm^{-2}.

Zhou and co-workers had studied nickel sulfide for OER in alkaline media.[253] The Ni_3S_2 nanorods on Ni foam was synthesized by hydrothermal reaction and exhibited a good catalytic activity for OER. Nickel sulfide, NiS_x, has also shown an efficient performance as bifunctional active catalysts and become a great demand for water electrolysis.[254,255] In another investigation NiSe nanostructures were tested and displayed good catalytic activities for HER process.[256] Indeed Ni- and Co-based chalcogenides have shown great promise for water electrolysis in alkaline medium.[258-260,277-279] In fact, these decent observations reveal that these transition metal chalcogenides due to their outstanding catalytic performance, could promisingly substitute precious materials electrocatalysts as their comparable catalytic activities toward the ORR and HER and much lower cost are considered. [254,280-288]

Metallic electrocatalysts have ignited great interest owing to their good conductivity and thus remarkable electroactivity.[289] CoS_2 has been investigated as a

promising alternative catalyst for the HER.[290] Also $CoSe_2$/DETA (DETA= diethylenetriamine) nanobelts[291] showed very good activities for the OER[292] and oxygen reduction reaction (ORR),[293] and electrocatalytic performance can be further enhanced by synergistic coupling with other functional nanostructures.[292,293] Yu et al. investigated a novel $MoS_2/CoSe_2$ hybrid with an excellent HER activity in acidic media[294] and an efficient CeO_2 /$CoSe_2$ composite electrocatalyst toward OER in alkaline solutions.[295] However, the development of metallic-material based bifunctional hybrids for efficient overall water splitting with less over potential remains to be further improved.

Chen et al.[261] have studied NiS on a stainless steel mesh support and the overpotential was observed at ~ 297 mV to deliver 11 mA cm^{-2} with a Tafel slope of 47 mV dec^{-1}. A similar OER activity for NiS microsphere was noted as well.[263] Incorporating foreign metal ions in these systems seems to work as well to improve OER activity. $FeNiS_2$ ultrathin nanosheets were investigated to show a notable performance,[296] with overpotential was observed at 290 mV to obtain a current density pf 10 mA cm^{-2} and a Tafel slope of 46 mV dec^{-1}. The insertion of Ni in $Co_{0.85}Se$ enhances electroconductivity and could improve OER performance. The overpotentials at 10 mA cm^{-2} for $Co_{0.85}Se$ and $(Ni,Co)_{0.85}Se$ were reported at 324 mV and 255 mV, respectively.[193] This ternary chalcogenide displayed long-term durability, however the overpotential to deliver a current density of 10 mA cm^{-2} was increased to 276 mV after 24 hours operation. Creating LDH on the surface of $(Ni, Co)_{0.85}Se$ by electrodeposition could further enhance the OER activity of $(Ni,Co)_{0.85}Se$–NiCo LDH and reduce the overpotential to 216 mV.[265] Interestingly, the CoSe and NiS transform into oxide forms on the surface during OER.[269,297] The phase

transformation might occur through oxidation from Ni^{2+}/Co^{2+} to Ni^{3+}/Co^{3+} which is similar to spinel cases.

Metal dichalcogenides were also reported as very promising candidates for OER. $CoSe_2$ nanobelts on nitrogen-doped graphene support have been synthesized and an overpotential of 366 mV was observed with Tafel slope of around 40 mV dec^{-1}. The active sites of $CoSe_2$ was increased (cobalt vacancy, Figure 3.7.(a)) using an exfoliation process and promoted the OER activity.[270] Striking OER activity of $FeNiSe_2$ derived oxide catalysts was achieved with an overpotential of ~ 195 mV at 10 mA cm^{-2} and a Tafel slope of 28 mV dec^{-1} (Figure 3.7.(b)). The energy dispersive spectrum (EDS) analysis confirmed that the Se content decayed with increasing the amount of O in $NixFe_{1-x}Se_2$ after OER, while $NixFe_{1-x}Se_2$ was assumed to transform into metal oxyhydroxide.[271] The derived oxide

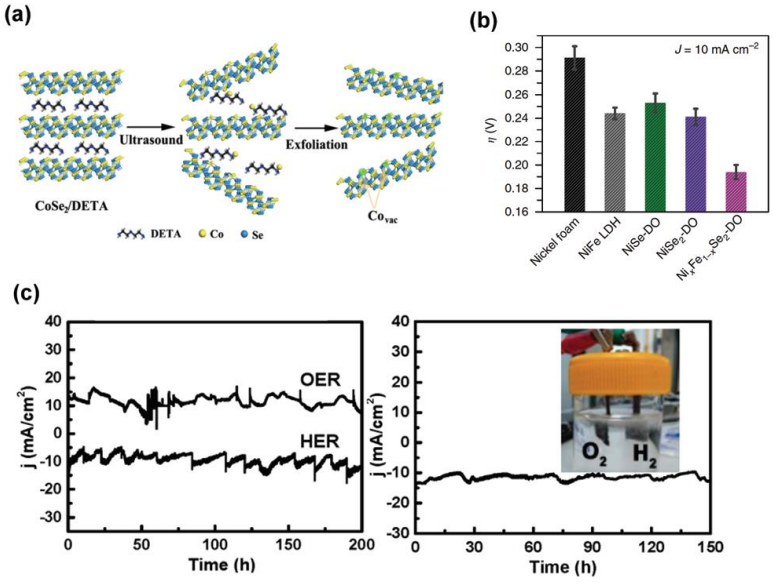

Figure 3.7. (a) A schematic illustration of the exfoliation process of $CeSe_2$ to increase the number of active sites (Covac).[270] (b) Overpotential (η) at 10 mA cm^{-2} for Ni foam, NiFe LHD, NiSe-DO, $NiSe_2$-DO and $NixFe_{1-x}Se_2$-DO (DO represent derived oxide).[271] (c) Current vs. time (I–t) of Ni_3S_2/NF for HER and OER (left) while the overall water electrolysis by Ni_3S_2/NF bifunctional electrodes at 1.76 V was recorded to 150 hours (right).[272]

($NixFe_{1-x}Se_2$-DO) displayed excellent OER activity, suggesting that the conductive $NixFe_{1-x}Se_2$ served as conductive scaffold for rapid charge transfer.[271] Hybrid materials between oxides and metal chalcogenides have shown improvement corresponding OER activities. Synergistic effects may also play important keys for the OER activity.

The phase transformation during OER might not have applied to all metal chalcogenides. In the case of Ni_3Se_2, the crystal structure and elemental analysis of the corresponding catalyst revealed that the Ni_3Se_2 was preserved even after 42 h of continuous O_2 evolution.[259] This observation indicates the high stability of Ni_3Se_2 and the OER activity could be attributed to nickel selenide itself without any phase transformation. Feng et al.[272] have reported a Ni_3S_2 nanosheet and demonstrated excellent bifunctional (HER and OER) electrocatalytic ability in alkaline electrolyte with remarkable long-term stability (over 150 hours, Figure 3.7. (c)).

3.2.2. Metal Pnictides (Nitrides and Phosphides). Due to their good electroconductivity and durability in harsh electrolytes, pnictides such as Co_2N, Co_3N, Co_4N, Ni_3N, AP and A_2P (A= Co and Ni) have also been explored for HER.[298-300] These electrocatalysts with remarkable HER activities ($\eta < 200$ mV) in alkaline electrolyte have encouraged bifunctional candidates for the water splitting reaction. Nevertheless, very few studies corresponding pnictides have been conducted regarding OER.[307-314] A similar observation of phase transformation to that of metal chalcogenides was noted for pnictides during the OER in which a thin metal oxide layer was formed along with metal pnictide layer to increase electroconductivity and facilitates electron transfer and therefore shows OER improvement.[310,311] A study of series cobalt nitrides (Co_2N, Co_3N and Co_4N) implied that the conductivity of these materials increase with increasing the amounts of cobalt and

thereby higher activity for OER.[312] Modifying material morphology of bulk Ni_3N to Ni_3N nanosheets was seen to be enhanced due to a higher density of states emerging for the Ni_3N nanosheet at the Fermi level based on theoretical calculations (Figure 3.8.(a)).[313]

The electroconductivity of the catalysts can also be enhanced through merging catalyst materials with conducting substrates such as carbon or nickel foam to create more active sites.[314,317] For instance, coupling of CoP with reduced graphene oxide showed overpotential values of ~ 340 mV and 105 mV at 10 mA cm^{-2} for OER and HER activities, respectively, and the overpotential was 445 mV for overall water-splitting.[318]

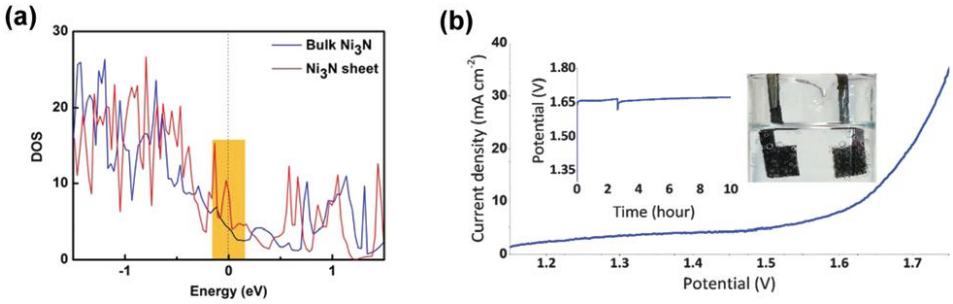

Figure 3.8. (a) Theoretical calculation of the density of states (DOS) of Ni_3N (bulk and sheet).[313] (b) Current vs. potential curve of bifunctional Ni_2P water electrolysis. Inset is current vs. time (I–t) for overall water electrolysis by Ni_2P bifunctional electrodes at constant 10 mA cm^{-2}.[311]

Another alternative approach to enhance electrocatalytic performance is through doping or partially replacing elements in catalyst materials. Commonly, doping of Fe into Co- or Ni-based electrocatalysts has demonstrated to improve OER activity. Duan et al.,[315] proposed that substituting anions in electrocatalysts, in which CoFePO (Fe- and O-doped Co_2P phase) were synthesized on Ni foam substrate, showed a remarkable low overpotential of 362 mV at 10 mA cm^{-2} for overall water splitting (274.5 mV and 87.5 mV for OER and HER, respectively). Although insertion of other transition metals into

pnictides electrocatalysts could improve their OER activities, their performance deteriorated just after long-term operation.[316] The surface oxidation with etching phosphorous of CoMnP may be a major reason for the decay in OER performance.[316] Precise control of the composition, morphology and even structure of the surface oxides derived from the doped catalysts is a difficult task. The surface composition of derived oxide might deviate resulting in undesired composition of that of the initial catalysts. Despite the uncertainty in doped metal pnictides, CoP and Ni_2P still prove durable electrocatalytic ability toward OER.[310,311,321] A core–shell assembly (Ni_2P/NiO_x) exhibited over 10 hours stability with overpotentials of 290 mV and 110 mV at 10 mA cm^{-2} for OER and HER, respectively (Figure 3.8.(b)).[311]

3.2.3. Organometallics. The main purpose of designing the catalyst materials in the field of water splitting is to mimic the "$CaMn_4O_5$ cluster" of the oxygen-evolving complex in photosystem II, (PSII).[317] Oxygen-evolving complex systems are mainly organometallic compounds containing transition metals such as Mn, Fe, Co, Ru and Ir. As mentioned in previous sections, oxide/non-oxide electrocatalyst materials for OER are heterogeneous catalysts for the water-splitting reaction while organometallics are homogenous catalysts and in some cases of composite catalysts are heterogeneous catalysts. Understanding the structures and electronic states of organometallics could shed light on their mechanisms for OER. However, low electroconductivities and poor stabilities hinder these materials from practical usage. Many attempts have been made to overcome these shortcomings of these organometallic compounds. Recently, composite materials such as mononuclear, multinuclear and cluster organometallic electrocatalysts have been studied to exhibit superior OER activity.[318-320] A manganese corrole complex displays

bifunctional properties for whole water splitting.[321] This complex was modified by replacing manganese with cobalt on multi-walled carbon nanotubes (MWCNTs) for improving the catalytic activity.[322] Excellent stability and OER performance without this substitution were observed, which could be attributed to the p–p interaction between the pyrene and multi-walled carbon nanotubes.[322] A bimetallic porphyrin system have been designed by incorporating Fe and Co (Figure 3.9.(a)) in the porphyrin.[323] The Fe is in the center of porphyrin and four pyridyl groups (FeTPyP–Co) bridge the Co and thereby exhibited the highest electrocatalytic activity for OER and ORR among all proposed catalysts (M^1TPyP < M^1TPyP–Fe < M^1TPyP–Co; M^1= Fe and Co). Sun et al.[324] demonstrated Ni- and Co-porphyrin anchored on reduced graphene oxide (rGO) to form a layer-by-layered architecture, in which the 8 layers compound was made to show an appreciable low overpotential of ~ 330 mV and a low Tafel slope of 50 mV dec^{-1}.

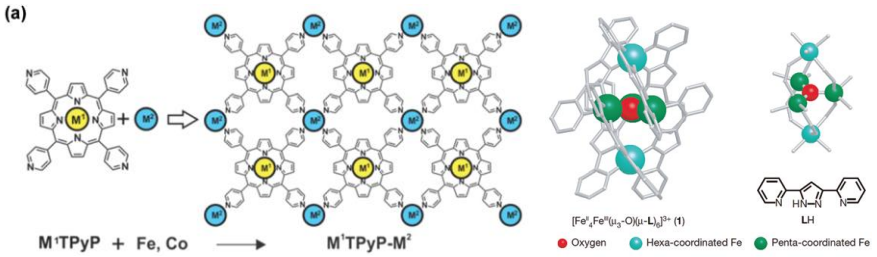

Figure 3.9. (a) Structure of M^1–TPyP and proposed structural model for extended bimetallic (M^1 and M^2) M^1–TPyP–M^2.[323] (b) Molecular structure of $[Fe^{II}_4Fe^{III}(\mu_3\text{-}O)(\mu\text{-}L)_6]^{3+}$ (left); core structure of Fe_5O and chemical structure the LH (right).[318]

Recently, some dinuclear, multinuclear organometallics, and cluster metal–organic compounds have also been investigated. Sheehan et al.[325] have demonstrated a very high stability of dinuclear Ir-based material binding to the electrode, while the deposited ligand on $[Ir(pyalc)(H_2O)(O)(\mu\text{-}O)]_2$ was observed intact under a high potential during OER.

Okamura et al.[318] proposed another pentanuclear iron catalyst with a weird trigonal-bipyramidal molecular shape. The O atom located in the center and Fe on the corner (Figure 3.9.(c)) while O_2 gas evolved via intramolecular O–O bond formation. This pathway mechanism for oxygen evolution was proposed by Ullman et al. as well.[326]

3.2.4. Non-Metal Compounds. Searching for low cost materials and efficient electrocatalysts for OER is not an easy task, but are still followed. Using Non-metal materials is among best approaches for developing efficient electrocatalysts. Mirzakulova et al.[328] reported an electrocatalyst of N(5)-ethylflavinium ion ($Et–Fl^+$) as first demonstration of a non-metal compound to promote the oxygen evolution reaction. The OER activity of N(5)-ethylflavinium ion was poor with η >1 V and a Faradaic efficiency of ~ 30 % in 0.1 M phosphate buffer solution. This pioneering work has opened a new avenue for the latter work in this area. The carbon between N and C=O (ketone group) was proposed as the active site, which due to its location could carry positive charge to adsorb OH^- and initiate the water oxidation process. This inspiring work has motivated other researchers to investigate other non-metal electrocatalysts for OER.

Carbon-based materials such as carbon black, carbon nanotubes, and graphene with N, O and S doping, have attracted attentions due to their good electroconductivities and are considered as chemically inert to acid and alkaline media.[328] For instance, carbon black (nitrogen-doped carbon) nanomaterials have demonstrated a remarkable activity with an overpotential of 380 mV at a current density of 10 mA cm^{-2} in KOH electrolyte.[329] At high anodic potential (above 0.9 V vs. RHE),[330] carbon black might undergo oxidation to produce carbon dioxide which indeed led to low stability. Carbon nanotubes and graphene/ graphene-like compounds are well-known to be more conductive and stable than carbon

black. Due to high conductivity of carbon nanotubes, Cheng et al.[331] have systematically studied the correlation between the numbers of the walls and their corresponding OER activities of carbon nanotubes (SWNTs and MWNTs). It was stated that the outermost wall is responsible for OER while the inner one serves as an efficient conducting layer to mediate the electron transfer. The OER activity could be enhanced with increasing the numbers of walls. However, too many walls in carbon nanotubes may suppress the OER activity, which could be attributed to the inhibition of electron transfer between the outermost wall and neighboring inner wall. Oxidizing the surface of the carbon nanotubes (Figure 3.10.(a)),[332] was suggested as a very effective way to increase the OER activity with a reported overpotential of ~ 360 mV at 10 mA cm^{-2} which is comparable to that reported for metal oxides/chalcogenides/pnictides. Chen et al.[333] have synthesized a 3D-conformation through the mixing of nitrogen and oxygen dual doped graphene and carbon nanotubes which could exhibit higher surface area and more active sites. This hybrid material reported an overpotential of 365 mV at 5 mA cm^{-2} while the Tafel slope was ~ 141 mV dec^{-1}. Mixing graphitic (g-C_3N_4) with graphene/carbon nanotube forms composite catalyst for OER.[334,335] An excellent OER activity should be expected as active sites increased (neighboring carbon atoms to nitrogen atoms are considered as the active sites). Indeed, g-C_3N_4/graphene showed a high OER performance with an overpotential of ~ 539 mV and a small Tafel slope of ~ 68.5 mV dec^{-1} in 0.1 M KOH.[335] Ma et al.[335] synthesized a 3D g-C_3N_4/carbon nanotubes structure (Figure 3.10.(b)) demonstrated higher OER activity and an overpotential of ~ 370 mV with a Tafel slope of ~ 83 mV dec^{-1} were recorded. Moreover, mixing g-C_3N_4 with other metal catalysts could show promising catalytic activities for OER as well as ORR. Ma et al.,[336] have recently prepared a hybrid

Film of overlapped g-C_3N_4 and Ti_3C_2 through an exfoliation process in which this composite material showed long-term stability toward OER. Recently, black phosphorus prepared by the thermal-vaporization transformation employed for OER to deliver a current density of 10 mA cm^{-2} at an overpotential of ~ 370 mV.[337] Further modification could guide to better OER activity than reported for the state-of-the-art RuO_2. To this end, non-oxide compounds have also demonstrated excellent OER and HER activities, and could be further developed to be utilized for the overall water splitting reaction.

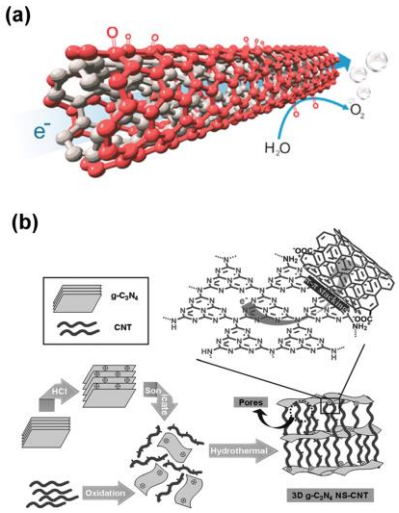

Figure 3.10. (a) A schematic illustration of the surface-oxidized multi-walled carbon nanotubes.[333] (b) A schematic flow chart for the process to fabricated of 3D g-C_3N_4 and NS-CNT porous composite.[335]

PAPER

I. NICKEL SELENIDE AS A HIGH-EFFICIENCY CATALYST FOR OXYGEN EVOLUTION REACTION

Energy Environ. Sci., 2016, **9**, 1771—1782

A. T. Swesi, J. Masud and M. Nath

Department of Chemistry

Missouri University of Science and Technology

Rolla, Missouri 65409-0050 USA

Email: nathm@mst.edu

ABSTRACT

A metal-rich form of Ni-selenide, nickel subselenide, Ni_3Se_2 has been investigated as a potential oxygen evolution electrocatalyst under alkaline conditions for the first time. The Ni_3Se_2 phase has a structure similar to the sulfur mineral heazlewoodite, which contains metal–metal bonding. The electrocatalytic activities of Ni_3Se_2 towards OER were seen to be at par with or even superior to the transition metal oxide based electrocatalyst in terms of onset overpotential for O_2 evolution as well as overpotential to reach a current density of 10 mA cm^{-2} (observed at 290 mV). The electrocatalytic Ni_3Se_2 films were grown by electrodeposition on conducting substrates and the deposition parameters including the pH of the electrolytic bath, deposition potential, and substrate composition were seen to

have some influence on the catalytic activity. So far, Ni_3Se_2 films deposited on the Au-coated Si substrate was seen to have the lowest overpotential. Annealing of the as-deposited electrocatalytic films in an inert atmosphere, enhanced their catalytic efficiencies by decreasing the overpotential (@10 mA cm^{-2}) as well as increasing the current density. The structure and morphology of these films has been characterized by powder X-ray diffraction, scanning and transmission electron microscopy, Raman, and X-ray photoelectron spectroscopy. Catalytic activities were investigated through detailed electrochemical studies under alkaline conditions, including linear sweep voltammetry, chronoamperometric studies at constant potential, electrochemical surface area determination and calculation of the Tafel slope. The Faradaic efficiency of this catalyst has been estimated by reducing the evolved O_2 in a RRDE set-up which also confirmed that the evolved gas was indeed O_2. In addition to low overpotentials, these Ni_3Se_2 electrodeposited films were seen to be exceptionally stable under conditions of continuous O_2 evolution for an extended period (42 h).

BROADER CONTEXT

Oxygen evolution is one of the most kinetically hindered process for water electrolysis. Thus, oxygen evolution catalysts containing earth abundant elements have recently been at the center of attraction to address this challenge both in terms of high performance and practical applicability. Nickel oxides are among the best precious metal-free commercial electrolyzers. However, replacing the oxides with selenides introduces several favorable factors which can further enhance the catalytic performance of the nickel

based electrocatalysts. This article describes the identification of Ni_3Se_2 as a high-efficiency oxygen evolution electrocatalyst with extended stability under alkaline conditions capable of generating oxygen at a much lower applied potential. Structural richness of the chalcogenides along with their amenable electronic properties holds a lot of promise for further tuning of the electrocatalyst performance and systematic studies with the nickel chalcogenides will significantly benefit the search for a water oxidation catalyst with low cost, high-efficiency and high durability.

1. INTRODUCTION

The splitting of water into H_2 and O_2 through the application of sunlight or electric pulse has been an attractive avenue for alternative energy generation using earth abundant resources for the last several decades.[1–3] The efficiencies of oxygen and hydrogen evolution reactions (OER and HER, respectively) which are the constituent half reactions for water splitting play a critical role in the advancement of renewable energy technologies like metal–air batteries or solar-to-fuel energy production. Among these, although the oxygen evolution reaction has the advantages of being sustainable and relatively benign in terms of impact on the environment and human health, however, OER typically being a 4 electron process requiring O–O bond formation is a kinetically slow process.[4] Several catalysts are normally used to expedite this inherently sluggish process by reducing the overpotential (η) at the respective electrode and also by increasing the rate of conversion.[5–13] The primary considerations for designing an efficient OER catalyst includes long term stability under corrosive conditions of oxygen evolution, low cost, and widely available materials together

with a low overpotential.[9,10,14] To date some of the most efficient and robust OER catalysts in acidic or alkaline medium are based on precious metal oxides like IrO_2 and RuO_2.[9,15,16] However, these precious metal oxides are not the most economically viable options for these catalytic processes based on cost considerations and scarcity of raw materials. The incessant search for efficient OER catalysts from earth abundant materials have resulted in identification of several transitionmetal based oxides as efficient OER catalysts with low η, some of them being comparable with the IrO_2 and RuO_2 catalysts. In particular, Ni and its oxides/hydroxides have long been studied for OER electrocatalytic activities in alkaline solution since the last century primarily due to their enhanced catalytic activity, stability in alkaline solutions and low cost of Ni.[17–30] Merrill and Dougherty assessed a series of transition metal (Mn–Cu) oxides as electrocatalysts for the electrolysis of water.[31] Among this group, a Ni–Fe oxide mixture was found as the optimum catalyst and it was stated that the catalytic properties of the metal oxides can be influenced through other variables of the electrodeposition reaction such as the total and relative concentration(s) and composition(s) of dissolved metal salts and extra electrolytes, the pH, and the duration of the electrodeposition current. Even though in recent times, the most efficient catalytic activity towards OER was obtained by using nickel oxides or hydroxides,[19–29] transition metal chalcogenides (MEn, M = Fe, Co, Ni; E = S, Se) have also been investigated as OER, HER, and ORR electrocatalysts.[32–34] Conventionally, transition metal chalcogenides due to their interesting electronic and optical properties,[35] has been extensively used for several high-tech applications, including high temperature superconductors,[36,37] photovoltaics,[38] and heterogeneous catalysts.[39] In addition their promising activity towards electrocatalysis[17,40,41] has made these materials especially attractive for advanced energy

related applications. Recently a composite electrode containing Ni_3S_2 nanorods synthesized on Ni foam by hydrothermal reaction exhibited very good catalytic activity for OER with a low onset overpotential of ~ 157 mV in alkaline solutions.[34] In a separate study NiSe nanostructures were shown to have good catalytic activities for the HER process.[42] In fact, these recent results illustrate that these transition metal chalcogenides, due to their unique electronic configuration and comparatively high catalytic activity, can be promising substitutes for the Pt-based electrocatalysts when their comparable catalytic activities toward the ORR and HER and much lower cost are considered.[40–49] However, more progress is still needed in order to reduce the cost and improve activity and stability of these electrocatalysts.

The promising OER electrocatalytic activities of nickel based compounds[19–34] including nickel sulfide,[34] and the expectation that increasing covalency might lead to better catalytic activities,[5,11] motivated us to investigate the catalytic activity of nickel selenide towards OER reactions. According to Horn and Goodenough's prediction, increased covalency of the metal–oxygen bond in the oxide electrocatalysts leads to better catalytic efficiency.[11] In this article we report a new nickel selenide based electrocatalyst (Ni_3Se_2) which enhances oxygen evolution with high efficiency under alkaline conditions and exhibits exceptional stability for prolonged time under continuous potentiostatic electrolysis conditions. Typically the efficiencies of OER electrocatalysts are benchmarked by measuring the overpotential (η) at which 10 mA cm^{-2} current density is achieved from the oxygen evolution reaction. For the Ni_3Se_2 electrocatalysts reported here, we observed that it can generate 10 mA cm^{-2} at overpotential as low as 290 mV (upon annealing or using Au-coated Si as the growth substrate) which is one of the lowest overpotentials observed

amongst the known OER catalysts, even better that RuO_2, IrO_2 and NiO_x, some of the best performing catalysts. It is interesting to note that this new electrocatalyst can effectively catalyze the OER without any additional modification (such as doping or hybridizing with graphene or noble metals). Ni_3Se_2 was electrodeposited on different conducting substrates including Au-coated glass, Au-coated Si, glassy carbon (GC), ITO-coated glass, and Ni foam. Detailed structural, morphological and electrochemical characterization of these Ni–Se based OER catalysts has been carried out, which shows that the OER activity was influenced by electrodeposition parameters including the deposition time and pH of the electrochemical bath, annealing, and the nature of the substrate.

2. EXPERIMENTAL AND METHODS

2.1. ELECTRODEPOSITION OF Ni_3Se_2

Nickel acetate tetrahydrate [$Ni(C_2H_4O_2)_2.4H_2O$ from J. T. Baker Chemical Company, USA], selenium dioxide (SeO_2) [Acros Chemicals], lithium chloride (LiCl) [Aldrich] and KOH [Fisher Chemicals] were all of analytical grade purity and were used without further purification. Au-coated glass and Au-coated Si used as substrates in electrodeposition were purchased from Deposition Research Lab Incorporated (DRLI), Lebanon, Missouri. The FTO- and ITO-coated glass slides were purchased from Fisher scientific. All solutions were prepared using deionized (DI) water with a resistivity of 18 MΩ cm. Prior to electrodeposition, the substrates were cleaned by ultrasonic treatment in micro-90 followed by isopropanol rinse three times and eventually rinsed with deionized water (15 min each step) to ensure the clean surface. Au-coated glass/Au-coated Si/ITO-

coated glass /FTO-coated glass plates were covered with a Teflon tape, leaving an exposed geometric area of 0.283 cm^2, and connected as the working electrode. Ni_3Se_2 was electrodeposited on the substrate by a controlled-potential deposition at - 0.80 V (vs. Ag/AgCl) for 40, 130, 300, and 600 s from an aqueous solution containing 10 mM $Ni(CH_3CO_2)_2.4H_2O$, 10 mM SeO_2 and 25 mM LiCl at 25 1C. The pH of the electrolytic bath was adjusted with dilute HCl to be in the range 2.5 - 4.5. After electrodeposition, the substrates were washed with deionized water in order to remove impurities and adsorbents from the surface.

2.2. ANNEALING OF THE Ni_3Se_2 FILMS

To investigate the effect of temperature on the catalytic activities, the as-deposited films were subjected to thermal annealing in the presence of N_2 at 300 ºC for 5–30 min. Annealing experiments were performed either inside a tube furnace under constant N_2 flow controlled by a mass flow controller (300 ºC for 30 min), or in a closed flask under rapid flow of N_2 (300 ºC for 5 min).

2.3. METHODS OF CHARACTERIZATION

2.3.1. Powder X-Ray Diffraction. The electrodeposited substrates were studied as such without any further treatment. The product was characterized through powder X-ray diffraction (PXRD) using Philips X-Pert using CuKa (1.5418 Å) radiation. The PXRD pattern was collected from the as-synthesized product spread on the growth substrate. Because the product formed a very thin layer on the substrate, the PXRD was collected at grazing angles in thin film geometry (GI mode with Göbel mirrors).

2.3.2. Scanning and Transmission Electron Microscopy (SEM and TEM). The SEM image of the modified electrode surfaces was obtained using a FEI Helios NanoLab 600 FIB/FESEM at an acceleration voltage of 10 kV and a working distance of 4.8 mm. Energy dispersive spectroscopy (EDS) along with line scan analysis was also obtained from the SEM microscope. FEI Tecnai F20 was used to obtain high resolution TEM images (HRTEM) and selected area electron diffraction (SAED) patterns of the catalyst. The probe current is 1.2 nA with a spot size of less than 2 nm. STEM mode in the TEM was also used for dark field imaging where the convergence angle was 13 mrad and the camera length was 30 mm. This scope is equipped using an Oxford ultra-thin (UTW) window EDS detector, which allows detection of the elements. For TEM studies a formvar coated Cu grid was positioned and immobilized on the electrode surface (mainly through capillary action) such that during electrodeposition, some material also deposited on the Cu grid directly, which was then analyzed in the TEM.

2.3.3. X-Ray Photoelectron Spectroscopy (XPS). XPS measurements of the catalysts were performed using a KRATOS AXIS 165 X-ray Photoelectron Spectrometer using the monochromatic Al X-ray source. The spectra were collected as is and after sputtering with Ar for 2 min which removes approximately 2 nm from the surface.

2.3.4. ICP-MS Analysis. Known quantities of solid samples were digested by 1.5 mL of concentrated optima-grade nitric acid. After digestion, the samples were diluted appropriate times (10 to 100 times for Fe and 100 to 100 times for Ni) and analyzed by the ICP-MS method. A NexION 350D ICP-MS (PerkinElmer, Inc. Shelton, CT) was used for the analysis. ICP-MS was operated in kinetic energy discrimination (KED) mode to minimize polyatomic interferences. Quantitation isotopes included ^{57}Fe and ^{60}Ni. The

sampling system was a cyclonic spray chamber with a Meinhard nebulizer, and the sampler and skimmer are platinum cones. ICP-MS operational parameters include: RF power, 1600 W; plasma gas flow, 18 L min^{-1}; auxiliary gas flow, 1.20 L min^{-1}; KED mode gas flow 4.5 mL min^{-1}; and nebulizer gas flow: 1.05 L min^{-1}. The US EPA method 200.8 quality control guideline was closed followed to ensure the high quality data.

2.3.5. Raman Spectra. The Horiba Jobin Yvon Lab Raman ARAMIS model was used to perform Raman microspectroscopy on the as-deposited catalyst films. The laser used was He–Ne with a power of about 1.7 mW over a range of 100–2000 cm^{-1}. The spectra were iterated over an average of 25 scans.

2.4. ELECTROCHEMICAL CHARACTERIZATION AND CATALYTIC STUDIES

The OER catalytic performance was estimated from linear scan voltammetry (LSV) plots while the stability of the catalyst was studied by chronoamperometry. Electrochemical measurements were performed in a three-electrode system with an IviumStat potentiostat using the Ag/AgCl and Pt mesh as reference and counter electrodes, respectively. All measured potentials vs. the Ag/AgCl were converted to the reversible hydrogen electrode (RHE) scale via the Nernst Equation (1).

$$E_{RHE} = E_{Ag/AgCl} + 0.059pH + E^{o}_{Ag/AgCl} \quad (1)$$

Where E_{RHE} is the converted potential vs. RHE, $E_{Ag/AgCl}$ is the experimentally measured potential against the Ag/AgCl reference electrode, and $E^{o}_{Ag/AgCl}$ is the standard potential of Ag/AgCl at 25 ºC (0.197 V). For most of the electrochemical characterization, the electrode area of the film surface was kept constant at 0.283 cm^2.

Faradaic efficiency of the Ni_3Se_2 catalytic films was estimated from the ORR–OER studies performed with the bipotentiostat mode of the IviumStat using a RRDE set-up where GC and Pt were used as a disk and ring electrode, respectively. Ni_3Se_2 was deposited on the interchangeable GC disk electrode for 300 s at a cathodic potential of -0.80 V vs. Ag/AgCl. The Pt ring was polished with an alumina slurry (0.05 mm), then washed and sonicated in DI water for 5 min. Before the measurements, the Pt ring was electrochemically cleaned in N_2 saturated 0.5 M H_2SO_4 until reproducible characteristic CVs of Pt was obtained. The disk electrode containing the electrocatalyst was held at the open circuit potential of OER where no Faradaic process occurs, while the Pt ring electrode was maintained at 0.2 V vs. RHE to obtain the background current of the ring electrode. The background ring current was lower than 20 mA. Then, the voltage of the disk electrode was held at several definite potentials in the OER kinetic region for 30 s, while, the ring current was recorded at 0.2 V vs. RHE.

2.4.1. Calculation of the Turnover Frequency (TOF). The turnover frequency (TOF) was calculated from the following Equation.

$$TOF = I/4 \times F \times m \quad (2)$$

Where I is the current in Amperes, F is the Faraday constant and m is the number of moles of the active catalyst.

2.4.2. Tafel Plots. The catalytic performance of the Ni_3Se_2 catalysts toward the OER has been carried out by measuring the Tafel plots based on the Equation given below.

$$\eta = a + (2.3RT/\alpha nF) \log(J) \quad (3)$$

Where η is the overpotential, j is the current density and the other symbols have their usual meanings. The Tafel Equation as shown in Equation (3) is a fundamental

Equation which acquires from the kinetically controlled region of OER, and relates the overpotential η with the current density *j* where the Tafel slope is given by (2.3RT)/ αnF. To calculate Tafel slopes, LSV plots were obtained with a slow scan speed (2 mV s^{-1}) in non-stirred solution.

3. RESULTS & DISCUSSION

3.1. STRUCTURAL AND MORPHOLOGICAL CHARACTERIZATION

The PXRD patterns of as-synthesized films deposited on Au-coated glass substrates showed peaks which could be matched with the Ni_3Se_2 phase (JCPDS # 019-0841) along with peaks characteristic of Au arising from the underlying substrate as shown in Figure 1. It was observed that as the deposition time increased the crystallinity of the deposited film was enhanced as depicted by the increasing intensity of the PXRD peaks. With very long deposition times (600 s), however, trace amounts of NiSe (JCPDS # 03-065-9451) could be detected in the films from their PXRD patterns. Almost an identical phase of nickel selenide (Ni_3Se_2) was observed in catalysts deposited at different pHs of the electrochemical bath (2.5, 3.5, and 4.5) as shown in Figure S1 (ESI†) with the film deposited at pH 2.5 showing the best pattern. Hence, the catalyst used in the rest of the study was synthesized at pH 2.5. Ni_3Se_2 has a structure very similar to the sulfide analogue, Ni_3S_2, also known as heazlewoodite, which is a sulfur poor nickel sulfide mineral.[50,51] Heazlewoodite contains Ni in a distorted tetrahedral environment with short Ni–Ni distances suggestive of metal–metal bonds. From local energy density studies it has been predicted that Ni–chalcogen and Ni–Ni bonds are intermediate in character between ionic

and covalent.[52,53] Unlike Ni_3S_2, detailed structural studies on Ni_3Se_2 are still rare. However, in analogy with the sulfide phase, it has been shown that Ni_3Se_2 also have Ni–Ni bonding

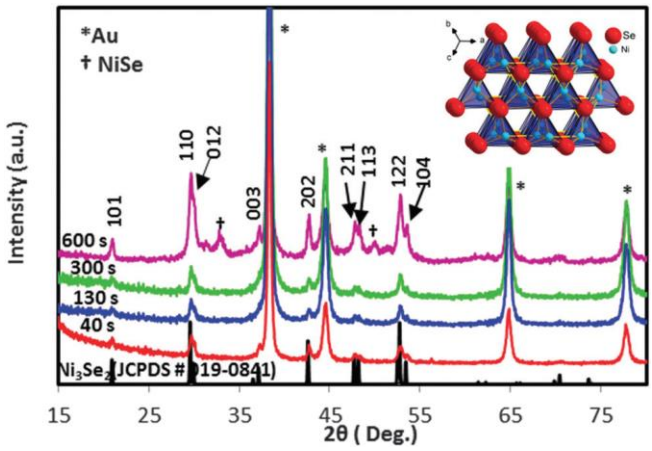

Figure 1. PXRD patterns of catalysts electrodeposited for different time periods showing the presence of Ni_3Se_2 (JCPDS # 019-0841) along with Au. The inset shows the crystal structure of Ni_3Se_2 with Ni – blue and Se – red.

in the structure with one of the Ni–Ni bonds being very short and similar to that found in metallic Ni.[54] The structure of Ni_3Se_2 has been shown in the inset of Figure 1.[§]

Detailed SEM studies of the as-deposited films showed that the films were mainly granular and composed of nanostructured grains (50 nm to several hundred nm) (Figure 2a). It was clear that the Ni_3Se_2 grain size increased with increasing deposition time from 40 s to 600 s and the films grow thicker, but smoother with the time (Figure S2a, ESI†). Typically the average thickness of the films varied between 0.9–5.2 mm (Table S1 in the ESI†). The amount of catalyst loading was also estimated from analyzing the electrodeposition curves (vide infra, Table 1) and the results show that the catalysts amount as well as loading per unit area increased with increasing deposition time.

EDS was used to measure the elemental compositions and the Ni to Se atomic ratios in these catalysts, and the results are shown in Figure 2b and Figure S2b (ESI†). Typically

SEM performed on a wide area of the film showed a uniform presence of Ni and Se, as evident by the line scan analyses shown in Figure S2b(i) (ESI†). SEM was also performed in STEM mode with HAADF (high angle annular dark field) imaging on individual grains which again showed that Ni and Se were present uniformly in individual grains and the distribution was similar to that obtained in the film (Figure S2b(ii), ESI†). The Ni : Se atomic ratio for the catalysts synthesized at 40 and 130 s is slightly higher than the theoretical atomic ratio of Ni_3Se_2 (1.5) whereas at 300 and 600 s of electrodeposition, the Ni : Se ratio was closer to the theoretical value. It should be noted that the relative atomic percentage of Se increased with increasing deposition time, which might be due to the competing deposition of Ni and Se during co-electrodeposition, as the metal chalcogenide process is known to be partially controlled by the diffusion of chalcogen ions to the cathode.[55] The deviation of the Ni : Se elemental ratio from the theoretical value of 1.5 might still be advantageous for enhancing the catalytic activity even further in the Se-deficient (i.e. Ni-rich) compositions.[56] Typically for the Ni-oxide based catalysts, it was observed that the creation of anion deficiency improved catalytic performance.[9,11]

Elemental compositions of the electrodeposited films were also investigated through XPS studies. The XPS spectrum of the catalysts (Figure 2c) exhibits two peaks at 852.6 and 869.8 eV, corresponding to Ni 2p3/2 and Ni 2p1/2 similar to that obtained from Ni_3S_2.[57,58] It should be noted that the binding energies for these peaks were more shifted towards the binding energies observed in metallic or alloyed Ni, as would be expected for Ni_3Se_2 which has substantial metal–metal bonding.

[§] The Ni_3Se_2 crystal can be described as formed by anion (Se) close packing and Ni occupying 3/4th of the tetrahedral holes. Ni sits in a distorted tetrahedral coordination of

Se, while Se sits within a distorted trigonal prismatic coordination formed by the neighbouring Ni atoms. Since a large number of tetrahedral holes have been occupied by Ni, the neighbouring Ni polyhedra have edgesharing bringing the Ni atoms close together favouring the formation of the metal–metal bond.

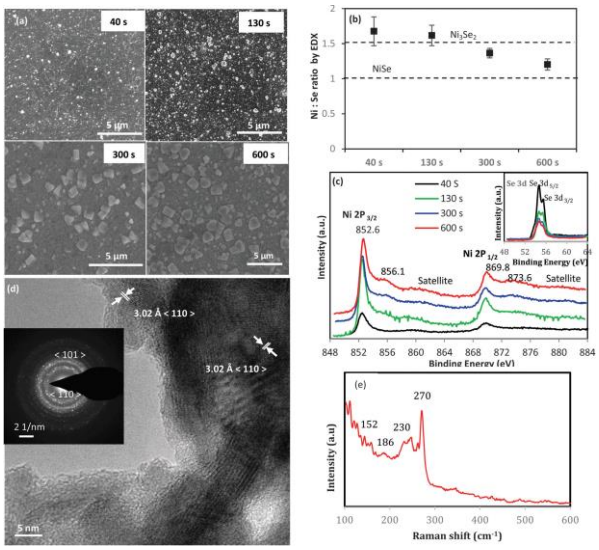

Figure 2. (a) SEM images of catalyst deposited for 40, 130, 300 and 600 s. (b) Ni to Se ratio obtained from the catalysts through EDS. Dotted lines represent the ratio lines for NiSe(bottom) and Ni_3Se_2 (top) phases. (c) XPS spectra of the catalyst showing the Ni 2p peaks. The inset shows peaks corresponding to Se 3d. (d) HRTEM image of the catalyst. The inset shows a typical SAED pattern. (e) Raman spectrum of the catalyst electrodeposited for 300 s.

Table 1. Electrochemical parameters of the Ni_3Se_2 catalysts measured in 0.3 M KOH.

D.t. (s)	**T.l. (mg)**	**L.a. (mg cm^{-2})**	**G.s. (nm)**	**ECSA (cm^2)**	**RF**	**Onset η^a/V**	**η to 10 mA cm^{-2}/V^a**	**Tafel slope /mV dec^{-1}**	**j_g,η=0.31 V/mA cm^{-2}**	**j_s,η=0.31 V/ mA cm^{-2}**
40	8.0	2.83 x 10^{-2}	30–150	2.5	8.8	0.22	0.37	99.6	3.36	0.38
130	31.3	11.1 x 10^{-2}	70-200	2.3	8.2	0.22	0.33	98.8	7.81	0.95
300	61.4	21.7 x 10^{-2}	150-1500	2.3	8.2	0.21	0.31	97.1	10.24	1.25
600	123.4	43.5 x 10^{-2}	300-2000	1.8	6.5	0.25	0.36	100.2	3.88	0.66

[a] Potential reported with respect to RHE, D.t. Deposition time, T.l. Total loading, L.a. Loading area, G.s. Grain sizes.

In films deposited for 600 s, another set of very weak intensity Ni 2p peaks was observed at 856.1 and 873.6 eV, which corresponds to Ni 2p3/2 and Ni 2p1/2 for NiSe and is also closer to the Ni–O phases.[59] Accordingly XPS was collected to detect O. Some surface oxygen was detected (Figure S3, ESI†) that reduced in intensity following sputtering for 2 min under Ar, indicating that the impurity phase was mostly on the surface. These XPS results along with XRD confirmed that the majority phase in these electrodeposited films was Ni_3Se_2. An obvious satellite was observed at higher energy of the Ni 2p peak (about 860.0 eV) which could be due to the antibonding orbital between the Ni atom and the Se atom. Similar satellite peaks has been reported for several Ni-based chalcogenides.[60] The binding energies of 3d5/2 levels of Se were obtained at 54.7 eV similar to the that from nickel selenides.[61]

The film morphology was also analyzed through TEM and HRTEM imaging which showed the crystalline nature of the granules in the film, with lattice fringes corresponding to the (110) lattice spacing of Ni_3Se_2 (Figure 2d). The SAED pattern shown as the inset of Figure 2d, also confirmed crystalline nature of the as-prepared films and the diffraction spots could be indexed to (101) and (110) lattice planes of Ni_3Se_2.

The Raman spectrum of the as-synthesized catalyst for 300 s is shown in Figure 2e. There are four Raman peaks at 152, 186, 230 and 270 cm^{-1} which can be assigned to the Raman active modes of Ni_3Se_2.[62] There is no evidence of elemental Se in the catalyst, as no peaks were observed at 141 and 235 cm^{-1}. The Raman analysis also did not show a major presence of any oxidic phases further confirming that the electrodeposited films were devoid of oxidic impurities.

3.2. ELECTROCHEMICAL PERFORMANCE AND OER CATALYTIC ACTIVITIES

The electrocatalytic performance for OER of the electrodeposited films was investigated through detailed electrochemical studies in alkaline solution (0.3 M KOH) near pH 13. The electrochemically active surface areas (ECSA) of the catalysts were estimated by measuring the electrochemical capacitance of the electrode–electrolyte interface in the double-layer regime of the voltammograms. Using N_2-saturated 0.3 M KOH, the electrode was potentiostatically cycled from -0.19 to -0.10 V vs. Ag/AgCl at scan rates between 2.5 and 40 mV s^{-1} (Figure 3). The capacitive current (i_{DL}) was estimated from the non-faradaic double-layer region. This current involves charge accumulation rather than chemical reactions or charge transfer and is directly proportional to the scan rate, υ (V s^{-1}) as shown in Equation (4).[9]

$$i_{DL} = C_{DL} \text{ x } v \quad (4)$$

Where C_{DL} is the specific capacitance of the electrode double layer (F cm^{-2} electrode). Thus, a plot of i_{DL} against υ shown in the inset of Figure 3 gave a straight line and the slope was equal to C_{DL}. Hence, the ECSA of the catalyst was calculated as (Equation (5)).

$$\text{ECSA} = C_{DL}/C_s \quad (5)$$

Cs is the specific capacitance and reported to be between 0.022 to 0.130 mF cm^{-2} in alkaline solution. In this study, we use the value of C_s is 0.040 mF cm^{-2} based on previously reported Ni-based OER catalysts.[9] The ECSA and the roughness factor (RF) of the various catalysts used in this study of the various catalysts used in this study are given in Table 1. It was observed that RF became less as the film deposition time increased which

corroborated with the fact that the films looked thicker and smoother with increasing deposition time.

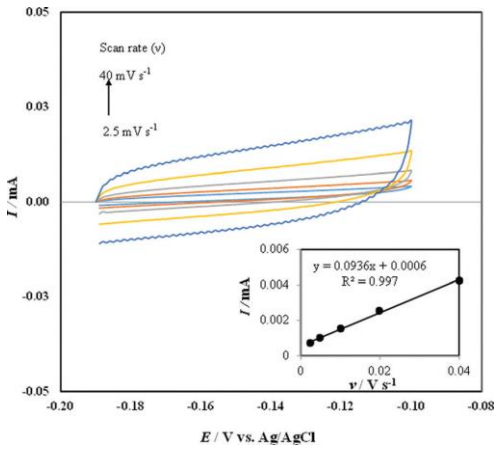

Figure 3. Cyclic voltammograms measured for the Ni_3Se_2 catalyst (electrodeposited for 300 s) in N_2 saturated 0.3 M KOH solution at different scan rates from 2.5 to 40 mV s^{-1}. The inset shows a plot of anodic currentmeasured at - 0.14 V as a function of scan rate.

To study the electrocatalytic activity of the Ni_3Se_2 for OER, linear sweep voltammetry (LSV) measurements were conducted in N_2-saturated 0.3 M KOH, at a scan rate of 10 mV s^{-1}. To the best of our best knowledge, this is the first time that Ni_3Se_2 has been reported as an OER-active electrocatalyst. Figure 4a shows the LSVs of electrochemical oxygen evolution with Ni_3Se_2 catalysts deposited for 40, 130, 300 and 600s. Typically rapid oxygen evolution from the Ni_3Se_2 catalyst surface was observed during the electrochemical studies. As observed, blank Au shows poor catalytic activity toward the OER. In contrast, after electrodeposition of Ni_3Se_2 the substrates showed high activity for OER with an onset overpotential of about 210 mV for 300 s, 220 mV for 40 and 130 s of deposition and 250 mV for 600 s deposition, respectively [all potentials have been reported with respect to RHE]. This ~ 30 mV shift in onset overpotential is expected as longer time (600 s) leads to bulk deposition of the catalyst (Table 1).

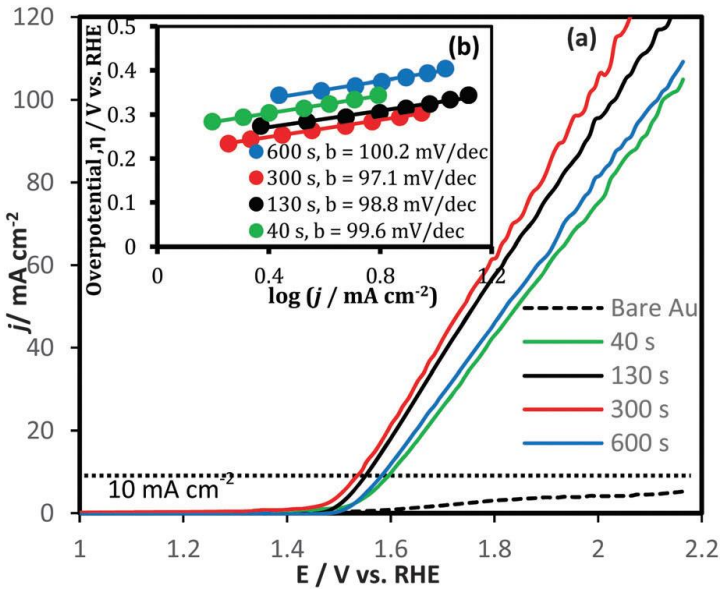

Figure 4. (a) LSVs measured for catalysts electrodeposited for different time periods in N_2 saturated 0.3 M KOH solution at a scan rate of 0.01 V s^{-1}. The dotted line shows the current density of 10 mA cm^{-2}. (b) Tafel plots of catalysts.

Conventionally, the effectiveness of OER catalysts is estimated by listing the overpotential required to reach a current density of 10 mA cm^{-2} (per geometric surface area), which is considered to be equivalent to 10% solar energy conversion efficiency.[9] The η for 10 mA cm^{-2} per geometric area of the Ni_3Se_2 catalysts electrodeposited for different time periods are reported in Table 1. It can be clearly found that the 300 s deposited catalyst exhibits the highest catalytic activity towards OER with a much lower η. It should be noted that with increasing deposition time and the increase of Ni_3Se_2 content in composites (Table 1), the catalytic activity for OER increased at first and then decreased (Figure S5, ESI†). After studying in detail electrochemical and surface specific properties, the authors conclude that this enhanced activity is due to a fine balance between the catalyst loading, surface roughness, thickness of the film, and grain sizes. It can be envisioned that catalyst loading will have a direct influence on the capability of O_2 evolution in the semiconductor-based water oxidation catalysts.[63] Increasing catalyst loading increases the amount of

catalytically active sites thereby facilitating the gas evolution reaction. As can be seen from Table 1, the catalyst loading increases with increasing deposition time. However as the thickness of the film increases with deposition time, some of the surface active sites will be blocked by overgrowth and multilayers, thereby reducing access of water molecules to the active sites. Additionally, larger thickness of these semiconductor films also affects mobility of charge carriers and electrical conductivity in the underlying Au layer. In the electrode composites, Ni_3Se_2 film provides catalytically active sites, while underneath the Au substrate favors the higher mobility of charge carriers and superior electrical conductivity. Thus, it is reasonable that the catalytic activity gradually increases with the increase in the thickness of Ni_3Se_2 within a certain range. However, when the Ni_3Se_2 thickness is further increased over its optimum value, the catalytic performance deteriorates, which may be due to the lower mobility of charges in the semiconductor chalcogenide. Surface roughness of the film on the other hand has a positive effect on the catalytic activity. Higher surface roughness (roughness factor) indicates exposure of more surface active sites for catalysis, thereby increasing catalytic efficiency. Thus it is apparent that to maximize catalyst efficiency, one needs to have high catalyst loading with high roughness factor and smaller thickness. From Table 1 it can be seen that the films deposited at 300 s satisfy all these criteria and strike a fine balance between the different parameters. Hence these films show the best catalytic activity among the Ni_3Se_2 films reported here.

It was observed that all the electrocatalysts were stable under the O_2 evolution conditions as revealed by chronoamperometric studies for 3 h (Figure S4, ESI†). Note that the overpotential required to achieve close to 10 mA cm^{-2} of 300 s catalyst (310 mV) is comparable with the widely used OER catalysts, IrO_x (320 mV) and RuO_2 (390 mV).[9,15]

Literature surveys are also showed that among the Ni-based catalysts, our synthesized Ni_3Se_2 catalyst exhibits a lower overpotential at the current density of 10 mA cm^{-2} (vide infra).

Specific activity is an intrinsic property of the catalyst and is important for comparison of the loading of the catalyst with varying deposition time. Activities of the OER catalysts were also determined from the specific current density at a constant overpotential of 310 mV. The specific current density, j_s, can be calculated from the ratio of the current density per geometric area (j_g) at 310 mV with the roughness factor (RF) of the surface as shown in Equasion (6).[9]

$$j_s = j_g / \mathrm{RF} \qquad (6)$$

The specific current density was measured for different catalysts and is shown in Table 1. The highest specific current density at 310 mV overpotential was obtained for 300 s catalyst, indicating that this was indeed the best OER catalyst among the Ni_3Se_2 films deposited for various time periods.

Tafel slopes are another important parameter that offers critical insights into the OER reaction kinetics. The Tafel slopes were collected from the steady-state LSVs at a scan rate of 2 mV s^{-1} in a non-stirred solution. The Tafel plots for Ni_3Se_2 electrodeposited films are shown in Figure 4b. A linear dependency of η vs. log(j) was achieved for all catalysts and they displayed different slopes. The Tafel slope values are listed in Table 1 and the slopes follow an order of 300 s < 130 s < 40 s < 600 s. The lowest value of the Tafel slope indicates facile catalytic activity for OER.

The evolved gas at the anode was analysed with the aid of electrochemical reduction in a bipotentiostat set-up. Typically O_2 can be reduced electrochemically by the

Pt cathode held at a potential of 0.2 V (vs. RHE). To confirm the composition of the evolved gas, Ni_3Se_2 was deposited on glassy carbon (GC) which was connected as the disk electrode in a RRDE set-up with Pt as the ring electrode. The ring electrode was maintained at a constant potential of 0.2 V (vs. RHE) and the current was recorded (ring current) as the potential of the disk electrode was scanned over a desired range. The electrolyte was purged with N_2 for 30 min before starting the electrochemical oxidation to get rid of any dissolved O_2 and blanketed with a N_2 atmosphere. Figure 5(a) shows the LSV at the GC disk electrode in 0.3 M KOH at 1600 rpm at a scan rate of 10 mV s^{-1} where in the absence of dissolved O_2 the ring current is minimal as observed. As the potential of the disk electrode was swept past 220 mV (onset overpotential), the characteristic increase of the cathodic ring current due to ORR indicated that the bubbles formed at the anode were indeed O_2. The ring current progressively increased with increasing potential as more and more O_2 was evolved at the anode. To further confirm that the ring current was indeed from the dissolved O_2 generated in situ from the Ni_3Se_2 catalyst, a series of experiments were performed where the disk current was collected after various periods of O_2 generation. The electrolyte was initially purged with N_2 gas for 30 min to get rid of dissolved O_2 and blanketed with a N_2 atmosphere during recording of the ring current. Then the disk electrode was held at constant 10 mA cm^{-2} current density per geometric area (which was sufficiently large to ensure O_2 generation) for 1, 2 and 6 h in 0.3 M KOH solution following which the ORR currents at the Pt ring electrode were measured as shown in Figure 5(b).

It was observed that ORR current increased with time of O_2 generation and after 6 h current was comparable to that obtained from a solution saturated with O_2 externally. To further confirm that the O_2 was obtained in situ, the same solution (after generation of O_2

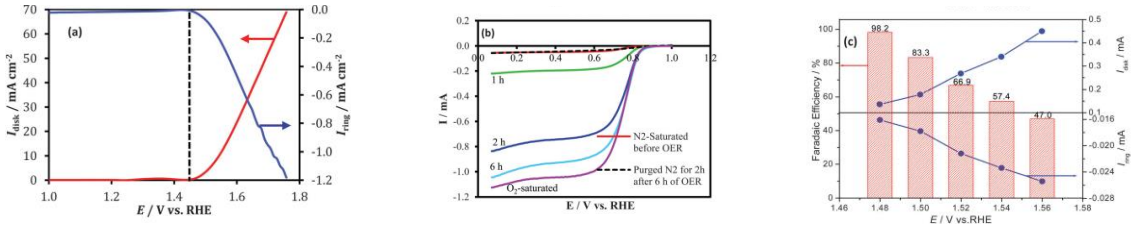

Figure 5. (a) OER at the Ni_3Se_2/GC disk electrode in N_2-saturated 0.3 M KOH and Pt ring current (held at 0.2 V vs. RHE) due to oxygen reduction as a function of disk potential. The black dash line shows the onset of OER at the disk electrode and ORR at the ring electrode. (b) Electrochemical evidence of O_2 generation at the disk electrode and reduction at the ring electrode when constant current of 10 mA cm^{-2} was applied at the disk electrode for varying periods of time (1, 2 and 6 h) in N_2 saturated and blanketed 0.3 M KOH. (c) Faradaic efficiency of the catalyst in 0.3 M KOH at 1600 rpm under N_2 saturation. The disk and ring currents of RRDE plotted as a function of the applied disk potential along with the calculated Faradaic efficiency.

for 6 h) was purged again with N_2 for 2 h to get rid of the evolved O_2, and ORR current was measured which showed that it had reduced back to minimal current as was seen before start of the experiment (black dashed curve in Figure 5b). This proves that the dissolved O_2 was indeed generated in situ by the anodic catalyst. The Faradaic efficiency of OER was determined by RRDE, where oxygen generated at the disk electrode was swept outward away from the disk electrode and towards the Pt ring electrode where it was reduced. The collection efficiency, N (0.24), of the rotating ring-disk electrode was determined by the ratio of the ring and disk current in 0.001 M $K_3Fe(CN)_6$ containing 0.3 M of KOH following the previously reported procedure (Figure S6, ESI†).[9,64] Prior to RRDE measurement, N_2 gas was purged in the cell for 30 min and then blanketed with N_2 during the experiment. The disk electrode was maintained at constant potential steps from 1.48 to 1.56 V (vs. RHE) for consecutive periods of 1 min each, while being rotated at a 1600 rpm under a N_2 gas blanket. The ring electrode was held at 0.2 V (vs. RHE)

throughout the experiment, which was sufficiently negative to reduce the collected oxygen rapidly. The Faradaic efficiency can be given as (Equation (7)).[9]

$$\text{Faradaic efficiency} = 2i_r / i_d N \quad (7)$$

Where i_r and i_d are the measured ring and disk currents, respectively, and N is the collection efficiency of RRDE, 0.24 in this work. Figure 5(c) shows the plot of the disk and ring currents of the Ni_3Se_2 catalyst in 0.3 M KOH as a function of the applied disk potential and Faradaic efficiency. The highest Faradaic efficiency was obtained to be about 98% at the applied disk potential of 1.48 V (vs. RHE), and decreased to 47% with the disk voltage increasing to 1.56 V (vs. RHE). This decrease can be attributed to apparently large amounts of undissolved oxygen bubbles generated at the relatively high applied disk potentials which might not be collected efficiently by the Pt ring electrode. This decrease in Faradaic efficiency has been observed by other researchers also with Ni–Fe based nanoparticle electrocatalysts in alkaline medium.[64] Thus, the 98% Faradaic efficiency which was achieved at 1.48 V (vs. RHE) (corresponding to about 1.0 mA cm^{-2} disk current density), has been presented as the OER efficiency of the Ni_3Se_2 catalyst because this disk current density is adequately high to generate oxygen.

The turnover frequency (TOF) of the Ni_3Se_2 catalyst deposited for 300 s, was calculated at an overpotential of 300 mV in 0.3 M KOH, assuming that all of the active materials in the catalysts are catalytically active for OER, and using the catalyst loading as mentioned in Table 1. The TOF value of Ni_3Se_2 was calculated to be 0.044 s^{-1}, which is higher than the previously reported TOF values for some Ni-based catalysts,[7] and is also roughly 5-fold higher than that of the reported IrO_x (0.0089 s^{-1}) catalyst,[7] indicating a better OER activity for Ni_3Se_2.

The stability of the Ni_3Se_2 electrocatalyst under conditions of continuous oxygen evolution was investigated through chronoamperometric measurements (*j* vs. t) at a overpotential where current density was around 10 mA cm^{-2} in 0.3 M KOH for 18 h and 42 h and is shown in the inset of Figure 6(b) and Figure S9(a) (ESI†), respectively. The onset potentials for the catalysts were measured in solutions which were not agitated. However, it was observed that as the electrochemical O_2 generation proceeded, there was a large amount of bubble formation most of which adhered to the surface of the catalyst, thereby slowing down the reaction. Hence, for studies including long-term stability the solution was stirred with the minimal speed (up to 300 rpm) to dislodge the bubbles from the catalyst surface and allow progress of the reaction. Structural and compositional stability of the films after extended periods of oxygen evolution (18 and 42 h at room temperature) was also studied through powder X-ray diffraction, XPS and LSV analyses (Figure 6). All catalysts exhibit excellent stability over extended periods of time. The LSV curves after 18 h of continuous O_2 evolution showed a similar onset potential and overpotential at 10mA cm^{-2} with a very minimal difference in the current density for OER activities as compared with the initial catalyst (Figure 6a). PXRD showed that the structural integrity was maintained even after 42 h of catalytic activity with no obvious sample degradation (Figure 6d). XPS spectra showed that the elemental composition was maintained after extended periods of catalytic activity (Figure 6c). In contrast to the Ni_3S_2 report where the XPS data after OER maintained after extended periods of activity showed complete depletion of the Ni_3S_2 layer on the surface.[34] In the present case, the catalyst after OER activity still showed a major presence of Se on the surface. The O 1s and Se 3d signal before and after OER activity showed a minimal change (Figure S7, ESI†). Raman studies

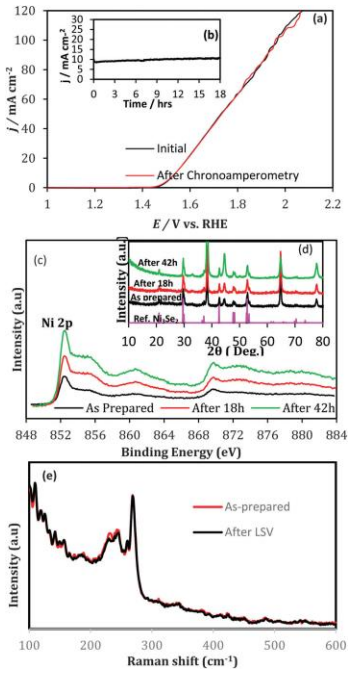

Figure 6. (a) LSVs of the catalyst synthesized for 300 s in N_2 saturated 0.3MKOH before and after chronoamperometry for 18 h, (b) an extended stability study of the catalyst under continuous O_2 evolution (at 10 mA cm^{-2}) for 18 h studied through chronoamperometry at constant potential. (c) XPS spectra before and after chronoamperometry for 18 and 42 h, and (d) XRD patterns before and after current transient experiment for 18 and 42 h. (e) Comparison of Raman shift before and after LSV for OER.

also indicated that the catalyst after OER activity was still Ni_3Se_2 and the characteristic peaks for Ni-oxide or hydroxide were not visible (Figure 6e). The long-term stability was also investigated from Raman studies performed on the Ni_3Se_2 catalyst after 18 h of continuous O_2 evolution, which still showed similar spectra with a marked absence of peaks characteristic of Ni-based oxide and/or hydroxide (Figure S8, ESI†). However the films after catalytic activity showed lesser Se content compared to the pristine films, indicating that the Ni_3Se_2 filmsmight be gettingmore Se deficient with prolonged catalytic activity.

Interestingly, the LSV curves after 42 h of continuous OER, showed that the catalyst became even more efficient after such prolonged activity (η = 310 mV at 10 mA

cm^{-2}) (Figure S9a, ESI†) while maintaining a similar composition and structure (Figure 6(c) and (d)). Improved catalytic efficiency with aging has been observed in Ni-oxide and hydroxide based catalysts before[7,65] and this has been attributed due to several factors including structural modification of the films. Some observations also suggested that prolonged aging (for several weeks) in impure KOH without potential cycling, led to Fe incorporation in the films from the reagent grade KOH which contains ~ 0.66 ppm of Fe as impurity.[65,66] Hence, we have analyzed the catalytic composition through ICP-MS studies after 42 h of continuous OER activity in alkaline medium. The ICP-MS studies revealed that there was a trace amount of Fe incorporation [Ni : Fe approximately 1 : 0.015] from the unpurified KOH upon extended exposure. In Boettcher's paper the authors have also suggested a way of purifying the KOH to be Fe-free by treatment with precipitated $Ni(OH)_2$.[65] Accordingly, we have also carried out similar treatment to the KOH electrolyte to generate a Fe-free solution, which was then tested with the Ni_3Se_2 films for OER activity. The effect of Fe incorporation was studied through cycling studies where the catalysts were cycled in purified and unpurified KOH for 100 runs and the LSV curves were compared. It was observed that in the case of unpurified KOH, the current density increased slightly with an increasing number of cycles, while for purified KOH the current density (at high potential) decreased slightly with increasing cycles (Figure S9b, ESI†).

Hence it can be concluded that like the Ni-oxyhydroxide based catalysts, in this case also Fe incorporation in the catalyst composition is possible and the catalytic activity can be enhanced through such doping. Taking cue from these observations including the ICP-MS data and research rported by Boettcher's group,[54,55] we are attempting to

intentionally incorporate Fe in these Ni-selenide based films and investigate their catalytic activities towards the OER process.[67]

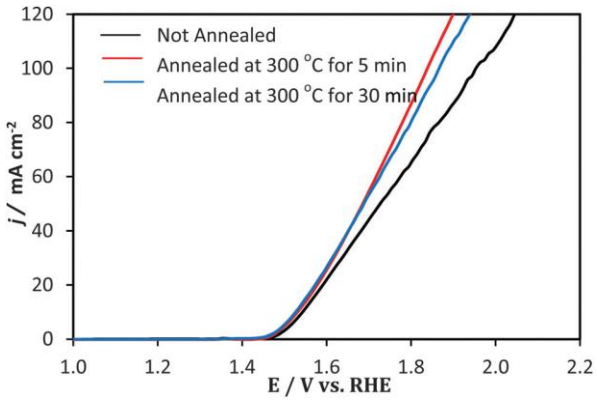

Figure 7. Comparison of LSVs measured before and after annealing at 300 ºC for 5 min and 30 min of the catalyst in 0.3 M KOH solution at 0.01 V s^{-1}.

Table 2. Comparison of the η (onset) and at 10 mA cm^{-2} with Ni_3Se_2 deposited on different substrates.

Ni_3Se_2@different substrates	**Onset overpotential, η, V/vs. RHE**	**Overpotential,V/vs. RHE to achieve current 10 mA cm^{-2}**
Au–Si	0.210	0.300 - 0.10
GC	0.220	0.310 - 0.20
Au–glass	0.220	0.320 - 0.20
Ni–foam	0.230	0.270 - 0.20
FTO	0.240	0.340 - 0.20
ITO	0.250	0.450 - 0.30

3.2.1. Effect of Annealing. Thermal annealing is considered to be an effective way to improve the activity of catalyst.[68] Figure 7 shows the LSVs of the Ni_3Se_2 catalyst before and after annealing at 300 ºC for 5 min on the hot plate as well as in a horizontal oven (30 min) under controlled flow of N_2 in either case. The OER activity of the catalyst improved significantly after the heat treatment, the current density of 10 mA cm^{-2} was achieved at an overpotential of 290 mV in 0.3 M KOH.

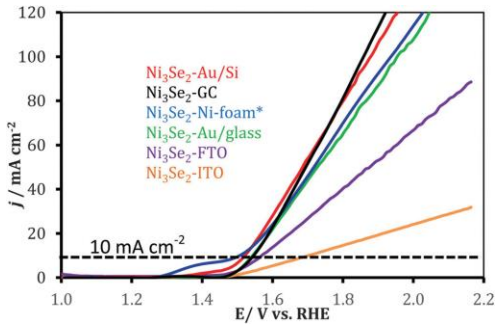

Figure 8. OER activities of Ni_3Se_2 catalysts electrodeposited on various substrates.* The geometric area of the catalyst was estimated from the area exposed to the electrolyte not considering the surface area of the Ni foam.

Structural, morphological and spectral analysis of the annealed films revealed that: (i) annealing at 300 ºC does not affect the surface morphology of the catalyst (supporting SEM images shown in Figure S10, ESI†); (ii) however the crystallinity of the catalyst improved significantly which was evidenced by PXRD (Figure S11, ESI†); (iii) the ratio of Ni to Se increases with the thermal treatment which was evident from EDS (Table S1, ESI†). Structurally enhanced more Se-deficient films formed through annealing may provide more active sites for OER, thus leading to better catalytic activity.

3.2.2. Effect of the Substrate on OER Activities. Besides Au-glass and Au-coated Si, GC, ITO, FTO-coated glass and Ni-foam were also used as underlying substratse to investigate the effect of substrate on OER. The LSVs of the respective electrocatalysts have been shown in Figure 8. The overpotentials required to achieve 10 mA cm^{-2} for the catalyst deposited for 300 s on various substrates are presented in Table 2. The catalyst deposited on Au-coated glass and Si substrates as well as GC exhibited the highest current density and the earliest onset of OER as compared with others. This observation suggests that the interaction between the underlying substrate and Ni_3Se_2 may play role in the OER activity.

Table 3. Comparison of the catalytic performances between different Ni-based catalysts and Ni_3Se_2.

Catalyst	**Onset overpotential (V), η (vs. RHE)**	**Overpotential (V), η(vs. RHE) required to get 10 mA cm^{-2}**	**Tafel slope, (mV dec^{-1})**	**Ref.**
IrO_x	-	0.32	-	9
RuO_2[c]	0.22*	0.39*	-	16
NFNTAs-20[a]	0.28	0.38(to get 5 mA cm^{-2})	105	27
NNCNTAs[b]	0.31	0.36	65	28
a-$Ni(OH)_2$	0.310*	0.331	42	26
Ni_3S_2–Ni foam	0.157	0.187	159.3	34
$NiCo_2O_4$	0.260*	0.34	75	60
$Ni_{0.9}Fe_{0.1}O_x$	0.250*	0.336	30	7 and 65
NiCo–LDH	0.290	0.410*	-	29
Ni_3Se_2–Au@Glass	0.220	0.320 ± 0.20	97.1	This work
Ni_3Se_2–Au@Glass (Annealed)	0.210	0.290 ± 0.10	97.2	This work
Ni_3Se_2–Au@Si	0.210	0.300 ± 0.10	122.0	This work
Ni_3Se_2–GC	0.220	0.310 ± 0.20	79.5	This work
Ni_3Se_2–Ni foam	0.230	0.270 ± 0.20	142.8	This work

[a] Ni–Fe oxide nanotube arrays (20% of Fe). [b] Ni@$[Ni^{(2+/3+)}Co_2(OH)_{6-7}]_x$ nanotube arrays.

[c] In acidic electrolyte. *Estimated from the references.

The effect of the substrate on OER activity has been previously reported in the literature for Ni-based catalysts.[10] In addition to planar substrates, Ni_3Se_2 films were also

electrodeposited directly into high surface area Ni foam. The LSV plots of the Ni_3Se_2–Ni foam composite exhibited the lowest onset overpotential for OER at 230 mV (vs. RHE) as shown Figure 8. The overpotential at 10 mA cm^{-2} for the Ni_3Se_2–Ni foam composite was also the lowest in the series (270 mV vs. RHE). However, the Ni foam being exceptionally porous with very high surface area, it may not be judicial to use the geometric surface area of the electrode to estimate the current density, and compare it with the planar substrates. Nevertheless, the high surface area of the foam makes sure that the entire Ni_3Se_2 catalyst is accessible to the electrolyte thereby can potentially and significantly enhance the catalytic efficiency.

4. CONCLUSIONS

A nickel selenide based compound, Ni_3Se_2, with structure analogous to mineral heazlewoodite has been observed to be catalytically active towards OER in alkaline medium (pH = 13) for the first time. The low onset overpotential required for O_2 evolution as well as low overpotential required to reach 10 mA cm^{-2}, gives this catalyst a very competitive edge amongst the known oxide based OER electrocatalysts. A comparison with the other reported Ni-based OER catalyst (Table 3) revealed that the Ni_3Se_2 system described in this paper is definitely as good as or even better than the best Ni-based OER catalyst. Moreover, this Se-deficient phase containing a rich architecture of the metal–metal bond can be further modified through solid state chemistry approaches to optimize the catalytic efficiency. These Ni_3Se_2 catalysts electrodeposited on conducting substrates also exhibited exceptional stability under the conditions of O_2 evolution for extended

periods of time. These findings coupled with the simple synthesis method, earth-abundancy of the raw materials and possibilities to tune the catalytic efficiencies even further, makes them lucrative for various energy-related practical applications.

ACKNOWLEDGEMENTS

MN would like to acknowledge the American Chemical Society Petroleum Research Fund (54793-ND10) for financial support. The authors would also like to acknowledge CS3M at Missouri S&T, Dr Honglan Shi and Kun Liu for help with the ICP-MS measurements, Materials Research Center for equipment usage and Dr Richard Brow for help with Raman measurements.

REFERENCES

1. N. S. Lewis and D. G. Nocera, Proc. Natl. Acad. Sci. U. S. A., 2006, 103, 15729–15735.

2. M. G. Walter, E. L. Warren, J. R. McKone, S. W. Boettcher, Q. Mi, E. A. Santori and N. S. Lewis, Solar Water Splitting Cells, Chem. Rev., 2010, 110, 6446–6473.

3. T. R. Cook, D. K. Dogutan, S. Y. Reece, Y. Surendranath, T. S. Teets and D. G. Nocera, Chem. Rev., 2010, 110, 6474–6502.

4. J. O. Bockris and A. K. N. Reddy, Modern Electrochemistry 1: Ionics, Plenum Press, New York, 1998.

5. W. T. Hong, M. Risch, K. A. Stoerzinger, A. Grimaud, J. Sunitvich and Y. S. Horn, Energy Environ. Sci., 2015, 8, 1404.

6. L. Trotochaud and S. W. Boettcher, Scr. Mater., 2014, 74, 25–32.

7. L. Trotochaud, J. K. Ranney, K. N. Williams and S. W. Boettcher, J. Am. Chem. Soc., 2012, 134, 17253–17261.

8. G. M. Whitesides and G. W. Crabtree, Science, 2007, 315, 796–798.

9. C. C. L. McCrory, S. Jung, J. C. Peters and T. F. Jaramillo, J. Am. Chem. Soc., 2013, 135, 16977–16987.

10. (a) E. Fabbri, A. Habereder, K. Waltar, R. Kotz and T. J. Schmidt, Catal. Sci. Technol., 2014, 4, 3800–3821; (b) J. Qi, X. Lai, J. Wang, H. Tang, H. Ren, Y. Yang, Q. Jin, L. Zhang, R. Yu, G. Ma, Z. Su, H. Zhao and D. Wang, Chem. Soc. Rev., 2015, 44, 6749–6773; (c) H. Tang, C. M. Hessel, J. Wang, N. Yang, R. Yu, H. Zhao and D. Wang, Chem. Soc. Rev., 2014, 43, 4281.

11. J. Suntivich, K. J. May, H. A. Gasteiger, J. B. Goodenough and Y. S. Horn, Science, 2011, 334, 1383–1385.

12. S. W. Lee, C. Carlton, M. Risch, Y. Surendranath, S. Chen, S. Furutsuki, A. Yamada, D. G. Nocera and Y. S. Horn, J. Am. Chem. Soc., 2012, 134, 16959–16962.

13. E. Mirzakulova, R. Khatmullin, J. Walpita, T. Corrigan, N. M. Vargas-Barbosa, S. Vyas, S. Oottikkal, S. F. Manzer, C. M. Hadad and K. D. Glusac, Nat. Chem., 2012, 4, 794–801.

14. X. Li, F. Walsha and D. Pletcher, Phys. Chem. Chem. Phys., 2011, 13, 1162–1167.

15. J. Rossmeisl, Z. W. Qu, H. Zhu, G. J. Kroes and J. K. J. Norskov, Electroanal. Chem., 2007, 607, 83–89.

16. Y. Lee, J. Suntivich, K. J. May, E. E. Perry and Y. S. Horn, J. Phys. Chem. Lett., 2012, 3, 399–404.

17. M. Gong and H. Dai, Nano Res., 2015, 8, 23–39.

18. H. N. Seiger and R. C. Shair, J. Electrochem. Soc., 1961, 108, C163.

19. Y.G. Li, P. Hasin and Y. Y.Wu, Adv. Mater., 2010, 22, 1926–1929.

20. G. P. Gardner, Y. B. Go, D. M. Robinson, P. F. Smith, J. Hadermann, A. Abakumov, M. Greenblatt and G. C. Dismukes, Angew. Chem., Int. Ed., 2012, 51, 1616–1619.

21. J. Landon, E. Demeter, N. Inoglu, C. Keturakis, I. E. Wachs, R. Vasic, A. I. Frenkel and J. R. Kitchin, ACS Catal., 2012, 2, 1793–1801.

22. M. Gong, Y. Li, H. Wang, Y. Liang, J. Z. Wu, J. Zhou, J. Wang, T. Regier, F. Wei and H. Dai, J. Am. Chem. Soc, 2013, 135, 8452–8455.

23. S. Chen and S. Z. Qiao, ACS Nano, 2013, 7, 10190–10196.

24. S. Chen, J. J. Duan, M. Jaroniec and S. Z. Qiao, Angew. Chem., Int. Ed., 2013, 52, 13567.

25. M. R. Gao, Y. F. Xu, J. Jiang, Y. R. Zheng and S. H. Yu, J. Am. Chem. Soc., 2012, 134, 2930–2933.

26. M. Gao, W. Sheng, Z. Zhuang, Q. Fang, S. Gu, J. Jiang and Y. Yan, J. Am. Chem. Soc., 2014, 136, 7077–7084.

27. Z. Zhao, H. Wu, H. He, X. Xu and Y. Jin, J. Mater. Chem. A, 2015, 3, 7179–7186.

28. Z. Zhao, H. Wu, H. He, X. Xu and Y. Jin, Adv. Funct. Mater., 2014, 24, 4698–4705.

29. J. Jiang, A. Zhang, L. Li and L. Ai, J. Power Sources, 2015, 278, 445–451.

30. M. R. Gao, Y. F. Xu, J. Jiang and S. H. Yu, Chem. Soc. Rev., 2013, 42, 2986–3017.

31. M. D. Merrill and R. C. Dougherty, J. Phys. Chem. C, 2008, 112, 3655–3666.

32. W. Xu, Z. Lu, X. Lei, Y. Li and X. Sun, Phys. Chem. Chem. Phys., 2014, 16, 20402–20405.

33. Q. Liu, J. Shi, J. Hu, A. M. Asiri, Y. Luo and X. Sun, ACS Appl. Mater. Interfaces, 2015, 7, 3877–3881.

34. W. Zhou, X. J. Wu, X. Cao, X. Huang, C. Tan, J. Tian, H. Liu, J. Wang and H. Zhang, Energy Environ. Sci., 2013, 6, 2921–2924.

35. H. Yuan, H. Wang and Y. Cui, Acc. Chem. Res., 2015, 48, 81–90.

36. F. C. Hsu, J. Y. Luo, K. W. Yeh, T. K. Chen, T. W. Huang, P. M. Wu, Y. C. Lee, Y. L. Huang, Y. Y. Chu, D. C. Yan and M. K. Wu, Proc. Natl. Acad. Sci. U. S. A., 2008, 105, 14262–14264.

37. N. C. Gresty, Y. Takabayashi, A. Y. Ganin, W. T. McDonald, J. B. Claridge, D. Giap, Y. Mizuguchi, Y. Takano, T. Kagayama, Y. Ohishi, M. Takata, M. J. Rosseinsky, S. Margadonna and K. Prassides, J. Am. Chem. Soc., 2009, 131, 16944–16952.

38. J. Puthussery, S. Seefeld, N. Berry, M. Gibbs and M. Law, J. Am. Chem. Soc., 2011, 133, 716–719.

39. F. Cao, R. X. Liu, L. Zhou, S. Y. Song, Y. Q. Lei, W. D. Shi, F. Y. Zhao and H. J. Zhang, J. Mater. Chem., 2010, 20, 1078–1085.

40. M. R. Gao, Q. Gao, J. Jiang, C. H. Cui, W. T. Yao and S. H. Yu, Angew. Chem., Int. Ed., 2011, 50, 4905–4908.

41. M. R. Gao, R. S. Liu, J. Jiang, C. H. Cui, W. T. Yao and S. H. Yu, J. Mater. Chem., 2010, 20, 9355–9361.

42. M. R. Gao, Z. Y. Lin, T. T. Zhuang, J. Jiang, Y. F. Xu, Y. R. Zheng and S. H. Yu, J. Mater. Chem., 2012, 22, 13662–13668.

43. R. A. Sidik and A. B. Anderson, J. Phys. Chem. B, 2006, 110, 936–941.

44. L. Zhu, D. Susac, M. Teo, K. C. Wong, P. C. Wong, R. R. Parsons, D. Bizzotto and K. A. R Mitchell, J. Catal., 2008, 258, 235–242.

45. Y. X. Zhou, H. B. Yao, Y. Wang, H. L. Liu, M. R. Gao, P. K. Shen and S. H. Yu, Chem. – Eur. J., 2010, 16, 12000–12007.

46. Y. G. Feng, T. He and N. Alonso-Vante, Chem. Mater., 2008, 20, 26–28.

47. E. Vayner, R. A. Sidik, A. B. Anderson and B. N. Popov, J. Phys. Chem., 2007, 111, 10508–10513.

48. Y. J. Feng, T. He and N. Alonso-Vante, Electrochim. Acta, 2009, 54, 5252–5256.

49. G. Wu, G. F Cui, D. Y. Li, P. K. Shen and N. Li, J. Mater. Chem., 2009, 19, 6581–6589.

50. J. B. Parise, Acta Crystallogr., 1980, 36, 1179–1180.

51. M. E. Fleet, Am. Mineral., 1977, 62, 341–345.

52. R. P. Agarwala and A. P. B. Sinha, Z. Anorg. Allg. Chem., 1957, 289, 203–206.

53. J. P. Rouche and P. Lecocq, Compt. Rendus Chem., 1966, 262, 555.

54. G. V. Gibbs, R. T. Downs, C. T. Prewitt, K. M. Rosso, N. L. Ross and D. F. Cox, J. Phys. Chem. B, 2005, 109, 21788–21795.

55. Z. Loizos and N. Spyrellis, Thin Solid Films, 1991, 204, 139–149.

56. I. M. Sadiek, A. M. Mohammad, M. E. El-Shakre, M. I. Awad, M. S. El-Deab and B. E. El-Anadouli, Int. J. Electrochem. Sci., 2012, 7, 3350–3361.

57. R. B. Shalvoy and P. J. Reucroft, J. Vac. Sci. Technol., 1979, 16, 567.

58. Y. Liao, K. Pan, Q. Pan, G. Wang, W. Zhou and H. Fu, Nanoscale, 2015, 7, 1623–1626.

59. W. Shi, X. Zhang and G. Chen, Int. J. Hydrogen Energy, 2013, 38, 7037–7045.

60. X. Lv, Y. Zhu, H. Jiang, X. Yang, Y. Liu, Y. Su, J. Huang, Y. Yao and C. Li, Dalton Trans., 2015, 44, 4148–4154.

61. A. B. Mandale, S. Badrinarayanan, S. K. Date and A. P. B. Sinha, J. Electron. Spectrosc. Relat. Phenom., 1984, 33, 61.

62. C. E. M. Camposa, J. C. de Limaa, T. A. Grandia, K. D. Machadoa, P. S. Pizanib and R. Hinrichs, Solid State Ionics, 2004, 168, 205–210.

63. J. Ran, J. Zhang, J. Yu, M. Jaroniec and S. Z. Qiao, Chem. Soc. Rev., 2014, 43, 7787–7812.

64. Y. Qiu, L. Xin and W. Li, Langmuir, 2014, 30, 7893–7901.

65. L. Trotochaud, S. L. Young, J. K. Ranney and S. W. Boettcher, J. Am. Chem. Soc., 2014, 136, 6744–6753.

66. D. A. Corrigan, J. Electrochem. Soc., 1987, 134, 377–384.

67. A. Swesi, J. Masud and M. Nath, unpublished results.

68. J. Masud, T. V. Nguyen, N. Singh, E.McFarland, M. Ikenberry, K. Hohn, C. J. Pan and B. J. Hwang, J. Electrochem. Soc., 2015, 162, F455–F462.

SUPPORTING INFORMATION

NICKEL SELENIDE AS A HIGH-EFFICIENCY CATALYST FOR OXYGEN EVOLUTION REACTION

Energy Environ. Sci., 2016, **9**, 1771—1782

A. T. Swesi, J. Masud and M. Nath

Department of Chemistry, Missouri University of Science and Technology, Rolla, Missouri 65409, United States.

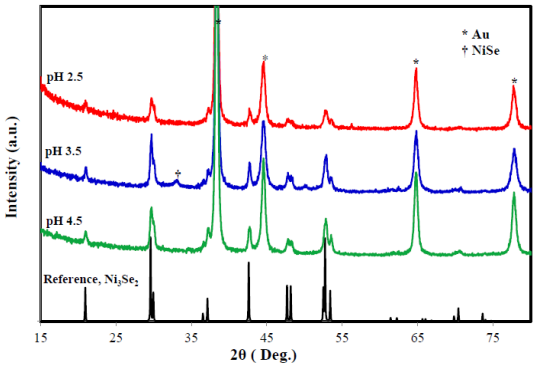

Figure S1. Pxrd patterns of catalysts deposited for 300 s at different pH of the electrochemical bath.

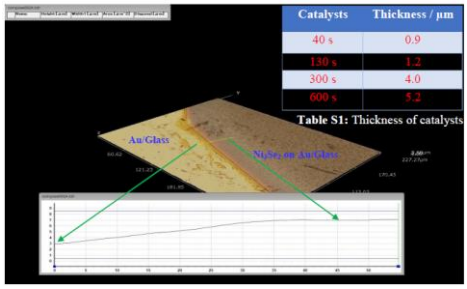

Figure S2a. 3D imaging and 3D profile of catalyst synthesized for 300 s. Table shows the thickness of catalysts that were synthesized for different time. The HIROX KH-8700 Digital Microscope, is the next generation system for the high precision of measurement and 3D profiling, was used to measure the approximate thickness of electrodeposited Ni_3Se_2 catalyst on Au/Glass.

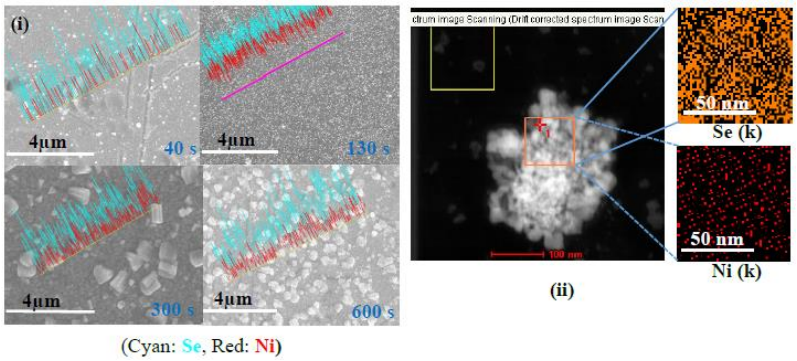

Figure S2b. (i) EDS line scanning of catalysts and (ii) HAADF image of electrodeposited Ni_3Se_2 along with the elemental mapping of Ni and Se from a specific area within the cluster.

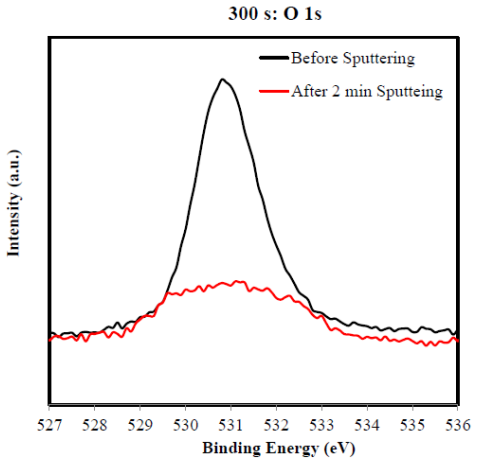

Figure S3. XPS spectra of O 1s peak obtained from the catalyst before and after 2 min sputtering.

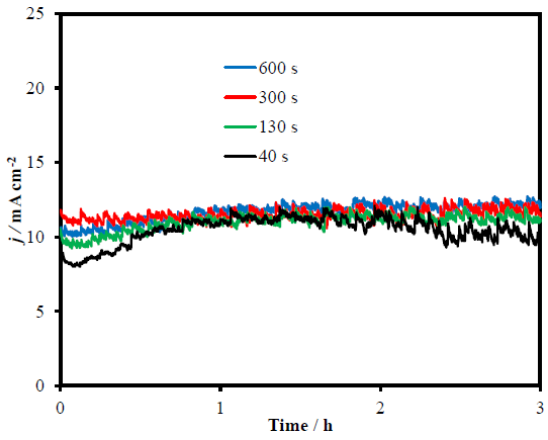

Figure S4. Current transient recorded at a constant overpotential to achieve 10 mA cm^{-2}.

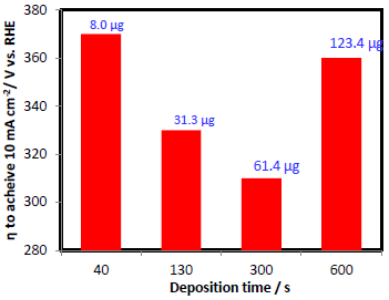

Figure S5. Overpotential required to achieve 10 mA cm^{-2} for different deposition time of the catalyst. Total catalyst loading for different deposition times are shown on the top of the column.

Collection Efficiency. The measured ratio of the ring limiting current to the disk limiting current is known as the collection efficiency (N) of that RRDE electrode and it can be written as-

$N = i_{\text{Limiting Ring}} / i_{\text{Limiting Disk}}$ (1)

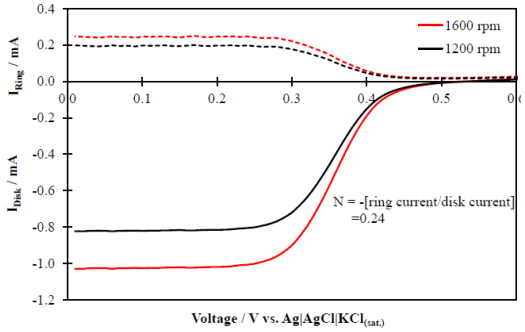

Figure S6. Rotating Ring-Disk voltamograms in N_2 saturated 0.001M $K_3Fe(CN)_6$ containing 0.3M of KOH at 0.05 V s^{-1} at different rotation rate. Ring potential was held on 0.7 V vs. Ag/AgCl which is sufficient to oxidize the product rapidly at ring. (Here ring current was shown as a potential of disk electrode).

At disk electrode, the reduction of ferricyanide ($Fe(CN)_6^{3-}$) to ferrocyanide (($Fe(CN)_6^{4-}$) took place, on the other hand ferrocyanide is oxidized to ferricyanide at ring at positive potential (0.7 V vs. Ag/AgCl). The value of N was calculated for different rotation and it was found to be independent of rotation (0.24).

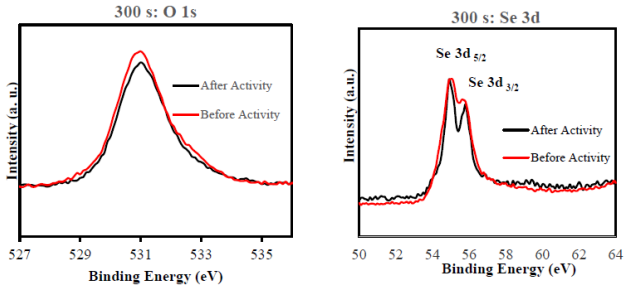

Figure S7. XPS spectra of O 1s and Se 3d peaks obtained from the catalyst before and after chronoamperometry (18h).

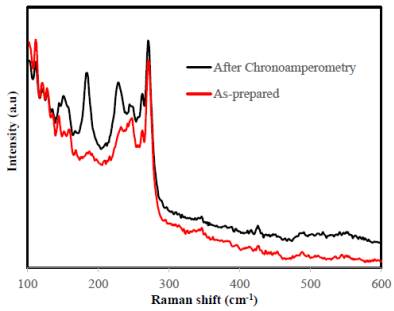

Figure S8. Raman spectra of Ni_3Se_2 before and after chronoamperometry for 18h.

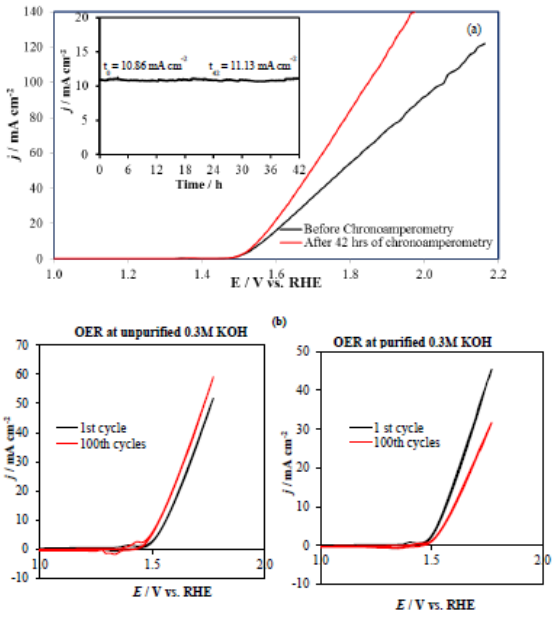

Figure S9. (a) Chronoamperometry at overpotential of 0.31 V (*vs.* RHE); comparison of (b) LSV before and after 42 h of chronoamperometry; and (c) cyclic voltammograms for OER of 1st cycle with 100th cycles in unpurified and purified 0.3 M KOH.

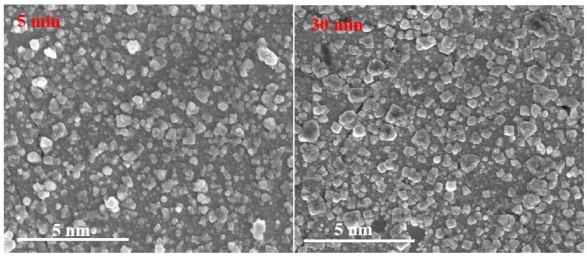

Figure S10. SEM images of the catalyst deposited for 300 s after 5 and 30 min annealing under N_2, respectively.

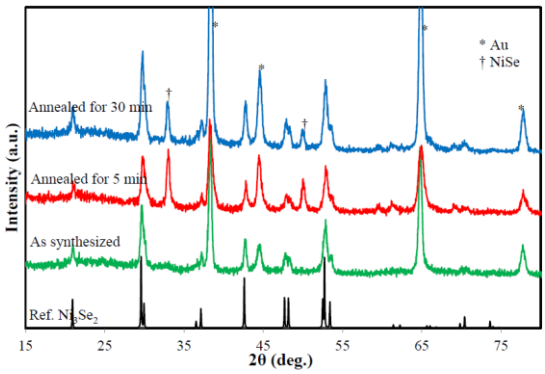

Figure S11. Pxrd patterns of catalysts deposited for 300 s before and after annealing under N_2.

Table ST1. Variation of Ni:Se ratio as a function of annealing.

Catalyst synthesized for 300 s	**Ni: Se**
As prepared	1.32
Annealing for 5 min	1.43
Annealing for 30 min	1.93

II. ENHANCING ELECTROCATALYTIC ACTIVITY OF BIFUNCTIONAL Ni_3Se_2 FOR OVERALL WATER SPLITTING THROUGH ETCHING-INDUCED SURFACE NANOSTRUCTURING

Journal of Material Research

Abdurazag T. Swesi, Jahangir Masud, Manashi Nath

Department of Chemistry

Missouri University of Science and Technology

Rolla, Missouri 65409-0050 USA

Email: nathm@mst.edu

ABSTRACT

Electrocatalysts for oxygen evolution reaction (OER) has been at the center of attention for water splitting reactions. In this article we have presented a methodology to significantly improvement the OER catalytic efficiency of electrodeposited Ni_3Se_2 films. Specifically, the pristine Ni_3Se_2 on surface nanostructuring induced through electrochemical etching shows a remarkable decrease of overpotential (@10 $mA.cm^{-2}$) to 190 mV, making it as one of the best OER elecrocatalyst known till date. Through detailed structural and morphological characterization of the catalyst film, we have learnt that such enhancement is possibly caused by the increased surface roughness factor and electrochemically active surface area of the etched film. The morphology of the film also changed from smooth to rough on etching further supporting the enhanced catalytic activity. Detailed characterization also revealed that the composition of the film was

unaltered on etching. Ni_3Se_2 film was also active for HER in alkaline medium making this a bifunctional catalyst capable of full water splitting in alkaline electrolyte with a cell voltage of 1.65 V.

1. INTRODUCTION

In this era of exploring alternative and sustainable energy resources, catalyst aided water splitting plays a substantial role. However, basic electrochemical water splitting is associated with substantial energy loss, fundamentally due to the high overpotentials required at the anode corresponding to the oxygen evolution reaction (OER). Although traditionally precious metal oxides such as RuO_x and IrO_x were viewed as efficient water oxidation catalysts,[1-3] scarcity of the raw materials and their high cost has been prohibitive for wide scale practical applications of these catalysts. To circumvent this issue, over the past several years, researchers have delved deeper into transition metal oxides as OER electrocatalyst with performance comparable to the precious metal oxides.[4-23]

More recently, new families of OER electrocatalysts has been identified comprising of transition metal chalcogenides M_xE_y (M = Ni, Fe, Co; E = S, Se),[24-28] some of which outperform even the transition metal oxides.[26,27] Some of the major advantages of using chalcogenides over oxides is that the electronegativity of S, Se, and Te being smaller than O, metal-chalcogen bonds show a higher degree of covalency, which leads to decreasing bandgap energy, as well as raising the valence band edge to be more closer to the water oxidation level. In fact theoretical band structure calculations have shown that the band gap and band edge energies does show a progressive change (decreasing band gap and

increasing valence band edge energy) from oxides to tellurides.[29,30] While most of the transition metal oxides are wide bandgap semiconductors, the selenides and tellurides are mostly semi-metal or metallic. Additionally, the transition metal chalcogenides are known to form a wide range of stoichiometries stabilizing the metal in different oxidation states, which leads to lower redox potential of the transition metal center. Cumulative effects of all these are expected to result in much better electrocatalytic activity in the chalcogenides. In fact, our recent report showed that a simple binary nickel selenide, Ni_3Se_2, can outperform some of the best OER electrocatalyst and produced 10 mA cm^{-2} exchange current density at an overpotential of 290 mV.[26] Following this report several other selenides were shown to be active for OER including diselenides,[24,27,31,32] monoselenides,[33] and sulfides such as Ni_3S_2.[34] Although the OER overpotential has been reduced substantially in these new families of electrocatalysts, further improvement of overpotentials is still desirable for the development of energy efficient water splitting devices.

Apart from higher efficiency, another important aspect of these transition metal oxides and chalcogenides electrocatalyst is that a good proportion of them are active for both OER and HER (hydrogen evolution reaction) in alkaline medium. Over the past couple of years, several bifunctional water splitting catalysts have been reported such as NiFe layered double hydroxide on nickel foam,[35] cobalt–cobalt oxide/N-doped carbon hybrids,[36] porous cobalt phosphide/cobalt phosphate thin film,[37] cobalt-phosphorous-derived film,[38] Ni_2P nanoparticles,[39] Ni_5P_4 film,[40] CoSe,[41] and NiSe nanowires film on Ni-foam.[42] A bifunctional catalyst active for both OER and HER in the same electrolytic solution can offer full water splitting and is even more attractive for practical applications.

However, such bifunctional electrocatalysts with reasonably good activity for both OER and HER is very challenging to design.

One of the possible ways to increase the catalytic activity is by increasing the active surface area which can be done though nanostructuring and increasing the surface roughness.[22] Along with this creating a porous surface is also advantageous for catalytic activities since reactants can diffuse into the catalyst layer easily on such structures and reduce the liquid sealing effect, hence improving the catalyst performance.[43] One of the favored methods to create a porous surface is through etching. In electrodeposited films, electrochemical etching can lead to partial dissolution of the film thereby forming porous rough films with higher surface area with well-preserved conductivity of the film.

Herein, we have demonstrated how the bifunctional electrocatalytic activity of Ni_3Se_2 film can be improved through electrochemical etching induced nanostructuring. The OER activity especially shows a significant improvement achieving 10 $mA.cm^{-2}$ at an overpotential of 190 mV in 1 M NaOH which is one of the lowest overpotential reported till date. The HER also shows a low overpotential of 230 mV at 10 mA cm^{-2}, making this bifunctional catalyst active for full water splitting at 1.65 V (*vs* RHE).

The catalyst showed exceptional stability under conditions of continuous O_2 and H_2 generation for extended periods of time exceeding 18 h with low Tafel slope values. Detailed structural and morphological characterization revealed that the films were compositionally stable after OER and HER activity.

2. EXPERIMENTAL AND METHODS

2.1. PREPARATION OF AS-DEPOSITED Ni_3Se_2 FILM AND ROUGHENED Ni_3Se_2 FILM

Electrodeposition of Ni_3Se_2 films was performed in a conventional three-electrode cell, using Ag|AgCl as the reference electrode while working and counter electrodes were made from Au-coated glass (Deposition Research Lab Incorporated (DRLI)) and platinum mesh, respectively. The details of the Ni_3Se_2 electrodeposition procedure has been published elsewhere.[21] The Au substrates were cleaned[21] by ultrasonic treatment in micro-90 detergent followed by isopropanol and deionized (DI) water. The clean Au substrates were masked with a scotch tape, leaving an exposed area for the electrodeposition. The solutions were prepared using analytical grade reagents and DI water (resistivity ~18 MΩ cm). Prior to mixing, the solutions were purged with N_2 gas to remove any dissolved O_2. Dilute HCl was added to maintain the pH at 2.5 and to prevent the formation of hydroxyl species. The deposition potential of Ni_3Se_2 was controlled at -0.80 V (vs. Ag|AgCl) for 300 s from an aqueous solution containing 10 mM $NiSO_4.6H_2O$, 10 mM Na_2SeO_3 and 25 mM LiCl at 25 ^oC. An IviumStat potentiostat was used to control the electrodeposition process and to monitor the current and voltage profiles. Immediately after deposition, the deposits were washed with deionized water in order to remove impurities and adsorbents from the surface.

Surface-roughened Ni_3Se_2 film was prepared by further electrochemical etching of the as-deposited Ni_3Se_2 film in 0.05 M HCl. Typically, Ni_3Se_2 film was connected as the anode while Pt was the cathode in the electrochemical cell, and a current density of 10 mA cm^{-2} was maintained between the two electrodes for 15 s and 30 s. Such treatment led to

partial dissolution of the Ni_3Se_2 film. After electrochemical dissolution, products were washed in deionized water, and then air-dried. The as-deposited Ni_3Se_2 film was silvery black and the surface of the coating was very bright. After electrochemical dissolution, the surface color remained same and no discolored patches were observed.

3. METHODS OF CHARACTERIZATION

3.1. POWDER X-RAY DIFFRACTION (XRD)

The electrodeposited substrates were studied as such without any further treatment. Philips X-Pert X-ray diffractometer was used to obtain the characteristic XRD pattern of the catalysts where the radiation source was CuKα (1.5418Å).As the deposited layer of catalyst on the substrate was very thin, the pxrd was collected at grazing angles in thin film geometry (GI mode with Göbel mirrors).

3.2. SCANNING ELECTRON MICROSCOPY (SEM)

FEI Helios NanoLab 600 FIB/FESEM at an acceleration voltage of 10 kV and a working distance of 4.8 mm was used to check the morphology of catalyst. The energy dispersive spectroscopy (EDS) analysis of the films was performed from the same SEM microscope. Cu tapes were used to connect the sample surfaces to the stubs in order to provide a good “path to ground” to reduce charging effect. ImageJ software was used for the measurement of the particles to determine the average particle size.

3.3. TRANSMISSION ELECTRON MICROSCOPY (TEM)

TEM, high-resolution TEM imaging (HRTEM), and selected area electron diffraction (SAED) patterns were obtained from a FEI Tecnai F20 microscope operating at 300 kV accelerating voltage. The sample for TEM analysis was prepared by scratching little bit of the powder from the Au-glass substrate (after dissolution) and dispersing it in methanol, followed by dropping it on the formvar-coated Cu TEM grids.

3.4. X-RAY PHOTOELECTRON SPECTROSCOPY (XPS)

KRATOS AXIS 165 X-ray Photoelectron Spectrometer with a source of monochromatic Al X-ray source was used to perform the XPS measurements of the elctrodeposited films. The spectra were collected after 2 min sputtering with Ar to remove the immediate oxide layer from the surface of catalyst. All XPS binding energies were corrected by using the reference C1s signal at 284.5 eV.

3.5. ELECTROCHEMICAL PERFORMANCE STUDY

LSV, CV and chronoamerometry techniques were used for the catalytic evaluation of the deposited films. Typical three-electrode system electrochemical cell coupled with an IviumStat potentiostat was used for the study where Ni_3Se_2 modified Au, Ag|AgCl|KCl-$_{(sat.)}$ and Pt mesh were used as working, reference and counter electrodes, respectively. All potentials obtained as Ag|AgCl|KCl$_{(sat.)}$ reference electrode were converted to the reversible hydrogen electrode (RHE) by using the following Equation.

$$E_{RHE} = E_{Ag|AgCl|KCl(sat.)} + 0.059\ pH + E^{o}_{Ag|AgCl|KCl(sat.)}$$

where E_{RHE} is the calculated potential as RHE, $E_{Ag|AgCl|KCl(sat.)}$ is the experimentally measured potential, $E^{o}_{Ag|AgCl|KCl(sat.)}$ is the thermodynamic potential at 25 ^{o}C (0.197 V).

4. RESULTS AND DISCUSSION

4.1. STRUCTURE AND MORPHOLOGY STRUCTURE OF Ni_3Se_2 FILMS

The pxrd patterns of as-synthesized films deposited on Au-coated glass substrates showed peaks corresponding to Ni_3Se_2 phase (PDF # 019-0841) along with peaks characteristic of Au arising from the underlying substrate as shown in Figure 1. Ni_3Se_2 has an interesting crystal structure (shown as inset of Figure 1) built up of anion close packing where Ni occupies 3/4th of the tetrahedral holes specifically showing a distorted tetrahedral coordination. Se on the other hand, shows a distorted trigonal prismatic coordination with the neighboring Ni atoms. Interestingly, energy density studies have suggested that Ni_3Se_2 may have Ni-Ni bonding influenced by the closeness of the edge-shared Ni polyhedra.[44]

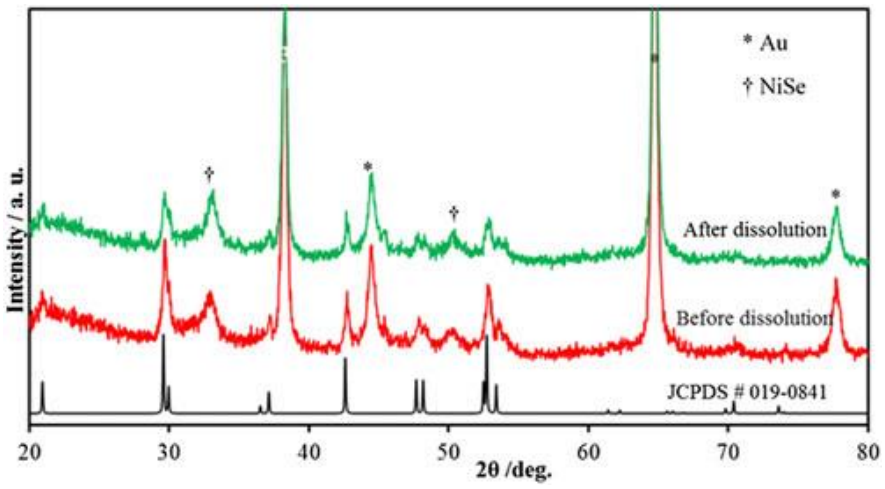

Figure 1. PXRD patterns of Ni_3Se_2 catalysts before and after dissolution (acid leaching) showing the presence of Ni_3Se_2 (PDF # 019-0841) along with Au.

The diffraction pattern obtained after electrochemical etching (as shown in Figure 1), still clearly shows the presence of crystalline Ni_3Se_2 with no other discernible impurity peaks, indicating that the film obtained after etching was indeed predominantly Ni_3Se_2. This confirmed that Ni_3Se_2 phase was not lost in electrochemical etching progress. However, the intensity of the diffraction peaks of Ni_3Se_2 phase became stronger after electrochemical dissolution. Figures 2a and 2b show morphology of the as-deposited Ni_3Se_2 film and the etched Ni_3Se_2 film, respectively. Detailed SEM study of the as-deposited film showed that the film was mainly granular and composed of micron sized grains with a broad size distribution (0.21 to 1.2 μm) and an average particle diameter of 0.74 μm. From the SEM (Figure 2a) it was also apparent that the as-deposited micron-sized grains had very smooth surfaces before electrochemical dissolution. After electrochemical etching SEM of the Ni_3Se_2 film showed a distinct difference as can be seen in Figure 2b. The film became noticeably porous with very rough surface of the grains which seemed to be covered with thin nanoflakes. Nevertheless, representative SEM images (Figure 2a and 2b) clearly showed that even after dissolution, the Au-glass substrate was still uniformly coated with the interconnected nanograins network structure without developing any fragmentation or obvious breakage. Particle size analysis revealed that the dimensions of the grains varied from 0.072 – 0.77 μm, where the lower limit was for the thickness of the flakes while the upper limit was the grain size. Average grain size was obtained to be around 0.31 μm.

The nanostructured film after dissolution was also studied by TEM and HRTEM imaging as shown in Figures 2c and 2d. Low-magnification TEM image (Figure 2c) shows the rough surface texture of the granules. Higher magnification HRTEM image on the other

hand, shows the crystalline nature of the granules with lattice fringes corresponding to <110> lattice planes of Ni_3Se_2 shown in Figure 2d. The crystalline nature of the nanostructured grains were also confirmed by SAED which showed diffraction rings corresponding to <220> and <232> lattice planes. Thus it was further confirmed with TEM and SAED analysis that the nanostructured grains were indeed crystalline Ni_3Se_2 after the dissolution step.

The composition of the film was further confirmed through quantitative EDS, elemental mapping, and XPS. While the elemental mapping clearly showed that Ni and Se were homogeneously distributed in nanograins, quantitative analysis showed that the relative ratio of Ni:Se was close to 3:2, which confirmed the film composition was indeed Ni_3Se_2 (Figure 2e). The Ni:Se ratio did not change after electrochemical dissolution confirming the stability of the film (Figure 2f). XPS spectra showed peaks corresponding to Ni $2p_{3/2}$ and $2p_{1/2}$ at 855 and 869 eV as shown in Figure 2g, while Se 3d peaks (Figure 2h) were observed at 54.5 and 55.6 eV ($3d_{5/2}$ and $3d_{3/2}$, respectively). These XPS peaks agrees very well with those reported for Ni_3Se_2.[26] Interestingly XPS did not show any evidence for the presence of oxidic impurities on the surface even after the electrochemical etching step. All of the above characterization confirmed that the composition of the film did not show a drastic change after electrochemical etching. In fact, this etching step can be possibly use as a surface cleaning technique where the acid removes soluble impurities from the surface (including oxides) thereby yielding a more pristine surface. Since this surface cleaning is achieved through electrochemical etching induced dissolution, this step has been simply referred to as dissolution hereafter.

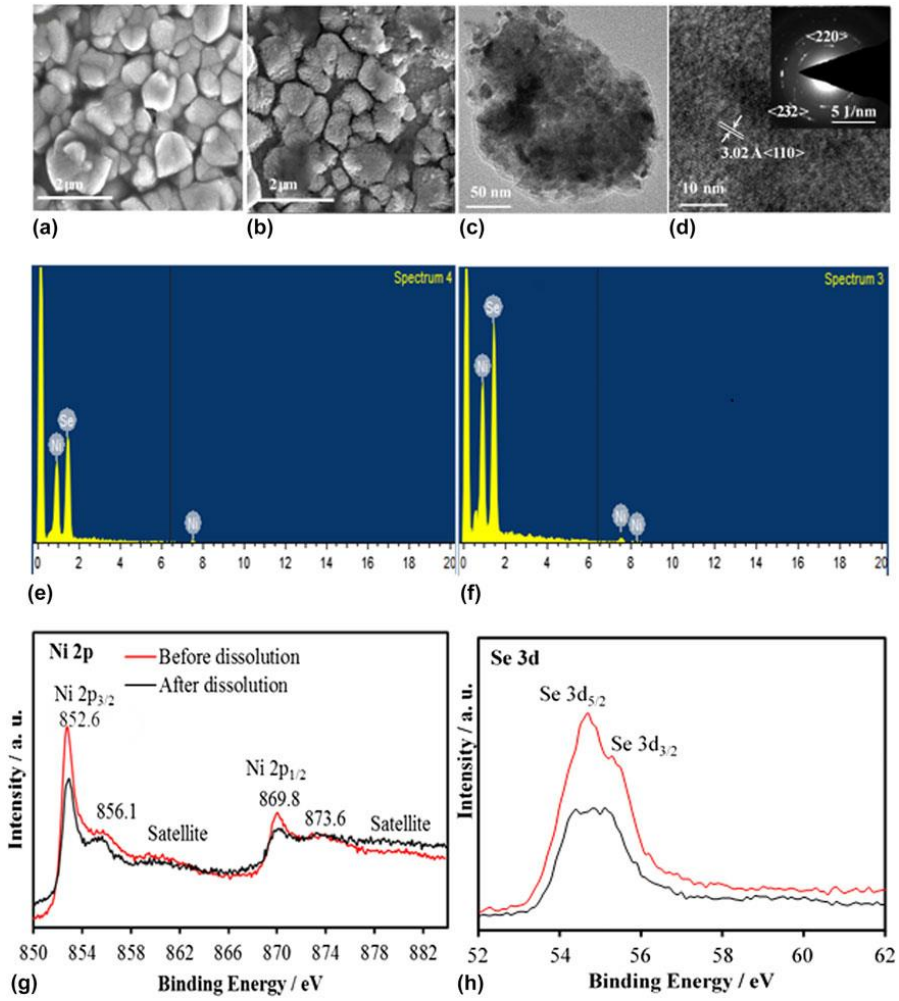

Figure 2. SEM images of Ni_3Se_2 (a) before and (b) after dissolution. (c) TEM and (d) HRTEM images of Ni_3Se_2 catalyst after dissolution. Inset in (d) shows the SAED pattern. (e) and (f) are the EDS spectra of Ni_3Se_2 before and after dissolution, respectively. (g) Ni 2p and (h) Se 3d XPS spectra where red and black lines indicate the before and after dissolution of catalysts.

4.2. ELECTROCHEMICAL PERFORMANCE OF Ni_3Se_2 FILMS

One of the very obvious changes observed after the dissolution was that the morphology of the film changed from smooth to rough and porous, which is accompanied by an increased surface area. Specifically, as the electrodeposited Ni_3Se_2 was aged as an anode in an acidic solution, it led to sporadic dissolution from the film surface thus creating a rough surface. This expectedly led to an increase of the electrode surface area which was

further confirmed through measuring the electrochemically active surface area (ECSA) and roughness factor (RF) of the film after dissolution and comparing it with the *as deposited* film. ECSA was estimated by measuring the double layer charging current at different scan speeds. The probed electrode was potentiostatically cycled (-0.25 to -0.1 V *vs* Ag|AgCl) with scan rates ranging between 10 to 160 mV s^{-1} while the charging current was collected (Figure 3a and 3b). The electrochemical double layer capacitance, C_{DL}, is proportional to the collected charging current, i_c, and inversely proportional to the scan rate, υ, as shown in the following Equation,

$$i_{DL} = C_{DL} * \nu \quad (1)$$

The C_{DL} was estimated as the slop of the plot of i_c as a function of v. The ECSA of the catalysts can be calculated based on the following Equation,

$$ECSA = C_{DL} / C_s \quad (2)$$

Where C_s is the specific capacitance (0.040 mF cm^{-2}) in 1 M NaOH.[21] The roughness factor (RF) of each electrode was then calculated by dividing obtained ECSAs by the geometric area (0.14 and 0.283 cm^2 for the catalyst with and without dissolution, respectively). It was observed that the ECSA increased more than 3-fold after dissolution for 30 s (1.5 cm^2 in pristine Ni_3Se_2 to 4.9 cm^2 after dissolution), while the roughness factor showed a more dramatic change, increasing almost 7-fold following the dissolution step (5.3 to 35, respectively).

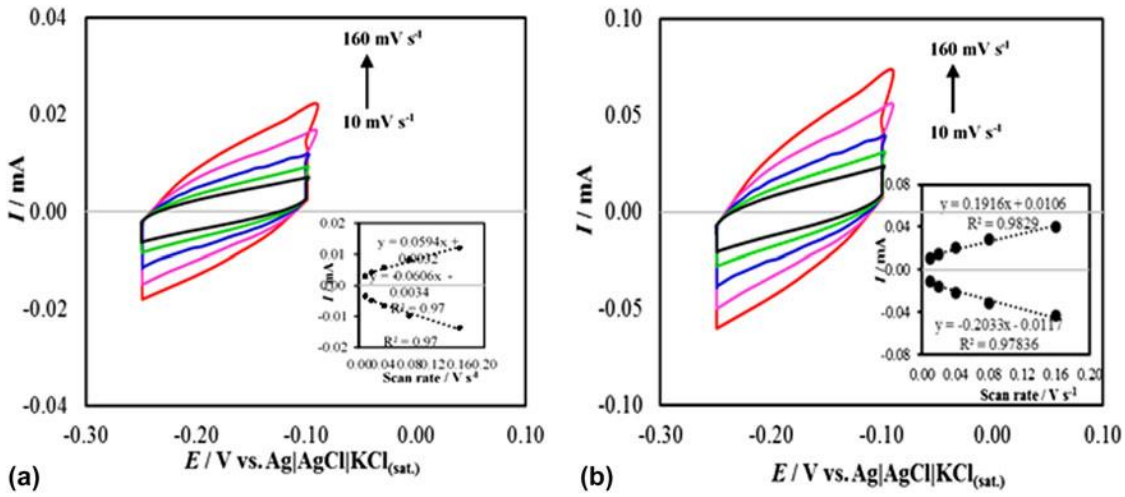

Figure 3. Cyclic voltammograms measured at (a) before and (b) after dissolution of Ni_3Se_2 catalysts in N_2 saturated 1.0 M NaOH solution at different scan rate from 10 to 160 mV s^{-1}. Inset shows plot of anodic and cathodic current measured at -0.19 V as function of scan rate.

The electrocatalytic performance for OER of the electrodeposited films was investigated through linear sweep voltammetry (LSV) in alkaline solution (1 M NaOH) near pH 14. For comparison, we had also checked electrodeposited RuO_2, and $Ni(OH)_2$ for OER catalytic activity. Figure 4a shows the LSVs of electrochemical oxygen evolution with Ni_3Se_2 catalysts, before and after dissolution, compared with that of RuO_2 and $Ni(OH)_2$. As observed, after electrodeposition of Ni_3Se_2 the substrates showed high activity for OER with onset overpotential of about 200 mV for the as-deposited Ni_3Se_2 electrode and 160 mV (170 mV) for the treated Ni_3Se_2 electrode for 15 s (30 s), respectively [all potentials have been reported with respect to reversible hydrogen electrode (RHE)]. This 30 - 40 mV shift in onset overpotential is expected as more catalytically active sites were exposed to the electrolyte resulting from the increased surface area and higher roughness factor. Specifically, the dissolution step creates high density of exposed active metal sites on the surface which in turn increases the electrocatalytic performance by reducing the overpotential and increasing current density.

Table 1. Electrochemical parameters of the catalysts measured in 1 M NaOH.

Catalysts	OER			HER		
	Onset potential / V[a]	η to 10 mA cm^{-2} / mV[a]	Tafel slope / mV dec^{-1}	Onset potential / V[a]	η to 10 $mAcm^{-2}$ / mV[a]	Tafel slope / mV dec^{-1}
Ni_3Se_2 (as is) @Au	1.43	260	87.1	0.19	292	188.1
Ni_3Se_2 (15 s dissolution) @Au	1.40	230	54.6	0.16	235	234.4
Ni_3Se_2 (30 s dissolution) @Au	1.39	190	48.9	0.16	234	230.4
$Ni(OH)_2$ @ Au	1.48	340	61.1	-	-	-
RuO_2 /Au	1.45	320	56.3	-	-	-
Pt	-	-	-	0.00	52	37.9

[a] Potential *vs* RHE

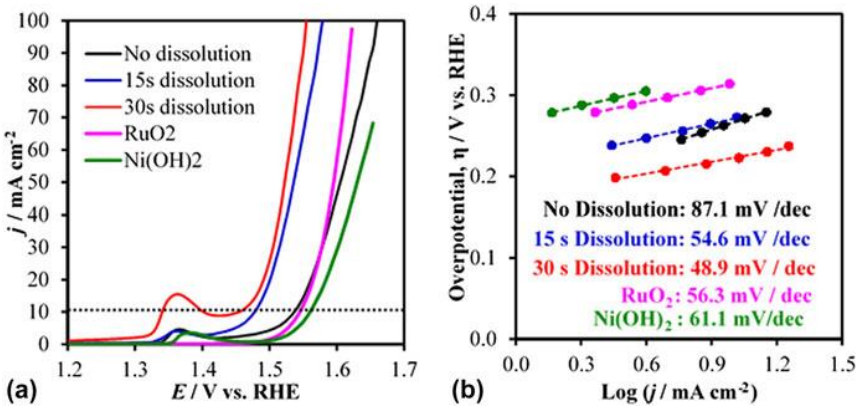

Figure 4. (a) LSVs measured at catalysts in N_2 saturated 1.0 M NaOH solution at a scan rate of 10 $mV.s^{-1}$. Dotted line shows the current density of 10 mA $cm^{-2.}$ (b)Tafel plots of catalysts.

Conventionally, the effectiveness of OER catalysts are estimated by listing the overpotential (η) required to reach a current density of 10 mA cm^{-2} (per geometric surface area), which is considered to be equivalent to 10 % solar energy conversion efficiency.[6] The η at 10 mA cm^{-2} per geometric area of all films are reported in Table 1. It can be clearly found that the surface-etched Ni_3Se_2 catalyst exhibits higher catalytic activity towards OER with a much lower η (190 mV). It should be mentioned here that this is one of the lowest overpotential that has been reported for OER electrocatalyst.

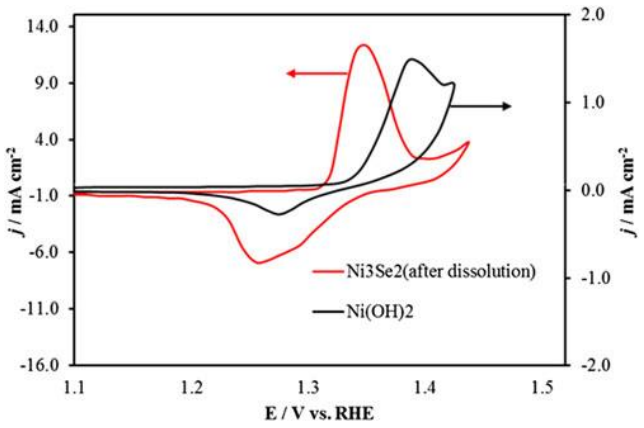

Figure 5. CVs measured at Ni_3Se_2 after 30 s dissolution and $Ni(OH)_2$ catalysts in N_2 saturated 1.0 M NaOH at 10 mV s^{-1}.

The kinetic parameters corresponding to the OER activities were estimated from the measured Tafel slope collected near the onset potential for OER. The Tafel plots for the as-prepared Ni_3Se_2 and surface-modified Ni_3Se_2 catalysts (after dissolution) in 1 M NaOH solution are shown in Figure 4b. The observed Tafel slope of the surface-modified Ni_3Se_2 catalyst were about 56.4 and 48.9 mV dec^{-1} for 15 and 30 s of dissolution, respectively which were much smaller than that of as-prepared Ni_3Se_2 catalysts (87.1 mV dec^{-1}), which can be attributed to the facilitated diffusion through the highly porous and rough surface of the modified electrode. The smaller Tafel slope of the modified electrode compared to that of the pristine electrode also suggest faster reaction kinetics.

In addition to reporting enhanced electrocatalytic activity for OER, it is also important to understand what causes such improvement of the onset and overpotential in the transition metal selenides, as compared to the oxides. It was observed from the LSV plots that in both Ni_3Se_2 as well as $Ni(OH)_2$, the OER activity was preceded by $Ni^2 \rightarrow Ni^{3+}$ oxidation peak and it has been widely accepted that Ni^{3+} is the actual catalytically active species.[45] We looked more closely at the $Ni^{2+} \rightarrow Ni^{3+}$ oxidation peak by measuring cyclic voltammograms (CV) across a short potential range and compared the CVs obtained from

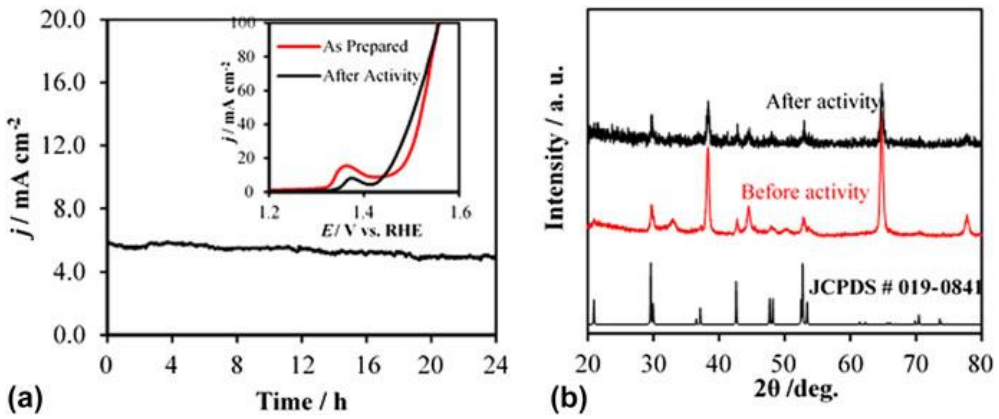

Figure 6. (a) Stability of catalyst under continuous O_2 evolution for 24 h studied at constant potential. Inset of (a) is the comparison of LSVs of catalyst in N_2 saturated 1.0 M NaOH before and after chronoamperometry for 24 h (b) XRD of catalyst before and after chronoamperometry for 24 h.

the Ni_3Se_2 with that obtained from $Ni(OH)_2$. This comparison very clearly showed that the pre-oxidation peak itself was shifted to lower potential (by about 50 mV) in the selenide compared to the oxide as shown in Figure 5. This indicates that the catalytically active species (Ni^{3+}) is generated at a much lower potential in the selenide. This observation coupled with the smaller bandgap and higher conductivity of the selenide matrix may be instrumental in enhancing their OER catalytic activity compared to the oxides.

In addition to the outstanding catalytic activity, the modified Ni_3Se_2 catalyst also showed good stability for OER (Figure 6). The chronoamperometry (current *vs* time) plot for porous Ni_3Se_2 electrode maintained at a constant potential of 0.42 V *vs*. Ag/AgCl exhibits stable current over 24 h of continuous operation suggesting that the modified Ni_3Se_2 catalyst displayed good durability for OER in 1 M NaOH. Comparison of LSVs before and after 24 h of electrolysis (inset of Figure 6a) also confirmed the stability of catalyst.

The compositional stability of the catalyst after periods of continuous O_2 evolution was also studied by XRD collected after 24 h OER activity. The pxrd study revealed that

the structural integrity of Ni_3Se_2 was maintained even after 24 h of continuous O_2 evolution as shown in Figure 6b indicating the durability of the catalyst.

The Ni_3Se_2 has also been studied for possible HER catalytic activity in the same electrolyte (1 M NaOH) by measuring the LSV between −0.5 and 0.0 V *vs.* RHE using a three-electrode system with a scan rate of 10 $mV.s^{-1}$. Au coated-glass was used as the substrate due to its negligible HER activity. Commercially available Pt was also used for comparison of the HER catalytic activity. Compared to the as-deposited Ni_3Se_2, the electrochemically treated Ni_3Se_2 showed better HER performance (Table 1), achieving 10 mA cm^{-2} at an overpotential of 234 mV and showing a Tafel slope of 230.4 mV dec^{-1} (Figure 7b). Chronoamperometric measurements at -0.2 V vs. RHE revealed that the catalysts retained stable HER activities even after 3 h (Figure 7c & d), suggesting their

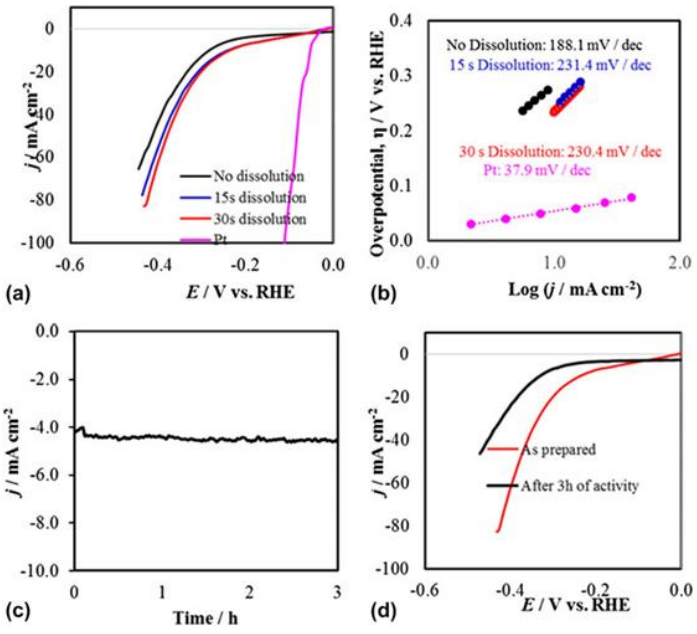

Figure 7. (a) Polarization curves for catalysts in N_2 saturated 1.0 M NaOH solution at a scan rate of 10 mV s^{-1}. (b) Tafel plots of catalysts. (c) Stability study of catalyst under continuous H_2 evolution for 3 h at constant potential and (d) is the LSVs of catalyst in N_2 saturated 1.0 M NaOH for comparison.

potential as an attractive bifunctional electrocatalyst for full water splitting. Accordingly, a cell was created by coating both the cathode and anode with surface modified Ni_3Se_2, and it was observed that this bifunctional catalyst could effectively split water producing a current density of 10 mA cm^{-2} at a cell voltage of 1.69 V. The electrolysis energy efficiency was calculated to be 84% following methods as has been reported previously.[46]

5. CONCLUSION

Morphology-controllable Ni_3Se_2 films were successfully prepared by electrodepositing Ni_3Se_2 film on Au substrate and following by electrochemical dissolution. In electrochemical dissolution process, Ni_3Se_2 phase is well-preserved and roughened, porous structure was formed. This technology is a promising way to fabricate other roughened high surface area films. The etched Ni_3Se_2 film showed an enhanced OER catalytic performance in comparison with the as-deposited Ni_3Se_2 film. This enhancement in catalytic activity could be explained by the increased surface roughness factor and flake-like morphology of the film which facilitates transfer of charge across the electrolyte-electrode interface. Introduction of pores on the catalyst surface through electrochemical dissolution also improves the catalytic performance. Specifically, the overpotential for OER catalytic activity exhibited by the etched Ni_3Se_2 is clearly the lowest amongst all other reported OER electrocatalyst (Table 1). This etched Ni_3Se_2 electrocatalyst competes other earth-abundant material-based OER and HER catalysts, and places itself as one of the best bifunctional electrocatalysts to date, with a high current density and excellent stability.

ACKNOWLEDGEMENTS

This research was funded through financial support from ACS PRF (grant #54793-ND10) and Energy Research and Development Center (ERDC) at Missouri S&T.

REFERENCES

1. C. C. L. McCrory, S. Jung, J. C. Peters and T. F. Jaramillo: Benchmarking heterogeneous electrocatalysts for the oxygen evolution reaction. *J. Am. Chem. Soc*. **135**, 16977 (2013).

2. J. Rossmeisl, Z. W. Qu, H. Zhu, G. J. Kroes and J. K. J.Norskov: Electrolysis of water on oxide surfaces. *Electroanal. Chem*. **607**, 83 (2007).

3. Y. Lee, J. Suntivich, K. J. May, E. E. Perry and Y. S. Horn: Synthesis and activities of rutile IrO_2 and RuO_2 nanoparticles for oxygen evolution in acid and alkaline solutions. *J. Phys. Chem. Lett*. **3**, 399 (2012).

4. M. Gong and H. Dai: A mini review of NiFe-based materials as highly active oxygen evolution reaction electrocatalysts. *Nano Res*. **8**, 23 (2015).

5. H. N. Seiger and R. C. Shair: Oxygen evolution from heavily doped nickel oxide electrodes. *J. Electrochem. Soc*.**108**, C163 (1961).

6. Y. G. Li, P. Hasin, Y. Y. Wu: $NixCo_3$-xO_4 nanowire arrays for electrocatalytic oxygen evolution, *Adv. Mater*. **22**, 1926 (2010).

7. G. P. Gardner, Y. B. Go, D. M. Robinson, P. F. Smith,J. Hadermann, A. Abakumov, M. Greenblatt and G. C.Dismukes: Structural requirements in lithium cobalt oxides for the catalytic oxidation of water. *Angew. Chem. Int. Ed*. **51**, 1616 (2012).

8. J. Landon, E. Demeter, N. Inoglu, C. Keturakis, I. E. Wachs,R. Vasic, A. I. Frenkel and J. R. Kitchin: Spectroscopic characterization of mixed Fe−Ni oxide electrocatalysts for the oxygen evolution reaction in alkaline electrolytes. *ACS Catal*. **2**, 1793 (2012).

9. M. Gong, Y. Li, H. Wang, Y. Liang, J. Z. Wu, J. Zhou, J. Wang,T. Regier, F. Wei and H. Dai: An advanced Ni-Fe layered double hydroxide electrocatalyst for water oxidation. *J. Am. Chem. Soc*. **135**, 8452 (2013).

10. S. Chen and S. Z. Qiao: Hierarchically porous nitrogen-doped graphene–$NiCo_2O_4$ hybrid paper as an advanced electrocatalytic water-splitting materia. *ACS Nano*. **7**, 10190 (2013).

11. S. Chen, J. J. Duan, M. Jaroniec and S. Z. Qiao: Three-dimensional N-doped graphene hydrogel/NiCo double hydroxide electrocatalysts for highly efficient oxygen evolution. *Angew. Chem., Int. Ed*. **52**, 13567 (2013).

12. M. R. Gao, Y. F. Xu, J. Jiang, Y. R. Zheng and S. H. Yu: Water oxidation electrocatalyzed by an efficient $Mn_3O_4/CoSe_2$ nanocomposite. *J. Am. Chem. Soc*. **134**, 2930 (2012).

13. M. Gao, W. Sheng, Z. Zhuang, Q. Fang, S. Gu, J. Jiang and Y. Yan: Efficient water oxidation using nanostructured α-nickel-hydroxide as an electrocatalyst. *J. Am. Chem. Soc*. **136**, 7077 (2014).

14. Z. Zhao, H. Wu, H. He, X. Xu and Y. Jin: Self-standing non-noble metal (Ni-Fe) oxide nanotube array anode catalysts with synergistic reactivity for high-performance water oxidation. *J. Mater. Chem. A*, **3**, 7179 (2015).

15. Z. Zhao, H. Wu, H. He, X. Xu and Y. Jin: A high-performance binary Ni–Co hydroxide-based water oxidation electrode with three-dimensional coaxial nanotube array structure. *Adv. Funct. Mater*. **24**, 4698 (2014).

16. J. Jiang, A. Zhang, L. Li and L. Ai: Nickel-cobalt layered double hydroxide nanosheets as high-performance electrocatalyst for oxygen evolution reaction. *J. Power Sources*. **278**, 445 (2015).

17. M. R. Gao, Y. F. Xu, J. Jiang and S. H. Yu: Nanostructured metal chalcogenides: synthesis, modification, and applications in energy conversion and storage devices. *Chem. Soc. Rev*. **42**, 2986 (2013).

18. M. D. Merrill and R. C. Dougherty: Metal oxide catalysts for the evolution of O_2 from H_2O. *J. Phys. Chem. C*. **112**, 3655 (2008).

19. X. Li, J. Yu, J. Low, Y. Fang, J. Xiaoc and X. Chen: Engineering heterogeneous semiconductors for solar water splitting. *J. Mater. Chem*. A. **3**, 2485 (2015).

20. X. Yan, K. Li, L. Lyu, F. Song, J. He, D. Niu, L. Liu, X. Hu, and X. Chen: From water oxidation to reduction: transformation from NixCo3−xO4 nanowires to NiCo/NiCoOx heterostructures. *ACS Appl. Mater. Interfaces*. **8**, 3208 (2016).

21. H. Cheng, Y. Su, P. Kuang, G. Chen and Z. Liu: Hierarchical $NiCo_2O_4$ nanosheet-decorated carbon nanotubes towards highly efficient electrocatalyst for water oxidation. *J. Mater. Chem. A*. **3**, 19314 (2015).

22. Q. Xu, Y. Su, H. Wu, H. Cheng, Y. Guo, N. Li and Z. Liu: Effect of morphology of Co_3O_4 for oxygen evolution reaction in alkaline water electrolysis. *Current Nanoscience*. **11**, 107 (2015).

23. X. Yan, L. Tian and X. Chen: Crystalline/amorphous Ni/NiO core/shell nanosheets as highly active electrocatalysts for hydrogen evolution reaction. *Journal of Power Sources*. **300**, 336 (2015).

24. Z. Pu, Y. Luo, A. M Asiri, and X Sun: Efficient electrochemical water splitting catalyzed by electrodeposited nickel diselenide nanoparticles based film. *ACS Appl. Mater. Interfaces*. **8**, 4718 (2016).

25. H. Wang, H. Lee, Y. Deng, Z. Lu, P. C, Hsu, Y. Liu, D. Lin and Y. Cui: Bifunctional non-noble metal oxide nanoparticle electrocatalysts through lithium-induced conversion for overall water splitting. *Nat. Commun*. **6**, 7261 (2015).

26. A. T. Swesi, J. Masud, and M. Nath: Nickel selenide as a high-efficiency catalyst for oxygen evolution reaction. *Energy Environ. Sci*. **9**, 1771 (2016).

27. J. Masud, A. T. Swesi, W. P. Liyanage and M. Nath: Cobalt selenide nanostructures: an efficient bifunctional catalyst with high current density at low coverage. *ACS Appl. Mater. Interfaces*. **8**, 17292 (2016).

28. G. Chen , T. Ma , Z. Liu , N. Li , Y. Su , K. Davey and S. Qiao: Efficient and stable bifunctional electrocatalysts Ni/Ni x M y (M = P, S) for overall water splitting. *Adv. Funct. Mater*. **26**, 3314 (2016).

29. Schuster, C.; Gatti, M. & Rubio, A. Electronic and magnetic properties of NiS_2, NiSSe and $NiSe_2$ by a combination of theoretical methods. *Eur. Phys. J. B* **85**, 325 (2012).

30. Rasmussen, F. A.; Thygesen, K. S. Computational 2D materials database: Electronic structure of transition metal dichalcogenides and oxides, *J. Phys. Chem. C*, **2015**, *119*, 13169-13174.

31. I. H. Kwak, H. S. Im, D. M. Jang, Y. W. Kim, K. Park, Y. R. Lim, E. H. Cha and J. Park: $CoSe_2$ and $NiSe_2$ nanocrystals as superior bifunctional catalysts for electrochemical and photoelectrochemical water splitting. *ACS Appl. Mater. Interfaces* **8**, 5327 (2016).

32. D. Kong, J. J. Cha, H. Wang, H. R. Lee, and Y. Cui: First-row transition metal dichalcogenide catalysts for hydrogen evolution reaction. *Energy Environ. Sci*. **6**, 3553 (2013).

33. C. Tang, N. Cheng, Z. Pu, W. Xing, and X. Sun. NiSe nanowire film supported on nickel foam: An efficient and stable 3D bifunctional electrode for full water splitting. *Angew. Chem. Int. Ed.* **54**, 9351 (2015).

34. W. Zhu, X. Yue, W. Zhang, S. Yu, Y. Zhang, J. Wang and J. Wang. Nickel sulfide microsphere film on Ni foam as an efficient bifunctional electrocatalyst for overall water splitting. *Chem. Commun*. **52**, 1486 (2016).

35. J. Luo, J.-H. Im, M. T. Mayer, M. Schreier, M. K. Nazeeruddin, N. G. Park, S. D. Tilley, H. Fan and M. Grätzel: Water photolysis at 12.3% efficiency via perovskite photovoltaics and Earth-abundant catalysts. *Science*. **345**, 1593 (2014).

36. H. Jin, J. Wang, D. Su, Z. Wei, Z. Pang and Y. Wang: In situ cobalt-cobalt oxide/N-doped carbon hybrids as superior bifunctional electrocatalysts for hydrogen and oxygen evolution. *J. Am. Chem. Soc*. **137**, 2688 (2015).

37. Y. Yang, H. Fei, G. Ruan and J. M. Tour: Porous cobalt-based thin film as a bifunctional catalyst for hydrogen generation and oxygen generation. *Adv. Mater*. **27**, 3175 (2015).

38. N. Jiang, B. You, M. Sheng and Y. Sun: Electrodeposited cobalt-phosphorous-derived films as competent bifunctional catalysts for overall water splitting. *Angew. Chem., Int. Ed*. **54**, 6251 (2015).

39. L. A. Stern, L. Feng, F. Song and X. Hu: Ni_2P as a Janus catalyst for water splitting: the oxygen evolution activity of Ni_2P nanoparticles. *Energy Environ. Sci.*, **8**, 2347 (2015).

40. M. Ledendecker, S. K. Calderon, C. Papp, H. P. Steinruck, M. Antonietti and M. Shalom: The synthesis of nanostructured Ni_5P_4 films and their use as a non-noble bifunctional electrocatalyst for full water splitting. *Angew. Chem., Int. Ed*. **127**, 12538 (2015).

41. T. Liu, Q. Liu, A. M. Asiri, Y. Luo and X. Sun: An amorphous CoSe film behaves as an active and stable full water-splitting electrocatalyst under strongly alkaline conditions. *Chem. Commun*. 51, 16683 (2015).

42. C. Tang, N. Cheng, Z. Pu, W. Xing and X. Sun: NiSe nanowire film supported on nickel foam: An efficient and stable 3D bifunctional electrode for full water splitting. *Angew. Chem., Int. Ed*. 54, 9351 (2015).

43. X. H. Lu, M. Yu, G. Wang, T. Zhai, S. Xie, Y. Ling, Y. X. Tong and Y. Li: H-TiO_2@MnO_2//H-TiO_2@C core–shell nanowires for high performance and flexible asymmetric Supercapacitors. *Adv. Mater*. **25**, 267 (2013).

44. R. P. Agarwala and A. P. B. Sinha: Crystal structure of nickel selenide - Ni_3Se_2. *Z. Anorg. Allg. Chem.* **289**, 203 (1957).

45. S. Zhang: Nanostructured thin films and coatings: mechanical properties. (CRC Press, Taylor & Francis Group), (2010).

46. W. Kreuter and H. Hofmann: Electrolysis: the important energy transformer in a world of sustainable energy, *Int. J. Hydrogen Energy* **23**, 661 (1998).

III. TEXTURED $NiSe_2$ FILM: BIFUNCTIONAL ELECTROCATALYST FOR FULL WATER SPLITTING AT REMARKABLY LOW OVERPOTENTIAL WITH HIGH ENERGY EFFICIENCY

Scientific Reports | 7: *2401* | DOI:10.1038/s41598-017-02285-z

Abdurazag T. Swesi, Jahangir Masud, Wipula P. R. Liyanage, Siddesh Umapathi,

Eric Bohannan, Julia Medvedeva & Manashi Nath

Department of Chemistry

Missouri University of Science and Technology

Rolla, Missouri 65409-0050 USA

Email: nathm@mst.edu

ABSTRACT

Herein we have shown that electrodeposited $NiSe_2$ can be used as a bifunctional electrocatalyst under alkaline conditions to split water at very low potential by catalyzing both oxygen evolution and hydrogen evolution reactions at anode and cathode, respectively, achieving a very high electrolysis energy efficiency exceeding 80% at considerably high current densities (100 mA cm^{-2}). The OER catalytic activity as well as electrolysis energy efficiency surpasses any previously reported OER electrocatalyst in alkaline medium and energy efficiency of an electrolyzer using state-of-the-art Pt and RuO_2 as the HER and OER catalyst, respectively. Through detailed electrochemical and structural characterization, we have shown that the enhanced catalytic activity is attributed to directional growth of the electrodeposited film that exposes a Ni-rich lattice plane as the

terminating plane, as well as increased covalency of the selenide lattice which decreases the Ni(II) to Ni(III) oxidation potential. Thereby, the high efficiency along with extended stability makes $NiSe_2$ as the most efficient water electrolyzer known to-date.

1. INTRODUCTION

Water splitting reactions producing readily useable clean fuel H_2, has been the focus of major research activities in alternative energy since they are benign in terms of impact on the environment and human health. The oxygen and hydrogen evolution reactions (OER and HER, respectively), an intricate part in water oxidation/reduction, respectively, also plays a crucial role in other alternative energy devices including fuel cells, metal-oxygen batteries and solar water splitting devices[1–3]. Among these the oxygen evolution reaction (OER) occurring at the anode is a major hurdle since it is a kinetically sluggish process that involves 4 electron transfer associated with the formation of dioxygen molecule from water, and requires a large anodic potential[4]. Therefore, this OER half reaction is regarded as the most limiting step for water splitting, and electrocatalysts/photocatalysts are typically used to reduce the applied potentials for O_2 evolution. The most commonly used high-efficiency catalysts are the precious metal oxides (IrO_x, RuO_x) which exhibit some of the lowest overpotential for practical current densities[5–12]. In addition significant advances have been recently made in identifying OER electrocatalysts[13] based on transition metal compounds including alloys (often containing significant amounts of Ni, Co or Fe)[5], oxide/hydroxide[6–8], phosphide[9], spinels[5, 10, 11] and perovskite oxides[5, 12]. Among these, Ni-based oxides, oxyhydroxides, and hydroxides, along with Ni-Fe based oxyhydroxides have

shown the most potent catalytic efficiencies with performance closer to that of precious metal oxides[14–17]. Very recently transition metal chalcogenides have been receiving increasing interest as OER and HER catalysts[18–21]. Compared to the oxides, the chalcogenides are expected to have more covalency, smaller bandgaps, and better band alignment with water redox levels for efficient charge transfer, thus promoting better catalytic efficiency. In particular Ni- and Co-based chalcogenides have shown great promise for water electrolysis in alkaline medium[18–25]. Indeed we have identified a nickel selenide, Ni_3Se_2 which shows a very low onset potential and overpotential and overpotential at 10 mA cm^{-2} for oxygen evolution in alkaline medium[20]. Other groups have also reported chalcogenides such as NiSx as a bifunctional HER and OER active catalysts[18]. The bifunctional electrocatalysts that can be applied both at the cathode and anode and produce hydrogen and oxygen, respectively, are highly appealing technologically for water electrolysis[22].

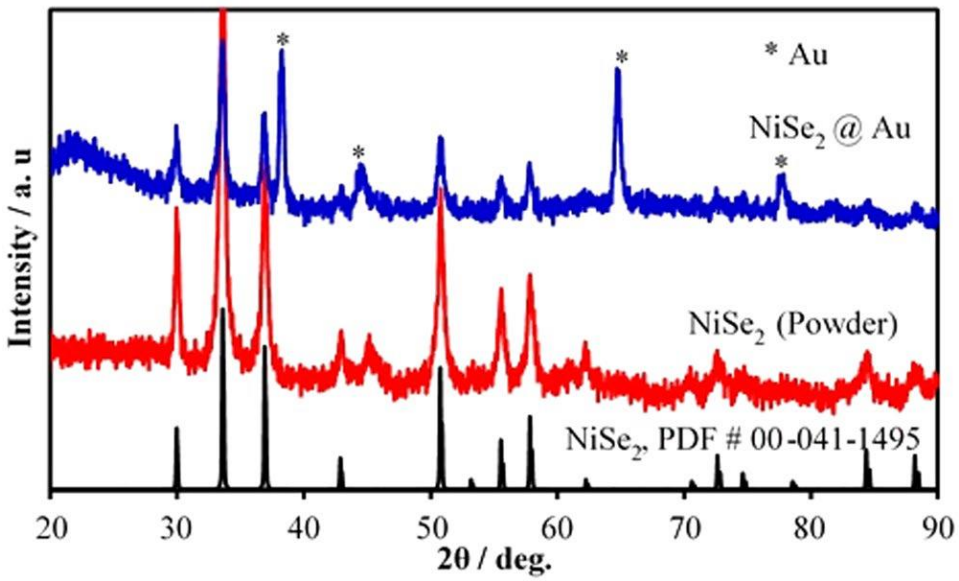

Figure 1. PXRD pattern of electrodeposited $NiSe_2$ @ Au (blue) and $NiSe_2$ powder (red) showing the presence of $NiSe_2$ (PDF # 00-041-1495).

Table 1. Electrochemical parameters of the $NiSe_2$ catalysts measured in 1.0 M KOH.

Catalyst	**Loading/ mg/cm^2**	**ECSA/ cm^2**	**RF**	**Onset potential/ V[a]**	**η to 10 mA cm^{-2} /V[a]**	**Tafel slope/ mV dec^{-1}**
$NiSe_2$/Au	0.13	4.7	16.6	1.36	0.14	48.7
$NiSe_2$ (powder)/CFP	1.40	-	-	1.38	0.22	56.6
RuO_2/Au	-	-	-	1.43	0.32	121.1

[a]Potential reported with respect to RHE.

In this article we report the highly efficient OER and HER catalytic activity of electrodeposited pure $NiSe_2$ films and emphasize the importance of film orientation and growth conditions on the catalytic activity. The OER catalytic activity in these films with the onset potential for O_2 evolution at 1.36 V (*vs* RHE) and overpotential at 10 mA cm^{-2} at 140 mV in alkaline medium, was observed to be superior to any other OER electrocatalysts reported till date including state-of-the-art precious metal oxides, transition metal oxides, and other nickel chalcogenides. There has been another report of the OER catalytic activity of $NiSe_2$ (coated with native oxide layer) *albeit* with much higher overpotential at 10 mA cm^{-2} (~290 mV)[18, 23]. This difference can be attributed to several factors including the surface chemistry, phase purity and the preferential growth direction which influences exposure of the catalytic sites to the electrolyte as discussed below. The later proposition has been conclusively proven in this manuscript whereby, we have grown randomly oriented $NiSe_2$ grains through hydrothermal methods and have shown their catalytic activity for OER to be less efficient than the electrodeposited oriented films, thereby providing a very valuable insight for the OER electrocatalysts. The onset potential for H_2 evolution was also very low as compared to other non-Pt based HER electrocatalyst. The $NiSe_2$ bifunctional electrocatalyst reported here could effectively split water at 1.43 V and achieve an electrolysis energy efficiency of 83% producing current density as high as 100

mA cm-^{2,} which is the highest that has been obtained so far for a bifunctional water electrolyzer. Electrodeposition being a facile, direct method to grow large area binder-free catalytic films, and the experimental proof that films with preferred orientation will show enhanced catalytic activity indeed highlights the novelty of this report.

2. RESULTS AND DISCUSSION

2.1. STRUCTURAL AND MORPHOLOGICAL CHARACTERIZATION

As mentioned above and described in the experimental section in Supporting Information, $NiSe_2$ electrocatalysts were grown by two methods – electrodeposition on Au-coated glass and by hydrothermal techniques. The powder X-ray diffraction patterns (PXRD) of as-synthesized $NiSe_2$ films electrodeposited on Au-coated glass substrates as well as $NiSe_2$ powder synthesized hydrothermally showed peaks that matched well with standard $NiSe_2$ (PDF # 00-041-1495) (Figure 1). The electrodeposited film also showed peaks characteristic of Au arising from the underlying substrate. The peaks were considerably broader indicating that the films were composed of nanostructured grains. Using the Scherrer formula (See Supplementary Information), average particle size in the electrodeposited film was estimated as 30.0 nm.

For the electrodeposited films, the catalyst loading was measured by weighing the electrode before and after electrodeposition, while the thickness of the catalytic film was estimated from 3-dimensional profiling (Supplementary Figure 1). Table 1 lists the typical catalyst loading and average thickness of the electrodeposited film. The morphology of the as-synthesized films was investigated through detailed SEM and TEM studies (Figure 2a

and b) which showed that they were indeed composed of nanostructured grains. The TEM and HRTEM images, Figure 2b and c, respectively, suggests that the film contained mainly

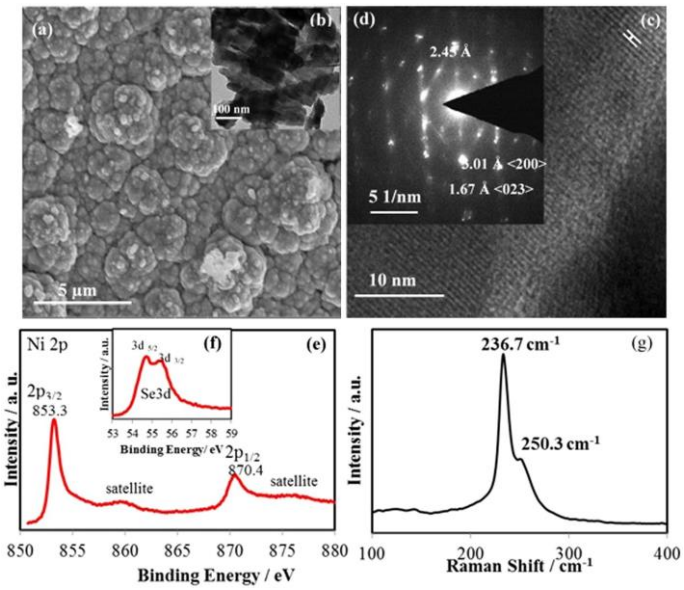

Figure 2. SEM (a) and TEM (b) images of electrodeposited $NiSe_2$, (c) HRTEM image of the catalyst showing lattice spacing of 2.45 A corresponding to <211> lattice planes, (d) Typical SAED pattern showing characteristic diffraction spots, (e) XPS spectra of the catalyst showing the Ni 2p peaks, (f) XPS peaks corresponding to Se 3d. (g) Raman spectrum of the catalyst.

nanocrystallites where individual grains were nanocrystallites where individual grains were single crystalline showing lattice fringes corresponding to ⟨211⟩ planes of $NiSe_2$. Selected area electron diffraction (SAED) collected from these nanocrystallites showed diffraction spots corresponding to ⟨200⟩ and ⟨023⟩ lattice planes of $NiSe_2$ (Figure 2d). The $NiSe_2$ granules were free of any amorphous or heterogeneous coating on the surface as apparent from the TEM images, also confirming the purity of these nanograins. The composition of the electrodeposited films were confirmed through EDS (Supplementary Figure 2) which confirmed the presence of Ni and Se in the film with an approximate ratio of 1:2 and validated the composition as NiSe2. The XPS binding energy observed at 853.3

and 870.4 eV as shown in Figure 2e, corresponds well to the Ni 2p3/2 and Ni 2p1/2 respectively, similar to that obtained from $NiSe_2$ [26, 27], while, binding energies of Se 3d5/2 and Se 3d3/2 observed at 54.0 eV and 54.6 eV (Figure 2f), respectively were similar to the reported values for nickel selenides[20, 23]. It should be noted that the peaks corresponding to metal oxide and/or selenium oxide were not observed in the XPS spectrum, indicating that the electrodeposited films were devoid of oxidic impurities.

The electrodeposited films were also studied with Raman spectroscopy which showed peaks at 236.7 and 250.3 cm^{-1} characteristic of $NiSe_2$ as shown in Figure 2g[28, 29]. The spectrum shows no other major Raman lines attributed to the Se phase and/or Ni–O modes[20]. All of these characterization indicates that the electrodeposited film was purely $NiSe_2$ with no discernible impurity phases.

2.2. ELECTROCHEMICAL PERFORMANCE, OER AND HER CATALYTIC ACTIVITIES

Electrochemical characterization of the electrodeposited $NiSe_2$ films was conducted in N_2-saturated 1 M KOH (pH 13.6) with a scan rate at 10 mV s^{-1} using a 3-electrode setup. The actual catalytically active region of the material was estimated from the electrochemical surface area (ECSA) measurement (see Supplementary Information, Supplementary Figure 3) and provided in Table 1.

The activity of the catalyst for OER was determined from LSVs and CVs (Figure 3a and b) by measuring the onset potential and overpotential at 10 mA cm^{-2} (*vs* RHE). All the potentials have been reported after iR compensation. Current density with bare Au-glass electrode and RuO_x coated electrodes were also measured for comparison. As expected bare Au-coated glass slide showed very minimal catalytic activity for OER, while

RuO_2 coated slide showed an onset potential of 1.43 V (vs. RHE) and overpotential of 320 mV at 10 mA cm^{-2}, which matches perfectly with the reported values[8]. It was observed that $NiSe_2$ on Au-coated glass electrode exhibits a very low onset potential of about 1.36 V, reaching current density 100 mA cm^{-2} at overpotential of about 200 mV. It must be mentioned here that these value of onset and overpotentials were very reproducible and different batches of $NiSe_2$ films on Au-glass showed similar values. The CV for $NiSe_2$ showed a large pre-oxidation peak before the increase of current density due to oxygen evolution. For Ni-based OER electrocatalysts, the pre-oxidation peak typically attributed to the Ni^{2+} to Ni^{3+} oxidation has been observed previously. The intensity of the oxidation

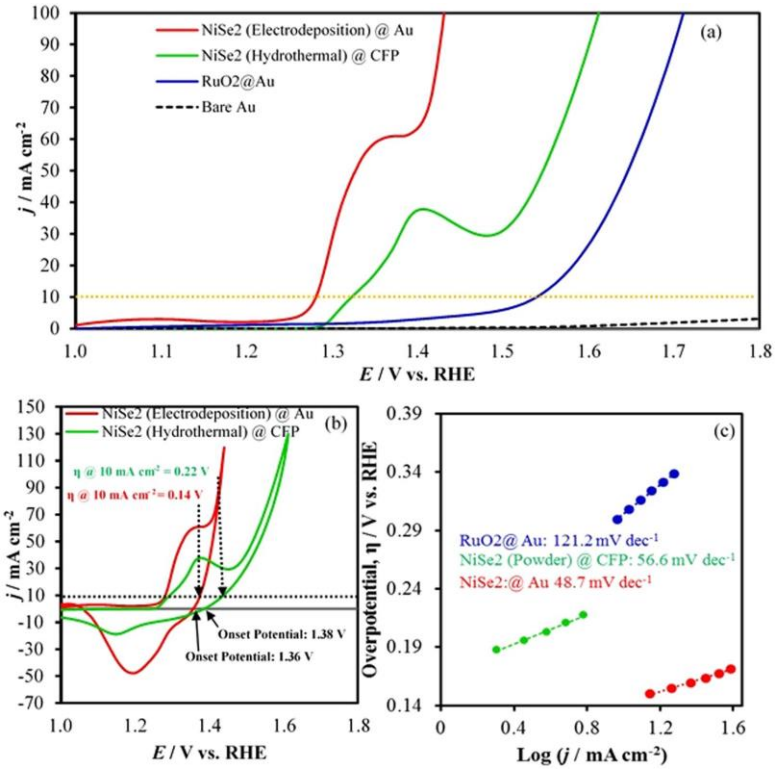

Figure 3. (a) LSVs measured at $NiSe_2$ (Electrodeposited) @ Au, $NiSe_2$ (Hydrothermal) @ CFP, RuO_2 @ Au and bare Au at in N_2 saturated 1.0 M KOH solution at a scan rate of 10 mV s^{-1}. (b) CVs measured under identical condition to estimate the overpotential at 10 mA cm^{-2}. (c) Tafel plots of catalysts.

peak was considerably large, possibly due to exposure of large number of catalytically active sites and high surface roughness that may lead to a high ECSA of the catalyst. Typically, activities of the OER electrocatalysts are benchmarked by comparing the overpotential at current densities of 10 mA cm^{-2} (per geometric surface area), which is considered to be equivalent to 10% solar water-splitting device under 1 sun illumination[30]. In the present case, however, the onset of OER activity as well as the overpotential at 10 mA cm^{-2} was heavily masked by the large pre-oxidation peak and the overpotential at 10 mA cm^{-2} was obtained from the cyclic voltammogram (CV) by analyzing the current density of the reverse scan which corresponds to the OER current only (Figure 3b). Accordingly, it was observed that a current density of 10 mA cm^{-2} was obtained at an overpotential of 140 mV. This value is much better than the RuO_2 (320 mV overpotential required to get 10 mA cm^{-2} current density) and is the lowest value reported till date amongst all the known OER electrocatalysts as well as amongst the recently reported chalcogenides (see Supplementary Table 1)[15]. To the best of our knowledge, this is the first time that pure $NiSe_2$ has been reported as an active electrocatalyst for OER with such a low onset potential as well as overpotential at 10 mA cm^{-2}. To understand the role of catalyst growth conditions, we have also measured the catalytic activity of $NiSe_2$ grown through hydrothermal methods. For this purpose, the $NiSe_2$ powder was mixed with Nafion and drop-casted on carbon fiber paper (CFP) and used as an anode in the OER set-up (see Supporting Information for details). The CV plot showed that $NiSe_2$ powder on CFP was still catalytically active for O_2 evolution with a low onset potential (1.38 V) and overpotential at 10 mA cm^{-2} (220 mV) (Figure 3b) indicating that this is indeed an intrinsic property of this material. Noticeably, the catalytic activity of hydrothermally grown pure

$NiSe_2$ powder was better than previous reports of $NiSe_2$ [23], possibly due to the nanostructured morphology of the $NiSe_2$ grains as has been frequently obtained with hydrothermal synthesis. Recently we have also shown that nanostructuring increases catalytic activity[31]. However the catalytic activity was inferior to the electrodeposited $NiSe_2$ film, thereby, emphasizing the fact that growth conditions indeed play a vital role in determining the catalytic activity of these electrocatalysts (*vide infra*). A small value of Tafel slope of 48.7 mV dec^{-1} for $NiSe_2$ compared to RuO2 (121.2 mV dec−1) confirmed that the catalytic process was very facile. All the parameters defining the electrocatalytic activity of $NiSe_2$ has been listed in Table 1.

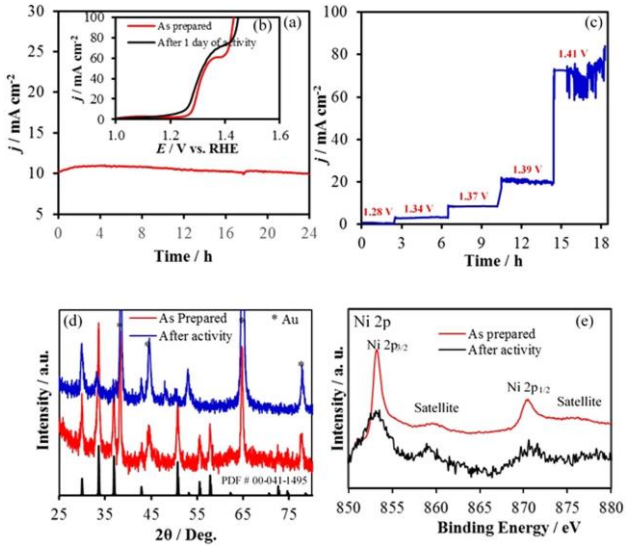

Figure 4. (a) Stability study of catalyst under continuous O_2 evolution at a constant potential to achieve 10 mA cm^{-2} for 24 h, (b) LSVs of catalyst in N_2 saturated 1.0 M KOH before and after chronoamperometry for 24 h, (c) Stability of catalyst at different potential by using potential step method. (d) XRD patterns before and after current transient experiment for 24 h and (e) XPS spectra before and after of stability.

A common concern with the Ni-based OER electrocatalysts in the alkaline medium is that the catalytic activity is obtained from the oxide-hydroxide phases formed *in situ*. To

address this issue, we have intentionally electrodeposited $Ni(OH)_2$ films following a reported procedure on Au-coated glass. The electrocatalytic activity of the $Ni(OH)_2$ was measured in the same way as described above. It was observed that the onset potential for O_2 evolution as well as overpotential at 10 mA cm^{-2} was much higher at 1.49 V vs RHE and 330 mV, respectively (Supplementary Figure 4). This proves that the highly efficient catalytic activity obtained with the electrodeposited $NiSe_2$ is definitely an intrinsic property of the selenide itself and not merely arising from the oxide-hydroxide. This claim has been supported by other electrochemical studies (*vide infra*).

The composition of the evolved gas was confirmed to be O_2 through further electrochemical studies using rotating ring disk electrodes (see Supplementary Information and Supplementary Figure 5a) and the Faradaic efficiency was observed at about 99.5% at the applied disk potential of 1.4 V (*vs*. RHE) (see Supplementary Information and Supplementary Figure 5b), that corresponds to about 1.0 mA cm^{-2} disk current density. As the disk voltage increased to 1.46 V (*vs*. RHE), the Faradaic efficiency decayed to 50.2%. This decrease could be attributed to large amounts of oxygen being produced at the disk electrode that cannot be efficiently collected by the Pt ring electrode[20].

Stability of the catalysts under conditions of continuous O_2 evolution (in 1.0 M KOH) was investigated using constant potential electrolysis (chronoamperometry) for 24 h where the potential was held at a constant value of (1.37 V *vs* RHE) to deliver 10 mA cm^{-2} per geometric area (Figure 4a). As can be seen from the chronoamperometry data, there was no degradation of the current density with time indicating extended catalyst stability. It should be noted here that the constant potential of 1.37 V was chosen based on the reverse scan of the CV plot which provided a better estimate of the potential needed for

achieving a 10 mA cm^{-2} (Figure 3b). A separate set of stability studies was conducted by holding the potential constant in several stages of the OER reaction (from onset to rapid O_2 evolution stage) and the current density was measured at each of these steps for extended period. As can be seen from Figure 4c, the current density at 1.28 V was almost 0, which can be expected from the LSV curve since it falls below the onset potential. As the potential step was increased to 1.34 and 1.37 V, the current density showed a steady step-wise increase to ~10 mA cm^{-2} where it stayed stable for the duration of the potential step. As the potential step was increased further to 1.39 V and 1.41 V respectively, the current density showed a much steeper increase indicating that OER was indeed the major process in these potential ranges. The current density at 1.41 V was noisy possibly due to evolution of large amounts of O_2 which led to accumulation of bubbles near the electrode surface and had to be dislodged with mechanical agitation, thereby producing a noisy data. The composition of the film after chronoamperometry and extended periods of continuous O_2 evolution was analyzed through PXRD (Figure 4d) and XPS (Figure 4e) studies which revealed that the films were still predominantly $NiSe_2$ even after 24 h of continuous O_2 evolution. However, a small intensity peak was also observed in the pxrd pattern that corresponds to $Ni_{0.85}Se$, indicating that there might be some Se loss from the films during extended period of O_2 evolution leading to formation of a selenium deficient phase. The formation of selenium deficiency on the surface after OER activity was also evidenced further by EDS (Supplementary Figure 6) as the ratio of Ni to Se increased slightly with progress of reaction.

XPS studies on the other hand, revealed that the Ni and Se (Supplementary Figure 7) XPS signals were unaltered after the chronoamperometric studies indicating that the

catalyst did not undergo a drastic decomposition. Also oxidic peaks were notably absent in the XPS spectra, demonstrating that the catalytic film did not undergo conversion to the oxide, as has been reported for some selenides[18, 23]. The O 1s signal was also monitored through XPS before and after chronoamperometry (Supplementary Figure 8) which revealed that there was no evidence of Ni-oxides. In the as-synthesized sample, the O 1s peak showed only surface adsorbed oxygen. The deconvoluted O 1s peak after chronoamperometry showed evidence of surface-absorbed oxygen along with physisorbed H_2O and traces of Se-oxide.

2.3. MECHANISM

As was observed with the OER catalytic process, the $Ni^{2+} \rightarrow Ni^{3+}$ oxidation preceded the oxygen evolution reaction indicating that Ni^{3+} may be the actual catalytic center as has been reported by other researchers for Ni-based OER electrocatalysts[6, 7, 31, 32]. However, in $NiSe_2$, the Ni^{2+}/Ni^{+3} oxidation potential shows a shift towards lower value as compared to that observed in the Ni-based oxides or oxide-hydroxides as seen from the LSVs. We have probed this point further by collecting cyclic voltammograms (CVs) with electrodes coated with pure $NiSe_2$ and $Ni(OH)_2$ in 1.0 M KOH with a three electrode set-up. It should be noted here that to check the oxidation peak, the CVs were measured on electrodes prepared with less $NiSe_2$ deposition time (5 min), such that the $Ni^{2+} \rightarrow Ni^{3+}$ oxidation peak was not masked by the stronger OER peak. It was observed that the Ni^{2+} to Ni^{3+} oxidation indeed occurs at much lower potential (1.345 V vs. RHE) compared to that in $Ni(OH)_2$ (1.395 V vs. RHE), indicating that the catalytically active species (Ni^{3+}) is generated at a lower potential in the $NiSe_2$ electrode (Figure 5).

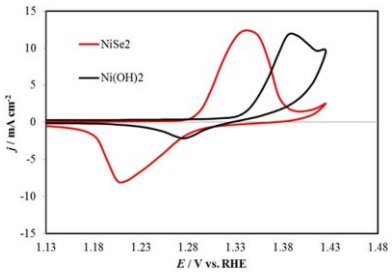

Figure 5. CVs measured at $NiSe_2$ and $Ni(OH)_2$ catalysts in N_2 saturated 1.0 M KOH at 10 mV s^{-1}. The $Ni(OH)_2$ CV has been scaled by a factor of 8.

Such kind of downward shift of the oxidation peak potential can be expected by considering the effect of surrounding ligands on the oxidation potential of the central metal atom. In fact, the electronegativity values of Ni (1.91) and Se (2.55) are very close to each other indicating that as the ligands change from oxo-based to seleno-based, the covalent nature of the metal-chalcogen bond increases. The observation of a lower Ni^{2+} to Ni^{3+} oxidation potential in seleno-based coordination environment is also supported by our recent studies with a seleno-based molecular Ni coordination complex containing tetrahedral NiSe4 core, similar to that found in most Ni-selenides[33]. Single crystals of this complex showed that Ni^{2+} to Ni^{3+} oxidation occurred at 1.34 V (*vs* Ag|AgCl) in 1.0 M KOH, confirming that the low $Ni^{2+} \rightarrow Ni^{3+}$ oxidation potential observed in $NiSe_2$ is indeed due to the selenide coordination. The increasing covalency in the selenides compared to oxides is also supported from Fajan's rule[34]. This increase in covalency leads to several important consequences including a decreased bandgap of the selenides as compared to that of oxides (3.5 eV) and an upward shift of the valence band edge. These changes in the orbital energy levels will directly influence their alignment with respect to the water oxidation and reduction levels, which in turn will affect the charge transfer between the catalyst and water. For the water splitting catalysts, one of the most influential factors in

light of the electronic band structure is that water oxidation-reduction levels are bracketed within the valence and conduction band edges of the catalyst. In these electrocatalytic systems charge transfer occurs at the semiconductor (catalyst)-electrolyte interface which will be influenced by the relative energy levels of the semiconductor and aqueous electrolyte, and an efficient charge transfer will occur when these two levels are closer in energy, thereby facilitating the catalysis mechanism as proposed above.

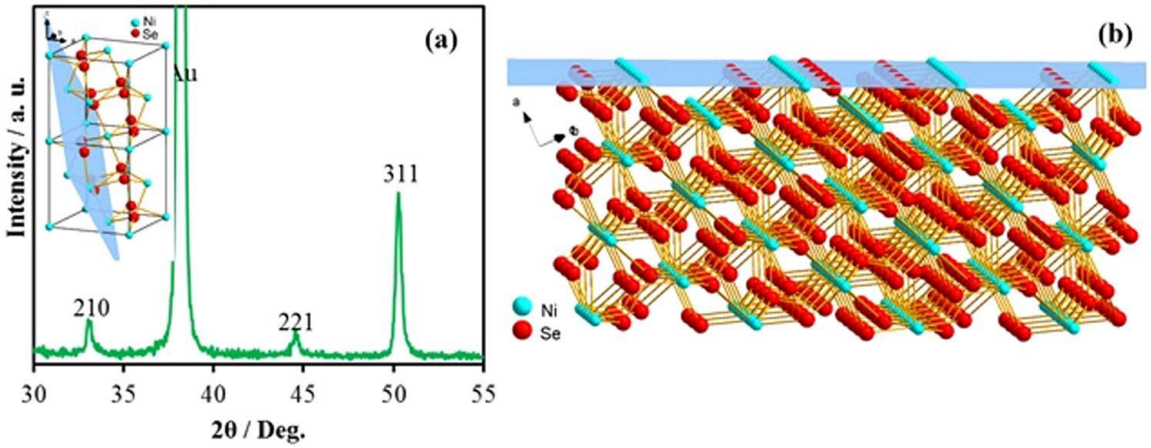

Figure 6. (a) Pxrd pattern of the (311) textured $NiSe_2$ film. Inset shows the crystal structure with the marked (311) plane. (b) An illustration of the $NiSe_2$ lattice terminated with the (311) plane showing excess Ni atoms on the surface.

Nickel selenides are an interesting family of compounds and have been researched by solid state chemists for a long time owing to their novel electronic as well as magnetic properties[35]. Several stoichiometries of the nickel selenides has been known including NiSe, $NiSe_2$, Ni_3Se_2, Ni_3Se_4, and Ni_7Se_8[36]. Among these, $NiSe_2$ has a pyrite structure (space group $T_h^{\ 6}(Pa_3)$) with dumbbell-shaped Se_2 units between two Ni atoms[36]. Most of these nickel selenides are reported to be narrow bandgap semiconductors or semimetals. Previous electronic band structure calculations reported zero bandgap for $NiSe_2$ as obtained using GGA, exact exchange hybrid functional, and GW approximation[37]. Another factor

that might enhance the catalytic activity is easy access to the active site, which in turn can be influenced by growth direction of the film. Hence, the preferential growth direction of the film was analyzed by studying the texture of the film from PXRD data. Specifically, to perform this kind of texturing study, a symmetric diffraction was utilized, where incident and detector angles were always equal. Under these conditions, diffraction from planes that are oriented parallel to the sample surface was only observed. This is the same general method used for powder samples. However, for a powder, all expected reflections are observed as the powder itself consists of randomly oriented grains. On the other hand, if texturing is present in the sample, it implies that there is a preferential growth direction, and the plane normal to that growth direction will predominate in the diffraction pattern. In this case, the pattern obtained was consistent with (311)-textured $NiSe_2$ (Figure 6) which crystallizes with a primitive cubic structure, penroseite[25]. Substantial (311) texture was evident by the enhanced intensity of the (311) reflection at 2θ ~50.5° when compared to the intensity of the (210) reflection at 2θ ~33.5° while the underlying Au substrate showed a ⟨111⟩ orientation as shown in Figure 6a. In a randomly oriented film, based on the theoretical PXRD generated from the atomic coordinates, one would expect the (311) reflection to be roughly one-third the intensity of the (210) as has been observed in Figure 1. Our results suggested that (311) planes are preferentially oriented parallel to the growth direction of the film. In other words, the average terminating planes of the film were the ⟨311⟩ lattice planes of $NiSe_2$. Similar texturing studies on the hydrothermally grown $NiSe_2$ did not show any preferred orientation. The Au surface with a preferred orientation along the ⟨111⟩ direction may play a substantial role in determining the growth direction of the film. Similar results has been recently reported by Switzer *et al*. by growing preferentially

oriented Cu_2O grains on Au-coated silicon substrates[38]. Figure 6b shows the (311) plane of the $NiSe_2$ lattice and interestingly it can be seen that this crystallographic plane is Ni-rich, and can be considered as predominantly Ni-terminated plane. Since, Ni is the catalytically active center for OER, the anion deficient terminating lattice plane will facilitate the attachment of the hydroxyl anions to the metal center leading to a low onset potential and low Tafel slope. The Ni-rich terminating lattice plane may also reduce Se loss with prolonged OER catalytic activity thereby reinforcing catalyst's stability. In fact, recently, another group has reported OER electrocatalytic activities of $NiSe_2$ in alkaline medium *albeit* with much higher overpotential (250 mV)[23]. They have also shown through *in situ* Raman measurements that the catalytic activity proceeds with the immobilization of OH^- on the surface. However, they have also mentioned that their as-prepared catalyst had a surface coating of oxide-hydroxide. That may be the reason the overpotential showed a higher value than the pure $NiSe_2$ reported in this study. As we have shown above, the generation of the catalytically active center (Ni^{3+}) is much more facile in the chalcogenide lattice than the oxide matrix. The higher conductivity of the inner $NiSe_2$ lattice will aid in faster electron transfer leading to higher current densities even at low potentials. Hence, the enhanced intrinsic OER catalytic activity in $NiSe_2$ can be explained from the increased covalency in the lattice which affects the electronic band structure of $NiSe_2$, band positioning, zero band gap of the material, while the highly efficient catalytic activity of the electrodeposited film can be explained from the preferential growth during electrodeposition. It should be also noted that the catalyst loading in this report was very comparable and in fact lower than that reported for other OER electrocatalysts (Supplementary Table 1). Nevertheless, to rule out any effect of catalyst loading on the

OER activity, we have compared the catalytic activity between the electrodeposited ⟨311⟩ -textured $NiSe_2$ film and hydrothermally synthesized $NiSe_2$ powder containing identical

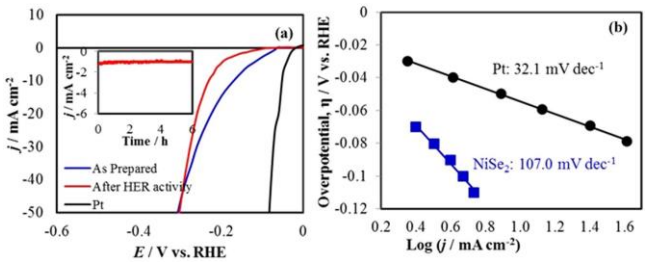

Figure 7. (a) LSVs measured at $NiSe_2$/Au and Pt in N_2 saturated 1.0 M KOH solution at a scan rate of 0.01 V s^{-1}. Inset shows the HER stability of $NiSe_2$. (b) Tafel plots of catalysts.

loading. As can be seen from the CV plot (Supplementary Figure 9), there was no change of overpotential with variation in catalyst loading, however, the current density increased with increased loading. More importantly, the overpotential for the textured $NiSe_2$ film showed the same difference with that obtained for the $NiSe_2$ powder, indicating that this difference in activity is intrinsic.

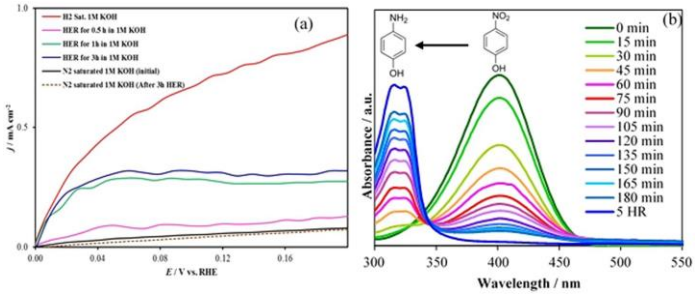

Figure 8. (a) Evidence of H_2 evolution was confirmed by electrochemical oxidation of hydrogen in a Pt electrode. Initially HER was performed at $NiSe_2$/Au at a constant potential of -0.2 V *vs* RHE for different periods of time (0.5, 1 and 3 h) under N_2 saturated and blanketed 1.0 M KOH. The evolved gas was then oxidized with Pt electrode, whereby the oxidation potential and current density confirmed the presence of H_2. In the absence of H_2 [before HER, (black solid line) and after purging with N_2 (reddish dashed line)] the current density was very close to zero. (**b**) Catalytic hydrogenation of p-nitrophenol to p-aminophenol monitored by the change in UV-visible absorbance spectra, confirming the evolution of active hydrogen.

2.4. ELECTROCATALYTIC PERFORMANCE FOR HER AND OVERALL WATER SPLITTING

Electrodeposited $NiSe_2$ showed considerable catalytic activity for HER in 1 M KOH measured using a three-electrode system with a scan rate of 10 mV s^{-1} and was compared with commercially available Pt electrocatalyst. As shown in the polarization curve (*j*s *vs*. *E*), $NiSe_2$ required an overpotential [η(HER)] of 170 mV to achieve 10 mA cm^{-2} (Figure 7a), which is slightly higher than that observed with Pt[39]. A Tafel slope of 107 mV dec^{-1} was obtained for the HER process (Figure 7b). Non-precious HER catalysts often exhibit Tafel slopes ranging from 40 to 120 mV dec^{-1} [40–49]. Remarkably, an early onset overpotential (50 mV *vs*. RHE), indicated that the negative current increased rapidly under more cathodic potentials. Such low onset potential places $NiSe_2$ amongst the most active non-precious HER catalysts in an alkaline medium[50–52]. Previous report of HER activity with $NiSe_2$ corroborates very well with our report signifying the accuracy of the results. Chronoamperometric studies for continuous H_2 evolution for 6 h showed that the catalyst was also stable for HER activities in 1.0 M KOH for extended time (inset of Figure 7a). To confirm that the composition of the evolved gas was indeed H_2 we designed an electrochemical experiment where the evolved gas was oxidized at Pt electrode. Specifically, a series of HER experiments were carried out in 1.0 M KOH, where H_2 was generated for different time intervals (0.5, 1 and 3 h) at $NiSe_2$/Au. After periods of continuous gas evolution for certain periods of time, the evolved gas was oxidized at Pt electrode. As has been shown previously, Pt can electrochemically oxidize H_2 at 0.0 V[53]. Hence monitoring the H_2 oxidation potential and oxidation current could confirm the composition of the gas was indeed H_2. Initially the electrolyte was purged with N_2 and as

expected the current density for H_2 oxidation at Pt electrode was very close to 0. After the HER reaction was done for 0.5, 1 and 3 h, the oxidation current density increased indicating the increasing concentration of dissolved H_2 in the electrolyte (Figure 8). This was further confirmed by measuring the oxidation current after purging the electrolyte with N_2 after 3h

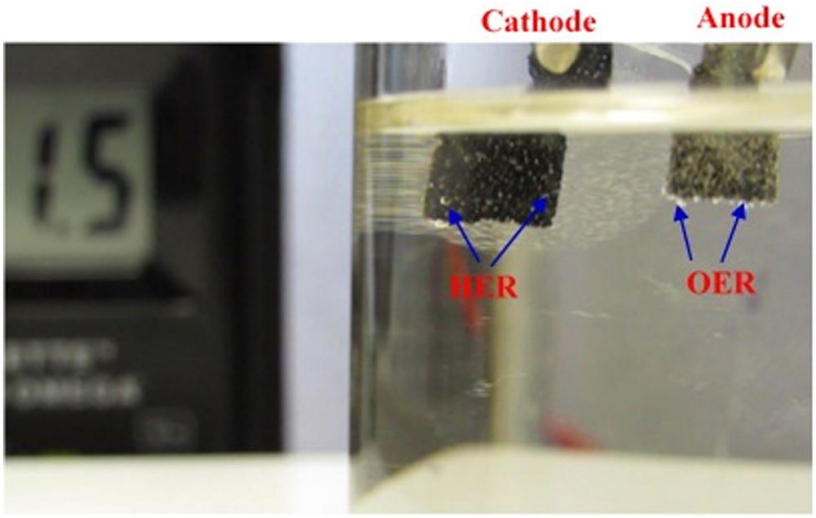

Figure 9. Demonstration of water-splitting device driven by a DC power supply at a cell voltage of 1.5 V to deliver a current density of ~6 mA cm^{-2}.

of HER to get rid of any dissolved gas. As expected, the oxidation current reduced back to the initial value after purging with N_2. This simple experiment proved conclusively that H_2 was indeed produced at the $NiSe_2$ electrode. The composition of the evolved gas was further confirmed as H_2 following the well-established catalytic hydrogenation of *para*-nitrophenol (PNP) to *para*-aminophenol (PAP). The hydrogenation reaction was performed as described in supporting information, and the progress of reaction was monitored through UV-Vis spectroscopy since PNP and PAP shows distinctly different λmax values (Supplementary Figure 10). When the electrolyte was maintained at conditions for HER, it was clearly observed that the absorbance peak due to PNP showed

a gradual decrease accompanied by an increase of the PAP absorbance (Figure 8b) indicating conversion of PNP to PAP. After 5 h, the conversion of PNP to PAP was complete and the solution turned nearly colorless. Two separate control experiments involved passing H_2 through the reaction mixture in the absence of applied voltage and maintaining a blank electrode (Au-glass) under the HER conditions mentioned above. In both of these control experiments, absorbance of PNP did not show any detectable change even after 5 h. This indicates that not only H_2 is being produced by $NiSe_2$, but it is actually forming catalytically active hydrogen capable of performing liquid phase hydrogenation under ambient conditions. This itself is a significant achievement with long-term technological impact.

The Faradic efficiency for HER process was calculated by quantifying the amount of H_2 produced and comparing it with the theoretical yield (details has been provided supplementary information). A Faradaic efficiency close to 100% was obtained for HER (Supplementary Figure 11).

Since $NiSe_2$ shows high catalytic activity for both OER and HER processes in alkaline medium, we have designed a full water splitting system using $NiSe_2$ for both anode and cathode. This bifunctional catalyst exhibits high performance towards overall water splitting and could deliver a current density of ~6 mA cm^{-2} with an applied cell voltage of 1.5 V in 1 M KOH (Figure 9) during which bubbles of O_2 and H_2 were steadily released at both electrodes. It should be noted here that although the thermodynamic water splitting voltage is 1.23 V, it is reckoned that an ideal electrolyzer should be able to split water at 1.48 V for maximum efficiency without any heat exchange with the surrounding, also referred to as the thermoneutral potential[54, 55]. In the present case, water electrolysis was

carried out in a closed electrochemical cell containing $NiSe_2$ as the anodic and cathodic catalyst without any external source of heat. Electrolysis energy efficiency is calculated as the ratio between 1.48 V and the water splitting cell voltage. Electrolysis energy efficiency of the $NiSe_2$ catalyst was calculated to be ~100% (Supplementary Table 2) at the onset potential of electrolysis (1.43 V), while at higher current densities (100 mA cm^{-2}) the efficiency was 83%. This was compared with the energy efficiency obtained from an electrolyzer containing Pt as the cathode catalyst for HER and RuO_2 as the anodic catalyst for OER, which gave a cell voltage of 1.83 V at 100 mA cm^{-2} (81% efficiency). In comparison with the reported literature, as a bifunctional catalyst, $NiSe_2$ exhibits the highest electrolysis energy efficiency obtained so far under ambient conditions and is closest to the elusive most efficient and green water electrolyzer.

3. CONCLUSIONS

In summary, we have electrodeposited nanostructured $NiSe_2$ films as an efficient bifunctional electrocatalyst for overall water splitting with energy efficiency exceeding 83% at high current density. As-deposited $NiSe_2$ reported here shows the lowest onset potential and overpotential at 10 mA cm^{-2} amongst all the Ni-based OER electrocatalysts (Supplementary Table 3). Through electrochemical measurements and structural characterization, we have proven that this enhancement in primarily due to lowering of the oxidation potential of Ni^{2+} to Ni^{3+} that in turn is a consequence of changing the oxide lattice to the more covalent selenide lattice, as well as the preferential growth direction of the film which exposes a Ni-rich surface as the terminating lattice plane.

REFERENCES

1. Chen, G., Bare, S. R. & Mallouk, T. E. Development of supported bifunctional electrocatalysts for unitized regenerative fuel cells. *J. Electrochem. Soc.* **149**, A1092–A1099, doi:10.1149/1.1491237 (2002).

2. Gorlin, Y. & Jaramillo, T. F. A bifunctional nonprecious metal catalyst for oxygen reduction and water oxidation. *J. Am. Chem. Soc.* **132**, 13612–13614, doi:10.1021/ja104587v (2010).

3. Cook, T. R. *et al*. Solar energy supply and storage for the legacy and nonlegacy worlds. *Chem. Rev.* **110**, 6474–6502, doi:10.1021/ cr100246c (2010).

4. Walter, M. G. *et al*. Solar water splitting cells. *Chem. Rev.* **110**, 6446–6473, doi:10.1021/cr1002326 (2010).

5. Lewis, N. S. & Nocera, D. G. Powering the planet: Chemical challenges in solar energy utilization. *Proc Natl Acad Sci USA* **103**, 15729–15735, doi:10.1073/pnas.0603395103 (2006).

6. Gong, M. & Dai, H. A mini review of NiFe-based materials as highly active oxygen evolution reaction electrocatalysts. *Nano Res.* **8**, 23–39, doi:10.1007/s12274-014-0591-z (2015).

7. Fabbri, E., Habereder, Waltar, A. K., Kotz, R. & Schmidt, T. J. Developments and perspectives of oxide-based catalysts for the oxygen evolution reaction. *Catal. Sci. Technol.* **4**, 3800–3821, doi:10.1039/C4CY00669K (2014).

8. Lee, Y., Suntivich, J., May, K. J., Perry, E. E. & Horn, Y. S. Synthesis and activities of rutile IrO_2 and RuO_2 nanoparticles for oxygen evolution in acid and alkaline solutions. *J. Phys. Chem. Lett.* **3**, 399–404, doi:10.1021/jz2016507 (2012).

9. Masud, J., Umapathi, S., Ashokan, N. & Nath, M. Iron phosphide nanoparticles as an efficient electrocatalyst for the OER in alkaline solution. *J. Mater. Chem. A* **4**, 9750–9754, doi:10.1039/C6TA04025J (2016).

10. Kinoshita, K. *Electrochemical Oxygen Technology* (Wiley-Interscience, New York 1992).

11. Hall, D. E. Alkaline water electrolysis anode materials. *J. Electrochem. Soc.* **132**, 41C–48C, doi:10.1149/1.2113856 (1985).

12. Hall, D. E. $Ni(OH)_2$-impregnated anodes for alkaline water electrolysis. *J. Electrochem. Soc.* **130**, 317–321, doi:10.1149/1.2119702 (1983).

13. Jasem, S. M. & Tseung, A. C. C. A potentiostatic pulse study of oxygen evolution on teflon-bonded nickel-cobalt oxide electrodes. *J. Electrochem. Soc.* **126**, 1353–1360, doi:10.1149/1.2129276 (1979).

14. Yu, X. *et al*. Nickel-based thin film on multiwalled carbon nanotubes as an efficient bifunctional electrocatalyst for water splitting. *ACS Appl. Mater. Interfaces* **6**, 15395–15402, doi:10.1021/am503938c (2014).

15. Zhou, W. J. *et al*. Ni_3S_2 nanorods/Ni foam composite electrode with low overpotential for electrocatalytic oxygen evolution. *Energy Environ. Sci.* **6**, 2921–2924, doi:10.1039/c3ee41572d (2013).

16. Merrill, M. D. & Dougherty, R. C. Metal oxide catalysts for the evolution of O_2 from H_2O. *J. Phys. Chem. C* **112**, 3655–3666, doi:10.1021/jp710675m (2008).

17. Gewirth, A. A. & Thorum, M. S. Electroreduction of dioxygen for fuel-cell applications: materials and challenges. *Inorg. Chem.* **49**, 3557–3566, doi:10.1021/ic9022486 (2010).

18. Pu, Z., Luo, Y., Asiri, A. M. & Sun, X. Efficient electrochemical water splitting catalyzed by electrodeposited nickel diselenide nanoparticles based film. *ACS Appl. Mater. Interfaces* **8**, 4718–4723, doi:10.1021/acsami.5b12143 (2016).

19. Xu, X., Song, F. & Hu, X. A nickel iron diselenide-derived efficient oxygen-evolution catalyst. *Nat. Commun.* **7**, 12324, doi:10.1038/ ncomms12324 (2016).

20. Swesi, A. T., Masud, J. & Nath, M. Nickel selenide as a high-efficiency catalyst for oxygen evolution reaction. *Energy Environ. Sci.* **9**, 1771–1782, doi:10.1039/C5EE02463C (2016).

21. Tang, C., Cheng, N., Pu, Z., Xing, W. & Sun, X. NiSe nanowire film supported on nickel foam: an efficient and stable 3D bifunctional electrode for full water splitting. *Angew. Chem. Int. Ed.* **54**, 9351–9355, doi:10.1002/anie.201503407 (2015).

22. Zhu, W. *et al*. Nickel sulfide microsphere film on Ni foam as an efficient bifunctional electrocatalyst for overall water splitting. *Chem. Commun.* **52**, 1486–1489, doi:10.1039/c5cc08064a (2016).

23. Kwak, I. H. *et al*. $CoSe_2$ and $NiSe_2$ nanocrystals as superior bifunctional catalysts for electrochemical and photoelectrochemical water splitting. *ACS Appl. Mater. Interfaces* **8**, 5327–5334, doi:10.1021/acsami.5b12093 (2016).

24. Masud, J., Swesi, A. T., Liyanage, W. P. R. & Nath, M. Cobalt Selenide Nanostructures: An Efficient Bifunctional Catalyst with High Current Density at Low Coverage. *ACS Appl.Mater. Interfaces* **8**, 17292–17302, doi:10.1021/acsami.6b04862 (2016).

25. Kong, D., Cha, J. J., Wang, H., Lee, H. R. & Cui, Y. First-row transition metal dichalcogenide catalysts for hydrogen evolution reaction. *Energy Environ. Sci.* **6**, 3553–3558, doi:10.1039/c3ee42413h (2013).

26. Heide, H. V. D., Hemmel, R., Bruggen, F. V. & Haas, C. X-Ray photodectron spectra of 3d transition metal pyrites. *J. Solid State Chem.* **33**, 17–25, doi:10.1016/0022-4596(80)90543-5 (1980).

27. Wagner, C. D. *Handbook of X-ray photoelectron Spectroscopy* (Perkin-Elmer Corporation: Minnesota 1979).

28. Heras, C. D. L. & Agullo-Rueda, F. Raman spectroscopy of $NiSe_2$ and $NiS_{2-x}Se_x$ ($0 < x < 1$) thin films. *J. Phys.: Condens. Matter.* **12**, 5317–5324, doi:10.1088/0953-8984/12/24/320 (2000).

29. Fan, H., Zhang, M., Zhang, X. & Qian, Y. Hydrothermal growth of $NiSe_2$ tubular microcrystals assisted by PVA. *J. Cryst. Growth* **311**, 4530–4534, doi:10.1016/j.jcrysgro.2009.08.005 (2009).

30. Louie, M. W. & Bell, A. T. An investigation of thin-film Ni–Fe oxide catalysts for the electrochemical evolution of oxygen. *J. Am. Chem. Soc.* **135**, 12329–12337, doi:10.1021/ja405351s (2013).

31. Swesi, A. T., Masud, J. & Nath, M. Enhancing electrocatalytic activity of bifunctional Ni_3Se_2 for overall water splitting through etching-induced surface nanostructuring. *J. Mater. Res.* **31**, 2888–2896, doi:10.1557/jmr.2016.301 (2016).

32. Trotochaud, L., Ranney, J. K., Williams, K. N. & Boettcher, S. W. Solution-cast metal oxide thin film electrocatalysts for oxygen evolution. *J. Am. Chem. Soc.* **134**, 17253–17261, doi:10.1021/ja307507a (2012).

33. Masud, J., Ioannou, P. C., Levesanos, N., Kyritsis, P. & Nath, M. A Molecular Ni-complex Containing Tetrahedral Nickel Selenide Core as Highly Efficient Electrocatalyst for Water Oxidation. *ChemSusChem*, doi:10.1002/cssc.201601054 (2016).

34. Douglas, B. E., McDaniel, D. H. & Alexander, J. J. *Concepts and Models of Inorganic Chemistry* (John Wiley & Sons, Inc. New York 1983).

35. Noue, I., Yasuoka, H. & Ogawa, S. Paramagnetism in $NiSe_2$. *J. Phys. Soc. Jpn.* **48**, 850–856, doi:10.1143/JPSJ.48.850 (1980).

36. Baker, H. ASM Handbook vol. 3: Phase Diagrams (New York 1992).

37. Schuster, C., Gatti, M. & Rubio, A. Electronic and magnetic properties of NiS_2, NiSSe and $NiSe_2$ by a combination of theoretical methods. *Eur. Phys. J. B* **85**, 325, doi:10.1140/epjb/e2012-30384-7 (2012).

38. Switzer, J. A., Hill, J. C., Mahenderkar, N. K. & Liu, Y. C. Nanometer-Thick Gold on Silicon as a Proxy for Single-Crystal Gold for the Electrodeposition of Epitaxial Cuprous Oxide Thin Films. *ACS Appl. Mater. Interfaces* **8**, 15828–15837, doi:10.1021/acsami.6b04552 (2016).

39. Luo, J. *et al*. Water photolysis at 12.3% efficiency via perovskite photovoltaics and earth-abundant catalysts. *Science* **345**, 1593–1596, doi:10.1126/science.1258307 (2014).

40. Jaramillo, T. F. *et al*. Identification of active edge sites for electrochemical H_2 evolution from MoS_2 nanocatalysts. *Science* **317**, 100–102, doi:10.1126/science.1141483 (2007).

41. Li, Y. *et al*. MoS_2 nanoparticles grown on graphene: an advanced catalyst for the hydrogen evolution reaction. *J. Am.Chem. Soc.* **133**, 7296–7299, doi:10.1021/ja201269b (2011).

42. Chen, Z. *et al*. Core–shell MoO_3–MoS_2 nanowires for hydrogen evolution: a functional design for electrocatalytic materials. *Nano Lett.* **11**, 4168–4175, doi:10.1021/nl2020476 (2011).

43. Kibsgaard, J., Chen, Z., Reinecke, B. N. & Jaramillo, T. F. Engineering the surface structure of MoS_2 to preferentially expose active edge sites for electrocatalysis. *Nat. Mater.* **11**, 963–969, doi:10.1038/nmat3439 (2012).

44. Lukowski, M. A. *et al*. Enhanced hydrogen evolution catalysis from chemically exfoliated metallic MoS_2 nanosheets. *J. Am. Chem. Soc.* **135**, 10274–10277, doi:10.1021/ja404523s (2013).

45. Laursen, A. B., Kegnaes, S., Dahl, S. & Chorkendorff, I. Molybdenum sulfides-efficient and viable materials for electro- and photoelectrocatalytic hydrogen evolution. *Energy Environ. Sci.* **5**, 5577–5591, doi:10.1039/c2ee02618j (2011).

46. Merki, D. & Hu, X. Recent developments of molybdenum and tungsten sulfides as hydrogen evolution catalysts. *Energy Environ. Sci.* **4**, 3878–3888, doi:10.1039/c1ee01970h (2011).

47. Chen, W. F. *et al*. Highly active and durable nanostructured molybdenum carbide electrocatalysts for hydrogen production. *Energy Environ. Sci.* **6**, 943–951, doi:10.1039/c2ee23891h (2013).

48. Popczun, E. J. *et al*. Nanostructured nickel phosphide as an electrocatalyst for the hydrogen evolution reaction. *J. Am. Chem. Soc.* **135**, 9267–9270, doi:10.1021/ja403440e (2013).

49. Brown, D. E., Mahmood, M. N., Man, M. C. M. & Turner, A. K. Preparation and characterization of low overvoltage transition metal alloy electrocatalysts for hydrogen evolution in alkaline solutions. *Electrochim. Acta* **29**, 1551–1556, doi:10.1016/0013-4686(84)85008-2 (1984).

50. Tang, C., Pu, Z., Liu, Q., Asiri, A. M. & Sun, X. NiS_2 nanosheets array grown on carbon cloth as an efficient 3D hydrogen evolution cathode. *Electrochim. Acta* **153**, 508–514, doi:10.1016/j.electacta.2014.12.043 (2015).

51. Tang, C. *et al*. Ni_3S_2 nanosheets array supported on Ni foam: A novel efficient three-dimensional hydrogen-evolving electrocatalyst in both neutral and basic solutions. *Int. J. Hydrogen Energy* **40**, 4727–4732, doi:10.1016/j.ijhydene.2015.02.038 (2015).

52. Gao, M. R. *et al*. An efficient molybdenum disulfide/cobalt diselenide hybrid catalyst for electrochemical hydrogen generation. *Nat. Commun.* **6**, 5982, doi:10.1038/ncomms6982 (2015).

53. Kumar, S. M. S., Hidyatai, N., Herrero, J. S., Irusta, S. & Scott, K. Efficient tuning of the Pt nano-particle mono-dispersion on Vulcan XC-72R by selective pre-treatment and electrochemical evaluation of hydrogen oxidation and oxygen reduction reactions. *Int. J. Hydrogen Energy* **36**, 5453–5465, doi:10.1016/j.ijhydene. 2011.01.124 (2011).

54. Kreuter, W. & Hofmann, H. Electrolysis: the important energy transformer in a world of sustainable energy. *Int. J. Hydrogen Energy* **23**, 661–666, doi:10.1016/S0360-3199(97)00109-2 (1998).

55. Wang, X., Li, W., Xiong, D. & Liu, L. Fast fabrication of self-supported porous nickel phosphide foam for efficient, durable oxygen evolution and overall water splitting. *J. Mater. Chem. A* **4**, 5639–5646, doi:10.1039/C5TA10317G (2016).

AUTHOR CONTRIBUTIONS

M.N. wrote the manuscript text with some contributions from A.T.S. and J.M. A.T.S. did most of the experiments. J.M. interpreted the data. S.U. performed the hydrothermal reaction and provided data for Figures 1, 3a and b. W.P.L. designed and collected data for Figure 8b. E.B. designed the texturing pxrd experiment and analyzed data presented in Figure 6a. Figures were prepared by A.T.S. (Figures 1, 2a, 3a,b, 4a,b,c,d, 5, 7a and 9), J.M. (Figures 2c, d,e,f,g, 3c, 4e, 7b and 8), W.P.L. (Figure 6, Figure 8b). J.E.M. helped with understanding the band structure calculations and its dependence on directionality.

SUPPORTING INFORMATION

TEXTURED $NiSe_2$ FILM: BIFUNCTIONAL ELECTROCATALYST FOR FULL WATER SPLITTING AT REMARKABLY LOW OVERPOTENTIAL WITH HIGH ENERGY EFFICIENCY

Abdurazag T. Swesi, Jahangir Masud, Wipula P. R. Liyanage, Siddesh Umapathi, Eric Bohannan, Julia Medvedeva, Manashi Nath

Department of Chemistry, Missouri University of Science and Technology, Rolla, MO 65409.

1. EXPERIMENTAL & METHODS

Materials were reagent grade and were used as received without further purification. Nickel sulfate hexahydrate $NiSO_4.6H_2O$ was purchased from Fisher Scientific Company and Sodium selenite (Na_2SeO_3), was purchased from Alfa Aeasar. Au-coated glass slide used as substrates in electrodeposition was purchased from Deposition Research Lab Incorporated (DRLI), Lebanon, Missouri.

1.1. ELECTRODEPOSITION OF $NiSe_2$

The electrocatalytic $NiSe_2$ films were prepared by direct electrodeposition on electrodes such as, Au-coated glass, glassy carbon (GC), carbon fiber paper (CFP), and Ni foam. The electrolytes were prepared using analytical grade reagents and deionized (DI) water with a resistivity of 18 MΩ·cm. Prior to electrodeposition, the substrates were cleaned by ultrasonic treatment in micro-90 detergent followed by rinse with isopropanol for three times and eventually rinsed with deionized water (15 min each step) to ensure

clean surface. Au-coated glass was covered with a Teflon tape, leaving an exposed geometric area of 0.283 cm^2, and connected as the working electrode. An IviumStat potentiostat was used to control the electrodeposition process and to monitor the current and voltage profiles. $NiSe_2$ was electrodeposited on the substrate by a controlled-potential deposition at -1.2 V (*vs* Ag/AgCl) for 30 min at 40 °C from an aqueous solution containing 63 mM $NiSO_4.6H_2O$ and 150 mM Na_2SeO_3. The pH of the electrolytic bath was adjusted to ~ 2.5 with dilute HCl. After each electrodeposition, the electrodeposited films were washed with deionized water in order to remove impurities and adsorbents from the surface.

1.2. SYNTHESIS OF $NiSe_2$ BY HYDROTHERMAL METHOD S1

$NiSe_2$ was synthesized by hydrothermal method. In a typical procedure, 5 mmols of $NiCl_2.6H_2O$ and 10 mmols of SeO_2 were mixed in 10 ml of deionized water. The solution was stirred on a magnetic stirrer. About 5 mins later 0.1 ml (0.3 mols) of hydrazine monohydrate was added. The solution of stirred for another 5 mins and then transferred to 23 ml Teflon - lined autoclave, which was sealed and maintained at 145°C for 24 h and then naturally cooled to room temperature. The resulting black solid was then washed several times with DI water and ethanol. The solid was dried in an oven maintained at 40 °C overnight.

1.3. PREPARATION OF ELECTRODE

4 mg of the powder $NiSe_2$ was dispersed in 200 μL of 1% Nafion in ethanol. The mixture was sonicated for 30 mins to produce a homogeneous ink. 20 μL of the catalyst

ink was drop casted on to the Carbon Fiber Paper (CFP) at room temperature. Finally the as prepared catalyst ink was allowed to dry at room temperature for 8 hrs.

1.4. ELECTRODEPOSITION OF $Ni(OH)_2$ S2

The nickel hydroxide was deposited on the Au/glass substrate from 0.08 M $Ni(NO_3)_2$ aqueous solution at a potential of -0.86 V vs. Ag|AgCl|KCl(sat) for 5 min.

2. METHODS OF CHARACTERIZATION

2.1. POWDER X-RAY DIFFRACTION (XRD)

2.1.1. Thin Film (Asymmetric) Diffraction. Diffraction patterns were obtained with a Cu source utilizing a PANalytical X'Pert Materials Research Diffractometer, with a fixed incident angle of 1 degree. The incident beam optic module was an x-ray mirror (PW 3088/60, PANalytical), while the diffracted beam optic module was a 0.18 degree parallel plate collimator (PW 3098/18, PANalytical).

2.1.2. Symmetric Diffraction (Figure 6). Diffraction patterns were obtained with a Cu source utilizing a PANalytical X'Pert Materials Research Diffractometer in gonio mode with incident and diffracted angles remaining equal to one another as the diffraction pattern was obtained. The incident beam optic module was a hybrid monochromator (PW 3147/00, PANalytical), consisting of an x-ray mirror and a 2-crystal Ge(220) 2-bounce monochromator. The diffracted beam optic module was a 0.18 degree parallel plate collimator (PW 3098/18, PANalytical).

The average catalyst particle size was calculated from the XRD diffraction peak width using the Scherrer Equation:[S3]

$$L = K\lambda/\beta\cos\theta \quad (1)$$

where L is the particle size, λ is the X-ray wavelength in nanometer (0.15418 nm), β is the peak width of the diffraction peak profile at half maximum height in radians and *K* is a constant, normally taken as 0.9.

2.2. SCANNING ELECTRON MICROSCOPY (SEM)

SEM image of the modified electrode surfaces was obtained using a FEI Helios NanoLab 600 FIB/FESEM at an acceleration voltage of 10 kV and a working distance of 4.8 mm. Energy dispersive spectroscopy (EDS) along with line scan analysis was also obtained from the SEM microscope.

2.3. X-RAY PHOTOELECTRON SPECTROSCOPY (XPS)

XPS measurements of the catalysts were performed by KRATOS AXIS 165 X-ray Photoelectron Spectrometer using monochromatic Al X-ray source. The spectra were collected as is and after sputtering with Ar for 2 min which removes approximately 2 nm from the surface.

2.4. RAMAN SPECTRA

Horiba Jobin Yvon Lab Raman ARAMIS model was used to perform Raman microspectroscopy on the as-deposited catalyst films. The laser used was He-Ne with a

power of about 1.7 mW over a range of 100 – 2000 cm^{-1}. The spectra were iterated over an average of 25 scans.

2.5. ELECTROCHEMICAL CHARACTERIZATION AND CATALYTIC STUDIES

The OER catalytic performance was estimated from linear scan voltammetry (LSV) plots while the stability of the catalyst was studied by chronoamperometry. All electrochemical measurements in this work were performed in a three-electrode system with an IviumStat potentiostat using Ag|AgCl|KCl(sat.) and Pt mesh as reference and counter electrodes, respectively unless otherwise noted. The Ag|AgCl|KCl(sat.) reference electrode was calibrated by measuring open circuit potential (OCP at -0.199V) at Pt wire in pure H_2 saturated 1.0 M H_2SO_4 solution.

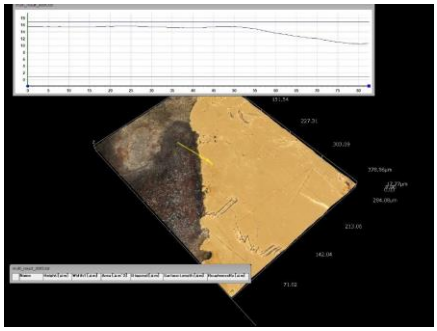

Supplementary Figure 1. 3D imaging and 3D profile of as prepared $NiSe_2$. The HIROX KH-8700 Digital Microscope, is the next generation system for the high precision of measurement and 3D profiling, was used to measure the approximate thickness of electrodeposited $NiSe_2$.

The measured potentials *vs* the Ag/AgCl at any given pH is were converted to the reversible hydrogen electrode (RHE) scale *via* Nernst Equation (equation 2).

$$E_{RHE}=E_{Ag|AgCl}+0.059pH+ E^{0}_{Ag|AgCl} \quad (2)$$

Where E_{RHE} is the converted potential vs. RHE, $E_{Ag|AgCl}$ is the experimentally measured potential against Ag|AgCl reference electrode, and $E^{0}_{Ag|AgCl}$ is the standard potential of Ag|AgCl at 25 ^{0}C (0.199 V). For most of the electrochemical characterizations, the electrode area of the film surface was kept constant at 0.283 cm^2.

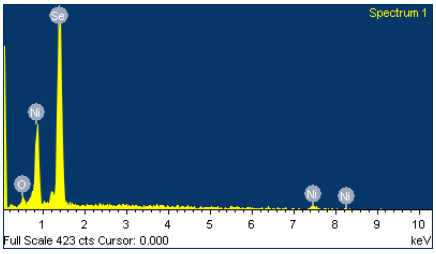

Supplementary Figure 2. EDS spectrum of as prepared $NiSe_2$.

Atomic ratio of Nickel and selenium

Element	Atomic%	Ni : Se
O K	4.25	
Ni L	31.30	1.0 : 2.05
Se L	64.45	
Totals	100	

2.5.1. Electrochemical Active Area (ECSA) of Catalyst. The ECSA of the $NiSe_2$ can be estimated by measuring the electrochemical capacitance of the electrode–electrolyte interface in the double-layer regime of the voltammograms. To estimate ECSA of the catalysts in a N_2 saturated 1 M KOH solution, the electrode was potentiostatically cycled from -0.34 to -0.27 V *vs*. Ag|AgCl at scan rates between 2.5 and 40 mV s^{-1} (Supplementary Figure S3). The capacitive current (i_{DL}) was evaluated from the non-faradaic double-layer

region. This current indeed is proportional to the scan rate, v (V s-1) as shown in equationn (3).

$$i_{DL}=C_{DL}\times \nu \quad (3)$$

Where C_{DL} is the specific capacitance of the electrode double layer (F cm^{-2} electrode).

Plotting of i_{DL} against v gives the value of C_{DL}. The ECSA of the catalyst was estimated from the double-layer capacitance from the following eqn (4):

$$ECSA = C_{DL}/C_s \quad (4)$$

C_s is the specific capacitance which is reported from 0.022 to 0.130 mF cm^{-2} in alkaline solution.[S3] Here, we use the value of C_s is 0.040 mF cm^{-2} based on previously reported Ni-based OER catalysts.[S3] The ECSA and the roughness factor (RF) of the $NiSe_2$ was calculated as 4.7 cm^2 and 16.6, respectively.

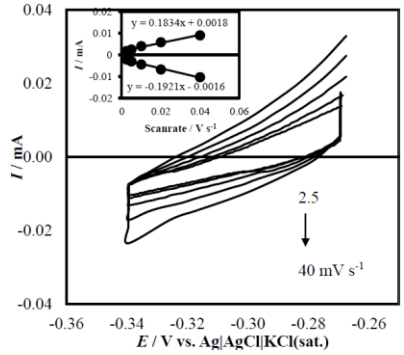

Supplementary Figure 3. Cyclic voltammograms measured for $NiSe_2$catalyst in N_2 saturated 1.0M KOH solution at different scan rate from 2.5 to 40 mV s^{-1}. Inset shows plot of anodic and cathodic current measured at -0.30V as function of scan rate.

2.5.2. Estimation of Onset Potential and Overpotential to Achieve 10 $mAcm^{-2}$.

In case of LSV at $NiSe_2$ catalyst, the onset of OER activity and overpotential at 10 mA cm^{-2} was heavily masked by the large pre-oxidation peak. Hence, to get a better idea about the

onset potential for oxygen evolution, we have carried out cyclic voltammograms (CVs) between 1.0 to 1.45 V *vs* RHE. The cyclic voltammogram for an as-deposited film in 1 M KOH (Supplementary Figure S4) exhibits a redox couple; $Ni^{2+} \rightarrow Ni^{3+}$ at 1.34 V *vs* RHE and $Ni^{3+} \rightarrow Ni^{2+}$ at 1.22 V *vs* RHE.[S4] A more accurate onset potential for water oxidation and overpotential at 10 mA cm^{-2} was obtained from the reverse plot in the CV. Accordingly it was observed that a current density of 10 mA cm^{-2} was obtained at an overpotential of 140 mV, which is the lowest value reported till date amongst all the known OER electrocatalysts.

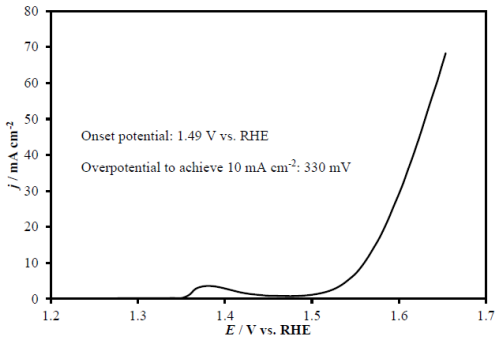

Supplementary Figure 4. LSV for OER at $Ni(OH)_2$ / Au-glass in N_2-saturated 1.0 M KOH at a scan rate of 10 mV s^{-1}.

2.5.3. Testing of Evolved Gas and Faradic Efficiency. An experiment was designed to probe that the bubbles formed at the anode were O_2. A series of ORR experiments were conducted after various periods of O_2 generation. The electrolyte was blanketed with a N_2 atmosphere to get rid of dissolved O_2 during measuring the ring current. The disk electrode was held at constant potential of 1.37 V vs RHE to deliver 10 mA cm_{-2} to ensure O2 generation for various times 0.5, 1 and 5 h in 1 M KOH solution. After each OER run, the evolved oxygen was reduced at Pt electrode as shown in Figure

S7a. It was observed that the ORR current increased as the generation time of O_2 increased. The highest current was after 5 h O_2 generation which was comparable to that obtained from a solution saturated by passing gaseous O_2. After 5 h generation of O_2, the same solution was purged again with N_2 for 2 h to remove all the dissolved O_2. The ORR current measured after N_2 saturation showed minimal current as was observed before start of the experiment. This proves that the source of O_2 was indeed from the anode where O_2 was evolved due to the electrocatalytic process.

The RRDE experiment was employed to determine the OER Faradaic efficiency for the $NiSe_2$ electrocatalyst. $NiSe_2$ was deposited on glassy carbon (GC) which was connected as the disk electrode in a RRDE set-up with Pt as the ring electrode. The applied disk potential was held at several voltages in the OER kinetic-limited region for 1 min, while being rotated at a 1600 rpm under a pure N_2 gas blanket. The ring current was collected at 0.2 V applied ring potential (*vs*. RHE) to reduce the produced oxygen from the disk (anode) sufficiently. The Faradaic efficiency was calculated as below.

$$\text{Faradaic Efficiency} = 2i_r / i_d N \quad (6)$$

Where i_r and id are the measured ring and disk currents, respectively, and N is the collection efficiency of RRDE, which was measured as ~ 0.24 in this work. Figure S7b shows the plot of the disk current as a function of the ring current and Faradaic efficiency over the $NiSe_2$ catalyst in 1.0 M KOH. The maximum Faradaic efficiency was observed at about 99.5 % at the applied disk potential of 1.4 V (*vs*. RHE), which is corresponding to about 1.0 mA cm^{-2} disk current density. As the disk voltage increased to 1.46 V (*vs*. RHE), the Faradaic efficiency decayed to 50.2 %. This decrease could be attributed to large

amounts of oxygen being produced at the disc electrode which cannot be completely reduced efficiently at the Pt ring electrode.[S5]

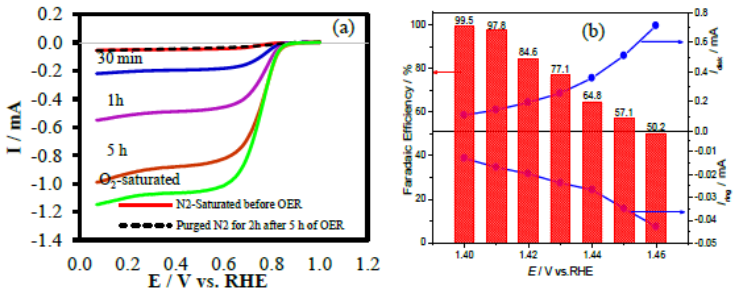

Supplementary Figure 5. (a) Electrochemical evidence of O_2 generation at the disk electrode and reduction at ring electrode when constant current of 10 mA cm^{-2} was applied at disk electrode for varying periods of time (0.5, 1 and 5 h) in N_2 saturated and blanketed 1.0 M KOH. (b) Faradaic efficiency of catalyst in 1.0 M KOH at 1600 rpm under N_2 saturation. The disk and ring currents of RRDE plotted as function of the applied disk potential along with the calculated Faradaic efficiency.

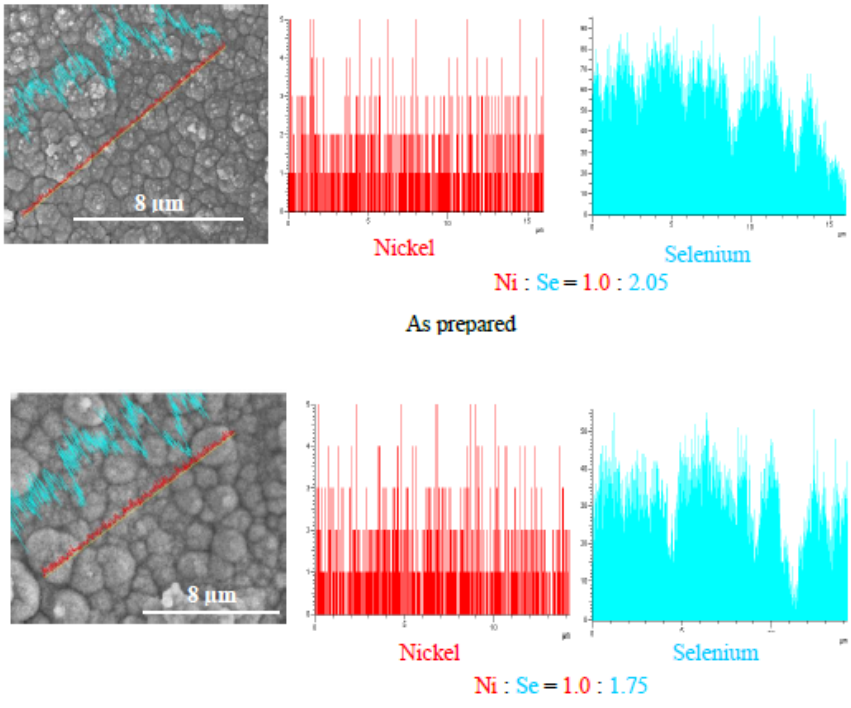

Supplementary Figure 6. SEM images and EDS line scanning of $NiSe_2$ before and after OER catalytic activity.

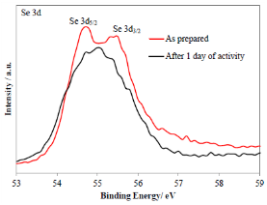

Supplementary Figure 7. XPS spectra of Se 3d peaks obtained from the catalyst before and after chronoamperometry (24h).

2.6. O1s XPS SPECTRA OF $NiSe_2$

The O 1s signals in as prepared $NiSe_2$ (Figure S8a) is largely due to surface-adsorbed oxygen which may be chemisorbed as due to exposure to atmosphere.S6 There is no evidence for formation of Ni-oxide on the surface (no peak at 528.5-529.0 eV)[S7] of the as prepared catalyst. The deconvoluted O1s XPS spectrum after 24 h of OER catalyst after activity, as shown in Figure S8b, revealed that it could be fitted into three contributions attributed to chemisorbed oxygen (530.8 eV) S6, surface-absorbed SeOx (532.9 eV),[S8] and physisorbed and chemisorbed water at or near the surface (535.0 eV).S8 The presence of Se-oxides is very common in most metal selenides. Interestingly, this spectrum also reveals the absence of XPS peaks corresponding to Ni-O even after prolonged catalytic activity.

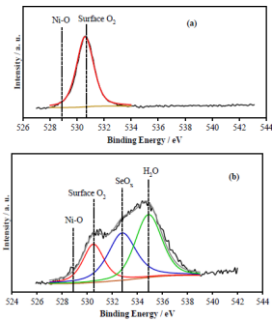

Supplementary Figure 8. XPS spectra of O 1s peaks obtained from the catalyst (a) before and (b) after chronoamperometry.

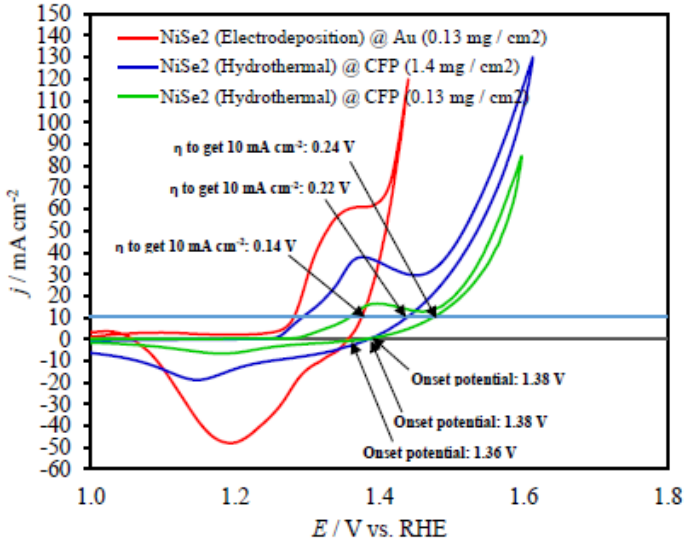

Supplementary Figure 9. Cyclic voltammogram for OER at $NiSe_2$ @ Au and $NiSe_2$ (Powder) @ CFP with variable loading of catalyst in N_2-saturated 1.0 M KOH at a scan rate of 10 mV s^{-1}.

2.7. H_2 GAS EVOLUTION TESTING

To confirm the H_2 evolution (HER) at $NiSe_2$ catalyst, a series of hydrogen oxidation reaction (HOR) experiments were performed after various periods of H_2 generation. First, HOR was carried out at Pt electrode in N_2 saturated and blanketed 1M KOH solution as a blank (Figure S11). Then, HER were conducted at constant potential of -0.2 V vs RHE for various times 0.5, 1 and 3 h in 1 M KOH solution. After each HER run, the evolved hydrogen was oxidized at Pt electrode (Figure S11). It was observed that the HOR current increased as the generation time of H_2 increased. The electrolyte solution was purge and saturated H_2 gas and again HOR experiment was performed at Pt electrode which was confirmed the reliability of experiment. Finally the same solution was purged again with N_2 for 2 h to remove all the dissolved H_2 and HOR was carried out that showed minimal current as was observed before start of the experiment. This series of experiments confirm H_2 evolution at $NiSe_2$ / Au electrode.

2.7.1. Catalytic Hydrogenation of *para*-nitrophenol (PNP) to *para*-aminophenol (PAP). H_2 gas was further confirm by well-established catalytic reduction of para-nitrophenol (PNP) to para-aminophenol (PAP) and conversion was monitored spectrophotometrically. In this process, 100 μM PNP was dissolved in the 1 M KOH electrolyte and the working electrode (Au-glass coated with $NiSe_2$) was maintained at a constant potential of -0.3 V *vs* RHE, with Pt as counter and Ag|AgCl as reference electrode. Copious quantities of gas bubbles were observed to be evolved from the surface of the working electrode. Aliquots were collected at every 15 min and the UV-Vis spectra of the aliquot were measured. The absorbance of pure PNP and PAP were collected separately in 1 M KOH solution (Figure 10). Two separate control experiments were performed in which the bare Au-glass electrode was maintained at -0.3 V (*vs* RHE) for up to 5h. In the second control experiment, the working electrode ($NiSe_2$@Au-glass) was maintained at zero applied potential and H_2 gas was bubbled through the solution for 5 h. In both of these cases the absorbance of PNP did not show any appreciable change even after 5 h.

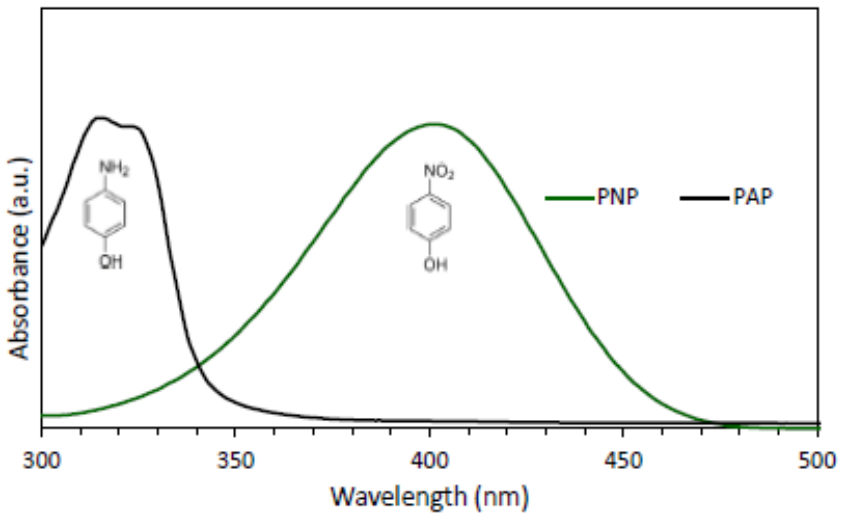

Supplementary Figure 10. UV-Vis spectra of *para*-nitrophenol (PNP) and *para*-aminophenol (PAP).

2.8. HER FARADAIC EFFICIENCY

The Faradic efficiency of a HER catalyst is defined as the ratio of the amount of H_2 evolved during the catalytic experiments to the amount of H_2 expected based on theoretical considerations. To measure the Faradic efficiency of HER, we carried out the following experiment. We collected the evolved H_2 gas (at constant potential of -0.5 V vs. RHE for 1h) by water displacement method,[S9] and then calculated the moles of H2 generated from the reaction with an ideal gas law. As for the theoretical value, we assumed that the current produced was solely due to HER process at the working electrode, based on the coupled HOR reaction. The theoretical amount of H_2 was then calculated by applying Faraday law.

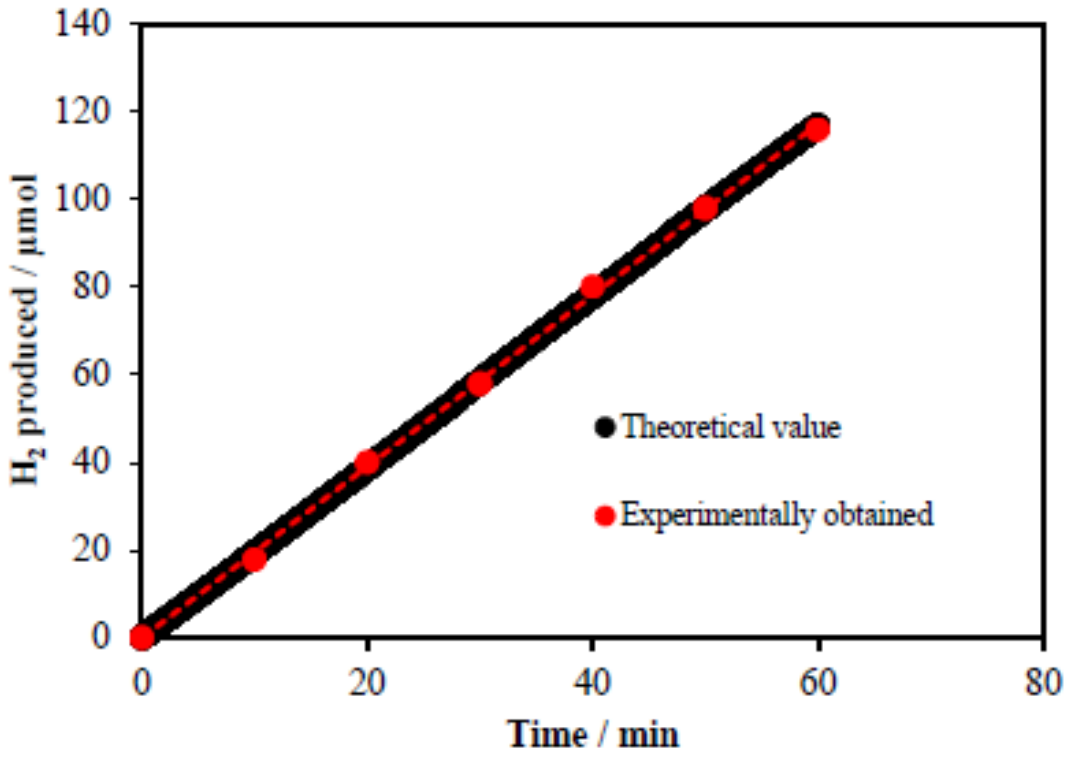

Supplementary Figure 11. HER faradaic efficiency of $NiSe_2$ catalyst where H_2 was evolved at a potential of -0.5 V vs. RHE for 1h and compare the theoretically calculated and experimentally obtained H_2 gas produced.

Supplementary Table 1. Comparison of OER activity at different nickel selenide based catalysts with loading.

Catalyst	**Loading**	**Activity**	**References**
$NiSe_2$	1 mg / cm^2	250 mV (10 mA cm^{-2})	*ACS Appl. Mater. Interfaces* 2016, **8**, 5327.
Co–Ni–Se/C/NF	1.5 mg / cm^2	275 mV (30 mA cm^{-2})	*J. Mater. Chem. A* 2016, **4**, 15148
Fe–NiSe/FeNi foam	4.8 mg / cm^2	245 mV (50 mA cm^{-2})	*Chem. Commun*. 2016, **52** ,4529
Co-doped $NiSe_2$	1.67 mg / cm^2	320 mV (100 mA cm^{-2})	*Nanoscale* 2016, **8**, 3911
$(Ni, Co)_{0.85}Se$	5 mg / cm^2	300 mV (97.5 mA cm^{-2})	*Adv.Mater.* 2016, DOI: 10.1002/adma.201503906
$Ni_xFe_{1-x}Se_2$-DO	4.1 mg / cm^2	195 mV (10 mA cm^{-2})	*Nat. Commun*. 2016, **7**, 12324
$NiSe_2$-DO	4.1 mg / cm^2	241 mV (10 mA cm^{-2})	
Ni_3Se_2 –Cu foam	3 mg / cm^2	284 mV (10 mA cm^{-2})	*Catal. Sci. Technol* 2015, **5**, 4954.
NiSe- Ni foam	2.8 mg / cm^2	251 mV (10 mA cm^{-2})	*Angew. Chem.Int. Ed.* 2015, **54**, 9351
$NiSe_2$ (Electrodeposition)	0.13 mg / cm^2	140 mV (10 mA cm^{-2})	**This work**
$NiSe_2$ (Hydrothermally)	1.4 mg / cm^2	220 mV (10 mA cm^{-2})	
$NiSe_2$ (Hydrothermally)	0.13 mg / cm^2	240 mV (10 mA cm^{-2})	

Supplementary Table 2. Calculation of energy efficiency of water electrolyzer (%).

Catalyst	**OER (V)[a]**		**HER (V)[a]**		**Water splitting cell voltage**		**Energy efficiency (%)[b]**	
	@ 10 mA cm^{-2}	@ 100 mA cm^{-2}	@ 10 mA cm^{-2}	@ 100 mA cm^{-2}	@ 10 mA cm^{-2}	@ 100 mA cm^{-2}	@ 10 mA cm^{-2}	@ 100 mA cm^{-2}
Pt	-	-	0.06	0.12	1.61	1.83	92	80.9
RuO_2	1.55	1.71	-	-				
$NiSe_2$	1.37	1.43	0.17	0.35	1.54	1.78	96.1	83.1

[a]All voltages are *vs* RHE. [b]Energy efficiency of water electrolysis$\cong (1.48\ V/E_{cell}) \times 100$.

Supplementary Table 3. Comparison of OER activity at different catalysts.

Electrocatalyst	**Electrolyte**	**Overpotential (mV *vs* RHE) @ 10^a, 20^b or 50^c mA cm^{-2}**	**Reference**
$NiSe_2$/Au	1 M KOH	140^a, 150^b & 170^c	This work
$NiSe_2$ (powder) / CFP		220^a, 260^b & 330^c	
Ni_3Se_2 / Au	0.3 M KOH	290^a	S5
NiSe/NiF	1 M KOH	270^a	S10
Fe-doped NiSe	1 M KOH	264 mV (100 mA cm^{-2})	S11
$Co_{0.85}Se$	1 M KOH	324^a	S12
$(Ni,CO)_{0.85}Se$	1 M KOH	255^a	
$Co_{0.13}Ni_{0.87}Se_2$/Ti	1 M KOH	320 mV (100 mA cm^{-2})	S13
$NiSe_2$/Ti	1 M KOH	350 mV (100 mA cm^{-2})	
$NiSe_2$	1 M KOH	250^a	S14
$CoSe_2$	1 M KOH		430^a
NiS/ Ni foam	1 M KOH	335^c	S15
Ni_3Se_2/Cu foam	1 M KOH	343^c	S16
$NixFe_{1-x}Se_2$-DO	1M KOH	195^a	S17
$NiSe_2$-DO	1M KOH		241^a
CoSe/Ti mesh	1 M KOH	341^c	S18
NiFe LDH/NF	1 M KOH	269^b & 349^c	S19
$Ni(OH)_2$	1 M KOH	313^b	S20
NiO nanoparticles	1 M KOH		347^b
NiO_x/C	1 M KOH	335^a	S21
$(Ni_{0.69}Fe_{0.31}O_x/C)$	1 M KOH		280^a
NiOOH	1 M KOH	525^a	S22
Amorphous NiO	1 M KOH	$>470^b$	S23
$NiCo_2O_4$	1 M KOH	391^b	S24
Ni/Ni_3N foam	1 M KOH	399^b	S25
NiCo LDH	1 M KOH	393^b	S26
Ni-Co-O@Ni-Co-S NA	1 M KOH	300^b	S27
CQDs/NiFe-LDH	1 M KOH	271^b	S28
Ni_5P_4/Ni foil	1 M KOH	363^c	S29
Ni–P/Cu foam	1 M KOH	410^c	S30
NiMo HNRs/Ti mesh	1 M KOH	344^c	S31

REFERENCES

S1. Sobhani, A. & Niasari, M. S. Synthesis and characterization of a nickel selenide series via a hydrothermal process *Superlattices and Microstructures* **65**, 79-90 (2014).

S2. Wu, H. Y. & Wang, H. W. Electrochemical synthesis of nickel oxide nanoparticulate films on nickel foils for high-performance electrode materials of supercapacitors. *Int. J. Electrochem. Sci.* **7**, 4405 – 4417 (2012).

S3. Masud, J.; Nguyen, T. V.; Singh, N.; McFarland, E.; Ikenberry, M.; Hohn, K.; Pan, C. J.; Hwang, B. J. A RhxSy/C catalyst for the hydrogen oxidation and hydrogen evolution reactions in HBr. *J. Electrochem. Soc.* **162**, F455-F462 (2015).

S4. Louie, M. W. & Bell, A. T. An investigation of thin-film Ni-Fe oxide catalysts for the electrochemical evolution of oxygen *J. Am. Chem. Soc*. **135**, 12329 – 12337 (2013).

S5. Swesi, A. T.; Masud, J. & Nath, M. Nickel selenide as a high-efficiency catalyst for oxygen evolution reaction. *Energy Environ. Sci*. **9**, 1771-1782 (2016).

S6. Parkinson, C. R.; Walker, M. & McConville, C. F. Reaction of atomic oxygen with a Pt(111) surface: chemical and structural determination using XPS, CAICISS and LEED. *Surf. Sci.* **545**, 19-33 (2003).

S7. Khawaja, E.E.; Salim, M.A.; Khan, M. A.; Al-Adel, F.F.; Khattak, G.D. & Hussain, Z. XPS, auger, electrical and optical studies of vanadium phosphate glasses doped with nickel oxide. *J. Non-cryst. Solids* **110**, 33 (1989).

S8. Xia, C.; Jiang, Q.; Zhao, C.; Hedhili, M. N. & Alshareef, H. N. Selenide-Based Electrocatalysts and Scaffolds for Water Oxidation Applications. *Adv. Mater*. **28**, 77–85 (2016).

S9. Wang, J.; Xia, H.; Peng, Z.; Lv, C.; Jin, L.; Zhao, Y.; Huang, Z. & Zhang, C. Graphene porous foam loaded with molybdenum carbide nanoparticulate electrocatalyst for effective hydrogen generation. *ChemSusChem* **9**, 855-862 (2016).

S10. Tang, C.; Cheng, N.; Pu, Z.; Xing, W. & Sun, X. NiSe nanowire film supported on nickel foam: an efficient and stable 3D bifunctional electrode for full water splitting. *Angew. Chem. Int. Ed*. **54**, 9351 –9355 (2015).

S11. Tang, C.; Asiri, A. M. & Sun, X. Highly-active oxygen evolution electrocatalyzed by a Fe-doped NiSe nanoflake array electrode. *Chem.Commun*. **52**, 4529-4532 (2016).

S12. Xia, C.; Jiang, Q.; Zhao, C.; Hedhili, M. N. & Alshareef, H. N. Selenide-based electrocatalysts and scaffolds for water oxidation applications. *Adv. Mater*. **28**, 77–85 (2016).

S13. Liu, T.; Asiri, A. M. & Sun, X. Electrodeposited Co-doped NiSe2 nanoparticles film: a good electrocatalyst for efficient water splitting. Nanoscale **8**, 3911- 3915 (2016).

S14. Kwak, I. H.; Im, H. S.; Jang, D. M.; Kim, Y. W.; Park, K.; Lim, Y. R.; Cha, E. H. & Park, J. CoSe2 and NiSe2 nanocrystals as superior bifunctional catalysts for electrochemical and photoelectrochemical water splitting. *ACS Appl. Mater. Interfaces* **8**, 5327−5334 (2016).

S15. Zhu, W.; Yue, X.; Zhang, W.; Yu, S.; Zhang, Y.; Wang, J. & Wang J. Nickel sulfide microsphere film on Ni foam as an efficient bifunctional electrocatalyst for overall water splitting. *Chem. Commun*. **52**, 1486-1489 (2016).

S16. Shi, J.; Hu, J.; Luo, Y.; Sun, X. & Asiri, A. Ni_3Se_2 film as a non-precious metal bifunctional electrocatalyst for efficient water splitting. *Catal. Sci. Technol*. **5**, 4954-4958 (2015).

S17. Xu, X.; Song, F. & Hu, X. A nickel iron diselenide-derived efficient oxygen-evolution catalyst. *Nat. Commun*. **7**, 12324 (2016).

S18. Liu, T.; Liu, Q., Asiri, A.; Luo, Y.; Sun, X. An amorphous CoSe film behaves as an active and stable full water-splitting electrocatalyst under strongly alkaline conditions. *Chem. Commun*. **51**, 16683-16686 (2015).

S19. Luo, J.; Im, J.-H.; Mayer, M.; Schreier, M.; Nazeeruddin, M.; Park, N.; Tilley, S.; Fan, H. & Gratzel, M. Water photolysis at 12.3% efficiency via perovskite photovoltaics and Earth-abundant catalysts. *Science* **345** 1593–1596 (2014).

S20. Stern, L. & Hu, X. Enhanced oxygen evolution activity by NiOx and $Ni(OH)_2$ nanoparticles. *Faraday Discuss*. **176**, 363 –379 (2014).

S21. Qiu, Y.; Xin, L. & Li, W. Electrocatalytic oxygen evolution over supported small amorphous Ni–Fe nanoparticles in alkaline electrolyte. *Langmuir* **30**, 7893–7901 (2014).

S22. Klaus, S.; Cai, Y.; Louie, M.; Trotochaud, L. & Bell, A. T. Effects of Fe electrolyte impurities on $Ni(OH)_2$/NiOOH structure and oxygen evolution activity. *J. Phys. Chem. C* **119**, 7243-7254 (2015).

S23. Kuai, L.; Geng, J.; Chen, C.; Kan, E.; Liu, Y.; Wang, Q. & Geng, B. A reliable aerosol-spray-assisted approach to produce and optimize amorphous metal oxide catalysts for electrochemical water splitting. *Angew. Chem. Int. Ed*. **53**, 7547–7551 (2014).

S24. Peng, Z.; Jia, D.; Al-Enizi, A.; Elzatahry, A. & Zheng, G. From water oxidation to reduction: homologous Ni–Co based nanowires as complementary water splitting electrocatalysts. *Adv. Energy Mater*. **5**, 1402031-1402038 (2015).

S25. Shalom, M.; Ressing, D.; Yang, X.; Clavel, G.; Fellinger, T. & Antonietti, M. Nickel nitride as an efficient electrocatalyst for water splitting. *J. Mater. Chem. A* **3**, 8171–8177 (2015).

S26. Liang, H.; Meng, F.; Acevedo, M.; Li, L.; Forticaux, A.; Xiu, L.; Wang Z. & Jin, S. Hydrothermal continuous flow synthesis and exfoliation of NiCo layered double hydroxide nanosheets for enhanced oxygen evolution catalysis. *Nano Lett*. **15**, 1421–1427 (2015).

S27. Xu, W.; Lu, Z.; Lei, X.; Li, Y. & Sun, X. A hierarchical Ni–Co–O@Ni–Co–S nanoarray as an advanced oxygen evolution reaction electrode. *Phys. Chem. Chem. Phys*. **16**, 20402–20405 (2014).

S28. Tang, D.; Liu, J.; Wu, X.; Liu, R.; Han, X.; Han, Y.; Huang, H.; Liu, Y. & Kang, Z. Carbon quantum dot/NiFe layered double-hydroxide composite as a highly efficient electrocatalyst for water oxidation. *ACS Appl. Mater. Interfaces* **6**, 7918–7925 (2014).

S29. Ledendecker, M; Calderon, S. K.; Papp, C.; Steinruck, H. P.; Antonietti, M. & Shalom, M. The synthesis of nanostructured Ni5P4 films and their use as a non-noble bifunctional electrocatalyst for full water splitting. *Angew. Chem. Int. Ed*. **127**, 12538–12542 (2015).

S30. Liu, Q.; Gu, S. & Li, C. Electrodeposition of nickel-phosphorus nanoparticles film as a Janus electrocatalyst for electro-splitting of water. *J. Power Sources* **299**, 342-346 (2015).

S31. Tian, J.; Cheng, N.; Liu, Q.; Sun, X.; He, Y.; Asiri A. Self-supported NiMo hollow nanorod array: an efficient 3D bifunctional catalytic electrode for overall water splitting. *J. Mater. Chem. A* **3**, 20056-20059 (2015).

IV. COBALT SELENIDE NANOSTRUCTURES: AN EFFICIENT BIFUNCTIONAL CATALYST WITH HIGH CURRENT DENSITY AT LOW COVERAGE

ACS Appl. Mater. Interfaces 2016, 8, 17292−17302

Jahangir Masud, Abdurazag T. Swesi, Wipula P. R. Liyanage, and Manashi Nath

Department of Chemistry

Missouri University of Science and Technology

Rolla, Missouri 65409-0050 USA

Email: nathm@mst.edu

KEYWORDS: OER, Co_7Se_8, water splitting, ORR, transition metal chalcogenides

ABSTRACT

Electrodeposited Co_7Se_8 nanostructures exhibiting flake-like morphology show bifunctional catalytic activity for oxygen evolution and hydrogen evolution reaction (OER and HER, respectively) in alkaline medium with long-term durability (>12 h) and high Faradaic efficiency (99.62%). In addition to low Tafel slope (32.6 mV per decade), the Co_7Se_8 OER electrocatalyst also exhibited very low overpotential to achieve 10 mA cm^{-2} (0.26 V) which is lower than other transition metal chalcogenide based OER electrocatalysts reported in the literature and significantly lower than the state-of-the-art precious metal oxides. A low Tafel slope (59.1 mV per decade) was also obtained for the HER catalytic activity in alkaline electrolyte. The OER catalytic activity could be further improved by creating arrays of 3-dimensional rod-like and tubular structures of Co_7Se_8

through confined electrodeposition on lithographically patterned nanoelectrodes. Such arrays of patterned nanostructures produced exceptionally high mass activity and gravimetric current density (~68 000 A g^{-1}) compared to the planar thin films (~220 A g^{-1}). Such high mass activity of the catalysts underlines reduction in usage of the active material without compromising efficiency and their practical applicability. The catalyst layer could be electrodeposited on different substrates, and an effect of the substrate surface on the catalytic activity was also investigated. The Co_7Se_8 bifunctional catalyst enabled water electrolysis in alkaline solution at a cell voltage of 1.6 V. The electrodeposition works with exceptional reproducibility on any conducting substrate and shows unprecedented catalytic performance especially with the patterned growth of catalyst rods and tubes.

1. INTRODUCTION

Catalyst-aided water splitting reactions producing oxygen and hydrogen as storable chemical fuel have stimulated extensive research to prevent accelerated depletion of fossil fuels.[1–5] Water electrolysis consists of two half-cell reactions, *viz*., oxygen evolution reaction (OER) and hydrogen evolution reaction (HER), occurring at the anode and cathode, respectively. However, the electrolysis of water, breaking the O−H bonds and forming O=O and/or H−H accompanied by the release of protons or electrons, is kinetically sluggish and generally requires a cell potential substantially higher than the thermodynamic value of 1.23 V (vs RHE), that is, a large overpotential.[6–9] Therefore, to increase the reaction rate and lower the overpotential, it is crucial to employ highly active catalysts for

efficient water splitting. Currently, state-of-the-art HER catalysts consist of Pt-based electrodes,[10] while the high performing OER catalysts are mostly based on oxides of Ir[1] and Ru.[11] Nevertheless, the scarcity and high cost of these precious metals practically limits them from being used on a large scale. Thus, a great effort has been made toward identifying efficient OER and HER catalysts with earth-abundant materials, such as transition metal oxides (TMOs) and/or layered double hydroxides of Ni and Ni−Fe, respectively,[12−16] cobalt phosphate,[10] perovskite oxides,[17,18] and recently transition metal chalcogenides.[19−24] Among these, even more challenging is the identification of a bifunctional catalyst active for both OER and HER with high performance and stability in the same electrolyte.[25] A stable bifunctional catalyst with nonprecious metal compositions showing high efficiency at low overpotential will be highly desirable to simplify and lower the cost of overall water splitting.

Recently, transition metal chalcogenides have been used extensively for advanced energy related applications due to their considerable activity toward water electrocatalysis.[26,27] The transition metal chalcogenides are well-known for their interesting magnetic and electronic properties. More importantly, the metal−chalcogen ratio in these transition metal chalcogenides can be varied over a wide range which can lead to subtle variation of their electronic properties, thereby offering opportunities to tune such properties. The high catalytic performance along with the low cost of the earth-abundant raw materials make these transition metal chalcogenides suitable for replacing the more expensive Pt-based electrocatalysts.[28−35] Among these, Co-based chalcogenides are attractive because of the earth abundance of Co, and over the past several years, great efforts have been devoted to develop Co-based water oxidation catalysts. Additionally, it

was predicted that the ideal OER electrocatalyst can be obtained if the number of electrons in the eg orbital of surface transition-metal cations is close to unity,[36] which is fulfilled in the case of a low-spin Co^{2+} ion.

Recently reported ultrathin $CoSe_2$ showed very good OER catalytic activity in alkaline solution exhibiting a low overpotential (320 mV).[37] Gao et al. have also reported a Mn_3O_4–$CoSe_2$ nanocomposite as an efficient water oxidation electrocatalyst.[38] Amorphous CoSe has also been reported as an active catalyst for HER in acidic solution.[39] However, in spite of all these reports, examples of Co chalcogenide based bifunctional catalysts for full water splitting in alkaline conditions have been rare, and only an amorphous CoSe catalyst has been reported recently.[40] Since different phases of cobalt selenide have shown OER, HER, and ORR activities separately, it would be interesting to pursue if any particular phase of cobalt selenide can be electrocatalytically active for OER, HER, as well as ORR processes.

In recent times, along with identifying new catalyst compositions, optimizing the morphology of these catalysts has also become a major focus. Since catalysis is a surfacesensitive phenomenon, nanostructured catalysts have become more important than thin films due to their enhanced surface area. Some of these OER and HER catalysts have shown much enhanced performance compared to their thin-film morphology.[41] Ordered arrays of nanostructured catalysts in the form of nanorods deserve a special mention in this regard since it provides an optimal geometry and specificity for catalytic processes. Recently arrays of electrocatalyst nanoislands arranged on a photoabsorber layer have been predicted as the most efficient geometry from solar hydrogen production.[42] The reduced usage of active materials is another attractive feature of the nanostructure arrays, and

recently it has been shown that InP and GaAs nanowire arrays with less than 15% coverage produced 80% of the photocurrent obtained from a bulk film.[43,44] An array of tubular nanostructures will be even more advantageous for catalytic activity attributed to the fully accessible catalytic sites on the inner and outer walls of the tubes along the entire thickness along with the pronounced edge effects at the open ends of the tubes. However, owing to the complexity of the structure there have been very few reports on the formation of catalyst nanorod arrays, while the nanotube arrays have not been reported to date as per the authors' knowledge.

Herein, we present a nanostructured cobalt selenide electrocatalyst (Co_7Se_8) which acts as a bifunctional catalyst and enhances OER and HER with high efficiency in strongly alkaline conditions. In this article we also report that growing this Co_7Se_8 film as an array of tubular or rod-like nanostructures significantly enhances the specific and gravimetric current densities for the OER process, thereby reducing the amount of active material required without compromising performance. Prolonged oxygen evolution under constant potential electrolysis showed that these Co_7Se_8 electrocatalysts were exceptionally stable and durable in alkaline conditions during OER activity. The cobalt selenide nanostructured films were prepared through simple electrodeposition on glassy carbon (GC) disks and Au-coated glass slides, and the asprepared films showed an onset potential of 1.45 V and attained a current density of 10 mA cm^{-2} at an overpotential of 260 mV after 6 h of continuous O_2 generation. This is among the lowest overpotential observed for the cobalt selenide based OER catalysts. The overall water splitting using Co_7Se_8 as both OER and HER catalyst was achieved at a cell voltage of 1.60 V. This is the first instance of growing this kind of electrocatalyst as porous tubular arrays, which can be readily applied to other

catalyst systems, especially in conjunction with underlying photoabsorber layers for more efficient solar-to-fuel energy conversion.

2. RESULTS AND DISCUSSION

2.1. STRUCTURE AND MORPHOLOGY OF THE ELECTRODEPOSITED

Films. The crystallinity of the electrodeposited film on Au was investigated by the powder X-ray diffraction (PXRD) technique. Figure 1 shows the PXRD patterns of the electrodeposited films at different deposition times from 1 to 5 min. As can be seen from

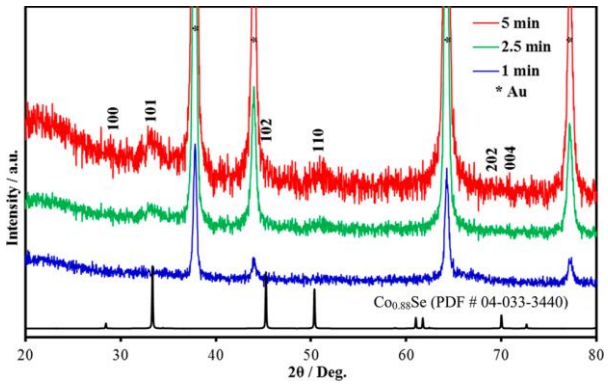

Figure 1. Powder X-ray diffraction pattern of the as-deposited catalyst film showing the formation of Co_7Se_8 (PDF # 04-003-3440) along with Au where the different experimental PXRD pattern represents different electrodeposition time.

the Figure, the PXRD pattern obtained for the film after 1 min deposition only exhibited reflections corresponding to the Au substrate and did not show any crystalline cobalt selenide species. The electrocatalyst was then deposited for longer deposition times, and it was noticed that as the deposition time was increased, along with increase in the film thickness, the crystallinity of the film also increased. Accordingly, the film deposited for 5

min showed better intensity of the diffraction peaks, and the pattern could be matched with that of Co_7Se_8 (PDF # 04-003-3440). Co_7Se_8 is a cobalt-deficient hexagonal phase with both Co and Se in an octahedral coordination and is frequently represented as the $Co_{0.88}Se$ phase (Supporting Figure S1). It must be noted here that among the cobalt selenides catalytic activities for oxygen evolution and hydrogen evolution have been reported for CoSe and $CoSe_2$.[37−40] This is the first example of Co_7Se_8 showing OER and HER catalytic activity by itself. The d-electron configuration of metal cations has a significant influence on the physical properties of transition metal dichalcogenides. The paramagnetic electronic configuration of Co^{2+} (d^7 in the form of $t_{2g}^{\ 6}e_g^{\ 1}$) makes Co_7Se_8 a metal-like conductor. This metallic property of Co_7Se_8 might help the catalyst performance by facilitating charge transport from the back electrode to the surface of the catalysts, which is desired for high catalytic activity.[37] Typical scanning electron microscopy (SEM) imaging were performed to investigate the morphologies and microstructural details of the composite. SEM image, as shown in Figure 2(a), revealed that the films deposited for 1 min were very rough containing randomly oriented nano flakes where the flakes were relatively uniform and well-dispersed. The flake-like morphology was retained with higher deposition time, and some agglomerations of the resulting catalyst were observed in 2.5 min of deposition. As seen in Figure 2(a) (right panel), Co_7Se_8 deposited for 5 min inhomogeneously covered the GC surface with randomly oriented nanoflakes and some agglomerations. These randomly oriented nanoflakes led to a very rough film with porous architecture which is very good for catalytic activity since it increases the active surface area. The amount of catalyst loading as well as thickness of the electrodeposited film were estimated (see Supporting Information) and have been presented in Table 1. As expected the catalyst loading and

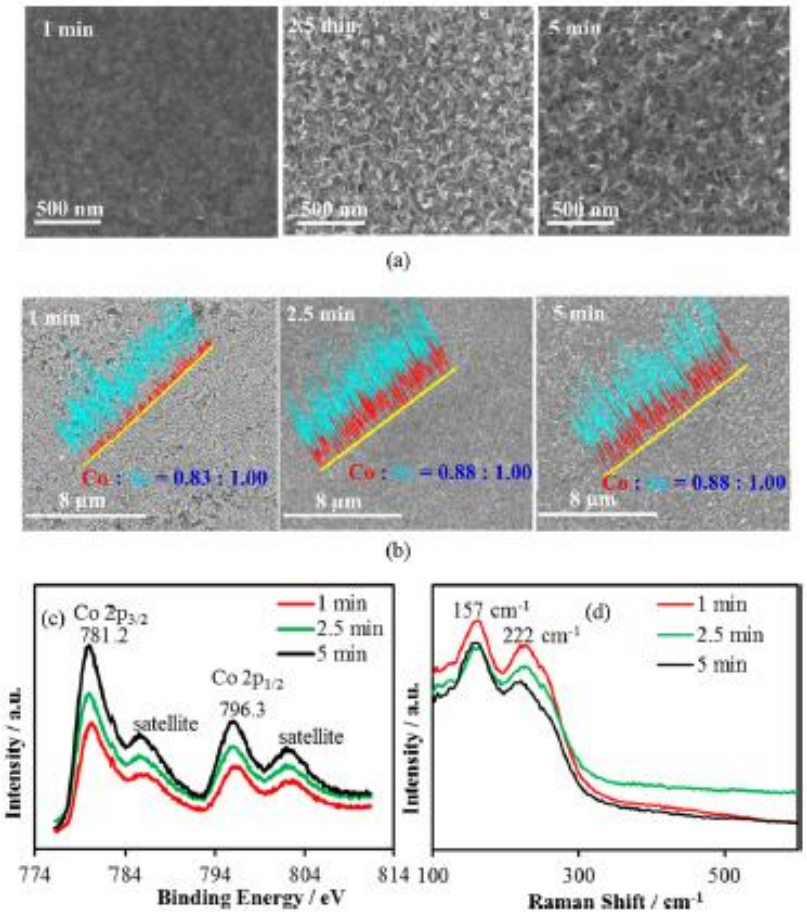

Figure 2. (a) Typical SEM images of electrodeposited catalysts. (b) EDS line scans of the deposited films. (c) Co 2p XPS spectra of the catalysts. (d) Raman shifts obtained from the catalyst films.

film thickness increased with increasing deposition time. Elemental line scan analysis through energy dispersive X-ray spectroscopy (EDS) as shown in Figure 2b revealed that the Co and Se were present uniformly throughout the film with a relative atomic ratio of Co to Se close to 0.88:1.0. This was in accordance with the PXRD result which confirmed the formation of Co_7Se_8. The composition of the electrodeposited films was also analyzed through quantitative X-ray photoelectron spectroscopy (XPS) which gave information about the surface electronic states of the elements. The binding energies of Co and Se for the composites have been shown in high-resolution XPS spectra in Figure 2c and

Supporting Figure S2, respectively. The first doublet at 781.2 and 796.3 eV indicated the presence of Co^{2+} as seen in $Co_{0.85}Se$.[45] An obvious satellite at the higher binding energies of the Co 2p signal was observed similar to that previously reported.[37] In the Se 3d spectra (Supporting Figure S2), the peak at 54.6 eV is consistent with Se 3d of cobalt selenide, while the peak in the range of 57.0−63.0 eV is assigned to Co 3p.[46]

Raman spectra of as-grown catalyst on GC are shown in Figure 2d which shows consistent spectral features, suggesting identical deposits at different deposition time. The peaks at 157 and 222 cm^{-1} have been reported previously for the hexagonal Co_7Se_8 phase.[39,47,48] It should be noted that Raman spectra displayed no signatures of oxygenated cobalt species indicating the films were free from any oxidic impurities.

2.1.1. Rod-Like and Tubular Structure Arrays. Nanostructure arrays with periodic ordered arrangement of the catalyst islands are expected to show higher catalytic performance with even lesser usage of active materials. Rod and more importantly tubular arrays of these Co_7Se_8 electrocatalysts have been prepared by a protocol recently developed in our laboratory involving confined electrodeposition on lithographically patterned nanoelectrodes.[49−52] Nanosphere photolithography was used to define nanoelectrodes for rods, while the tubular structures were grown on shell-shaped nanoelectrodes patterned through e-beam lithography (see Methods section and Supporting Information).[50,52] The electrodeposition was performed at -0.8 V (vs. Ag|AgCl) for 50 s from the same electrochemical bath described in the Materials and Methods Section. For comparison, thin films of Co_7Se_8 was also deposited for 50 s on the GC electrode. Figure 3 shows the SEM images of the patterned substrate with the Co_7Se_8 rods (a) and tubes (b). As had been observed previously in our group, Co_7Se_8 deposited exclusively on the nanoelectrodes

defined through lithography, and the rest of the substrate was absolutely clean. The diameter of the rod was about 400 nm, and the length could be varied between 500 and 1000 nm. The wall thickness of the tube was typically 400 nm, while length could be varied between 500 and 800 nm. As can be seen from the SEM images, the surface of these catalyst structures was very rough. Elemental line scan analysis across the tube walls and the rods showed that these structures were composed of Co and Se exclusively (Supporting Figure S3).

2.2. ELECTROCHEMICAL PERFORMANCE AND CATALYTIC ACTIVITIES

The catalytic efficiency of Co_7Se_8 electrodeposited film in 1 M KOH for oxygen and hydrogen evolution reactions was tested through standard electrochemical measurements,[55] details of which have been provided in the Supporting Information. Generally, catalytic activity of any material is strongly influenced by its surface area.

Hence, the electrochemically active surface area (ECSA) of the Co_7Se_8 films was determined by double-layer capacitance (CDL) according to Equation 1.

$$\text{ECSA} = C_{DL}/C_s \quad (1)$$

Where C_s is the specific capacitance of the sample and typical values have been reported in the range of C_s = 0.022−0.130 mF cm^{-2} in NaOH and KOH solutions, respectively.[53,54] In this study, C_s = 0.04 mF cm^{-2} was used similar to the previously reported value for metal oxide/selenide based catalysts in alkaline solution.[53−55] CDL was calculated from the slope of the line in the plot of capacitive current (iDL) versus scan rates, ν (V/s).

$$i_{DL} = C_{DL}v \quad (2)$$

Cyclic voltammograms (CVs) were recorded in N_2-saturated 1 M KOH in the double-layer regime (-0.19 to -0.05 V vs Ag| AgCl) with varying scan rates ranging from 2.5 to 40 mV s^{-1} (Figure 4). The working electrode was held at each end potential for 20 s before beginning the next sweep.

Table 1. Electrocatalytic Activity of Co_7Se_8 Catalysts in 1 M KOH.

deposition time/ min	**catalyst loading /µg**	**thickness/ nm**	**ECSA/ cm^2**	**RF**	**TOF/ s^{-1}**	**onset η/Va**	**η to 10 $mAcm^{-2}$/ Va**	**Iη= 0.3 $A\ g^{-1}$**	**Tafel slope/ mV dec^{-1}**
1	5.2	34	1.1	5.6	0.077	0.23	0.31	215	36.2
2.5	10.5	70	1.5	7.7	0.083	0.22	0.29	234	32.6
5	19.2	128	1.6	8.1	0.047	0.22	0.29	134	34.1

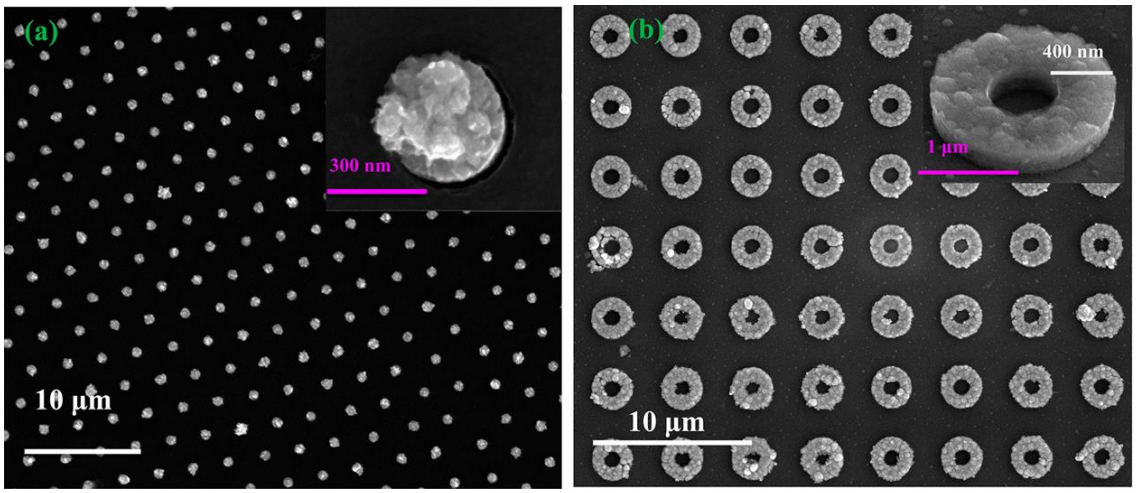

Figure 3. SEM images of Co_7Se_8 (a) nanorods and (b) nanotubes.

A plot of i_{DL} against ν is shown in the inset of Figure 4. The ECSA and the roughness factor (RF) of catalysts at different deposition times are shown in Table 1. While

the roughness factor increases progressively with increasing deposition time, the ECSA is observed to be more or less saturated after 2.5 min, indicating that the catalyst might be at the optimal geometry by this deposition time, with high roughness factor, high ECSA, and moderate film thickness.

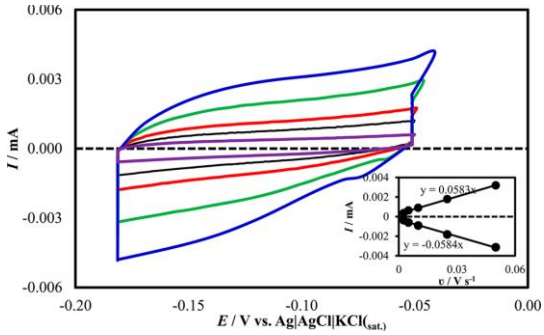

Figure 4. Cyclic voltammograms measured for Co_7Se_8 catalyst, deposited for 2.5 min, in N_2-saturated 1.0 M KOH. The scan rates were varied from 2.5 to 40 mV s^{-1}, and the variation of anodic and cathodic current obtained at -0.12 V at different scan rate is shown in the inset.

2.2.1. Oxygen Evolution Reaction Catalysis. The electrocatalytic activity of Co_7Se_8 for OER on a GC electrode was evaluated in N_2-saturated 1 M KOH using a standard threeelectrode system with Pt as the counter electrode and Ag|AgCl as the reference electrode. Linear sweep voltammetry (LSV) measurements were performed with a sweep rate of 5 mV s^{-1} to obtain the standard current−voltage polarization curves. All OER data have been iR corrected (the resistance, R, of 1 M KOH was about 5 Ω, as obtained from impedance analysis discussed later). The *iR* corrected plots (for HER/OER) show a clear difference compared to the original plot as seen in Figure S4. Figure 5a shows the typical LSVs corresponding to rapid oxygen evolution with Co_7Se_8 catalysts deposited for 1, 2.5, and 5 min on GC and comparison with electrodeposited RuO_2 on GC. The onset

potentials for the Co_7Se_8 films were very low and were recorded as follows: 1.46 V vs RHE for 1 min and 1.45 V vs RHE for 2.5 and 5 min deposition, respectively.

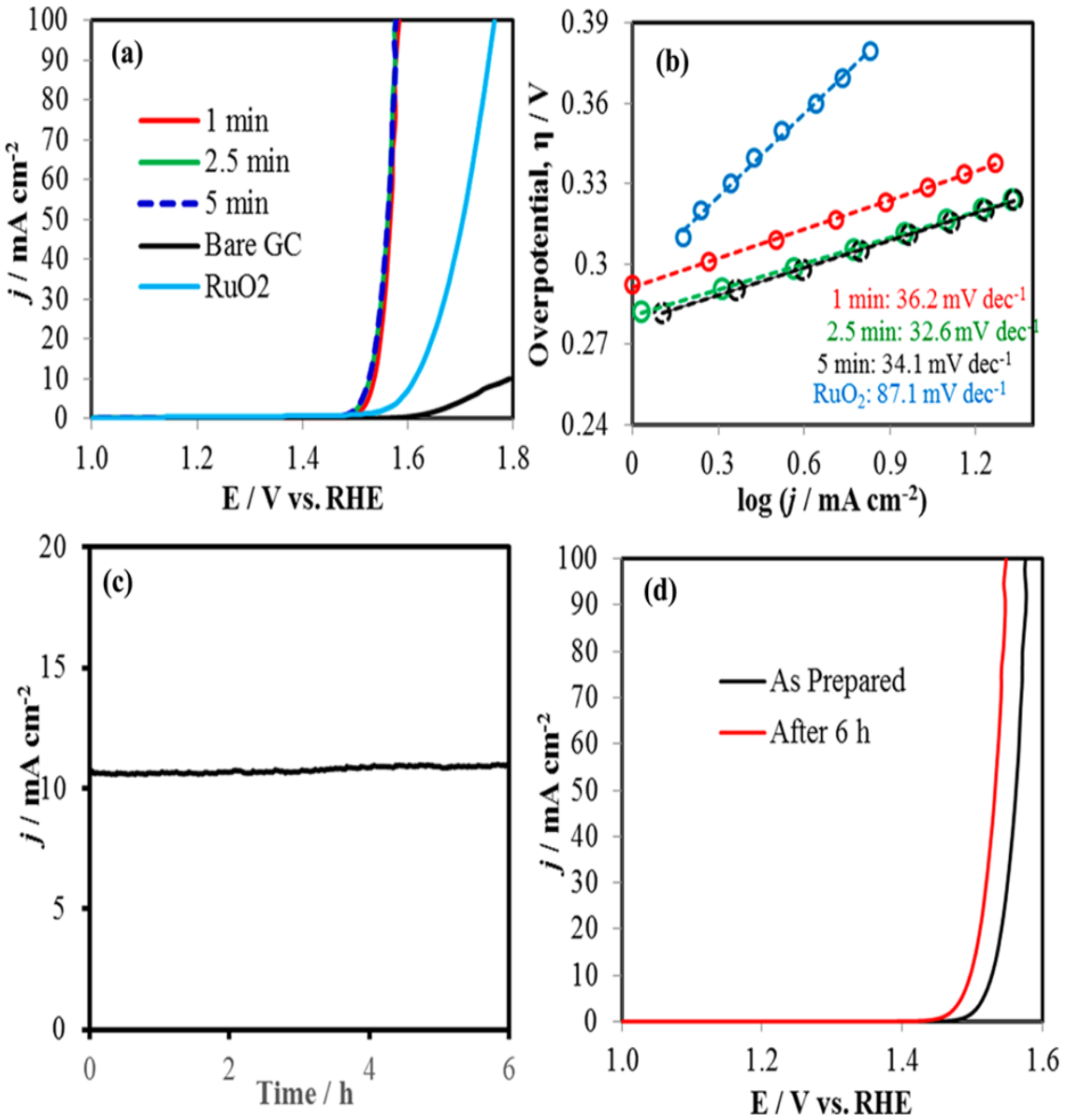

Figure 5. (a) Current−voltage plots measured for OER in 1 M KOH with Co_7Se_8 electrocatalysts deposited for various times. The scan rate was maintained at 5 mV s^{-1}. (b) Tafel plots of Co_7Se_8 compared with that of RuO_2. (c) Chronoamperometry study at constant potential (@ 10 mA cm^{-2}) illustrating stability of the catalyst for 6 h under conditions of steady O_2 evolution. (d) LSVs of catalyst synthesized for 2.5 min in N_2-saturated 1.0 M KOH before (black) and after chronoamperometry (red) for 6 h.

Table 2. Comparison of Performance for Different Cobalt Selenide Based OER Electrocatalyst.

Catalysts	**Onset potential/V (vs RHE)**	**η@*J* = 10 mA cm^2/mV**	**Mass activity/ A g^{-1}**	**Tafel slope/ mV dec^{-1}**	**TOF/s^{-1}**	**Ref.**
Ultrathin $CoSe_2$	1.48a	320	-	44	0.335@ η=500 mV	37
CoSe/Ti mesh	1.52a	292	-	69	-	40
NG-$CoSe_2$	1.523	366	63.45@ η = 366 mV	40	0.03565@ η=366 mV	61
$CoSe_2$	1.602	484	2.75@ η = 366 mV	66	0.00773@ η=366 mV	61
RuO_2	1.481	366	50.00@ η = 366 mV	69	0.01724@ η=366 mV	61
20 wt % Pt/C	1.603	556	9.86@ η = 366 mV	127	0.00505@ η=366 mV	61
Co_7Se_8/GC	1.45	290	234@ η = 300 mV	32.6	0.083@ η = 300 mV	This work

[a]Calculated from the references.

A current density of 10 mA cm^{-2} was achieved at overpotential of 310 mV for 1 min of catalyst deposition, whereas catalyst deposited for 2.5 and 5 min required an overpotential of 290 mV. The bare GC electrode was tested separately; as expected it shows almost no OER activity, while OER activity of RuO_2/GC measured in a similar setup showed that 360 mV overpotential was required to achieve 10 mA cm^{-2} which matches exactly with the reported value (see Table 2). The onset potential as well as overpotential @ 10 mA cm^{-2} for Co_7Se_8 on GC are significantly better than the cobalt selenide phases reported previously and are comparable to some of the nickel selenide based

electrocatalysts recently produced from our group.[55] It should be noted that these values are among the best for OER electrocatalysts in alkaline medium and outperform most of the conventional oxides as well as the high performing transition metal oxides and hydroxides.

The Tafel slope is an important parameter which provides valuable insight into the kinetics of the OER/HER process, by underlining the influence of potential or overpotential on steady-state current density. Hence, to understand the kinetic parameters, Tafel slopes of these catalysts were retrieved from the LSVs following standard procedures[55] and are presented in Figure 5b (details have been provided in the Supporting Information). It was observed that the η vs log(*j*) plot was linear for all deposition times, with almost similar slopes (Table 1) indicating that the reaction mechanism follows a similar pathway. The Tafel slope initially decreased slightly with increasing deposition time, showing a minimum at 2.5 min deposition. The trend observed for the Tafel slope was 2.5 min (32.6 mV dec^{-1}) < 5 min (34.1 mV dec^{-1}) < 1 min (36.2 mV dec^{-1}) indicating that the catalyst deposited for 2.5 min showed the best rate for O_2 evolution, highlighting the effect of an optimal nanostructured surface along with porous network. Impressively, the estimated Tafel slopes of these catalysts are lower than RuO_2/GC (87.1 mV/dec) and some of the welle stablished OER catalysts such as IrO_2 (ca. 49 mV/dec),[56] Ir/C (ca. 40 mV/dec),[57] and other cobalt-based catalysts.[37,58] These lower Tafel slopes indicate faster charge transfer from electrolyte to electrode, which can possibly explain the enhanced performance of these electrocatalysts.

Stability is a major aspect in the practical development of electrocatalysts. In order to check the stabilities of these catalysts, long-term controlled potential electrolysis was

performed by using the chronoamperometric technique at a constant rotation rate of 1600 rpm. For the OER stability, the potential was held at an overpotential, η = 290 mV, to achieve 10 mA cm^{-2} where the current was measured vs time and presented in Figure 5c. The stable current over 6 h of continuous operation suggests that the Co_7Se_8-modified (2.5 min) GC electrode exhibits high durability for OER in 1.0 M KOH. As shown in the inset of Figure 5c, the polarization curve after 6 h of chronoamperometry shows even better performance than the initial one, with the lowest onset overpotential, η= 190 mV, and lower overpotential to achieve 10 mA cm^{-2} (η = 260 mV). Long-term stability tests were also performed where the catalyst held at constant potential for 15 h showed steady current and continuous O_2 evolution as shown in Supporting Figure S5a. The LSV plot collected after 15 h chronoameprometry study (Supporting Figure S5b) showed that there was no degradation of the catalytic performance, confirming the extended stability of this OER electrocatalyst.

To investigate the enhanced catalytic activity these catalysts were studied by SEM, EDX, XRD, and XPS analyses after periods of continuous catalytic process. The SEM (Supporting Figure S6) shows that the porosity of films was greatly increased after 6 h of continuous electrolysis (during OER) which increases the active surface of the catalyst. Correspondingly, the ECSA of catalyst was also increased and found to be 2.1 cm^2 after continuous OER which is higher than the initial ECSA. EDX line scan shows the uniform distribution of Co and Se in the film even after 6 h of chronoamperometry; however, the relative atomic ratio of Co:Se increased slightly (0.91:1) in the film. Some Se could have been lost due to leaching at highly alkaline solution which can possibly decrease the Se content after extensive electrolysis, making the films metal rich. It should be noted here

that the O content in the films was more or less constant and did not show progressive increase with increasing electrolysis time. The PXRD pattern of the Co_7Se_8 catalyst however remained unchanged after the OER activity (Supporting Figure S7a). The XPS spectra of the catalytic film after OER activity showed that the Co 2p and Se 3d maintained their peak positions and intensities indicating that the catalyst compositions was unaltered to a large extent (Supporting Figure S7b and S7c).

Another parameter that defines the efficiency of a catalyst is the turnover frequency (TOF) which was calculated at 300 mV overpotential using an Equation (Equation S1) as shown in the Supporting Information.[55] To calculate TOF it was assumed that all the metal ions were catalytically active; however, this may lead to gross underestimations of the actual TOF because every metal atom may not be catalytically active or involved in the reaction. Nevertheless, the TOF of Co_7Se_8 is still promising (Table 1), and it exhibited much higher values than the previously reported Co-based catalysts[59–61] at an overpotential of 300 mV. Besides TOF, the calculated mass activity for Co_7Se_8/GC is 234 A g^{-1}, which outperforms other cobalt selenide based catalysts and even RuO_2.[61] The comparison of OER activity of different catalysts has been presented in Table 2. As can be seen, the Co_7Se_8 reported here shows one of the best catalytic activities among the cobalt selenide based OER electrocatalyst in terms of both onset potential and overpotential at 10 mA cm^{-2} as well mass activity and gravimetric current density.

The composition of the evolved gas at the anode was analyzed electrochemically using a rotating ring disk electrode (RRDE) where O_2 was reduced at the Pt ring electrode (cathode), while Co_7Se_8 electrodeposited on GC was connected as the disk electrode. This procedure has been published previously[55] and is described in detail in the Supporting

Information. The basic theme of this experiment is combining the ORR and OER processes such that the gas evolved at the anode (OER) is carried over to the Pt ring electrode, and if the gas is indeed O_2, the Pt electrode (maintained at 0.2 V) should be able to reduce it (ORR), thereby producing the reduction current. In the absence of evolved oxygen, the disk/ring current should be minimal. A scanning across the potential range will thus give an insight about the potential at which oxygen evolution starts at the anode. Figure 6a shows the combined ORR−OER plot at 1600 rpm rotating speed of the electrode with a scan rate of 5 mV s^{-1} in 1 M KOH. The upper blue curve in Figure 6a shows the ring current, while the lower red curve is the LSV corresponding to the OER process (disk current).

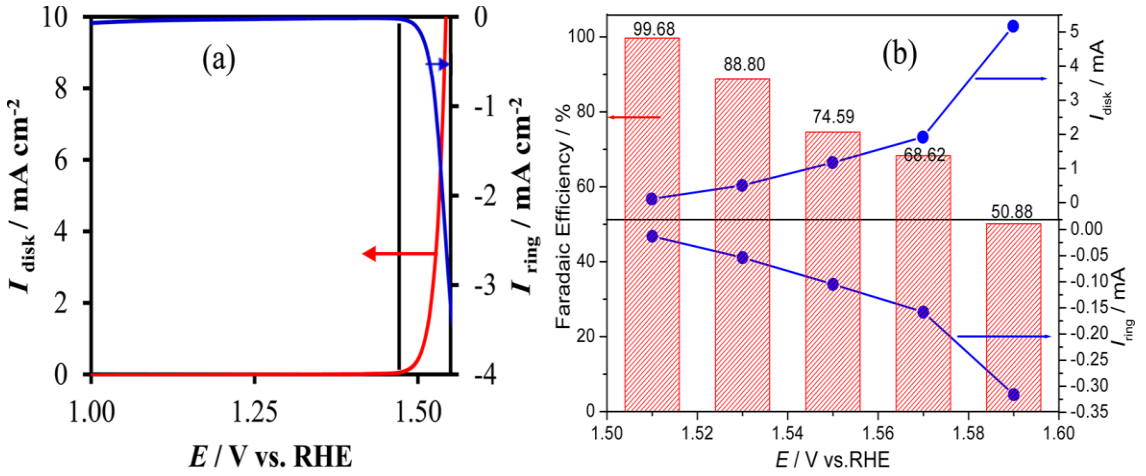

Figure 6. (a) Plots for the ORR−OER reaction showing OER current density at Co_7Se_8/GC disk electrode in N_2-saturated 1.0 M KOH and ORR current density at Pt ring electrode maintained at 0.2 V vs RHE as a function of applied disk potential. Black line indicates the onset potential for OER at the disk electrode corresponding with the onset of ORR at the ring electrode. (b) Faradaic efficiency of catalyst measured in N_2-saturated 1.0 M KOH at 1600 rpm rotation speed.

From the Figure it can be clearly seen that when there is no oxygen evolution (V < 1. 45 V) ring current is much less. However, the ring current (corresponding to ORR) showed a sharp increase as soon as the disk electrode reached the onset potential for oxygen

evolution (1.45 V) and kept increasing with further increase of the applied disk potential which led to generation of more oxygen. Hence this combined OER−ORR experiment can provide conclusive proof that the gas evolved in the anode was indeed O_2.

The theme of the ORR−OER combined experiment was also used to estimate the Faradaic efficiency following a similar principle, whereby at a constant potential the O_2 generated at the disk anode was swept outward toward the Pt ring electrode where it was reduced to water. Details of the experimental conditions to determine Faradaic efficiency have been provided in the Supporting Information. The Faradaic efficiency is given by[53]

$$\text{Faradaic efficiency} = 2i_r / i_d N \quad (3)$$

Where i_d and i_r correspond to the measured disk and ring currents, respectively, and the collection efficiency of RRDE is represented by N (taken as 0.24). The plot of the disk and ring currents of Co_7Se_8 catalyst in 1 M KOH as a function of the applied disk potential is shown in Figure 6b. It was observed that the Faradaic efficiency decreased with increasing disk voltage, and the highest efficiency (99.68%) was obtained slightly above the onset potential (1.51 V) for the OER process.

Such decrease of Faradaic efficiency with increasing voltage has been observed previously[55] and is attributed to the inefficient collection of the generated O_2 by the Pt ring electrode at higher disk potential. Hence, the 99.68% Faradaic efficiency which was achieved at 1.51 V (vs RHE) is presented as the OER catalytic efficiency of the Co_7Se_8 catalyst.

2.2.2. Effect of Morphology: Rod-Like and Tubular Structure Arrays. After observing the enhanced catalytic activity of the nanoflakes and how increasing porosity improves the catalytic performance, we have attempted to texture these nanostructured

catalytic films even further by creating islands of rods and more importantly tube-like structures. These vertically ordered 3-dimensional textured arrays can expectedly increase the active surface area of the catalyst. Among these the tubular geometry is even more lucrative since that architecture offers even more surface area for catalytic activities. Hence we have grown the Co_7Se_8 as ordered arrays of rods and tubes following a protocol developed by Nath et al.,[49,50] which involves confined electrodeposition in lithographically patterned nanoelectrodes on conducting substrates (see Supporting Information).

LSV plots from the nanorod and nanotube arrays were collected without further treatment. For the comparison of OER activity of nanostructure arrays with the thin films, linear sweep voltammetry (LSV) measurements were conducted in a N_2-saturated 1 M KOH solution at 5 mV s^{-1} and shown in Figure 7a. In all the examples, measured currents were normalized with the geometric area of deposited catalyst on GC electrode. For the comparison of rod- or tubular-like structure arrays with thin film, current density (mA cm^{-2}) at an overpotential of 310 mV was measured (Table 3). The Tafel plots for the tubes, rods, and thin films of Co_7Se_8 catalysts are shown in Supporting Figure S8. The observed Tafel slope of the thin film was about 44.1 mV dec^{-1}, while those of tube- and rod-like catalysts were 45.3 and 53.5 mV dec^{-1}, respectively. Stability of these nanostructured arrays was investigated through chronoamperometry studies at a potential to achieve current density of 10 mA cm^{-2}. As seen in Figure 7b, both tube- and rod-like arrays showed excellent stability to generate O_2 continuously for the period of 1 h.

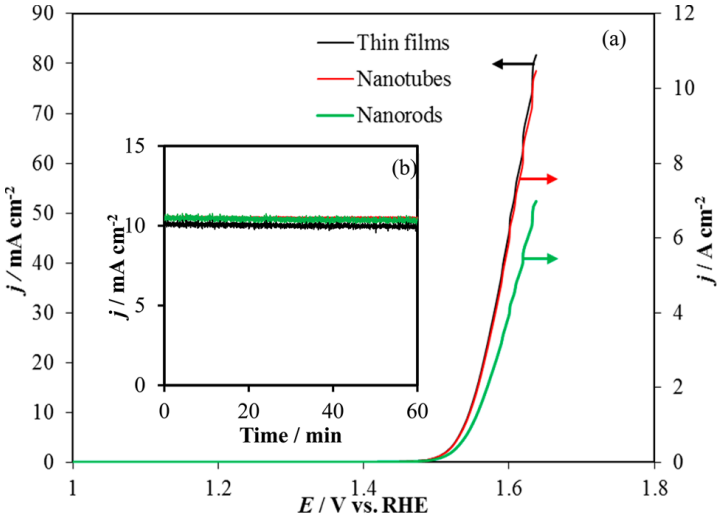

Figure 7. (a) Plots showing LSVs for Co_7Se_8 nanostructured films compared with those obtained from tubular and rod-like nanostructure arrays. All LSVs were measured in N_2-saturated 1 M KOH with a scan speed of 5 mV s^{-1}. (b) Chronoamperometry at constant potential to achieve 10 mA cm^{-2}.

Table 3. Comparison of Current Density of Different Nanostructures Arrays of Co_7Se_8.

Nanostructures	**Area of deposited catalysts, mm^2**	**Current density, mA cm^{-2} at η = 0.31 V**	**Jη=0.3, A g^{-1}**
Nanotubes	0.01	887	68,000
Nanorods	2.0	480	39,000
Thin films	19.6	10	220

The essence of using catalyst nanostructure arrays was visible on comparing the current density obtained from these catalyst surfaces while considering the actual geometric area covered by the catalysts. While for the bulk film, the entire GC electrode was covered with the catalyst film (0.196 cm^2), for the rod- and the tube-like arrays, less than 12% of the GC surface was covered with the catalyst nanostructures. The actual coverage could be calculated very precisely by considering the uniform diameter and wall thickness of the rods and tubes, respectively, and counting the total number of rods/tubes

in the patterned area. It was observed that while the nanorods covered an area approximately 1/10 of the GC electrode the nanotube arrays covered an even smaller area. The Co_7Se_8 tubular array exhibited the highest current density (880 mA cm^{-2}) at 310 mV overpotential compared to those of Co_7Se_8 rods (590 mA cm^{-2}) and thin films (10 mA cm^{-2}). Typically, the actual specific current density with the rod and tube arrays was more than 2 orders of magnitude higher than that obtained with the planar film as shown in Figure 7a. The high OER activity for the hollow Co_7Se_8 tubular structures could be also ascribed to their unique morphology as it offers high exposed surface area and a porous interior, which can confine the electrolyte and reactant leading to enhanced local concentration of the active species, thereby providing an additional impetus to accelerate the oxygen evolution reaction.

Another way to understand the usefulness of the nanostructure arrays is by comparing their mass activity through gravimetric current densities of the 3-dimensional rod and tube arrays with the planar film. As can be seen from Table 3, the rod and tube arrays show very high gravimetric current density (A g^{-1}) at specific potential compared to the thin films. Hence, such rod-like/tubular structure arrays provide the optimal geometry for further increasing catalytic efficiency while reducing material consumption.

2.2.3. Effect of Substrates on OER Activity. The effect of underlying supporting substrate of catalyst on OER catalytic activity was investigated. Figure 8 represents the OER activity of Co_7Se_8 deposited for 5 min on GC- and Au-coated glass substrates. Catalyst deposited on Au exhibited lower onset potential as well as lower overpotential to yield 10 mA cm^{-2} compared to the GC surface (260 mV for Au coated glass vs 290 mV for

GC). The effect of substrate on the OER activity was similar to that observed for Ni_3Se_2 electrocatalyst.[55]

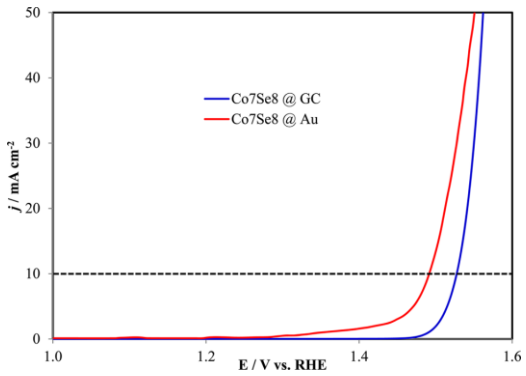

Figure 8. Current−voltage plot for Co_7Se_8 electrocatalysts deposited on different substrates (Au and GC) in N_2-saturated 1.0 M KOH solution at a scan rate of 5 mV s^{-1}.

Typically conductivity of the substrate surface as well as roughness and texturing are expected to have an effect on the charge transfer at the catalyst−electrode interface. This observation supports that the interaction between the underlying substrate and Co_7Se_8 may play a role in the OER catalytic activity.

2.3. ELECTROCHEMICAL IMPEDANCE SPECTROSCOPY MEASUREMENTS

Electrochemical impedance spectroscopy (EIS) of Co_7Se_8 catalysts electrodeposited for different times was performed in N_2-saturated 1.0 M KOH solution at 1.53 V vs RHE, and the Nyquist plots are shown in Figure 9. From the equivalent circuit of the impedance spectra (inset of Figure 9), electrolyte resistance (Rs) and the electron charge transfer resistance (Rct) could be obtained, and the values have been listed in Table 4. For all three samples the electrolyte resistance was obtained as ca. 5 Ω. This value was subsequently used for *iR* correction. The electron transfer resistance (Rct), on the other

hand, controls kinetics of the interfacial charge transfer reaction which directly relates to the OER process on the catalyst surfaces. Hence, the smaller the value of Rct, the more efficient is the OER reaction rate leading to a better catalyst.[62,63] From fitting of the equivalent circuit it was clearly observed that the Rct of catalyst synthesized at 2.5 min (419.4 Ω) was smaller than that of 5 min (458.2 Ω) and followed by 1 min (521.5 Ω), which is consistent with the electrocatalysis measurements reported above.

2.3.1. Hydrogen Evolution Reaction Catalysis. The electrocatalytic activity for cathodic HER with Co_7Se_8@GC was also assessed in N_2-saturated 1.0 M KOH solution at a scan rate of 5 mV s^{-1} and a constant rotation of 1600 rpm. As shown in Figure 10a, catalysts synthesized for 2.5 min exhibited much superior activity and required an over

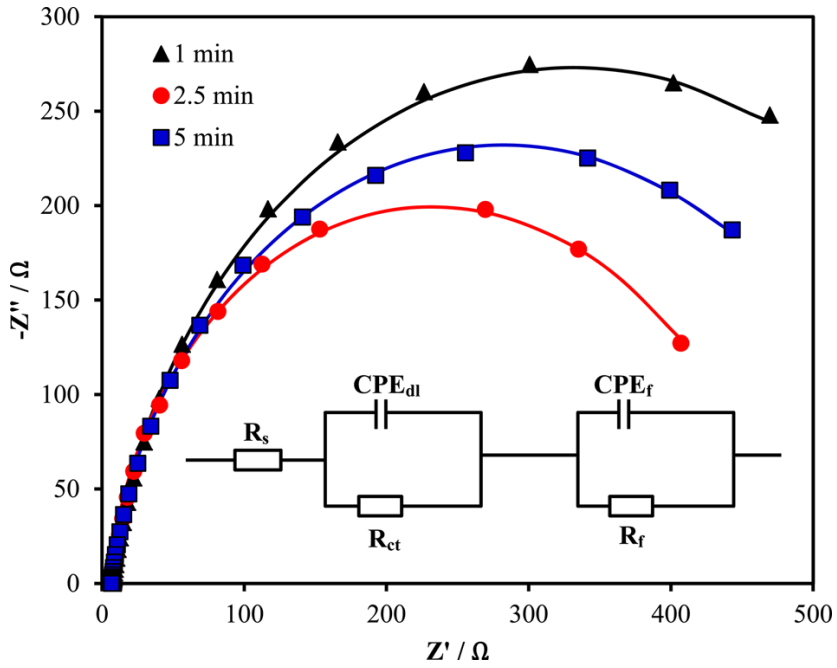

Figure 9. Nyquist plots obtained from EIS measurements at potential of 1.53 V vs RHE in N_2-saturated 1 M KOH solution. Symbols indicate the raw data, while continuous lines represent the corresponding fit to equivalent circuit model. Inset shows the equivalent circuit of catalyst. Here R_s is the resistance of the electrolyte; R_{ct} is the electron transfer resistance; CPE_{dl} is the constant phase element of double-layer nonideal capacitance; R_f is resistance of the catalyst layer; and CPE_f is the capacitance.

Table 4. Equivalent Circuit Parameters Obtained from Fitting of EIS Experimental Data.

catalysts/min	**R_s/Ω**	**R_{ct}/Ω**	**CPE_{dl}/F**	**R_f/Ω**	**CPE_f/F**
1	5.0	521.5	0.93	116.2	0.88
2.5	4.9	419.4	0.92	94.8	0.89
5	4.9	458.2	0.94	102.0	0.88

potential (HER) of 472 mV to achieve 10 mA cm^{-2} compared to the catalysts synthesized for 1 and 5 min (Table 5). The corresponding Tafel slopes of catalysts are given in Figure 10b. The observed Tafel slopes of catalysts synthesized for 1, 2.5, and 5 min were 62.9, 59.1, and 70.2 mV per decade, respectively. However, Pt requires only 59 mV to get 10 mA cm^{-2} with a small Tafel slope of 30.2 mV/dec (Supporting Figure S9). Even though the HER activity is not as efficient compared to Pt, it is still comparable and even better than other nonprecious metal-based electrocatalysts. So far this is the first report of cobalt selenide as HER electrocatalyst in alkaline solution. The comparison of HER activity of Co_7Se_8 with other electrocatalysts has been presented as Supporting Table S1.

As shown in Figure 10c, the catalyst was stable under H_2 evolution conditions for 6 h at a constant potential of -340 mV to achieve 5 mA cm^{-2} of HER current and LSV after constant potential electrolysis for 6 h exhibits higher activity from the initial as presented the inset of Figure 10c. This enhanced activity can be explained by the increased ECSA after periods of continuous H_2 evolution as was measured from double-layer capacitance (1.9 cm^2), which increases the porosity and accessibility on the catalyst surface. SEM, EDS, XRD, and XPS analyses revealed that the composition of the catalyst remained unchanged even after prolonged H_2 evolution for 6 h (Supporting Figures S6 and S7).

2.3.2. Full Water Splitting. Since it was observed that Co_7Se_8 was catalytically active for both OER and HER in alkaline electrolyte, Co_7Se_8 film deposited on Au was used as both anode and cathode in 1 M KOH electrolyte, and a current was passed between the electrodes in a simple water splitting cell setup affording 1 mA cm^{-2} at a cell voltage of 1.6 V as shown in Figure 11.

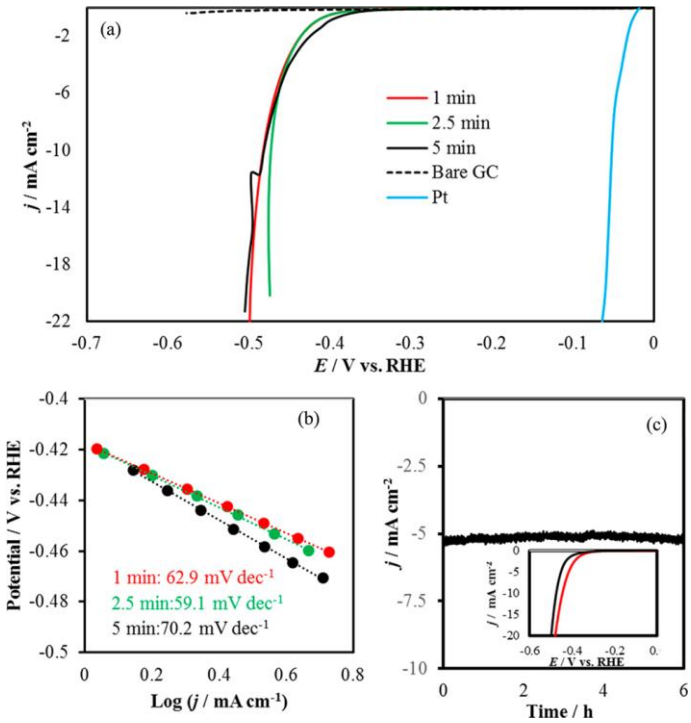

Figure 10. (a) Polarization curves for HER activity measured in 1 M KOH at a scan speed of 5 mV s^{-1} with Co_7Se_8 catalysts electrodeposited for different times. (b) Tafel plots of catalysts. (c) Chronoamperometric study for continuous H_2 evolution for 6 h at constant potential to achieve 5 mA cm^{-2}. Inset of (c) is the LSVs of catalyst synthesized for 2.5 min in N_2-saturated 1.0 M KOH before (black) and after chronoamperometry (red) for 6 h.

Table 5. Parameters for HER Catalysis in N_2-Saturated 1 M KOH.

deposition time/min	**Onset overpotential, η vs RHE**	**overpotential (η vs RHE) to achieve 10 mA cm^{-2}**	**Tafel slope, mV dec^{-1}**
1	0.327	0.481	62.9
2.5	0.317	0.472	59.1
5	0.317	0.481	70.2

It was observed that as the cell voltage reached 1.6 V hydrogen formed at the cathode, while oxygen bubbles were visible at the anode. The evolution of both these gases was very visible through rapid bubble formation at the electrodes (video provided as Supporting Information, Movie S1).

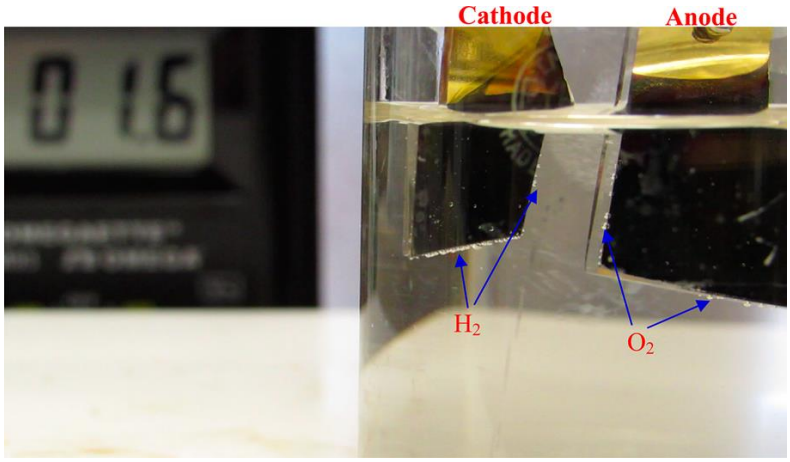

Figure 11. Full water-splitting device operating at a cell voltage of 1.6 V.

3. CONCLUSION

In summary, we have synthesized Co_7Se_8 nanostructured films and reported their activity as a bifunctional catalyst with high efficiency for full water splitting in alkaline medium. The Co_7Se_8 exhibited an excellent OER activity in 1.0 M KOH with a small overpotential of 290 mV at the current density of 10 mA cm^{-2}. Moreover, this catalyst was found to be effective for hydrogen evolution reaction in the same media. It can effectively split water at a cell voltage of 1.6 V under ambient conditions. Nanotexturing of the catalyst films by depositing them as an array of rod-like and tubular structures significantly increased the exchange current density to several A cm^{-2}, which is among the highest

current densities reported. The catalyst films were synthesized through electrodeposition, which is a reproducible, scalable, and cost-effective method. The excellent catalytic activity along with stability as well as the facile fabrication process offer promising features for potential use of this catalyst as a noble-metal-free full water-splitting catalyst in technological devices.

4. MATERIALS AND METHODS

4.1. ELECTRODEPOSITION OF Co_7Se_8

Cobalt acetate tetrahydrate [Co-$(C_2H_3O_2)_2 \cdot 4H_2O$ from Alfa Aesar], selenium dioxide (SeO_2) [Acros Chemicals], and lithium chloride (LiCl) [Aldrich] were all of analytical grade purity and were used without further purification. An interchangeable glassy carbon (GC, area 0.196 cm^2) disk was used as substrates for electrodeposition. Deionized water (18 MΩ·cm resistivity) was use to prepare all electrolytic solutions. The substrates for electrodeposition were cleaned following standard procedure as has been described in the Supporting Information. A constant potential electrodeposition at -0.80 V (vs Ag|AgCl) was carried out to deposit Co_7Se_8 on different substrates. The electrolytic bath contained 10 mM $Co(OOCCH_3)_2 \cdot 4H_2O$, 20 mM SeO_2, and 25 mM LiCl at 25 °C dissolved in water and maintained at a pH of 3.5. Impurities and any kind of surface adsorbates were removed from the electrodeposited film by washing with deionized water. The details of the characterization techniques along with instrumental details have been provided in the Supporting Information.

The thickness of the electrodeposited film can be estimated from the volume (V) of the deposit, which in turn depends on the surface area (A) and thickness (t) of the film, t = V/A. Mass (m) of the electrodeposited film can be estimated from the volume and specific density (ρ) of the deposited solid by the relationship, ρ = m/V. Thus

$t = V/A = m/A\rho$

Where A is area of electrode, 0.196 cm^2, and ρ is the density of Co_7Se_8, 7.65 g/cm^3.

4.2. ROD-LIKE AND TUBULAR ARRAYS OF CATALYST

The GC substrates for lithography were cleaned following standard procedures as has been published elsewhere.[50] The tubular patterns were prepared on GC substrate by electron beam lithography (EBL), while arrays of rod-like structures were developed by nanosphere photolithography (NPL) onto the GC substrate. Details of the lithography procedures have been published previously for CdTe,[50,51] and specific details are provided in Supporting Information. The electrodeposition of Co_7Se_8 was carried out on the lithographically modified GC electrode whereby it deposited exclusively on the exposed nanoelectrodes formed through lithographic patterning.

5. ASSOCIATED CONTENT

5.1. SUPPORTING INFORMATION

The Supporting Information is available free of charge on the ACS Publications website at DOI: 10.1021/acsami.6b04862. Details of lithography procedure and electrochemical measurements, XPS spectra of Se 3d, EDS line scan analysis of nanorod

and nanotube arrays, iR-corrected OER and HER LSV plots, SEM and EDS images after activity, Co 2p XPS spectra after OER and HER activity, and Tafel plots of tube and rod arrays for OER activity (PDF). Evolution of both gases visible through rapid bubble formation at the electrodes (AVI).

ACKNOWLEDGEMENTS

The authors would like to acknowledge American Chemical Society Petroleum Research Fund (54793-ND10) and Energy Development and Research Center (ERDC) at Missouri S&T for financial support. The authors would also like to acknowledge Materials Research Center for equipment usage and Dr. Richard Brow for help with Raman measurements.

REFERENCES

1. Walter, M. G.; Warren, E. L.; McKone, J. R.; Boettcher, S. W.; Mi, Q.; Santori, E. A.; Lewis, N. S. Solar Water Splitting Cells. Chem. Rev. 2010, 110, 6446−6473.

2. Osterloh, F. E. Inorganic Nanostructures for Photoelectrochemical and Photocatalytic Water Splitting. Chem. Soc. Rev. 2013, 42, 2294−2320.

3. Kim, D.; Sakimoto, K. K.; Hong, D.; Yang, P. Artificial Photosynthesis for Sustainable Fuel and Chemical Production. Angew. Chem., Int. Ed. 2015, 54, 3259−3266.

4. Gratzel, M. Photoelectrochemical cells. Nature 2001, 414, 338−344.

5. Jin, H.; Wang, J.; Su, D.; Wei, Z.; Pang, Z.; Wang, Y. In situ Cobalt−Cobalt Oxide/N-Doped Carbon Hybrids as Superior Bifunctional Electrocatalysts for Hydrogen and Oxygen Evolution. J. Am. Chem. Soc. 2015, 137, 2688−2694.

6. Esswein, A. J.; Nocera, D. G. Hydrogen Production by Molecular Photocatalysis. Chem. Rev. 2007, 107, 4022−4047.

7. Armaroli, N.; Balzani, V. The Future of Energy Supply: Challenges and Opportunities. Angew. Chem., Int. Ed. 2007, 46, 52−66.

8. Ma, W.; Ma, R.; Wang, C.; Liang, J.; Liu, X.; Zhou, K.; Sasaki, T. A Superlattice of Alternately Stacked Ni-Fe Hydroxide Nanosheets and Graphene for Efficient Splitting of Water. ACS Nano 2015, 9, 1977−1984.

9. Hong, W. T.; Risch, M.; Stoerzinger, K. A.; Grimaud, A.; Suntivich, J.; Shao-Horn, Y. Toward the Rational Design of Non-Precious Transition Metal Oxides for Oxygen Electrocatalysis. Energy Environ. Sci. 2015, 8, 1404−1427.

10. Tian, J.; Liu, Q.; Asiri, A. M.; Sun, X. Self-Supported Nanoporous Cobalt Phosphide Nanowire Arrays: An Efficient 3D Hydrogen-Evolving Cathode Over the Wide Range of pH 0−14. J. Am. Chem. Soc. 2014, 136, 7587−7590.

11. Lee, Y.; Suntivich, J.; May, K. J.; Perry, E. E.; Shao-Horn, Y. Synthesis and Activities of Rutile IrO_2 and RuO_2 Nanoparticles for Oxygen Evolution in Acid and Alkaline Solutions. J. Phys. Chem. Lett. 2012, 3, 399−404.

12. Jiao, F.; Frei, H. Nanostructured Cobalt Oxide Clusters in Mesoporous Silica as Efficient Oxygen-Evolving Catalysts. Angew. Chem., Int. Ed. 2009, 48, 1841−1844.

13. Park, S. A.; Lee, E. K.; Song, H.; Kim, Y. T. Bifunctional Enhancement of Oxygen Reduction Reaction Activity on Ag Catalysts Due to Water Activation on LaMnO3 Supports in Alkaline Media. Sci. Rep. 2015, 5, 13552.

14. Liang, H.; Li, L.; Meng, F.; Dang, L.; Zhuo, J.; Forticaux, A.; Wang, Z.; Jin, S. Porous Two-Dimensional Nanosheets Converted from Layered Double Hydroxides and Their Applications in Electrocatalytic Water Splitting. Chem. Mater. 2015, 27, 5702−5711.

15. Takahara, Y.; Kondo, J. N.; Lu, D.; Domen, K. Synthesis and Application for Overall Water Splitting of Transition Metal-Mixed Mesoporous Ta Oxide. Solid State Ionics 2002, 151, 305−311.

16. Jin, J.; Walczak, K.; Singh, M. R.; Karp, C.; Lewis, N. S.; Xiang, C. An Experimental and Modeling/Simulation-Based Evaluation of the Efficiency and Operational Performance Characteristics of an Integrated, Membrane-Free, Neutral pH Solar-Driven Water-Splitting System. Energy Environ. Sci. 2014, 7, 3371−3380.

17. Zhu, H.; Zhang, P.; Dai, S. Recent Advances of Lanthanum- Based Perovskite Oxides for Catalysis. ACS Catal. 2015, 5, 6370−6385.

18. Montoya, J. H.; Garcia-Mota, M.; Nørskov, J. K.; Vojvodic, A. Theoretical Evaluation of the Surface Electrochemistry of Perovskites with Promising Photon Absorption Properties for Solar Water Splitting. Phys. Chem. Chem. Phys. 2015, 17, 2634−2640.

19. Chen, W.; Wang, H.; Li, Y.; Liu, Y.; Sun, J.; Lee, S.; Lee, J. S.; Cui, Y. In Situ Electrochemical Oxidation Tuning of Transition Metal Disulfides to Oxides for Enhanced Water Oxidation. ACS Cent. Sci. 2015, 1, 244−251.

20. Zheng, Y. R.; Gao, M. R.; Yu, Z. Y.; Gao, Q.; Gao, H. L.; Yu, S. H. Cobalt Diselenide Nanobelts Grafted on Carbon Fiber Felt: an Efficient and Robust 3D Cathode for Hydrogen Production. Chem. Sci. 2015, 6, 4594−4598.

21. Zhou, W.; Wu, X. J.; Cao, X.; Huang, X.; Tan, C.; Tian, J.; Liu, H.; Wang, J.; Zhang, H. Ni_3S_2 Nanorods/Ni Foam Composite Electrode With Low Overpotential for Electrocatalytic Oxygen Evolution. Energy Environ. Sci. 2013, 6, 2921−2924.

22. Zheng, Y. R.; Gao, M. R.; Gao, Q.; Li, H. H.; Xu, J.; Wu, Z. Y.; Yu, S. H. An Effective CeO2/CoSe2 Nanobelt Composite for Electrochemical Water Oxidation. Small 2015, 11, 182−188.

23. Kibsgaard, J.; Chen, Z.; Reinecke, B. N.; Jaramillo, T. F. Engineering the Surface Structure of MoS2 to Preferentially Expose Active Edge Sites for Electrocatalysis. Nat. Mater. 2012, 11, 963−969.

24. Jasion, D.; Barforoush, J. M.; Qiao, Q.; Zhu, Y.; Ren, S.; Leonard, K. C. Low-Dimensional Hyperthin FeS_2 Nanostructures for Efficient and Stable Hydrogen Evolution Electrocatalysis. ACS Catal. 2015, 5, 6653−6657.

25. Wang, H.; Lee, H. W.; Deng, Y.; Lu, Z.; Hsu, P. H.; Liu, Y.; Lin, D.; Cui, Y. Bifunctional Non-Noble Metal Oxide Nanoparticle Electrocatalysts Through Lithium-Induced Conversion for Overall Water Splitting. Nat. Commun. 2015, 6, 7261.

26. Peng, Z.; Jia, D.; Al-Enizi, A. M.; Elzatahry, A. A.; Zheng, G. From Water Oxidation to Reduction: Homologous Ni−Co Based Nanowires as Complementary Water Splitting Electrocatalysts. Adv. Energy Mater. 2015, 5, 1402031−1402037.

27. Zhao, W.; Zhang, C.; Geng, F.; Zhuo, S.; Zhang, B. Nanoporous Hollow Transition Metal Chalcogenide Nanosheets Synthesized via the Anion-Exchange Reaction of Metal Hydroxides with Chalcogenide Ions. ACS Nano 2014, 8, 10909−10919.

28. Gao, M. R.; Lin, Z. Y.; Zhuang, T. T.; Jiang, J.; Xu, X. F.; Zheng, Y. R.; Yu, S. H. Mixed-Solution Synthesis of Sea Urchin-Like NiSe Nanofiber Assemblies as Economical Pt-Free Catalysts for Electrochemical H_2 Production. J. Mater. Chem. 2012, 22, 13662−13668.

29. Sidik, R. A.; Anderson, A. B. Co_9S_8 as a Catalyst for Electroreduction of O_2: Quantum Chemistry Predictions. J. Phys. Chem. B 2006, 110, 936−941.

30. Zhu, L.; Susac, D.; Teo, M.; Wong, K. C.; Wong, P. C.; Parsons, R. R.; Bizzotto, D.; Mitchell, K. A. R.; et al. Investigation of CoS_2- Based Thin Films as Model Catalysts for the Oxygen Reduction Reaction. J. Catal. 2008, 258, 235−242.

31. Zhou, Y. X.; Yao, H. B.; Wang, Y.; Liu, H. L.; Gao, M. R.; Shen, P. K.; Yu, S. H. Hierarchical Hollow Co_9S_8 Microspheres: Solvothermal Synthesis, Magnetic, Electrochemical, and Electrocatalytic Properties. Chem. - Eur. J. 2010, 16, 12000−12007.

32. Feng, Y. G.; He, T.; Alonso-Vante, N. In Situ Free-Surfactant Synthesis and ORR-Electrochemistry of Carbon-Supported Co_3S_4 and $CoSe_2$ Nanoparticles. Chem. Mater. 2008, 20, 26−28.

33. Vayner, E.; Sidik, R. A.; Anderson, A. B.; Popov, B. N. Experimental and Theoretical Study of Cobalt Selenide as a Catalyst for O_2 Electroreduction. J. Phys. Chem. C 2007, 111, 10508−10513.

34. Feng, Y. J.; He, T.; Alonso-Vante, N. Oxygen Reduction Reaction on Carbon-Supported $CoSe_2$ Nanoparticles in an Acidic Medium. Electrochim. Acta 2009, 54, 5252−5256.

35. Wu, G.; Cui, G. F.; Li, D. Y.; Shen, P. K.; Li, N. Carbon-Supported $Co_{1.67}Te_2$ Nanoparticles as Electrocatalysts for Oxygen Reduction Reaction in Alkaline Electrolyte. J. Mater. Chem. 2009, 19, 6581−6589.

36. Suntivich, J.; May, K. J.; Gasteiger, H. A.; Goodenough, J. B.; Shao-Horn, Y. A Perovskite Oxide Optimized for Oxygen Evolution Catalysis from Molecular Orbital Principles. Science 2011, 334, 1383− 1385.

37. Liu, Y.; Cheng, H.; Lyu, M.; Fan, S.; Liu, Q.; Zhang, W.; Zhi, Y.; Wang, C.; Xiao, W.; Wei, S.; Ye, B.; Xie, Y. Low Overpotential in Vacancy-Rich Ultrathin $CoSe_2$ Nanosheets for Water Oxidation. J. Am. Chem. Soc. 2014, 136, 15670−15675.

38. Gao, M. R.; Xu, Y. F.; Jiang, J.; Zheng, Y. R.; Yu, S. H. Water Oxidation Electrocatalyzed by an Efficient $Mn_3O_4/CoSe_2$ Nanocomposite. J. Am. Chem. Soc. 2012, 134, 2930−2933.

39. Carim, A. I.; Saadi, F. H.; Soriaga, M. P.; Lewis, N. S. Electrocatalysis of the Hydrogen-Evolution Reaction by Electrodeposited Amorphous Cobalt Selenide Films. J. Mater. Chem. A 2014, 2, 13835−13839.

40. Liu, T.; Liu, Q.; Asiri, A. M.; Luo, Y.; Sun, X. Amorphous CoSe Film Behaves as an Active and Stable Full Water Splitting Electrocatalyst Under Strongly Alkaline Conditions. Chem. Commun. 2015, 51, 16683−16686.

41. Callejas, J. F.; Read, C. G.; Popczun, E. J.; McEnaney, J. M.; Schaak, R. E. Nanostructured Co_2P Electrocatalyst for the Hydrogen Evolution Reaction and Direct Comparison with Morphologically Equivalent CoP. Chem. Mater. 2015, 27, 3769−3774.

42. Chen, Y.; Sun, K.; Audesirk, H.; Xiang, C.; Lewis, N. S. A Quantitative Analysis of the Efficiency of Solar-Driven Water-Splitting Device Designs Based on Tandem Photoabsorbers Patterned with Islands of Metallic Electrocatalysts. Energy Environ. Sci. 2015, 8, 1736−1747.

43. Wallentin, J.; Anttu, N.; Asoli, D.; Huffman, M.; Aberg, I.; Magnusson, M. H.; Siefer, G.; Kailuweuit, F. P.; Dimroth, F.; Witzigmann, B.; Xu, H. Q.; Samuelson, L.; Deppert, K.; Borgstrom, M. T. InP Nanowire Array Solar Cells Achieving13.8% Efficiency by Exceeding the Ray Optics Limit. Science 2013, 339, 1057−1060.

44. Krogstrup, P.; Jørgensen, H. I.; Heiss, M.; Demichel, O.; Holm, J. V.; Aagesen, M.; Nygard, J.; Morral, A. F. Single Nanowire Solar Cells Beyond the Shockley-Queisser Limit. Nat. Photonics 2013, 7, 306−310.

45. Song, J. M.; Zhang, S. S.; Yu, S. H. Multifunctional $Co_{0.85}Se$-Fe_3O_4 Nanocomposites: Controlled Synthesis and Their Enhanced Performances for Efficient Hydrogenation of p -Nitrophenol and Adsorbents. Small 2014, 10, 717−724.

46. Jiang, Q.; Hu, G. $Co_{0.85}Se$ Hollow Nanoparticles as Pt-Free Counter Electrode Materials for Dye-Sensitized Solar Cells. Mater. Lett. 2015, 153, 114−117.

47. Campos, C. E. M.; de Lima, J. C.; Grandi, T. A.; Machado, K. D.; Drago, V.; Pizani, P. S. Hexagonal CoSe Formation in Mechanical Alloyed $Co_{75}Se_{25}$ Mixture. Solid State Commun. 2004, 131, 265−270.

48. Campos, C. E. M.; de Lima, J. C.; Grandi, T. A.; Machado, K. D.; Pizani, P. S. Structural Studies of Cobalt Selenides Prepared by Mechanical Alloying. Phys. B 2002, 324, 409−418.

49. Mishra, S.; Nath, M. Growth of Vertically Aligned CdTe Nanorod Arrays Through Patterned Electrodeposition. Nano Energy 2013, 2, 1207−1213.

50. Liyanage, W. P. R.; Wilson, J. S.; Kinzel, E. C.; Durant, B. K.; Nath, M. Fabrication of CdTe Nanorod Arrays Over Large Area Through Patterned Electrodeposition for Efficient Solar Energy Conversion. Sol. Energy Mater. Sol. Cells. 2015, 133, 260−267.

51. Liyanage, W. P. R.; Mishra, S.; Wilson, J. C.; Kinzel, E.; Nath, M. Patterned Electrodeposition of CdTe Nanorod and Nanotube Arrays for Solar Cells. Nanomater. Energy 2014, 3, 167−176.

52. Liyanage, W. P. R.; Nath, M. Growth of Ordered Nanostructure Arrays including Nanotubes and Nanorods for High Efficiency Solar Cells. ECS Trans. 2015, 66, 1−7.

53. McCrory, C. C. L.; Jung, S.; Peters, J. C.; Jaramillo, T. F. Benchmarking Heterogeneous Electrocatalysts for the Oxygen Evolution Reaction. J. Am. Chem. Soc. 2013, 135, 16977−16987.

54. Asnavandi, M.; Suryanto, B. H. R.; Zhao, C. Controlled Electrodeposition of Nanostructured Pd Thin Films from Protic Ionic Liquids for Electrocatalytic Oxygen Reduction Reactions. RSC Adv. 2015, 5, 74017−74023.

55. Swesi, A.; Masud, J.; Nath, M. Nickel Selenide as High-Efficiency Catalyst for Oxygen Evolution Reaction. Energy Environ. Sci. 2016, 9, 1771−1782.

56. Trotochaud, L.; Ranney, J. K.; Williams, K. N.; Boettcher, S. W. Solution-Cast Metal Oxide Thin Film Electrocatalysts for Oxygen Evolution. J. Am. Chem. Soc. 2012, 134, 17253−17261.

57. Gong, M.; Li, Y.; Wang, H.; Liang, Y.; Wu, J. Z.; Zhou, J.; Wang, J.; Regier, T.; Wei, F.; Dai, H. An Advanced Ni−Fe Layered Double Hydroxide Electrocatalyst for Water Oxidation. J. Am. Chem. Soc. 2013, 135, 8452−8455.

58. Lv, X.; Zhu, Y.; Jiang, H.; Yang, Y.; Liu, Y.; Su, Y.; Huang, J.; Yao, Y.; Li, C. Hollow Mesoporous $NiCo_2O_4$ Nanocages as Efficient Electrocatalysts for Oxygen Evolution Reaction. Dalton Trans. 2015, 44, 4148−4154.

59. Song, F.; Hu, X. Ultrathin Cobalt−Manganese Layered Double Hydroxide Is an Efficient Oxygen Evolution Catalyst. J. Am. Chem. Soc. 2014, 136, 16481−16484.

60. Song, F.; Hu, X. Exfoliation of Layered Double Hydroxides for Enhanced Oxygen Evolution Catalysis. Nat. Commun. 2014, 5, 4477.

61. Gao, R. R.; Cao, X.; Gao, Q.; Xu, Y. F.; Zheng, Y. R.; Jiang, J.; Yu, S. H. Nitrogen-Doped Graphene Supported $CoSe_2$ Nanobelt Composite Catalyst for Efficient Water Oxidation. ACS Nano 2014, 8, 3970−3978.

62. Meng, Y.; Song, W.; Huang, H.; Ren, Z.; Chen, S. Y.; Suib, S. L. Structure−Property Relationship of Bifunctional MnO_2 Nanostructures: Highly Efficient, Ultra-Stable Electrochemical Water Oxidation and Oxygen Reduction Reaction Catalysts Identified in Alkaline Media. J. Am. Chem. Soc. 2014, 136, 11452−11464.

63. Gao, Y.; Li, H.; Yang, G. Amorphous Nickel Hydroxide Nanosheets with Ultrahigh Activity and Super-Long-Term Cycle Stability as Advanced Water Oxidation Catalysts. Cryst. Growth Des. 2015, 15, 4475−4483.

SUPPORTING INFORMATION

COBALT SELENIDE NANOSTRUCTURES: AN EFFICIENT BIFUNCTIONAL CATALYST WITH HIGH CURRENT DENSITY AT LOW COVERAGE

Jahangir Masud, Abdurazag T. Swesi, Wipula, P. R. Liyanage, and Manashi Nath

Department of Chemistry, Missouri S&T, Rolla, MO 65409.

1. CHARACTERIZATIONS

1.1. POWDER X-RAY DIFFRACTION

Powder X-ray diffraction (PXRD) of the as-synthesized films were obtained using a Philips X-Pert diffractometer with CuKα (1.5418Å) radiation. The PXRD was collected at grazing angle incidence in thin film geometry (GI mode with Göbel mirrors).

1.2. SCANNING ELECTRON MICROSCOPY (SEM)

A FEI Helios NanoLab 600 FIB/FESEM operating at 10 kV accelerating voltage with a working distance of 4.5 mm was used to obtain **s**canning electron microscopy (SEM) images, energy dispersive X-ray analysis (EDX) spectroscopy and the elemental mapping.

1.3. X-RAY PHOTOELECTRON SPECTROSCOPY (XPS)

X-ray Photoelectron Spectroscopy (XPS) was performed by using a KRATOS AXIS 165 X-ray Photoelectron Spectrometer using mono-chromatic Al X-ray source. The spectra were collected *as is* and after sputtering with Ar for 2 min which removes approximately 2 nm from the surface. Calibration of binding energy was carried out by setting the binding energy of C 1s peak to 284.5 eV.

1.4. RAMAN SPECTRA

Raman spectra from the as-deposited films were obtained from Horiba Jobin Yvon Lab Raman Aramis model using a He-Ne laser. The laser power was maintained at 1.7 mW/cm^2 over a range of 100 – 2000 cm^{-1}. A typical spectra was iterated over at least 25 scans.

1.5. ELECTROCHEMICAL MEASUREMENTS

All the electrochemical measurements were carried out with an electrochemical workstation (IvumStat potentiostat) in a standard three-electrode cell with Ag|AgCl and Pt mesh as the reference electrode and counter electrode, respectively. A glassy carbon (GC) rotating disk electrode (RDE) acted as the working electrode. OER and HER measurements were conducted in 1 M KOH as the electrolyte, which was saturated with nitrogen during the experiments. The LSVs were performed at a scanning rate of 5 mV s^{-1} while electrode was rotating at 1600 rpm.

In this study, we used Ag|AgCl|KCl($_{sat.}$) as the reference electrode in all measurements. This reference electrode was calibrated by measuring open circuit potential (OCP, -0.199V) at Pt wire in pure H_2 saturated 1.0 M H_2SO_4 solution. Potentials measured *vs* Ag|AgCl electrode were converted to a reversible hydrogen electrode (RHE) on the basis of Nernst Equation as follows.

$$E_{\mathrm{RHE}} = E_{\mathrm{Ag|AgCl}} + 0.059\mathrm{pH} + E^{\mathrm{o}}_{\mathrm{Ag|AgCl}}$$

Where E_{RHE} is the converted potential vs. RHE.

$E_{\mathrm{Ag|AgCl}}$ is the experimentally measured potential against Ag|AgCl reference electrode. $E^{o}_{\mathrm{Ag|AgCl}}$ is the standard potential of Ag|AgCl at 25 ^{o}C (0.199 V).

1.5.1. Cleaning of GC Electrode. Prior to the electrodeposition, a bare GC electrode (5mm in diameter, 0.2196 cm^2 of geometric surface area) was mechanically polished to produce a clean GC surface. Electrode was polished with alumina slurry (0.05 µm) with the help of a polishing microcloth until to get the mirror like surface. To remove the slurries, the electrode was washed ultrasonically in DI water for 15 min.

2. ELECTRODEPOSITION OF RuO_2 ON GC[S1]

Electrodeposition of RuO_2 on GC substrate was carried out from a mixture of $RuCl_3$ (0.452 g) and KCl (2.952 g) in 40 ml of 0.01M HCl by using cyclic voltammetry from 0.015 to 0.915 V (vs. Ag|AgCl) for 100 cycles at a scan rate of 50 mV s^{-1}. Finally heated at 200 ^{o}C for 3 h in presence of Air.

3. QUALITATIVE ANALYSIS OF THE EVOLVED GAS

RRDE experiment was carried out with Pt as the ring electrode and GC-Co_7Se_8 as the disk electrode to confirm the composition of the evolved gas where O_2 produced at disk electrode (anode) was reduced at Pt ring electrode. The Pt ring electrode was maintained at a constant potential of 0.2 V (*vs*. RHE) which is sufficient to reduce O_2, and the ring current was monitored as a function of applied disk potential. The electrolyte was purged with N_2 for 30 min to get rid of any dissolved O_2 and blanketed with N_2 atmosphere during measurements.

4. ELECTROCHEMICAL MEASUREMENTS

4.1. FARADAIC EFFICIENCY

RRDE technique was employed to calculate the Faradaic efficiency of deposited Co_7Se_8 catalyst where GC and Pt were used as a disk and ring electrode, respectively following standard procedures. The collection efficiency, N (0.24), of the rotating ring-disk electrode was determined by the ratio of ring and disk current in 0.001M $K_3Fe(CN)_6$ containing 1M of KOH. Prior to RRDE measurement, N_2 gas was purged in the cell for 30 min and then blanketed with N_2 during the experiment. Co_7Se_8 was deposited at interchangeable GC disk electrode for 2.5 min at -0.8 V (vs. Ag|AgCl). Pt ring was polished with Alumina slurry (0.05µm), washed and sonicated in DI water for 5 min. Before the measurements, Pt ring was electrochemically cleaned in N_2 saturated 0.5 M H_2SO_4 until to get the reproducible

characteristic CVs of Pt. The disk electrode was held at the open circuit potential of OER where no Faradaic process occurs, while the Pt ring electrode was maintained at 0.2 V vs RHE to get the background current of the ring electrode. The background ring current was lower than 20 μA. Then, the voltage of disk electrode was held at several definite potentials in the OER kinetic region for 30 sec, while, the ring current was recorded at 0.2 V vs. RHE.

4.2. TURNOVER FREQUENCY (TOF)

The turnover frequency (TOF) was calculated from the following Equation (S1):

$$\text{TOF} = \frac{I}{4 \times F \times M} \quad \text{(S1)}$$

Where *I* is the current in Amperes, *F* is the Faraday constant and *M* is number of moles of the active catalyst.

4.3. TAFEL PLOTS

The Tafel slope was calculated from the following Equation.

$$\eta = a + \frac{2.3\,RT}{\alpha nF} log(j) \quad \text{(S2)}$$

Where η is the overpotential, j is the current density and the other symbols have their usual meanings.

The Tafel Equation as shown (S2) is a fundamental Equation which is acquired from the kinetically control region of OER / HER, and relates the overpotential η with the current density j where the Tafel slope is given by 2.3RT/αnF. To calculate Tafel slopes, LSV plots were obtained with slow scan speed (2 mV s^{-1}) in non-stirred solution.

4.3.1. Nanostructuring of Electrode by Lithography. E-Beam Lithography (EBL): For the development of tubular pattern on the glassy carbon (GC) substrate by EBL, the e-beam resist was prepared by spin coating two layers of polymethylmethacrylate (PMMA, 495k mol. wt. followed by 950k) polymer on GC. First PMMA layer (mol. wt. 495K) was spin coated, baked for 3 minutes on a hotplate at 180^{o}C, and allowed to cool to room temperature before coating the second PMMA layer (mol. wt. 950K). Substrate was again baked for 3 minutes on a hotplate at 180^{o}C and allowed to cool to room temperature. As prepared resist layer had a thickness of approximately 300 nm. These PMMA layers were selectively exposed to the electron beam through image-guided pattern writing in the EBL process. After that the exposed area of the polymer could be removed by dipping the substrate in methyl isobutyl ketone (MIBK) - isopropyl alcohol (IPA) (1:3 v/v) mixture for 55 seconds, while unexposed polymer remained intact. During this pattern development process, the underlying GC was exposed through the shell-like nanoholes defined by EBL thus forming confined nanoelectrodes on the substrate.

Nanosphere Photolithography (NPL): Arrays of rod-like structures was developed by Nanosphere Photolithography (NPL) onto GC substrate. Spin coating was used to deposit 450 nm of S-1805 (positive tone photoresist) onto the substrates (5000 rpm for 1 min) and baked at 115 ^{o}C for 90s. A solution of polystyrene nanospheres (10% by weight of 1.7 μm polystyrene microspheres which was mixed with a 1:400 Triton X-100 to methanol surfactant solution in 7:1 volume ratio) was then spin-coated onto the surface. During spin coating, the nanospheres self-assemble onto the surface of the photoresist to form a hexagonal close-packed lattice. The photoresist was exposed by illuminating the nanospheres with UV light from an i-line mask aligner for 0.7s at10 mW/cm^2. Following

exposure the photoresist was developed in MF-319 developer solution for 30s and rinsed in DI water, before hard baking at145 ^{o}C for 30 min. During the development process the microspheres were washed away along with the exposed photoresist leaving the hole array pattern in the photoresist, with open channels to the GC layer.

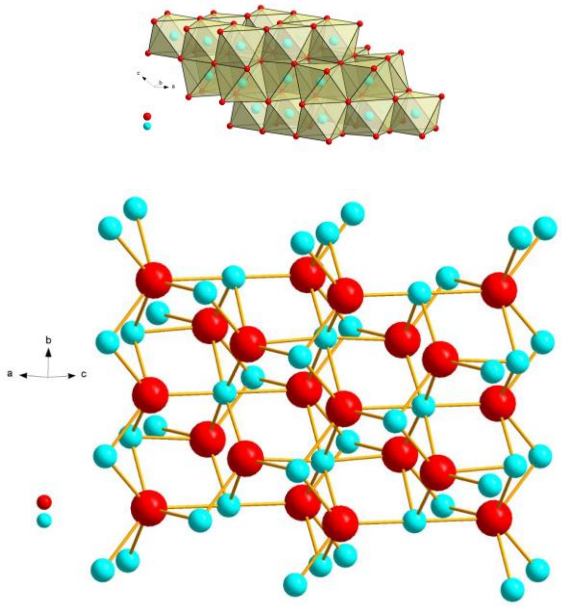

Figure S1. Crystal structure of Co_7Se_8 showing polyhedral view (top) and ball-and-stick model (bottom).

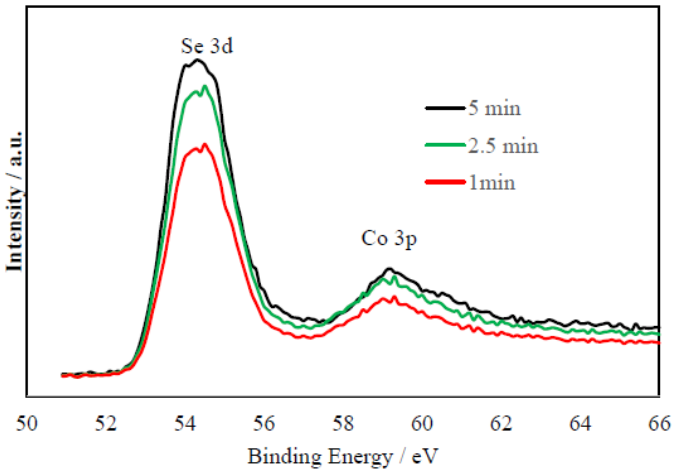

Figure S2. XPS spectra of Se 3d and Co 3p of Co_7Se_8/GC

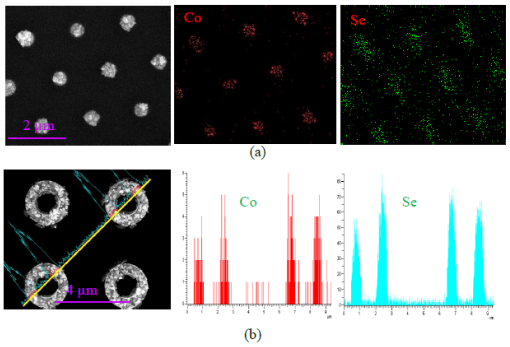

Figure S3. EDS elemental mapping of nanorods (a) and line scan of nanotube (b).

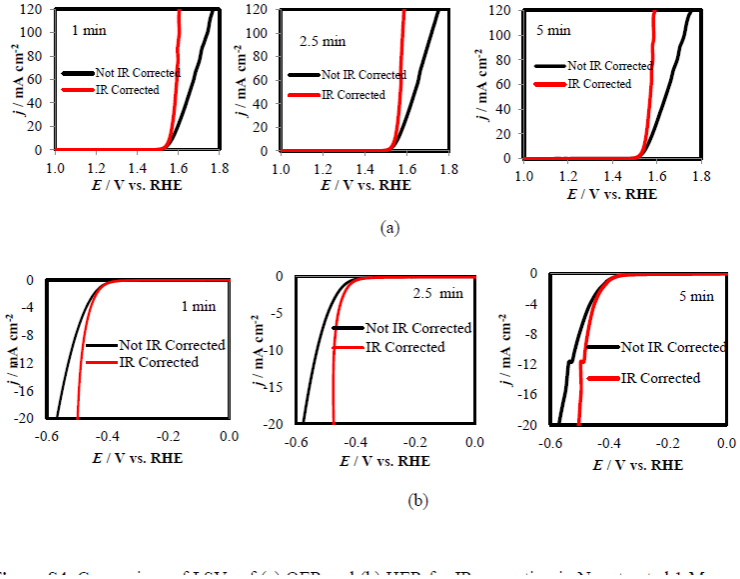

Figure S4. Comparison of LSVs of (a) OER and (b) HER for IR correction in N_2 saturated 1 M KOH solution.

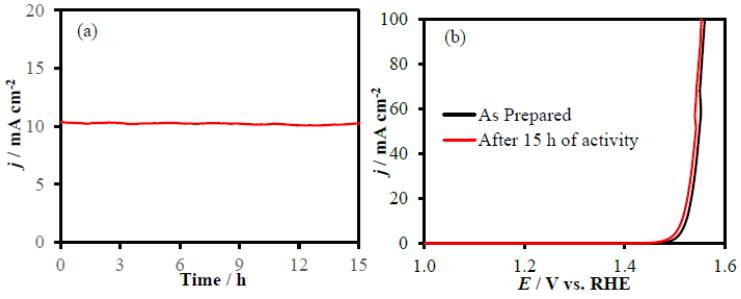

Figure S5. Extended OER stability of catalyst (a) and (b) comparison of LSVs of the catalyst before and after OER.

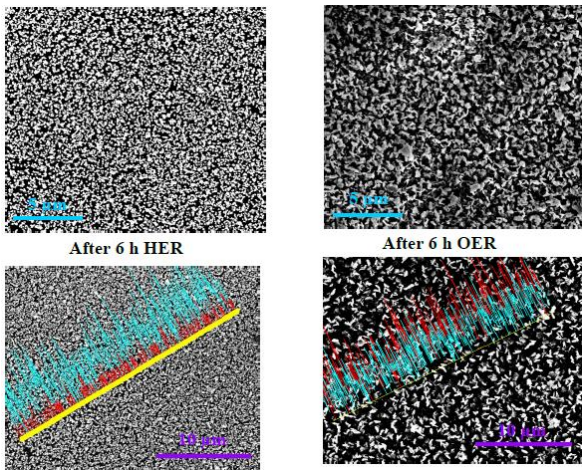

After 6 h HER After 6 h OER

Figure S6. SEM images and EDS line scans of catalyst after 6 h of HER and OER.

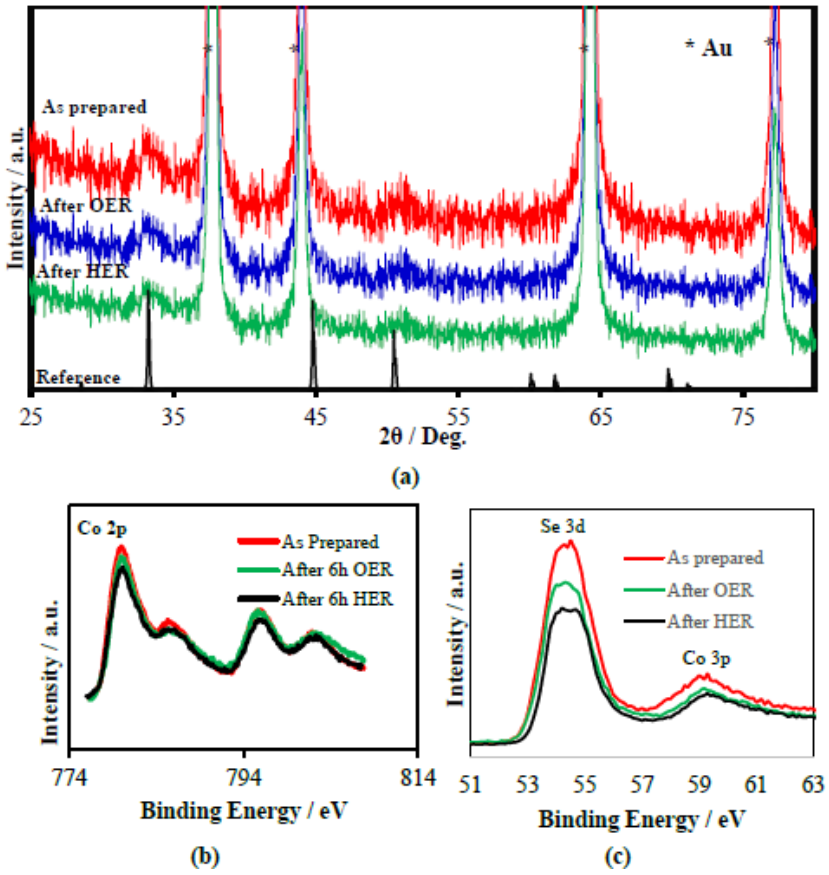

Figure S7. Comparison of (a) XRD; (b) Co 2p XPS and (c) Se 3d XPS spectra of the catalyst before and after 6 h of HER and OER.

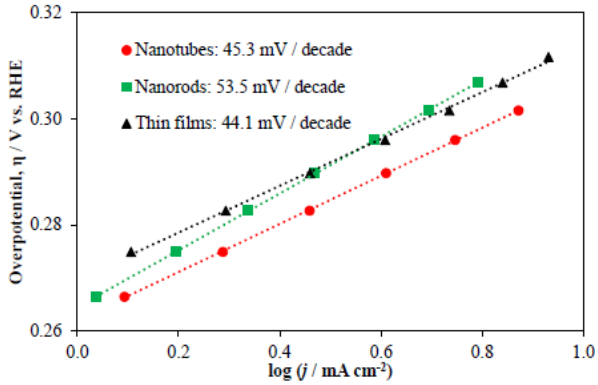

Figure S8. Tafel plots of tubes, rods and thin films of Co_7Se_8 for OER.

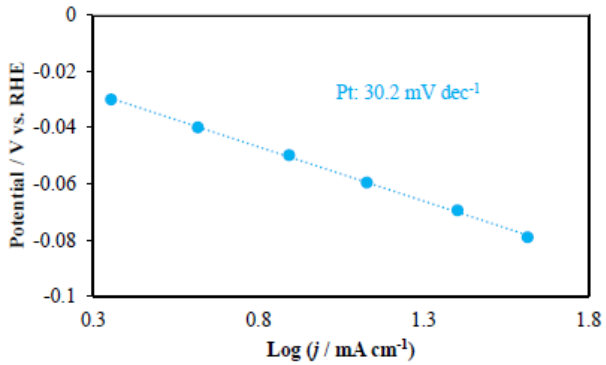

Figure S9. Tafel plot of Pt for HER.

4.3.2. Calculation The Mass Of Catalyst Deposited On GC. According to the Faraday's second law of electrolysis, the amount of a material deposited on an electrode is proportional to the amount of electricity used. Thus from the electrodeposition curve, the mass of catalyst can be calculated as-

Mass = (Molecular weight of cobalt selenide X Charge)/ (No. of electron involved in process X Faraday Constant)

Here, we can get the total charge from the deposition curve at constant potential (-0.8 V vs. Ag|AgCl). As selenium cation (Se^{4+}) is electrochemically reduced to Se^{2-}, thus the number of electron involved in the process is 6.

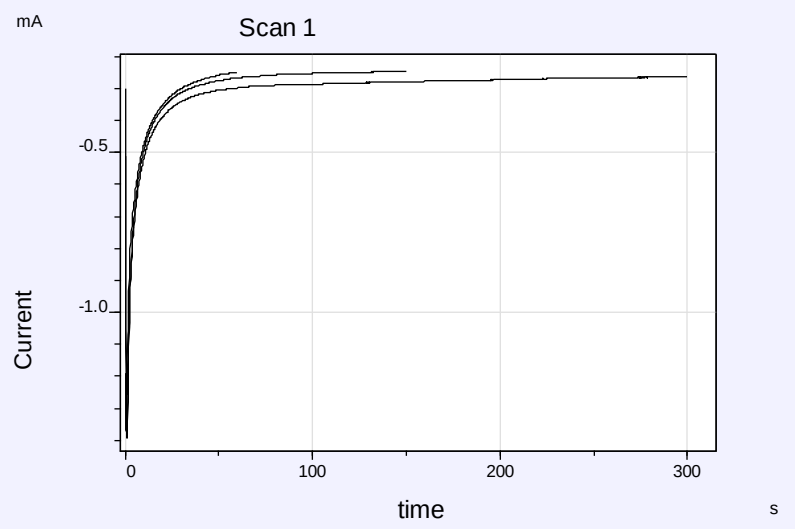

Figure S10. Electrodeposition curve for cobalt selenide.

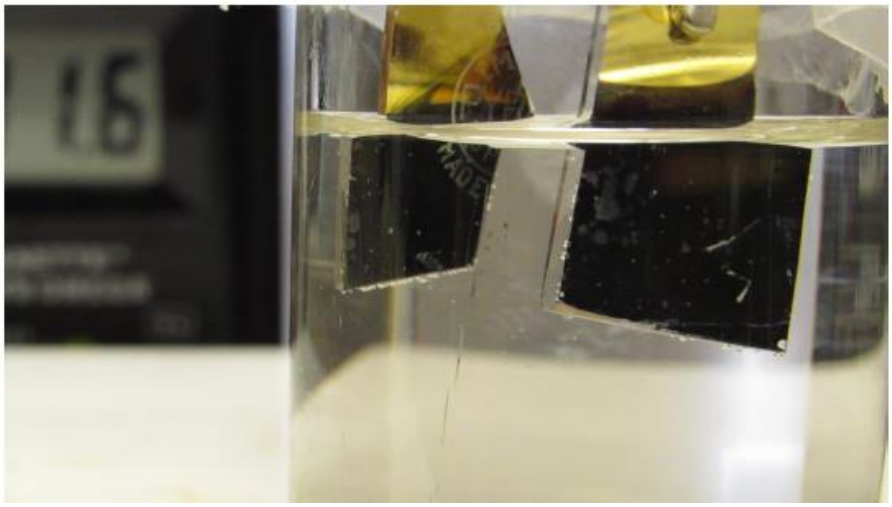

Figure S11. Movie for the full water splitting at 1.6 V.

Table S1. Comparison of HER Activity Data for Different Catalysts.

Catalyst	**Electrolyte**	**Onset, mV**	**η to achieve 10 mA cm^{-2} /Mv**	**Tafel slopes, mV dec^{-1}**	**Ref.**
NiMo(a)	H_2 sat.- 1.0 M NaOH	-	50	-	S1
CoNiFe	H_2 sat.- 1.0 M NaOH	-	250	-	
MoS	H_2 sat.- 1.0 M NaOH	-	490	-	
$CoSe_2$ nanowire on Carbon fiber paper	H_2 sat.- 0.5 M H_2SO_4	-	165 mV	34	S2
P-$CoSe_2$-300 ^{0}C	H_2 sat.- 0.5 M H_2SO_4	70	150 mV	32	S3
Amorphous CoSe	H_2 sat.- 0.5 M H_2SO_4	110	135	62	S4
$CoSe_2$ NP-CP	H_2 sat.- 0.5 M H_2SO_4	90	139	41	S5
$NiSe_2$ –CP	H_2 sat.- 0.5 M H_2SO_4	110	147	50.1	
CoP-Carbon cloth	H_2 sat.- 1.0 M KOH	115	209	129	S6
NiS_2-GS	H_2 sat.- 1.0 M NaOH	110	190	80	S7
Mn_1Ni_1	H_2 sat.- 0.1 M KOH	150	360	-	S8
$Mn_{0.1}Ni_1$	H_2 sat.- 0.1 M KOH	150	420	-	
Co_7Se_8-GC	**N_2 sat.- 0.1 M KOH**	**317**	**476**	**59.1**	

REFERENCES

S1. McCrory, C.C.L.; Jung, S.; Ferrer, I.M.; Chatman, S.M.; Peters, J.C.; Jaramillo, T.F. Benchmarking Hydrogen Evolving Reaction and Oxygen Evolving Reaction Electrocatalysts for Solar Water Splitting Devices. *J. Am. Chem. Soc*. **2015**, *137*, 4347−4357.

S2. Wang, K.; Xi, D.; Zhou, C.; Shi, Z.; Xia, H.; Liu, G.; Qiao, G. $CoSe_2$ necklace-like nanowires supported by carbon fiber paper: a 3D integrated electrode for the hydrogen evolution reaction, *J. Mater. Chem. A* **2015**, *3*, 9415 – 9420.

S3. Zhang, H.; Yang, B.; Wu, X.; Li, Z.; Lei, L.; Zhang, X. Polymorphic $CoSe_2$ with Mixed Orthorhombic and Cubic Phases for Highly Efficient Hydrogen Evolution Reaction. *ACS Appl. Mater. Interfaces* **2015**, *7*, 1772−1779.

S4. Carim, A. I.; Saadi, F. H.; Soriaga, M. P.; Lewis, N. S.Electrocatalysis of the hydrogen-evolution reaction by electrodeposited amorphous cobalt selenide films, *J. Mater. Chem. A* **2014**, *2*, 13835–13839.

S5. Kong, d.; Wang, H.; Lu, Z.; Cui, Y. $CoSe_2$ Nanoparticles Grown on Carbon Fiber Paper: An Efficient and Stable Electrocatalyst for Hydrogen Evolution Reaction. *J. Am. Chem. Soc.* **2014**, *136*, 4897−4900.

S6. Shi, Y.; Zhang, B. Recent advances in transition metal phosphide nanomaterials: synthesis and applications in hydrogen evolution reaction. *Chem. Soc. Rev.* **2016**, *45*, 1529-1541.

S7. Wu, X.; Yang, B.; Li, Z.; Lei, L.; Zhang, X. Synthesis of supported vertical NiS2 nanosheets for hydrogen evolution reaction in acidic and alkaline solution. *RSC Adv.* **2015**, *5*, 32976–32982.

S8. Ledendecker, M.; Clavel, G.; Antonietti, M.; Shalom, M. Highly Porous Materials as Tunable Electrocatalysts for the Hydrogen and Oxygen Evolution Reaction. *Adv. Funct. Mater.* **2015**, *25*, 393–399.

V. $CoNi_2Se_4$ AS AN EFFICIENT BIFUNCTIONAL ELECTROCATALYST FOR OVERALL WATER SPLITTING

Chem. Commun., 2017, **53**, 5412-5415

Bahareh Golrokh Amin, Abdurazag T. Swesi, Jahangir Masud, and Manashi Nath

Department of Chemistry

Missouri University of Science and Technology

Rolla, Missouri 65409-0050 USA

Email: nathm@mst.edu

ABSTRACT

$CoNi_2Se_4$ with vacancy-ordered spinel structure-type shows excellent bifunctional electrocatalytic activity for water splitting in alkaline medium producing 10 mA cm^{-2} at a cell voltage of 1.61 V. For OER, an overpotential of 160 mV was needed for 10 mA cm^{-2} which is one of the lowest overpotential reported till date.

1. INTRODUCTION

Water electrolysis has taken a center stage in the recent quest for alternative sustainable energy, since this provides clean energy with minimal environmental impact.[1,2] Water splitting comprises of both oxygen evolution reaction (OER) and hydrogen evolution reaction (HER).[3-6] In fact, this is one of the most promising approach to produce pure molecular hydrogen,[7-12] an ideal fuel with high energy density and excellent energy

conversion efficiency with zero CO_2 emission.[8,13] However, the kinetically sluggish four electron oxygen evolution reaction limits rate of water electrolysis at low applied potentials.[14-16] A well-designed OER electrocatalyst can lower the applied potential and hence can expedite the overall process.[17] Although OER catalysts have been over-represented with noble metal based composition such as IrOx and RuOx, recently,[18,19] there has been a lot of progress in non-precious metal based OER electrocatalysts. Of these the selenide based OER electrocatalysts has made quite an impact due to their superior performance in terms of lowering the overpotential and increased current density.[17,20-26] Mixed metal selenides are expected to show better catalytic activity due to possibilities of charge delocalization between the metal cations through *d-d* overlap within the crystalline lattice thereby increasing the Lewis acidity and subsequently the adsorption rate of the hydroxyl species on the catalyst surface. It is also believed that high electrical conductivity for electron delocalization between cations with mixed valence could offer facile donor-acceptor chemisorption sites for reversible adsorption of oxygen.[27] Accordingly, Ni-Co-oxides have outperformed the OER catalytic activity of Ni-oxides.[27-31] In the mixed metal chalcogenides family also transition metal doped chalcogenides have shown efficient OER catalytic activity in alkaline medium.[32,33] However, efficient OER catalytic activity in ordered ternary selenides with well-defined stoichiometry is still rare. In this communication, we have reported the OER catalytic activity of $CoNi_2Se_4$ for the first time, which shows an overpotential of 160 and 210 mV at 10 and 50 mA cm^{-2}, respectively, which represents one of the lowest overpotentials reported till date. Beside the excellent OER catalytic activity, $CoNi_2Se_4$ also shows efficient HER catalytic activity exhibiting an overpotential of only 220 mV to deliver 10 mA cm^{-2}. The potential required for overall

water splitting with this bifunctional catalyst was estimated at 1.61 V at 10 mA cm^{-2}. Previously, Nickel cobalt based oxide and sulfide have been reported for OER catalytic activity albeit with higher overpotential.[32-38] However, this is the first report of bifunctional catalytic activity of spinel type vacancy-ordered $CoNi_2Se_4$. Even in its pristine state $CoNi_2Se_4$ outperforms any other ternary selenides OER electrocatalysts known till date. $CoNi_2Se_4$ was synthesized by electrodeposition on various conducting substrates including carbon fiber paper (CFP) as well as Au-coated glass. Growing the catalytic films directly by electrodeposition offers the advantage of producing binder and other additive-free films, which can thus utilize the catalyst's full potential. The as-grown films were characterized through scanning electron microscopy (SEM), powder X-ray diffraction (pxrd), and X-ray photoelectron spectroscopy (XPS) to confirm their structure and morphology, while the OER and HER catalytic activities were studied through electrochemical measurements. Details of the synthesis procedure, sample preparation and instrumental details has been provided as supporting information. The composition of the electrodeposited film was confirmed with pxrd as shown in (Figure 1a) which revealed that the film was indeed crystalline and the diffraction peaks matched with the standard diffraction pattern of $CoNi_2Se_4$ (JCPDS No: 04-006-5239).

SEM image of the electrodeposited film showed that it was a granular, rough film with nanoflakes-like morphology (Figure 1b) and there was uniform coverage on the substrate. As can be seen from the SEM image, the nanoflakes were quite thin (~50 nm) and randomly oriented providing a high surface area for the film. Elemental composition analyzed from energy dispersive Xray spectroscopy (EDS) confirmed that the film was

indeed composed of Ni, Co, and Se (Figure S1) with an approximate elemental ratio of 2:1:4 (Ni:Co:Se).

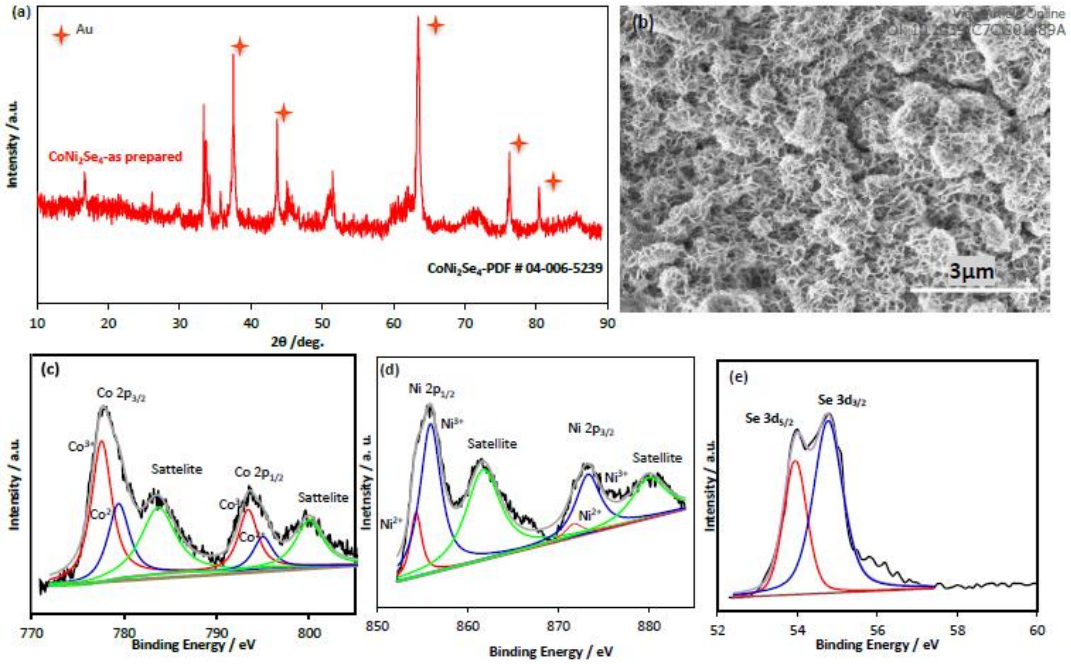

Figure 1. (a) Pxrd pattern of the electrodeposited film confirming formation of $CoNi_2Se_4$. (b) SEM image of the as-synthesized film showing formation of nanoflakes. Deconvoluted XPS spectra of (c) Co2p (d) Ni 2p and (e) Se 3d collected from as-synthesized catalyst.

TEM studies also confirmed the nanostructured morphology of the electrodeposited film (Figure S2a), while SAED pattern revealed crystalline nature of the nanoparticle ensemble (Figure S2b). The chemical composition of the electrodeposited film was further characterized by X-ray photoelectron spectroscopy, XPS. All binding energies for Ni, Co and Se were calibrated with respect to the C 1s (284.5 eV) as a reference binding energy. The chemical composition and oxidation state of catalyst has been investigated from the deconvoluted XPS spectra, and the corresponding results are presented in (Figure 1c-e). The deconvoluted Ni 2p and Co 2p confirmed the presence of mixed valence of metal ions

which might play a significant role on their catalytic activity.[39] As shown in (Figure 1c), the binding energies at around 777.6 and 794.2 eV of Co 2p are assigned to Co^{3+} and at 780.2 and 795.5 eV is attributed to Co^{2+} with its shake-up satellite peak at 785.2 and 800.5 eV.[40,41] Similarly, in Figure 1d the Ni 2p spectra, the peaks at 854.3 and 871.8 eV correspond to Ni^{2+} while 856.1 and 873.3 eV corroborates with Ni^{3+}.[42,43] For the Se 3d XPS spectrum in Figure 2e, peaks at 54.0 and 54.9 eV corresponding to Se 3d5/2 and Se 3d3/2, respectively, which were comparable with the binding energies commonly observed in the transition metal selenides.[44] The approximate percentage of variable oxidation states of Co^{2+}/ Co^{3+} and Ni^{2+} / Ni^{3+} were calculated from the area of deconvoluted spectra corresponding to Co 2p and Ni 2p peaks (Figures 1c and 1d). It was found that as prepared catalyst contained 10% of Co^{3+}, 20% of Co^{2+} and 14% of Ni^{2+}, 56% of Ni^{3+}.

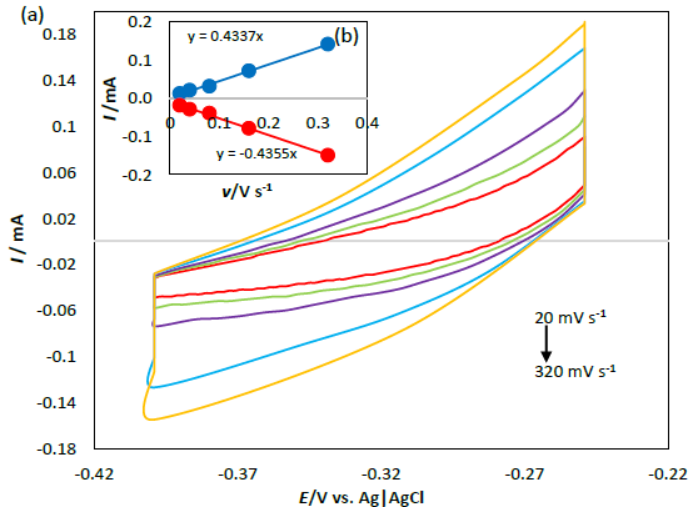

Figure 2. (a) CV measured for $CoNi_2Se_4$ catalyst in N_2 saturated 1.0 KOH solution at different scan rates. (b) Anodic and cathodic current measured at -0.32 V as a function of scan rates.

Accordingly the composition of the film can be written as $Co_{1-x}Ni_x(Ni_{2-y}Coy)Se_4$ where x= 0.4 and y = 0.3. The vacancy ordered spinel structures are generally represented

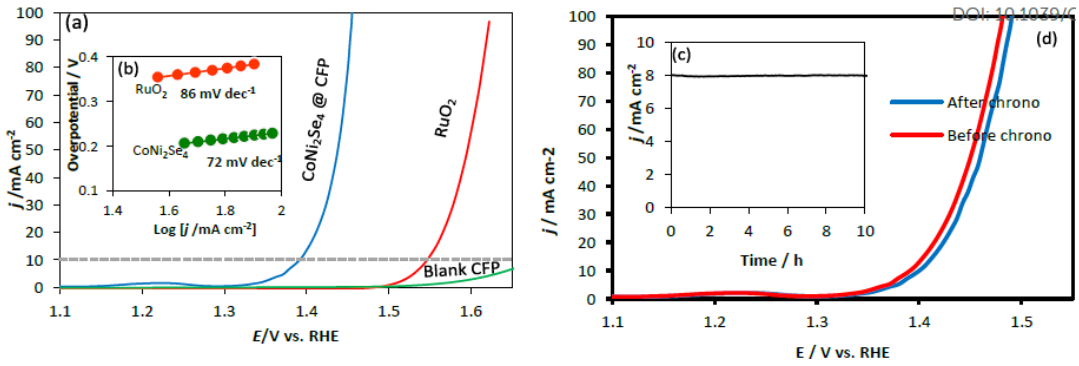

Figure 3. (a) LSV curves of $CoNi_2Se_4$ and RuO_2 in 1 M KOH at scan rate of 10 mV s^{-1} for OER. (b) Tafel plots of $CoNi_2Se_4$@CFP and RuO_2. (c) Chronoamperometry plot for $CoNi_2Se_4$ for 10 h at 1.38 V applied potential. (d) Comparison of LSVs before and after 10 h stability in 1 M KOH.

as AB_2Se_4 where *A* is a divalent cation while *B* is a trivalent cation.[45] However, frequently it has been observed that there can be cation substitution both in the divalent and trivalent sites leading to mixed valence of both cations.[46] It seems that in the present case, there is substantial mixing both in *A* and the *B* sites with Ni^{3+} predominantly occupying the *B* site while the *A* site is predominantly occupied by Co^{2+}. There is nominal substitution of Ni^{2+} in the *A* site and Co^{3+} in the *B* site. It must be noted here that this is one of the few examples of Ni-containing OER catalysts which contains Ni^{3+} in the nascent state, while in other reported catalysts, the Ni^{3+} is generated *in situ* through a precatalytic oxidation state.

The electrocatalytic activity of $CoNi_2Se_4$ was measured in 1 M KOH utilizing a three electrodes cell, with Pt as the counter, Ag|AgCl as reference, and $CoNi_2Se_4$ as working electrode. The electrocatalytic activity was investigated through linear scan voltammetry (LSV), while the catalyst stability was estimated from constant voltage chronoamperometry measurement. Electrochemically active surface area (ECSA) as shown in Figure 2 was determined by measuring the double layer charging current at different scan rates following procedure reported elsewhere[20] and given in supporting

information. For comparison, RuO_2, was also electrodeposited and the electrocatalytic activity was performed in the same solution. All the plots have been shown after *iR* correction.

The OER polarization plot of $CoNi_2Se_4$ electrode measured in 1 M KOH solution at a scan rate of 10 mV s has been shown in Figure 3a. As can be seen from the LSV plot, $CoNi_2Se_4$ was indeed active for OER and showed a low onset potential of 1.34 V *vs* RHE. For $CoNi_2Se_4$, the current density increased very rapidly and 50 mA cm^{-2} was achieved at an overpotential of 210 mV indicating superior catalytic activity over RuO_2 (360 mV at 10 mA cm^{-2}). This overpotential is one of the lowest values that has been reported in Ni-based chalcogenide systems for OER activity (see Table ST1 in supporting information). In order to study the effect of substrate, OER catalytic activity of $CoNi_2Se_4$ on different substrates [Au-glass, carbon fiber paper (CFP), carbon cloth (CC)] was measured as shown in Figure S3. It can be observed that, $CoNi_2Se_4$ showed comparable activity in all the substrates with the best being on carbon fiber paper (CFP) possibly due to the porous nature and high surface area of the substrate. High OER catalytic activity of $CoNi_2Se_4$ was also confirmed form Tafel plot which showed a modest slope of 72 mV $decade^{-1}$ as shown in Figure 3b. Stability of the catalyst for extended period of time under the operational conditions, is a crucial factor to evaluate the practical usability of the catalyst. Chronoamperometric measurement where the potential was held constant at 1.38 V *vs* RHE to achieve a current density of 8.0 mA cm^{-2}, was performed to estimate the stability of the catalyst for 10 h. As can be seen from Fig. 3c, the current density was more or less constant for 10 h with more than 95% of the initial current being preserved and the loss was negligible. These results indicate that the catalytic activity of $CoNi_2Se_4$ was preserved for extended hours of

operation in N_2 saturated 1.0 M KOH. Stability of the catalyst was also confirmed by re-measuring the catalytic activity after 10 h of chronoamperometric study, which showed no change in the onset potential and overpotential (Figure 3d). The compositional stability of catalyst after 10 h of chronoamperometry was also demonstrated by the pxrd pattern which showed presence of only $CoNi_2Se_4$ and no other peaks corresponding to free metals or their oxides (Figure S4). EDS analysis (after stability, Figure S5 confirmed the overall compositional stability of catalyst. The composition of the postcatalytic activity sample was also confirmed through XPS which showed no change in the Ni, Co and Se binding energies (Figure S6). Electrocatalytic activity of $CoNi_2Se_4$ for hydrogen evolution reaction (HER) at the cathode in an alkaline electrolyte was also investigated. It was observed that $CoNi_2Se_4$ showed decent catalytic activity for HER in N_2-staurated 1 M KOH

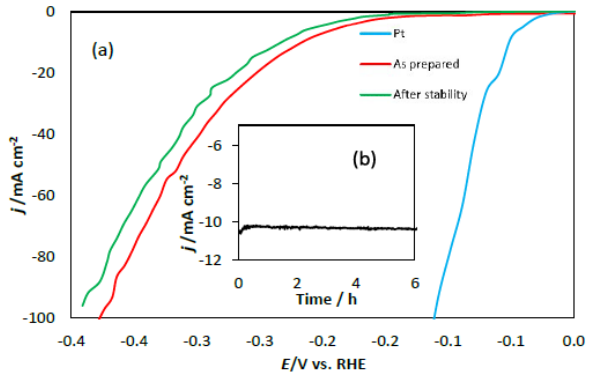

Figure 4. (a) LSV curves for $CoNi_2Se_4$@Au/glass and Pt in 1.0 M KOH at scan rate of 10 mV s^{-1} for HER (b) Chronoamperometry at -0.23 V (vs RHE) for continuous HER in 1.0 M KOH for 6 h.

as shown in Figure 4a. LSV for $CoNi_2Se_4$ showed an overpotential of 220 mV for achieving cathodic current density of 10 mA cm^{-2}. The stability of the catalyst was checked under continuous operation for 6 h (Figure 4b) at an applied potential of -0.23 V *vs* RHE. As can be seen from the chronoamperometry plot, there was minimal variation in the current

density, and the LSV plot showed almost similar behavior before and after chronoamperometry.

In summary, the bifunctional catalytic activity of electrodeposited $CoNi_2Se_4$ nanoflakes for OER and HER has been reported for the first time. The simple one-step synthesis by electrodeposition of stoichiometric $CoNi_2Se_4$ enables reproducibility and scalability. Detailed electrochemical measurements revealed superior catalytic activity of $CoNi_2Se_4$ for both OER and HER where only 160 and 220 mV overpotential was required to achieve 10 mA cm^{-2} (OER and HER, respectively). The observed overpotential for OER is one of the lowest that has been reported till date. Based on compositional analysis, it can be inferred that the presence of Ni^{3+} in the assynthesized catalyst composition has a positive influence in reducing the overpotential for oxygen evolution to a very low value. $CoNi_2Se_4$ can be applied as both anode and cathode catalysts in a full water electrolysis system, and it requires a potential of only 1.61 V to deliver a current density of 10 mA cm^{-2} through overall water splitting. The catalyst showed high functional and compositional stability for extended period of time which is a necessary parameter for evaluation of an electrocatalyst. $CoNi_2Se_4$ exposed new path for exploration of using mixed transition metal selenide nanostructures, specifically those containing Ni^{3+}, as economical and efficient bifunctional catalyst for overall water splitting.

REFERENCES

1. N. S. Lewis, G. Crabtree, A.J. Nozik, M.R. Wasielewski and P. Alivisatos, *Basic Research Needs for Solar Energy Utilization, Report of Department of Energy*, USA, 2005.

2. M. G. Walter, E. L. Warren, J. R. McKone, Shannon W. Boettcher, Q. Mi, E. A. Santori, and N. S. Lewis, *Chem. Rev.*, 2010, **110**, 11.

3. Q. Yin, J. M. Tan, C. Besson, Y. V. Geletii, D. G. Musaev, A. E. Kuznetsov, Z. Luo, K. I. Hardcastle, and C. L. Hill, *Science*, 2010, **328**, 328.

4. M. W. Kanan, D. G. Nocera, *Science*, 2008, **321**, 1072.

5. D. Merki and X. Hu, *Energy Environ. Sci*., 2011, **4**, 3878.

6. H. B. Gray, *Nat. Chem*., 2009, **1**, 7.

7. J. A. Turner, *Science*, 2004, **305**, 972.

8. Y. Zheng, Y. Jiao, M. Jaroniec, and S. Qiao, *Angew*. *Chem*. *Int. Ed*., 2015, **54**, 52.

9. H. Wang, H. W. Lee, Y. Deng, Z. Lu, P. C. Hsu, Y. Liu, D. Lin, and Y. Cui, *Nat. Commun*, 2015, **6**, 7261.

10. X. Zhang, H. Xu, X. Li, Y. Li, T. Yang, and Y. Liang, *ACS Catal*. 2016, **6**, 580.

11. X. Lv, Y. Zhu, H. Jiang, X. Yang, Y. Liu, Y. Su, J. Huang, Y. Yao, and C. Li, *Dalton Trans*, 2015, **44**, 4148.

12. L. Kuai, J. Geng, C. Chen, E. Kan, Y. Liu, Q. Wang, and B. Geng, *Angew. Chem. Int. Ed*, 2014, **53**, 7547.

13. M. G. Walter, E. L. Warren, J. R. McKone, S. W. Boettcher, Qixi Mi, E. A. Santori, and N. S. Lewis, *Chem. Rev*, 2010, **110**, 6446.

14. F. Lin, S. W. Boettcher, *Nat*. *Mater*., 2014, **13**, 81.

15. K. Zeng, D. Zhang, *Prog. Energy Combust. Sci*., 2010, **36**, 307.

16. Y. Liu, H. Cheng, M. Lyu, S. Fan, Q. Liu, W. Zhang, Y. Zhi, C. Wang, C. Xiao, S. Wei, B. Ye and Y. Xie, *J. Am. Chem. Soc*., 2014, **136**, 15670.

17. I. H. Kwak, H. S. Im, D. M. Jang, Y. W. Kim, K. Park,Y. R. Lim, E. H. Cha, and J. Park, *ACS Appl. Mater. Interfaces*, 2016, **8**, 5327.

18. J. Tian, Q. Liu, A. M. Asiri, and X. Sun, *J. Am. Chem. Soc*., 2014, **136**, 7587.

19. Y. Lee, J. Suntivich, K. J. May, E. E. Perry, and Y. Shao-Horn, *J. Phys. Chem. Lett.*, 2012, **3**, 399.

20. A. T. Swesi, J. Masud, and M. Nath, *Energy Environ. Sci.*, 2016, **9**, 1771.

21. J. Masud, A. T. Swesi, W. P. R. Liyanage and M. Nath, *ACS Appl. Mater. Interfaces*, 2016, **8**, 17292.

22. J. Masud, P. Ioannou, N. Levesanos, P. Kyritsis and M. Nath, *ChemSusChem*, 2016, **9**, 3123.

23. D. Kong, H. Wang, Z. Lu and Y. Cui, *J. Am. Chem. Soc*. ,2014, **136**, 4897.

24. X. Xu, P. Du, Z. Chen, and M. Huang, *J. Mater. Chem. A*, 2016, **4**, 10933.

25. Z. Wang, J. Li, X. Tian, X. Wang, Y. Yu, K. A. Owusu, L. He and L. Mai, *ACS Appl. Mater. Interfaces*. 2016, **8**, 19386.

26. X. Xu, F. Song and X. Hu, *Nat. commun.* 2016, **7**, 12324.

27. M. Hamdani, R. Singh and P. Chartier, *Int. J. Electrochem. Sci.*, 2010, **5**, 556.

28. F. Basharat, U. A. Rana, M. Shahida and M. Serwara, *RSC Adv*., 2015, **5**, 86713.

29. Q. Dong, C. Sun, Z. Dai, X. Zang and X. Dong, *ChemCatChem*, 2016, **8**, 3484.

30. Z. Zhang, S. Liu, F. Xiao and S. Wang, *ACS Sustainable Chem. Eng*., **2017**, 5 ,529.

31. J. Liang, Y.Z. Wang, C.C. Wang and S.Y. Lu, *J. Mater. Chem. A*, 2016, **4**, 9797.

32. Z. Peng, D. Jia, A. M. Al-Enizi, A. A. Elzatahry and G. Zheng, *Adv. Energy Mater*, 2015, **5**, 1402031.

33. D. Liu, Q. Lu, Y. Luo, X. Sun and A. M. Asiri, *Nanoscale*, 2015, **7**, 15122.

34. Q. Liu, J. Jin and J. Zhang, *ACS Appl. Mater. Interfaces*, 2013, **5**, 5002.

35. A. Sivanantham, P. Ganesan and S. Shanmugam, *Adv. Funct. Mater.* 2016, ***26***, 4661.

36. J. Yin, P. Zhou, L. An, L. Huang, C. Shao, J. Wang, H. Liua and P. Xi, *Nanoscale*, 2016, **8**, 1390-1400.

37. X. Gao, H. Zhang, Q. Li, X. Yu, Z. Hong, X. Zhang, C. Liang and Z. Lin, Angew, *Chem. Int. Ed.*, 2016, **55**, 6290.

38. H. Cheng, Yu-Zhi Su, P. Kuang, Gao-Feng Chen, and Zhao-Qing Liu, *J. Mater. Chem. A*, 2015, **3**, 19314.

39. M. Gao, Y. Xu, J. Jiang, Y. Zheng and S. Yu, *J. Am. Chem. Soc*., 2012, **134**, 2930.

40. C. Jin, F. Lu, X. Cao, Z. Yang and R. Yang, *J Mater Chem A*, 2013, **1**, 12170.

41. T. Z. Su, Q. Z. Xu, G. F Chen, H. Cheng, N. Li and Z. Q. Liu, *Electrochim Acta*, 2015, **174**, 1216.

42. H. Shi, G. Zhao, *J. Phys. Chem. C*, 2014, **118**, 25939.

43. E. Umeshbabu, G. Rajeshkhanna, P. Justin and G. Ranga Rao, *RSC Adv*, 2015, **5**, 66657.

44. A. B. Mandale, S. Badrinarayanan, S. K. Date and A. P. B. Sinha, *J. Electron Spectrosc. Relat. Phenom.*1984, **33**, 61.

45. A. Hayashi, K. Imada, K. Inoue, Y. Ueda, K. Kosuge, *Bull. Inst. Chem. Res*., Kyoto Univ. 1986, **64**, 186.

46. W. Hu, R. Chen, W. Xie, L. Zou, N. Qin and D. Bao, *ACS Appl. Mater. Interfaces*, 2014, **6**, 19318.

SUPPORTING INFORMATION

$CoNi_2Se_4$ AS AN EFFICIENT BIFUNCTIONAL ELECTROCATALYST FOR OVERALL WATER SPLITTING

Bahareh Golrokh Amin, Abdurazag T. Swesi, Jahangir Masud, and Manashi Nath

Department of Chemistry, Missouri University of Science and Technology, Rolla, MO 65409.

1. EXPERIMENTAL & METHODS

Materials were reagent grade and were used as received without further purification. Nickel acetate tetrahydrate [Ni $(C_2H_4O_2)_2.4H_2O$ from J. T. Baker chemical company, USA and cobalt acetate tetrahydrate [$Co(C_2H_4O_2)_2.4H_2O$ from Alfa Aesar, SeO_2 [Acros Chemicals] and lithium chloride (LiCl) [Aldrich] were used. Au-coated glass slide (purchased from Deposition Research Lab Incorporated (DRLI), Lebanon, Missouri) and Carbon fiber paper (CFP) and Carbon cloth (CC) (purchased from Fuel cells Etc company, college station, Texas) were used as substrates in electrodeposition.

2. ELECTRODEPOSITION OF $CoNi_2Se_4$

The electrolytes were prepared using analytical grade reagents and deionized (DI) water with a resistivity of 18 MΩ·cm. Prior to electrodeposition, Au / glass substrates were cleaned by ultrasonic treatment in micro-90 detergent followed by rinse with isopropanol for three times and eventually rinsed with deionized water (15 min each step) to ensure clean surface. Au-coated glass was covered with a Teflon tape, leaving an exposed

geometric area of 0.283 cm^2, and connected as the working electrode. An IviumStat potentiostat was used to control the electrodeposition process and to monitor the current and voltage profiles. $NiCo_2Se_4$ was electrodeposited on the substrate by a controlled-potential deposition at -0.8 V (vs Ag/AgCl) at room temperature from an aqueous solution containing 10 mM Ni $(C_2H_4O_2)_2.4H_2O$, 25 mM Co $(C_2H_4O_2)_2.4H_2O$ and 40 mM SeO_2. The pH of the electrolytic bath was adjusted to ~ 2.5 with dilute HCl. After each electrodeposition, the electrodeposited films were washed with deionized water in order to remove impurities and adsorbents from the surface.

3. ELECTROCHEMICAL MEASUREMENTS

Oxygen and hydrogen (OER and HER) evolution reaction was performed in 1M KOH solution by using Iviumstat. Ag|AgCl|KCl (sat.) and Pt mesh were using as reference and counter electrode, respectively. The measured potential *vs.* the Ag/AgCl was converted to the reversible hydrogen electrode (RHE) *via* the Nernst Equation (1).

$$E_{RHE} = E_{Ag|AgCl} + 0.059pH + E^{o}_{Ag|AgCl} \quad (1)$$

Where E_{RHE} is the converted potential vs. RHE, $E_{Ag|AgCl}$ is the experimentally measured potential against Ag|AgCl reference electrode, and $E^{o}_{Ag|AgCl}$ is the standard potential of Ag|AgCl at 25 ^{0}C (0.199 V).

4. SURFACE CHARACTERIZATIONS

4.1. SEM and EDS

A FEI Helios Nanolab 600 FIB/FESEM at an acceleration voltage of 10 kV and a working distance of 5.0 mm was employed to obtain SEM image of the modified electrode surfaces. Energy dispersive spectroscopy (EDS) accompanied by line scan analysis was also acquired from the SEM microscope.

4.2. XRD

The product was characterized through powder X-ray diffraction (pxrd) with Philips X-Pert utilizing CuKα (1.5418Å) radiation. Pxrd pattern was collected from the pristine product with no further treatments. Because the product formed a very thin layer on the substrate, the pxrd was collected at grazing angles in thin film geometry (GI mode with Göbel mirrors).

4.3. XPS

KRATOS AXIS 165 X-ray Photoelectron Spectrometer using monochromatic Al X-ray source was used for all XPS measurements of the catalyst.

4.4. ELECTROCHEMICALLY ACTIVE SURFACE AREA (ECSA)

The ECSA of the $NiCo_2Se_4$ can be determine by measuring the double layer charging current at different scan rates following here.

$$ECSA = C_{DL}/C_s \quad (2)$$

Where C_s is the specific capacitance (0.040 mF cm^{-2}) in N_2 saturated 1 M KOH solution. C_s is the specific capacitance which is reported in a range between 0.022 to 0.130 mF cm^{-2} in alkaline solutions.[S1] Here, the value of 0.040 mF cm^{-2} was used based on previously reported Ni-based OER catalysts.[S1]

C_{DL} was calculated as a slope of the plot of capacitive current (i_{DL}) from a non-faradaic double-layer region against scan rate v (V s^{-1}). The ECSA was measured to be 10.8 cm^2 on CFP.

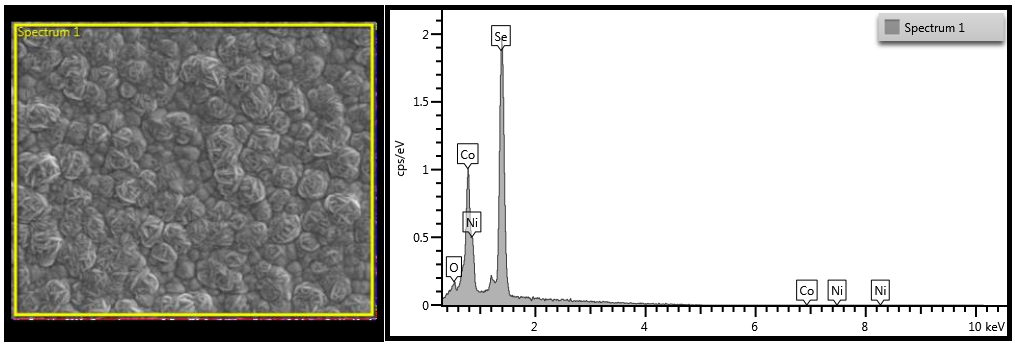

Figure S1. Elemental analysis of as prepared CoNi2Se4 by using EDS

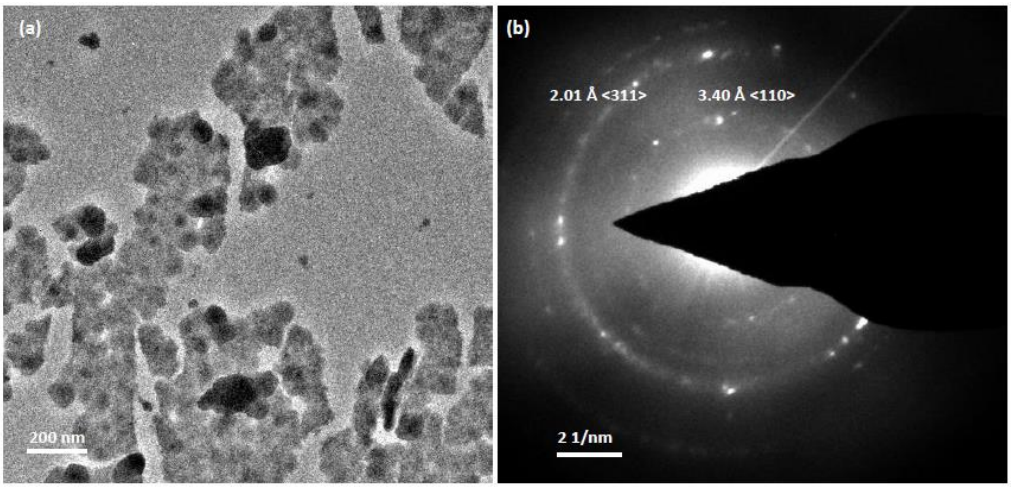

Figure S2. TEM image (a) and SAED pattern (b) of CoNi2Se4 catalyst.

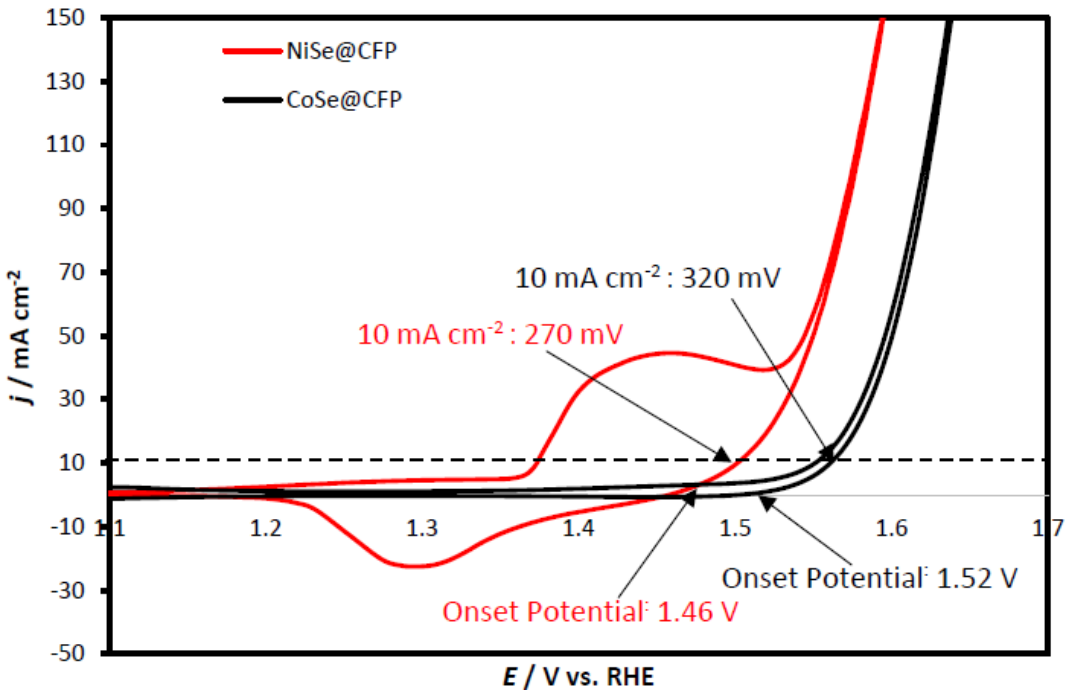

Figure S3. OER catalytic activity of NiSe and CoSe on CFP in N2 saturated 1M KOH solution.

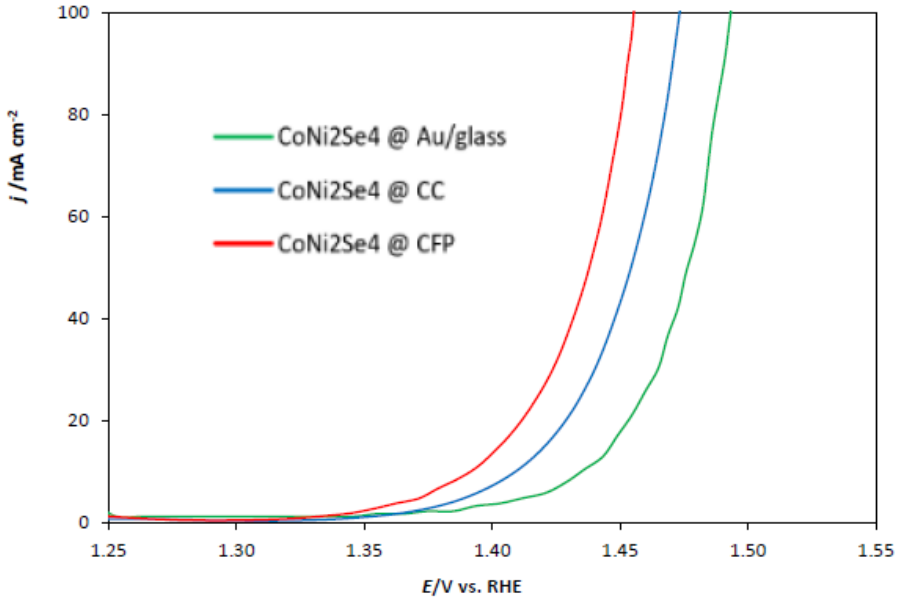

Figure S4. Comparison of OER catalytic activity of CoNi2Se4 grown on different substrates. All measurements were done in 1M KOH solution.

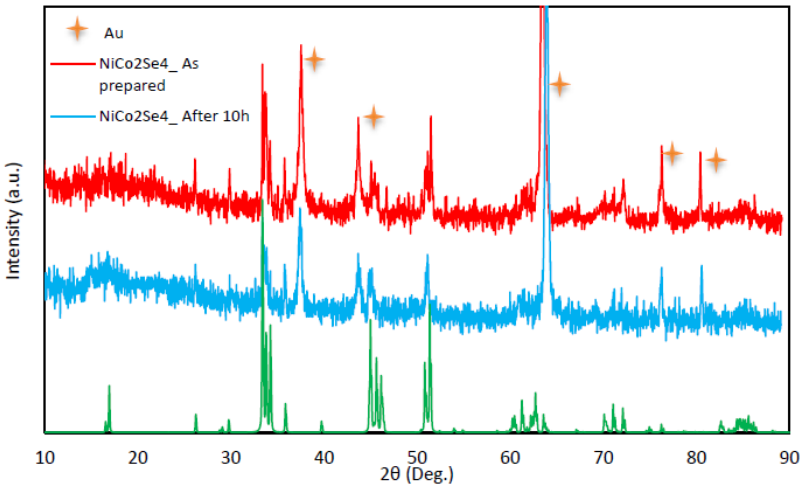

Figure S5. Comparison of pxrd before and after chronoamperometry.

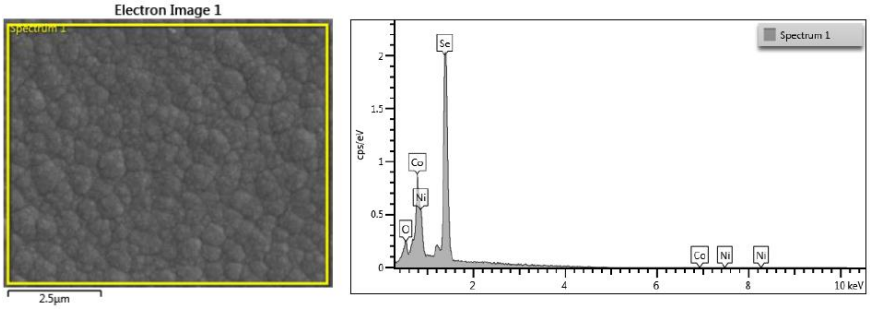

Figure S6. EDS analysis after 10h of chronoamperometry.

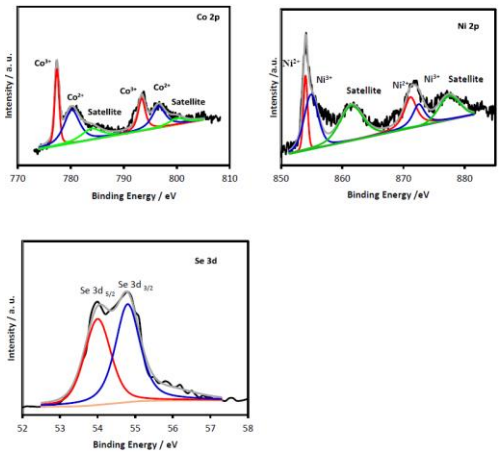

Figure S7. Comparison of XPS (Ni 2p, Co 2p and Se 3d) before and after Chronoamperometry for 10h.

ST1. Comparison of OER activity of the $NiCo_2Se_4$@ C.P. with recently reported catalysts.

Electrocatalyst	**Catalyst Loading**	**Electrolyte**	**Overpotential (mV *vs.* RHE) @ 10[a], 20[b] or 50[c] mA cm^{-2}**	**Reference**
$CoNi_2Se_4$@CFP	**4.7 mg cm^{-2}**	**1 M KOH**	**160[a], 210[c]**	**This work**
$NiCo_2S_4$@graphene	-	0.1 M KOH	470[a]	S2
$NiCo_2S_4$ NA/CC	4.0 mg cm^{-2}	1 M KOH	340 mV (100 mA cm^{-2})	S3
$NiCo_2S_4$ NW/NF	-	1 M KOH	260[a]	S4
$NiCo_2O_4$ hollow microcuboids	~1 mg cm^{-2}	1 M NaOH	290[a]	S5
Ni-Co-O@Ni-Co-S NA	-	1 M KOH	300[b]	S6
$NiCo_2O_4$	-	1 M KOH	391[b]	S7
(a-CoSe/Ti)	3.8 mg cm^{-2}	1 M KOH	292[a]	S8
$Co_{0.85}Se$	-	1 M KOH	324[a]	S9
$(Ni,CO)_{0.85}Se$	-	1 M KOH	255[a]	S9
$Co_{0.13}Ni_{0.87}Se_2$/Ti	1.67 mg cm^{-2}	1 M KOH	320 mV (100 mA cm^{-2})	S10
$NiSe_2$ /Ti		1 M KOH	350 mV (100 mA cm^{-2})	S10
$NiSe_2$	1 mg cm^{-2}	1 M KOH	250[a]	S11
$CoSe_2$	1 mg cm^{-2}	1 M KOH	430[a]	S11
NiS/ Ni foam	-	1 M KOH	335[c]	S12
Ni_3Se_2/Cu foam	-	1 M KOH	343[c]	S13
CoSe/Ti mesh	3.8 mg cm^{-2}	1 M KOH	341[c]	S14
Fe-doped NiSe	4.8 mg cm^{-2}	1 M KOH	264 mV (100 mA cm^{-2})	S15
$Ni(OH)_2$	142 μg cm^{-2}	1 M KOH	313[b]	S16
NiO nanoparticles	-	1 M KOH	347[b]	S16
Amorphous NiO	0.1 mg cm^{-2}	1 M KOH	>470[b]	S17
NiOx/C	-	1 M KOH	335[a]	S18
($Ni_{0.69}Fe_{0.31}O_x$/C)	-	1 M KOH	280[a]	S18
NiOOH	-	1 M KOH	525[a]	S19
NiCo LDH	~ 0.17mg cm^{-2}	1 M KOH	393[b]	S20

REFERENCES

S1. A. T. Swesi, J. Masud, and M. Nath, Energy Environ. Sci. 2016, 9, 1771-1782.

S2. Q. Liu, J. Jin, and Junyan Zhang, *ACS Appl. Mater. Interfaces*. 2013, **5**, 5002−5008.

S3. D. Liu, Q. Lu, Y. Luo, X. Sun, and A. M. Asiri, *Nanoscale*. 2015, **7**, 15122–15126.

S4. A. Sivanantham, P. Ganesan, and S. Shanmugam, *Adv. Funct. Mater.* 2016, DOI: 10.1002/adfm.201600566.

S5. X. Gao, H. Zhang, Q. Li, X.Yu, Z. Hong, X. Zhang, C. Liang, and Zhan Lin, *Angew.Chem.Int. Ed.* 2016, **55**, 6290–6294.

S6. W. Xu, Z. Lu, X. Lei, Y. Li, and X.A. Sun, *Phys. Chem. Chem. Phys.* 2014, **16**, 20402–20405.

S7. Z. Peng, D. Jia, A. Al-Enizi, A. Elzatahry , and G. Zheng , *Adv. Energy Mater.* 2015, **5**, 1402031-1402038.

S8. T. Liu, Q. Liu, A. M. Asiri, Y. Luo, and X. Sun, *Chem. Commun.* 2015, **51**, 16683.

S9. C. Xia, Q. Jiang, C. Zhao, M.N. Hedhili, H.N. Alshareef, *Adv. Mater*. 2016, **28**, 77–85.

S10. T. Liu, A. M Asiri, and X. Sun, *Nanoscale*. 2016, **8**, 3911- 3915.

S11. I.H. Kwak, H.S. Im, D.M. Jang, Y.W. Kim, K. Park, Y.R. Lim, E.H. Cha, and J. Park, J., *ACS Appl. Mater. Interfaces*. 2016, **8**, 5327−5334.

S12. W. Zhu, X. Yue, W. Zhang, S. Yu, Y. Zhang, and J. Wang, *Chem. Commun.*, 2016, **52**, 1486-1489.

S13. J. Shi, J. Hu, Y. Luo, X. Sun, A.M. Asiri, *Catal. Sci. Technol.*, 2015, **5**, 4954-4958.

S14. T. Liu, Q. Liu, A.M. Asiri, Y. Luo, X. Sun, *Chem. Commun.* 2015, **51**, 16683-16686.

S15 C. Tang, A.M. Asiri, and X. Sun, *Chem.Commun.* 2016, **52**, 4529-4532.

S16. L. Stern, and X. Hu, *Faraday Discuss.* 2014, **176**, 363 –379.

S17. Kuai, L.; Geng, J.; Chen, C.; Kan, E.; Liu, Y.; Wang, Q. & Geng, B, *Angew. Chem. Int. Ed.* 2014, **53**, 7547–7551.

S18. Y. Qiu, L. Xin, and W. Li, Langmuir. 2014, **30**, 7893–7901.

S19. S. Klaus, Y. Cai, M. Louie, L. Trotochaud, and A.T. Bell, *J. Phys. Chem. C*, 2015, **119**, 7243-7254.

S20. H. Liang, F. Meng, M. Acevedo, L. Li, A. Forticaux, L. Xiu, Z. Wang, and S. Jin, *Nano Lett.* 2015, **15**, 1421–1427.

VI. $NiFe_2Se_4$ BASED TERNARY ELECTROCATALYST FOR ENHANCING OXYGEN EVOLUTION REACTION IN ALKALINE MEDIA

Abdurazag T. Swesi, Jahangir Masud and Manashi Nath

Department of Chemistry

Missouri University of Science and Technology
Rolla, Missouri 65409-0050 USA

Email: nathm@mst.edu

Manuscript in Preparation

ABSTRACT

Water splitting using earth abundant and environmentally benign catalyst is critical for renewable energy technologies. In spite of tremendous efforts to develop a catalyst with low cost with high activity and stability, it remains a challenge to match the performance of platinum group catalyst. Herein we report a $NiFe_2Se_4$ based as an efficient and dependable electrocatalyst for oxygen evolution reaction (OER) under alkaline conditions. The constructed hybrid catalyst is capable of catalyzing water oxidation at a small overpotential of 210 mV at 10 mA/cm^2 with a Tafel slope of 97.1 mV/decade. The extended stability of this catalyst was investigated in 1M KOH and 25% of NaOH solution and exhibited the robust nature in strong alkaline media. This study gives a new direction in the selenide based hybrid catalysts, which may be extended to prepare other metal selenide hybrids for a broad range of technological applications.

1. INTRODUCTION

Due to increasing the energy demand and its adverse impact on the environment, intensive research has been devoted to the development of advanced technologies particularly with high efficiency. Oxygen evolution reaction (OER), using cost effective, durable, non-toxic and environmentally benign materials, has been known as one of the most promising process to produce and store renewable energy in chemical form. However, the electrocatalytic OER at the anode is kinetically sluggish due to multistep proton-coupled transfer that represents an efficiency loss in electrolysis of water.[1] Therefore, an effective electrocatalyst is needed to expedite the OER process through reducing the large overpotential (~ 1.23 V) and thus enhance the energy conversion efficiency. Precious metal-based materials (IrO_2 and RuO_2) are known as the most active electrocatalysts for OER in acid or alkaline media.[2,3] However, these catalysts comprise critical elements[4-6] that are expensive and along with their lack sufficient abundance limiting their widespread use.[7] Extensive efforts have been devoted to design efficient, durable, and low-cost alternative electrocatalysts such as perovskite[8] and first-row transition metal oxides[9] as electrode materials for many renewable energy applications. However so far, most nonprecious metal catalysts developed still underperform the state-of-the-art Ir.[10,11]

Recently, Ni-based OER electrocatalysts was found to exhibit outstanding electrocatalytic activity towards OER in alkaline solution. It was stated that catalytic properties of this kind of catalysts can be influenced through other variables of the electrodeposition reaction such as the total and relative concentration(s) and composition(s) of dissolved metal salts and extra electrolytes, the pH, and the duration of

the electrodeposition current.[12] Interestingly, nickel is always found in combination with iron (Fe) on earth and Fe impurities in the nickel hydroxide ($Ni(OH)_2$) electrodes can cause destructive effects on Ni-based alkaline batteries by greatly lowering the OER overpotential.[13,14] Due to its corrosion-resistant nature, nickel ferrite has attracted much attention as a promising OER electrocatalyst. NiFe mixed compounds (spinel $NiFe_2O_4$) exhibit outperformance Fe alone (Fe_3O_4) and Ni alone (NiO) in OER electrocatalytic activity.[15] A plenty of researches have recently been emphasized on substituting the Ni by other cations (e.g., Cr, V, Mo and Co) in order to enhance the electrocatalytic activity.[16–19]

Horn and Goodenough have stated that the highest OER activity can be attained by *increasing covalency* in the *metal-oxygen bond* in the oxide electrocatalysts.[20,21] In this regard, for the first time, we report here a structural and electrochemical investigation of $NiFe_2Se_4$ electrocatalysts used for the OER in alkaline electrolyte. Another key aspect of this electrocatalyst is the appropriate Fe content that can be a significant factor impacting the OER electrocatalytic activity, and varying Fe content could potentially improve the OER electrocatalytic performance.[22–25] We demonstrate that the Ni−Fe selenide films show surprisingly high OER activity and stability in alkaline media, which outperforms most Ni−Fe thin films previously reported and commercial Ir-based electrocatalysts in terms of onset overpotential for O_2 evolution as well as overpotential to reach a current density of 10 mA cm^{-2} (observed at 210 mV). This novel system also exhibit high efficiency for HER in basic media. This is a very promising result with catalysts based on Ni-Fe, and suggests the potential opportunities in which non-precious metal catalysts can be used for practical sustainable energy conversion and storage applications. The structure and morphology of the electrodeposited Ni−Fe films have been characterized with powder X-ray diffraction,

Raman, X-ray photoelectron spectroscopy, Scanning and Transmission electron microscopy.

Electrocatalyst electrodes containing Ni and/or Fe were grown by electrodeposition onto conducting substrates (Au coated-glass). These Au-coated glass substrates (Deposition Research Lab Incorporated (DRLI), Lebanon, Missouri) were masked with a scotch tape, leaving exposed surface areas of 0.283 cm^2. The electrodeposition bath consisted of an aqueous solution of nickel sulfate hexahydrate (Fisher Scientific Company), sodium selenite (Alfa Aesar) and/or iron sulfate heptahydrate (Fisher Chemical). The metal concentrations were varied between 0 and 10 mM such that deposition baths with less than 50% Fe contained 10 mM Ni and a varying Fe concentration, and baths with greater than 50% Fe contained 10 mM Fe and a varying Ni concentration. For the electrodeposition of the spinel films, a typical three-electrode electrochemical cell was used that comprised the conducting substrate, platinum and Ag/AgCl/KCl (3 M) as the working, counter and reference electrodes, respectively. The substrates were ultrasonically pre-cleaned by sequential rinses with micro-90 detergent, isopropanol and eventually with deionized water (15 min each step) to ensure the clean surface. The cell was connected to a potentiostat (IviumStat technologies, Netherlands) that was used for the preparation of Ni-Fe selenide films and other electrochemical measurements. In order to prevent precipitation of insoluble FeOOH, the solutions were purged with N_2 gas for at least 30 min before adding $FeSO_4 \cdot 7H_2O$. Typical depositions at − 0.85 V (*vs*. Ag/AgCl electrode) for 300 s gave effective film thicknesses of ∼# nm. After deposition, the films were rinsed with de-ionized water and then dried with a gentle stream of air to remove impurities and adsorbents from the surface before being transferred to the

electrochemical cell. The Fe/Ni ratio in the films was higher than that in the deposition solutions as determined by XPS. For an OER fair comparison, the electrocatalytic efficiency of a RuO_2 standard[26] and the Au coated-glass background were also investigated. All resulting materials including FeSe, Ni_3Se_2 and $NiFe_2Se_4$ deposited on Au-coated glass substrates were characterized through powder X-ray diffraction (PXRD) using Philips X-Pert using CuKa (1.5418 Å) radiation. The PXRD pattern (Figure 1) of final product was compared to polycrystalline $NiFe_2Se_4$ (PDF#01-089-1968) standards. XRD patterns provided evidence for the exact crystalline phase for all desired materials along with the observation of another few intense peaks arising from the Au substrate. However, by analyzing all peaks in XRD patterns of $NiFe_2Se_4$, it could be observed trace amounts of $NiSe_2$ (PDF # 00-041-1495).[27]

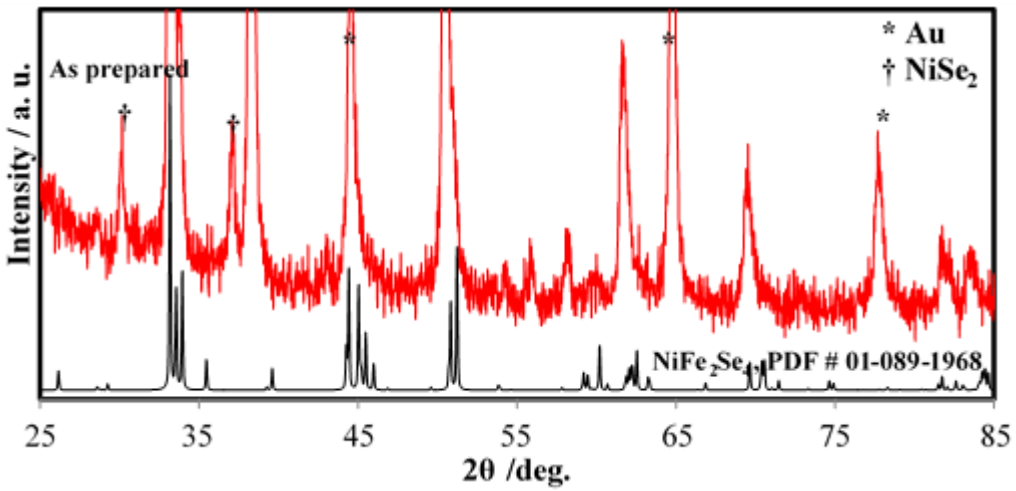

Figure 1. Pxrd pattern of $NiFe_2Se_4$ catalyst along with the reference (PDF#01-089-1968).

The electrocatalyst surface compositions have been checked, including FeSe, Ni_3Se_2 and $NiFe_2Se_4$, through XPS technique as shown in Figure 2. Ar sputtering of catalyst surfaces was performed to remove (~ 2 nm) any oxygen content. All binding

energies of corresponding materials were calibrated respecting to the binding energy of C 1s peak locates at 284.5 eV. Two binding energy values of XPS spectrum of Ni 2p are 853.1 eV and 870.8 eV for $NiFe_2Se_4$ could be attributed to the Ni2p3/2 and Ni2p1/2, which can be assigned to Ni^{2+}. The Fe XPS results of the mixed selenide sample were also observed. Two peaks were observed at 706.1 and 711 eV, can be assigned to Fe 2p3/2 and Fe 2p1/2 which can be assigned to Fe^{3+}. It should be noted that with relatively narrow peak width, the 2p3/2 to 2p1/2 separation of 5.7 eV, and the absence of satellite peak altogether convey the absence of Fe^{2+} and the Fe^{3+} is the dominant cation in the $NiFe_2Se_4$ phase.[56]

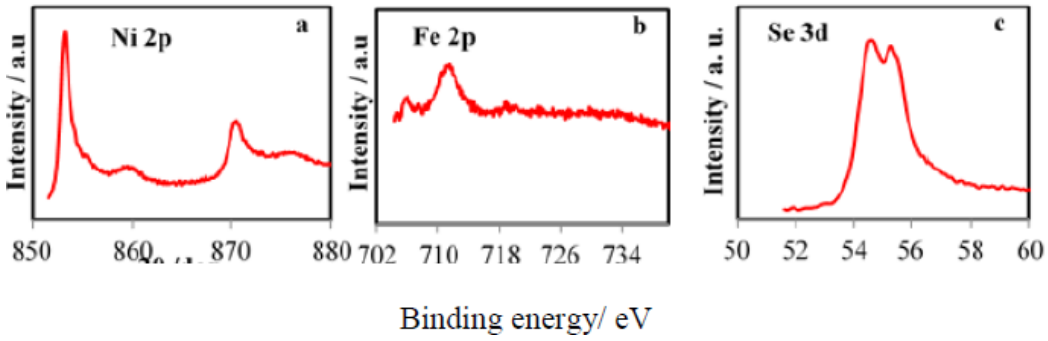

Figure 2. XPS of (a) Ni 2p, (b) Fe 2p and (c) Se 3d of $NiFe_2Se_4$ catalyst

The morphology of the catalysts was observed through scanning electron microscope (SEM). From the SEM images, all catalysts were found to be uniformly nanoparticles dispersed, as shown in Figure 3. The energy-dispersive X-ray (EDX) spectrum of electrodeposited films (Figure 3b-3e) indicates the existence of Ni, Fe and Se elements. Representative SEM images and corresponding EDX elemental mapping images of Fe, Ni, and Se for $NiFe_2Se_4$ clearly show that the overall interconnected nanograins

network structure on gold substrate is well-preserved. Furthermore, these nanograins uniformly and fully cover the gold substrates.

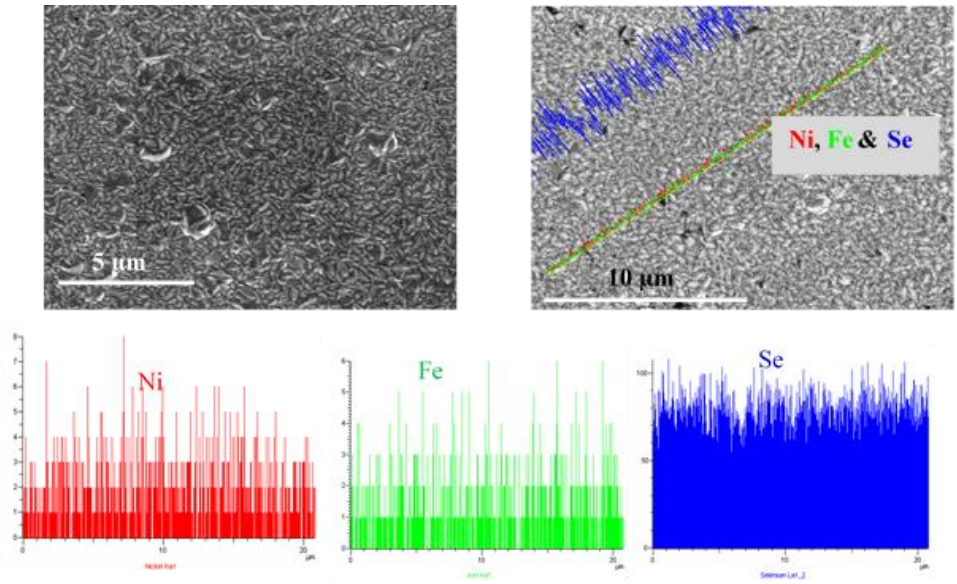

Figure 3. SEM image and EDS line scan of $NiFe_2Se_4$.

The electrochemical OER performance of the $NiFe_2Se_4$ was investigated in N_2 saturated 1 M KOH with a scan rate of 10 mV s^{-1}, using a standard three-electrode system. The electrochemical OER performance of the blank Au, Ni_3Se_2/Au, FeSe/Au and RuO_2/Au electrodes was also measured side-by-side for comparison. During the measurements, the solution was continuously stirred at 500 rpm to remove the generated oxygen bubbles from working electrode surface. All measured potentials were calibrated with the reversible hydrogen electrode (RHE) and resistance tests were made because the as-measured reaction currents cannot directly reflect the intrinsic behavior of catalysts due to the effect of ohmic resistance.[38] The following Equation was used for all measurements.

$E_{(RHE)} = E_{(Ag/AgCl)} + 0.197\ V + 0.059\ pH - E_u$.

Where, $E_u = iR$ is an uncompensated resistance (Ohmic resistance).

Representative linear sweep voltammograms for all catalyst series are shown in Figure 4a. The cyclic voltammograms for an as-deposited Ni based catalysts film (Figure 4b) show two characteristic peaks, an onset peak around 1.29 V vs RHE is assigned to the Ni(II)/Ni(III or IV) redox process[28,29] and a positive oxidation at overpotentials greater than 0.14 V vs RHE is due to the evolution of oxygen. The anodic current recorded with

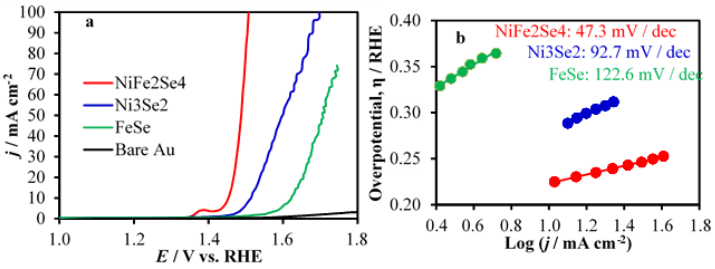

Figure 4(a). LSVs measured in N_2-saturated 1M KOH solution at a scan rate of 10 mVs^{-1}. (b). Tafel plots of catalysts.

the blank Au was negligible and was observed as a moderate for FeSe toward the OER while RuO_2/Au is highly active with an overpotential of 320 mV at 10 mA cm^{-2}. Ni_3Se_2/Au is also exhibits earlier onset OER potential with the need for an overpotential of 280 mV to drive 10 mA cm^{-2}.[27] However, $NiFe_2Se_4$ exhibits a much higher OER current than do all electrodes studied here including state-of-the-art RuO_2/Au. The OER current at 1.44 V *vs* RHE recorded from the LSVs (Figure 4a) of $NiFe_2Se_4$ is *j* 10 mA cm^{-2}, while on FeSe and Ni_3Se_2, *j* 0.8 and 1.3 mA cm^{-2} respectively. This low overpotential of 200 ± 10 mV could be considered as among the lowest overpotential reported till date for OER electrocatalysts including IrO_x (320 mV), RuO_x (390 mV) and non-precious metal electrocatalysts (Table S1).[30–36]

Moreover, the OER performances of the $NiFe_2Se_4$ were further assessed by Tafel measurements in 1 M KOH. The $NiFe_2Se_4$ catalyst displayed a Tafel slope (52 mV dec^{-1})

which is better than that of FeSe and Ni_3Se_2 as shown in Figure 4b. The observed small slope of $NiFe_2Se_4$ reveals fast charge and mass transfer between the catalyst and the electrolyte. This value was even smaller than the state-of-the-art IrO_2 and RuO_2 catalysts.[37-39]

The excellent OER catalytic activity of $NiFe_2Se_4$ was further assessed through electrochemical surface area (ECSA) and roughness factor (RF). The ECSA was estimated based on the double-layer charging current of the $NiFe_2Se_4$ electrode in 1M KOH (Table 1).[27] A Chronoamperometry measurement was carried out in 1 M KOH (Figure 5a and 5b) show that this voltage can support a constant current for a long period of continuous operation, suggesting the $NiFe_2Se_4$ catalyst is very durable. Full characterization through powder X-ray diffraction and SEM (Figure 5c-5e) showed that the structural solidity was maintained after long term of catalytic activity. Generally, the overall performance of $NiFe_2Se_4$ electrode is considered amongst the most active non-noble overall water splitting catalyst reported to date.

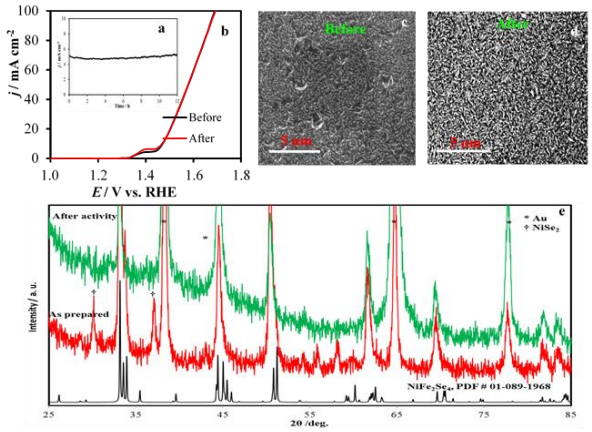

Figure 5 (a). Stability of catalyst in 1M KOH solution in continuous evolution of O_2 at 1.44 V (vs. RHE). (b) LSVs measured in 1M KOH before and after chronoamperometry. SEM images of catalyst before (c) and after (d) of the stability. (e) Comparison of PXRD of $NiFe_2Se_4$.

Table 1. Electrochemical parameters of the catalysts measured in 1 M KOH.

Catalyst	µg	ECSA /cm^2	RF	Onset η / V[a]	η@10 mAcm^{-2}/ V[a]	Tafel slope / mV dec^{-1}	$j_{g,\ \eta\ =0.31\ V}$ / mA cm^{-2}	$j_{s,\ \eta\ =0.31\ V}$ / mA cm^{-2}
Fe_xSe_y	8.0	2.5	8.8	0.27	0.39	99.6	3.36	0.38
Ni_3Se_2	31.3	2.3	8.2	0.21	0.29	98.8	7.81	0.95
$NiFe_2Se_4$	61.4	2.3	8.2	0.14	0.21	97.1	10.24	1.25

[a] potential reported with respect to RHE

Industrially, water electrolyzers need to be operated in a very high concentration base (25 – 30 wt%).[40] Therefore, the electrocatalytic performance of the $NiFe_2Se_4$ electrode was further examined in ~ 25 wt% NaOH. Surprisingly, this electrode displayed low onset potential along with higher current density (Figure 6a). To deliver a high current density of 100 mA cm^{-2}, an overpotential of only 240 mV was needed. To attain the same amount of current density in 1 M NaOH, 270 mV of overpotential was required. Besides the high activity under hard alkaline condition, this catalyst shows stable electrocatalytic activity and a mechanically robust material (Figure 6b).

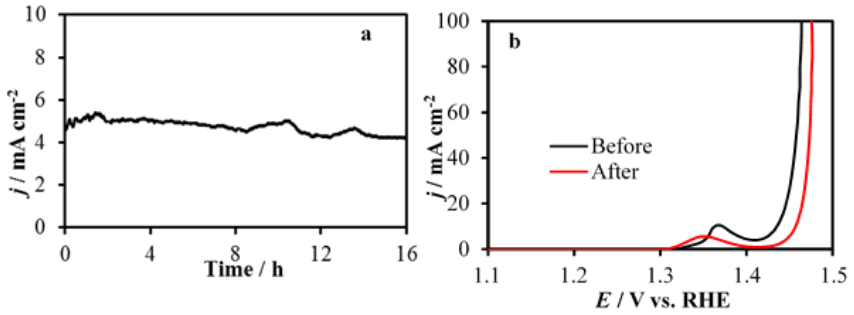

Figure 6 (a). Stability of catalyst was performed in 25 wt% of NaOH solution at 1.42 V vs. RHE and (b) is the comparison of LSVs before and after stability.

2. CONCLUSION

In summary, the $NiFe_2Se_4$ electrode has been proven to be an excellent in activity and durability for OER and HER in alkaline electrolyte. The overall water splitting polarization of $NiFe_2Se_4$ bifunctional catalyst enables a high-performance alkaline water electrolyzer with 10 mA cm^{-2} at a cell voltage of 1.78 V which is still slightly larger than the benchmark combination.

REFERENCES

1. Cook, T. R.; Dogutan, D. K.; Reece, S. Y.; Surendranath, Y.; Teets, T. S.; Nocera, D. G. Solar energy supply and storage for the legacy and nonlegacy worlds. *Chem. Rev*. **2010**, *110*, 6474-6502.

2. Walter, M. G.; Warren, E. L.; McKone, J. R.; Boettcher, S. W.; Mi, Q.; Santori, E. A.; Lewis, N. S. Solar water splitting cells. *Chem. Rev*. **2010**, *110*, 6446-6473.

3. Lee, Y.; Suntivich, J.; May, K. J.; Perry, E. E.; Shao-Horn, Y. Synthesis and Activities of Rutile IrO_2 and RuO_2 Nanoparticles for Oxygen Evolution in Acid and Alkaline Solutions. *J. Phys. Chem. Lett*. **2012**, *3*, 399-404.

4. Fabbri, E.; Habereder, Waltar, A. K.; Kotz, R.; Schmidt, T. J. Developments and perspectives of oxide-based catalysts for the oxygen evolution reaction. *Catal. Sci. Technol.* **2014**, *4*, 3800-8321.

5. Lee, Y.; Suntivich, J.; May, K. J.; Perry, E. E.; Horn, Y. S. *J. Phys. Chem. Lett*. **2012**, *3*, 399.

6. Gong, M.; Dai, H. A mini review of NiFe-based materials as highly active oxygen evolution reaction electrocatalysts. *Nano Researc.* **2015**, *8*, 23-39.

7. K. Kinoshita, *Electrochemical Oxygen Technology*, Wiley-Interscience, New York, 1992, *chapter 2*, pp. 78-99.

8. J. Suntivich, K. J. May, H. A. Gasteiger, J. B. Goodenough, Y. Shao-Horn. A perovskite oxide optimized for oxygen evolution catalysis from molecular orbital principles. *Science*. **2011**, *334*, 1383 – 1385

9. C. C. McCrory, S. Jung, J. C. Peters, T. F. Jaramillo. Benchmarking heterogeneous electrocatalysts for the oxygen evolution reaction. *J. Am. Chem. Soc*. **2013**, *135*, 16977 – 16987.

10. M. G. Walter, E. L. Warren, J. R. McKone, S. W. Boettcher, Q. Mi, E. A. Santori, N. S. Lewis, *Chem. Rev*. **2010**, *110*, 6446–6473.

11. Lee, Y., Suntivich, J., May, K. J., Perry, E. E. & Shao-Horn, Y. Synthesis and activities of rutile IrO_2 and RuO_2 nanoparticles for oxygen evolution in acid and alkaline solutions. *J. Phys. Chem. Lett*. **2012**, *3*, 399–404.

12. McCrory, C. C. L.; Jung, S. H.; Peters, J. C.; Jaramillo, T. F. Benchmarking heterogeneous electrocatalysts for the oxygen evolution reaction *J. Am. Chem. Soc*. **2013**, *135*, 16977-16987.

13. Munshi, M. Z. A.; Tseung, A. C. C.; Parker, J. The dissolution of iron from the negative material in pocket plate nickel-cadmium batteries. *J. Appl. Electrochem.* **1985**, *15*, 711-717.

14. E. Mirzakulova, R. Khatmullin, J. Walpita, T. Corrigan, N. M. Vargas-Barbosa, S. Vyas, S. Oottikkal, S. F. Manzer, C. M. Hadad, and K. D. Glusac. Electrode-assisted catalytic water oxidation by a flavin derivative. *Nature Chem*. **2012**, ***4***, 794-801.

15. Singh, N. K.; Singh, R. N. Electrocatalytic properties of spinel type $Ni_xFe_{3-x}O_4$ synthesized at low temperature for oxygen evolution in KOH solutions. *Indian J. Chem. Sect A–Inorg. Bio–Inorg. Phys. Theor. Anal. Chem.* **1999**, *38*, 491–495.

16. Singh, R. N.; Singh, J. P.; Lal, B.; Thomas, M. J. K.; Bera, S. New $NiFe_{2-x}Cr_xO_4$ spinel films for O_2 evolution in alkaline solutions. *Electrochim Acta* **2006**, *51*, 5515–5523.

17. Anindita, A.; Singh, R. N. Effect of V substitution at B-site on the physicochemical and electrocatalytic properties of spinel-type $NiFe_2O_4$ towards O_2 evolution in alkaline solutions. *Int. J.Hydrogen Energ.* **2010**, *35*, 3243–3248.

18. Kumar, M.; Awasthi, R.; Sinha, A. S. K.; Singh, R. N. New ternary Fe, Co, and Mo mixed oxide electrocatalysts for oxygen evolution. *Int. J. Hydrogen Energ.* **2011**, *36*, 8831–8838.

19. Chanda, D.; Hnat, J.; Paidar, M.; Bouzek, K. Evolution of physicochemical and electrocatalytic properties of $NiCo_2O_4$ (AB(2)O(4)) spinel oxide with the effect of Fe substitution at the A site leading to efficient anodic O_2 evolution in an alkaline environment. *Int. J. Hydrogen Energ.* **2014**, *39*, 5713–5722.

20. W. T. Hong, M. Risch, K. A. Stoerzinger, A. Grimaud, J. Sunitvich and Y. S. Horn. Toward the rational design of non-precious transition metal oxides for oxygen electrocatalysis. *Energy Environ. Sci.* 2015, 8, 1404-1427.

21. J. Suntivich, K. J. May, H. A. Gasteiger, J. B. Goodenough and Y. S. Horn. A perovskite oxide optimized for oxygen evolution catalysis from molecular orbital principles. *Science*, 2011, 334, 1383–1385.

22. Solmaz, R.; Kardas, G. Electrochemical deposition and characterization of NiFe coatings as electrocatalytic materials for alkaline water electrolysis. *Electrochim. Acta*. 2009, **54**, 3726–3734.

23. Hu, C. C.; Wu, Y. R. Bipolar performance of the electroplated iron-nickel deposits for water electrolysis. *Mater. Chem. Phys.* **2003**, *82*, 588–596.

24. Ullal, Y.; Hegde, A. C. Electrodeposition and electrocatalytic study of nanocrystalline Ni-Fe alloy. *Int. J. Hydrogen Energ.* **2014**, *39*, 10485–10492.

25. Li, X.; Walsh, F. C.; Pletcher, D. Nickel based electrocatalysts for oxygen evolution in high current density, alkaline water electrolyzers. *Phys. Chem. Chem. Phys.* **2011**, *13*, 1162–1167.

26. Zhao, Y.; Hernandez-Pagan, E. A.; Vargas-Barbosa, N. M.; Dysart, J. L.; Mallouk, T. E. A High Yield Synthesis of Ligand-Free Iridium Oxide Nanoparticles with High Electrocatalytic Activity. *J. Phys. Chem. Lett*. **2011**, *2*, 402−406.

27. A. T. Swesi, J. Masud, and M. Nath: Nickel selenide as a high-efficiency catalyst for oxygen evolution reaction. *Energy Environ. Sci*. **2016**, *9*, 1771-1782.

28. Corrigan, D. A. & Knight, S. L. Electrochemical and spectroscopic evidence on the participation of quadrivalent nickel in the nickel-hydroxide redox reaction. *J. Electrochem. Soc*. **1989**, *136*, 613-619.

29. Mary W. Louie and Alexis T. Bell. An investigation of thin-film Ni-Fe oxide catalysts for the electrochemical evolution of oxygen. *J. Am. Chem. Soc*. **2013**, *135*, 12329−12337.

30. Esswein, A. J.; McMurdo, M. J.; Ross, P. N.; Bell, A. T.; Tilley, T. D. Size-Dependent Activity of Co_3O_4 Nanoparticle Anodes for Alkaline Water Electrolysis. *J. Phys. Chem. C*. **2009**, *113*, 15068-15072.

31. Li, Y. G.; Hasin, P.; Wu, Y. Y. $Ni_xCo_{3-x}O_4$ Nanowire Arrays for Electrocatalytic Oxygen Evolution. *Adv. Mater*. **2010**, *22*, 1926-1929.

32. Liang, Y. Y.; Li, Y. G.; Wang, H. L.; Zhou, J. G.; Wang, J.; Regier, T.; Dai, H. Co_3O_4 nanocrystals on graphene as a synergistic catalyst for oxygen reduction reaction. *Nat. Mater*. **2011**, *10*, 780-786.

33. Gorlin, Y.; Jaramillo, T. F. A bifunctional nonprecious metal catalyst for oxygen reduction and water oxidation, *J. Am. Chem. Soc*. **2010**, *132*, 13612-13614.

34. Cui, B.; Lin, H.; Li, J. B.; Li, X.; Yang, J.; Tao. Core–Ring Structured $NiCo_2O_4$ Nanoplatelets: Synthesis, Characterization, and Electrocatalytic Applications. *J. Adv. Funct. Mater*. **2008**, *18*, 1440-1447.

35. Li, X. H.; Walsh, F. C.; Pletcher, D. Nickel based electrocatalysts for oxygen evolution in high current density, alkaline water electrolysers. *Phys. Chem. Chem. Phys*. **2011**, *13*, 1162-1167.

36. Kleiman-Shwarsctein, A. NiFe-oxide electrocatalysts for the oxygen evolution reaction on Ti doped hematite photoelectrodes. Hu, Y. S.; Stucky, G. D.; McFarland, E. W. *Electrochem. Commun*. **2009**, *11*, 1150-1153.

37. Lee, Y., Suntivich, J., May, K. J., Perry, E. E. & Shao-Horn, Y. Synthesis and activities of rutile IrO_2 and RuO_2 nanoparticles for oxygen evolution in acid and alkaline solutions. *J. Phys. Chem. Lett*. **2012**, *3*, 399–404.

38. Ouattara, L., Fierro, S., Frey, O., Koudelka, M. & Comninellis, C. Electrochemical comparison of IrO_2 prepared by anodic oxidation of pure iridium and IrO_2 prepared by thermal decomposition of H_2IrCl_6 precursor solution. *J. Appl. Electrochem*. **2009**, *39*, 1361–1367.

39. Tsuji, E., Imanishi, A., Fukui, K. & Nakato, Y. Electrocatalytic activity of amorphous RuO_2 electrode for oxygen evolution in an aqueous solution. *Electrochim. Acta*. **2011**, *56*, 2009–2016.

40. Kaveh Mazloomi1, Nasri b. Sulaiman1, Hossein Moayedi. Electrical Efficiency of Electrolytic Hydrogen Production. *Int. J. Electrochem. Sci*. **2012**, *7*, 3314 – 3326.

SECTION

4. CONCLUSION

The promising water splitting activities of non-noble metal based,[196,339] motivated us to investigate a new family of non-noble metal selenide catalysts for water electrolysis and several requirements have been considered to enhance the catalytic performance. The major requirements for designing these catalysts were as following;

1) increasing covalency in the metal-anion bond,

2) high surface area,

3) attempting directional growth,

4) doping a metal in nickel selenide,

5) introduction of overlayer strategies

6) long-term mechanically and chemically stable, and

7) available materials and low cost fabrication.

Although many studies have attempted non-noble metal based electrodes for water splitting, so far none of them has been able to reach the benchmark water splitting performance of the best catalysts reported in this investigation.[340]

Going forward, we have planned to further reduce overpotential and hence improve the OER catalytic performance of the proposed catalysts through forming hybrid materials modified with other foreign functional materials. We target thin $Ni_{0.85}Se/Fe_3Se_4/ Ni_{0.85}Se$ mutilayer prepared by electrodeposition methods (Figure 4.1). This strategy shows that the combination of the overlayers yields a cathodic shift in current onset potential towards 160

mV (*vs* RHE) comparing to that observed for a pure $Ni_{0.85}Se$. The hybrid catalysts showed intriguing activities toward OER electrocatalysis with 120mV (*vs* RHE) overpotential at a current density of 10 mA cm^{-2}. This new avenue demonstrated a new champion to be superior to any other OER electrocatalysts reported till date including precious metal oxides, to make it the best OER catalyst.

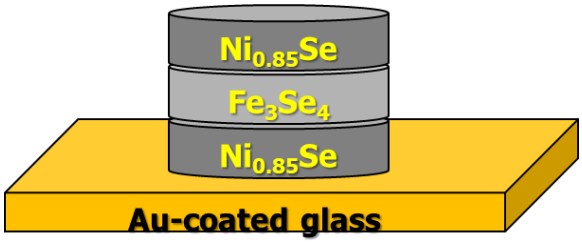

Figure 4.1. The schematic presentation of the integrated $Ni_{0.85}Se/Fe_3Se_4/Ni_{0.85}Se$ electrocatalyst system.

Furthermore, to examine whether Fe_3Se_4 can function as OER photoanode in the water spltting catalysts, we deposited $Ni_{0.85}Se$ as a hole storage layer onto Fe_3Se_4 (Figure 4.2) and the photoelectrochemical (PEC) cell performance in alkaline media was investigated. The proposed photoanode exhibited a remarkably low onset potential at 0.68 V (*vs* RHE) under UV illumination. Considering the abundance of the materials, the $Fe_3Se_4/Ni_{0.85}Se/Fe_3Se_4$ photoanode for oxygen generation from solar water splitting is demonstrated to deliver unprecedentedly high photocurrent densities of ~ 16 mA cm^{-2} at 1.23 v (*vs* RHE), establishing a new benchmark for non-noble based photoelectrodes. Following the electrodeposition technique, all catalysts reported in this study have been anodically grown on conductive substrates. Interestingly, electrochemical measurements

and detailed characterization of all proposed catalysts revealed the exceptional stability after long term water splitting activity.

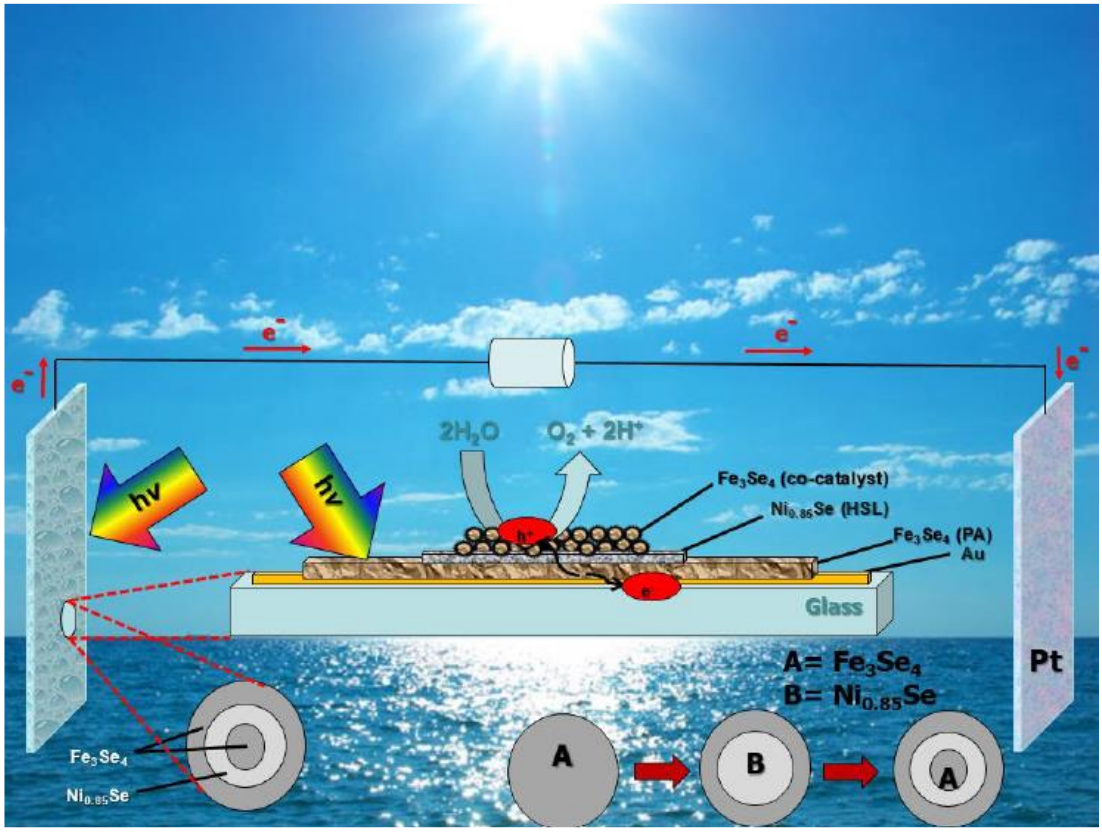

Figure 4.2. The schematic presentation of the integrated Fe_3Se_4 photoanode system.

BIBLIOGRAPHY

1. Cook, T. R.; Dogutan, D. K.; Reece, S. Y.; Surendranath, Y.; Teets, T. S.; Nocera, D. G. *Chem. Rev.* **2010**, *110*, 6474.

2. Gray, H. B. *Nat. Chem.* **2009**, *1*, 7.

3. Liang, Y. Y.; Li, Y. G.; Wang, H. L.; Dai, H. J. *J. Am. Chem. Soc.* **2013**, *135*, 2013.

4. Wang, H. L.; Dai, H. J. *Chem. Soc. Rev.* **2013**, *42*, 3088.

5. U.S. Energy Information Administration. International Energy Statistics; U.S. Department of Energy: Washington DC; www.eia.doe.gov.

6. Lewis, N. S.; Nocera, D. G. *Proc. Natl. Acad. Sci. U.S.A.* **2006**, *103*, 15729.

7. Turner, J. A. *Science*. **2004**, *305*, 972.

8. Zheng, Y.; Jiao, Y.; Jaroniec, M.; Qiao S. *Angew. Chem., Int. Ed*. **2015**, *54*, 52.

9. Naterer, G. F.; Fowler, M.; Cotton, J.; Gabriel, K. *International Journal of Hydrogen Energy.* **2008**, *33*, 6849.

10. Zeng, K.; Zhang, D. *Prog Energ Combust.* **2010**, *36*, 307.

11. Crabtree, G. W.; Dresselhaus, M. S.; Buchanan, M. V. *Phys Today*. **2004**, *57*, 39.

12. Carmo, H.; Fritz, D. L.; Mergel, J. S. *Int J Hydrogen Energy.* **2013**, *38*, 4901.

13. http://gcep.stanford.edu/research/exergy/resourcechart.html.

14. Rojas, D.; Beermann, J.; Klein, S.; Reindl, D. *Solar Energy*. **2008**, *82*, 746.

15. Villar, N. M; López, J. Muñoz, F. D.; García, E. R.; Andrés, A. C. *Solar Energy*. **2009**, *83*, 1086.

16. Tang, R.; Yang, Y.; Gao, W. *Solar Energy*. **2011**, *85*, 1381.

17. Abbott, D. *Proceedings of the IEEE*. **2010**. *1998, 1*, 42.

18. Marshall, A., *Norwegian University of Science and Technology: Trondheim*. **2005**, *231*.

19. Carmo, M.; Fritz, D. L.; Merge, J.; Stolten, D. *Int. J. Hydrogen Energy*. **2013**, *38*, 4901.

20. Gong, M.; Zhou, W.; Tsai, M. C.; Zhou, J. G.; Guan, M. Y.; Lin, M. C.; Zhang, B.; Hu, Y. F.; Wang, D. Y.; Jiang, J. *Nat. commun.* **2014**, *5*, 4695. 264.

21. Holladay, J. D.; Hu, J.; King, D. L.; Wang, Y. *Catal. Today*. **2009**, *139*, 244.

22. Tueysuez, H.; Hwang, Y. J.; Khan, S. B.; Asiri, A. M.; Yang, P. *Nano Res.* **2013**, *6*, 47.

23. Bavykin, D. V.; Friedrich, J. M.; Walsh, F. C. *Advanced Materials*. **2006**, *18*, 2807.

24. Ochiai, T.; Fujishima, A. *Journal of Photochemistry and Photobiology C: Photochemistry Reviews*. **2012**, *13*, 247.

25. Phelan, P. E.; Otanicar, T. P.; Singh, H.; Taylor, R. A. *Journal of Nanotechnology in Engineering and Medicine*. **2012**, *303*, 1003.

26. Wiki-fuel cell PEM Fuel Cell Technology.

27. Saidur, R.; Leong, K.; Mohammad, H. *Renewable and Sustainable Energy Reviews*. **2011**, *15*, 1646.

28. Kreuter, W.; Hofmann, H. *Int. J. Hydrogen Energy*. **1989**, *23*, 661.

29. Neagu, C.; Jansen, H.; Gardeniers, H.; Elwenspoek, M. *Mechatronics*. **2000**, 571.

30. Carmo, H.; Fritz, D. L.; Mergel, J. S. *Int J Hydrogen Energy*. **2013**, *38*, 4901.

31. Hall, D. E. *J. Electrochem. Soc.* **1985**, *132*, 42.

32. Miles, M. H.; Huang, Y. H. *J. Electrochem. Soc.* **1978**, *125*, 1930.

33. Floner, D. L.; Leger, J. M. *Surface Science*. **1990**, *243*, 87.

34. Millet, P.; Andolfatto, F. Durand, R. *Int. J. Hydrogen Energy*. **1996**, *21*, 87.

35. Stucki, S.; Scherer, G. G.; Schlagowski, S.; Fischer, E. *J. Applied Electrochemistry*. **1998** *28*, 1041.

36. Proceedings of the DOE Hydrogen Program Review. **2001**, NREL/CP-570-30535.

37. Markovic, N, M.; Ross, P. N. *Surf Sci Rep*. **2002**, *45*, 121.

38. Bockris, J. O. *Int. J. Hydrogen Energy*. **2008**, *33*, 2129.

39. Pletcher, D.; Robinson, D.; *Woodhead Publishing*. **2010**, 229-250.

40. Kanan, M. W.; Nocera, D. G. *Science*. **2008**, *321*, 1072.

41. Koper, M. T. M. *J. Electroanal. Chem.* **2011**, *660*, 254. 265.

42. Zeng, K.; Zhang, D. *Prog. Energy Combust. Sci*. **2010**, *36*, 307.

43. Greeley, J.; Markovic, N. M. *Energy Environ Sci*. **2012**, *5*, 9246.

44. Grätzel, M. *Chem Lett*. **2005**, *34*, 8.

45. Brimblecombe, R. Dismukes, G. C. Swiegers, G. F.; Spiccia, L. *Dalton Trans*. **2009**, *43*, 9374.

46. Nocera, D. G. *Acc Chem Res*. **2012**, *45*, 767.

47. Joya, K. S.; Joya, Y. F.; Ocakoglu, K. van de Krol, R. *Angew Chem Int Ed*. **2013**, *52*, 10426.

48. Trasatti, S. *In: Lipkowski J, Ross PN (eds) Electrochemistry of novel materials. VCH*, New York, 207–295.

49. Greeley, J.; Markovic, N. M. *Energy Environ Sci*. **2012**, *5*, 9246.

50. Bockris, J. O. *J Chem Phys*. **1956**, 24, 817.

51. Bard, A. J.; Faulkner, L. R. *Electrochemical Methods*; Wiley, **2000**.

52. Bockris, J. O.; Reddy, A. K. N. Modern Electrochemistry 1: Ionics, Plenum Press, New York, **1998**.

53. Isabela, C. *ChemCatChem*. **2011**, *3*, 1159.

54. Nørskov, J. K.; Rossmeisl T. J.; Christensen, C. H. *Nat. Chem*. **2009**, *1*, 37.

55. Rossmeisl, J.; Qu, Z. W.; Zhu, H.; Kroes, G. J.; Norskov, J. K. *J. Electroanal. Chem*. **2007**, *607*, 83.

56. Nørskov, J. K.; Rossmeisl, J.; Logadottir, A.; Lindqvist, L.; Kitchin, J. R.; Bligaard, Jonsson, T. *J. Phys. Chem. B*. **2004**, *108*, 886.

57. Nørskov, J.; Bligaard; K.; Rossmeisl, T.; Christensen, J. *Nat Chem*. **2009**, *1*, 37.

58. Trasatti, S., *ELECTROCHEMICAL THEORY | Oxygen Evolution*, in *Encyclopedia of Electrochemical Power Sources*, J. Garche, Editor. Elsevier: Amsterdam. **2009**, 49-55.

59. Lee, Y.; Suntivich, J.; May, K. J.; Perry, E. E.; Horn, Y. S. *J. Phys. Chem. Lett*. **2012**, *3*, 399.

60. Trasatti, S. *Electrochimica Acta*. **1991**, *36*, 225. 266.

61. Trasatti, S. *Electrochimica Acta*. **1984**, *29*, 1503.

62. Betley, T. A.; Wu, Q.; Van Voorhis, T.; Nocera, D. G. *Inorg. Chem*. **2008**, *47*, 1849.

63. Liu, F.; Concepcion, J.; Jurss, W.; Cardolaccia T.; Templeton, J.; Meyer, T. *Inorg. Chem*. **2008**, *47*, 1727.

64. Brimblecombe, R.; Dismukes, G. C.; Swiegers, G. F.; Spiccia, L. *Dalton Trans*. **2009**, 9374.

65. Bockris, J.; Otagawa, T. *J Electrochem Soc*. **1984**, *131*, 290.

66. Suntivich, J.; Gasteiger, H.; Yabuuchi, N.; Nakanishi, H; Goodenough, J.; Shao-Horn, Y. *Nature Chemistry*. **2011**, *3*, 546.

67. Ballhausen, C. J.; Gray, H. B. *Inorg. Chem.* **1962**, *1*, 111.

68. Betley, T. A.; Wu, Q.; Van, V. T.; Nocera, D. G. *Inorg. Chem*. **2008**, *47*, 1849.

69. Suntivich, J.; May, K. J.; Gasteiger, H.; Goodenough, J. B. Horn, S. Y. *Science*. **2011**, *334*, 1383.

70. Nørskov, J. K.; Bligaard, T.; Rossmeisl, J.; Christensen C. H. *Nat Chem*. **2009**, *1*, 37.

71. Chang, S. H. Danilovic, N. Chang, K. C.; Subbaraman, R.; Paulikas, A. P.; Fong, D. D.; Highland, M. J.; Baldo, P. M.; Stamenkovic, V. R.; Freeland, J. W. Eastman, J. A. Markovic, N. M. *Nat Commun*. **2014**, *5*, 4191.

72. Desilvestro, J.; Corrigan D. A.; Weaver, M. J. *J Phys Chem*. **1986**, *90*, 6408.

73. Corrigan, D. A. *J Electrochem Soc*. **1987**, *134*, 377.

74. Corrigan, D. A.; Conell, R. S.; Fierro, C. A.; Scherson, D. A. *J Phys Chem*. **1987**, *91*, 5009.

75. Landon, J.; Demeter, E.; Inoglu, N.; Keturakis, C. Wachs, I. E.; Vasic, R.; Frenkel, A. I.; Kitchin, J. R. *ACS Catal*. **2012**, *2*, 1793.

76. Trotochaud, L.; Ranney, J. K. Williams, K. N. Boettcher, S. W. *J Am Chem Soc*. **2012**, *134*, 17253.

77. McCrory, C. C. L.; Jung, S. H.; Peters, J. C.; Jaramillo, T. F. *J Am Chem Soc*. **2013**, *135*, 16977.

78. Gong, M.; Li, Y.; Wang, H.; Liang, Y.; Wu, J. Z. Zhou, J. Wang, J.; Regier, T.; Wei, F.; Dai, H. *J Am Chem Soc*. **2013**, *135*, 8452. 267.

79. Smith, R. D. L.; Prevot, M. S. Fagan, R. D. Zhang, Z.; Sedach, P. A.; Siu, M.; Trudel, S.; Berlinguette, C. P. *Science*. **2013**, *340*, 60.

80. Louie, M. W.; Bell, A. T. *J Am Chem Soc*. **2013**, *135*, 12329.

81. Kim, T. W.; Choi, K. S. *Science*. **2013**, *343*, 990.

82. Trotochaud, L.; Ranney, J. K.; Williams, K. N.; Boettcher, S. W. *J Am Chem Soc*. **2012**, *134*, 17253.

83. El-Deab, M. S.; Awad, M. I.; Mohammad, A. M. Ohsaka, T. *Electrochem Commun*. **2007**, *9*, 2082.

84. Mohammad, A. M. Awad, M. I. El-Deab, M. S.; Okajima, T.; Ohsaka, T. *Electrochim Acta*. **2008**, *53*, 4351.

85. Gorlin, Y. Chung, C. J.; Benck, J. D.; Nordlund, D.; Seitz, L.; Weng, T. C. Sokaras, D.; Clemens, B. M.; Jaramillo, T. F. *J Am Chem Soc*. **2014**, *136*, 4920.

86. Yeo, B. S.; Bell, A. T. *J Am Chem Soc*. **2011**, *133*, 5587.

87. Lu, X.; Ng, Y.; Zhao, C. *ChemSusChem*. **2014**, *7*, 82.

88. Yeo, B. S.; Bell, A. T. *J Phys Chem C*. **2012**, *116*, 8394.

89. Liao, P.; Keith, J. A.; Carter, E. A. *J Am Chem Soc*. **2012**, *134*, 13296.

90. Garcia-Mota, M.; Vojvodic, A.; Metiu, H.; Man, I. C.; Su, H.; Rossmeisl, J.; Nørskov, J. K. *ChemCatChem*. **2011**, *3*, 1607.

91. Petrykin, V.; Macounova, K.; Shlyakhtin, O. A.; Krtil, P. *Angew Chem Int Ed*. **2010**, *49*, 4813.

92. Halck, N. B.; Petrykin, V.; Krtil, P.; Rossmeisl, J. *Phys Chem Chem Phys*. **2014**, *16*, 13682.

93. Busch, M.; Ahlberg, E.; Panas, I. *Phys Chem Chem Phys*. **2011**, *13*, 15062.

94. Busch, M.; Ahlberg, E.; Panas, I. *Phys Chem Chem Phys*. **2011**, *13*, 15069.

95. Busch, M.; Ahlberg, E.; Panas, I. *Catal Today*. **2013**, *202*, 114.

96. Zhan, Y.; Xu, C.; , Lu, M.; Liu, Z.; Lee, J. *J. Mater. Chem. A*. **2014**, *2*, 16217.

97. Singh, N. K.; Tiwari, S. K.; Anitha, K. L.; Singh, R. N. *J Chem Soc Faraday Trans*. **1996**, *92*, 2397. 268.

98. Rios, E.; Chartier, P.; Gautier, J. L. *Solid State Sci*. **1999**, *1*, 267.

99. Merrill, M. D.; Dougherty, R. C. *J Phys Chem C*. **2008**, *112*, 3655.

100. Yeo, B. S. Bell, A. T. *J Am Chem Soc*. **2011**, *133*, 5587.

101. Yeo, B. S. Bell, A. T. *J Phys Chem C*. **2012**, *116*, 8394.

102. Trotochaud, L.; Young, S. L.; Ranney, J. K.; Boettcher, S. W. *J Am Chem Soc*. **2014**, *136*, 6744.

103. Corrigan, D. A.; Conell, R. S.; Fierro, C. A.; Scherson, D. A. *J Phys Chem*. **1987**, *91*, 5009.

104. Kim, S. Tryk, D. A. Antonio, M. R. Carr, R. Scherson, D. J. Phys Chem. **1994**, *98*, 10269.

105. Balasubramanian, M.; Melendres, C. A.; Mini, S. *J Phys Chem B*. 2000, *104*, 4300.

106. Pourbaix, M. Atlas of electrochemical equilibria in aqueous solutions, 2nd edn. National Association of Corrosion Engineers. **1974**, Houston, TX.

107. Schweitzer, G. K.; Pesterfield, L. L. The aqueous chemistry of the elements. **2010**, Oxford University Press, Oxford.

108. Fabbri, E.; Habereder, A.; Waltar, K.; K€otz, R.; Schmidt, T. J. *Catal Sci Technol*. **2014**, *4*, 3800.

109. Chang, S. H. Connell, J. G. Danilovic, N.; Subbaraman, R.; Chang, K. C.; Stamenkovic, V. R.; Markovic, N. M. *Faraday Discuss*. **2015**, *176*, 125.

110. Danilovic, N.; Subbaraman, R.; Chang, K.; Chang, S. H.; Kang, Y. J.; Snyder, J.; Paulikas, A. P.; Strmcnik, D.; Kim, Y.; Myers, D. Stamenkovic, V. R.; Markovic, N. M. *J Phys Chem Lett*. **2014**, *5*, 2474.

111. Chang, S. H.; Connell, J. G.; Danilovic, N.; Subbaraman, R.; Chang, K. C.; Stamenkovic, V. R. Markovic, N. M. Faraday Discuss. **2015**, *176*, 125.

112. Danilovic, N.; Subbaraman, R.; Chang, K.; Chang S. H. Kang, Y.; Snyder, J.; Paulikas, A. P.; Strmcnik, D.; Kim, Y. T.; Myers, D.; Stamenkovic, V. R.; Markovic, N. M. *Angew Chem Int Ed*. **2014**, *53*,14016.

113. Reier, T.; Oezaslan, M.; Strasser, P. *ACS Catal*. **2012**, *2*, 1765. 269.

114. Diaz-Morales, O.; Calle-Vallejo, F.; de Munck, C.; Koper, M. *Chem Sci*. **2013**, *4*, 2334.

115. Ruban, A. V.; Skriver, H. L.; Nørskov, J. K. *Phys Rev B*. **1999**, *59*, 15990.

116. Novell-Leruth, G.; Carchini, G.; Lopeza, N. *J Chem Phys*. **2013**, *138*, 194706.

117. Schwab, G. M. In: Anderson JR, Boudart M (eds) Catalysis – science and technology. **1981**, vol 2. Springer, Berlin, p 4.

118. Burke, L. D.; Collins, J. A.; Horgan, M, A.; Hurley, L. M.; O'Mullane, A. P. *Electrochim Acta*. **2000**, *45*, 4127.

119. Burke, L. D.; O'Connell, A. M.; O'Mullane, A. P. *J Appl Electrochem*. **2003**, *33*, 1125.

120. Somorjai, G. A. *Chem Rev*. **1996**, *96*, 1223.

121. Sun, K.; Kohyama, M.; Tanaka, S.; Takeda, S. *J Phys Chem A*. **2012**, *116*, 9568.

122. Nowicka, A. M.; Hasse, U.; Sievers, G.; Donten, M.; Stojek, Z.; Fletcher, S.; Scholz, F. *Angew Chem Int Ed*. **2010**, *49*,3006.

123. Burke, L. D.; O'Sullivan, E. J. M. *J Electroanal Chem*. **1981**, *117*, 155.

124. Lyons, M. E. G.; Burke, L. D. *J Chem Soc Faraday Trans*. **1987**, *83*, 299.

125. O'Sullivan, E. J. M.; Burke, L. D. *J Electrochem Soc*. **1990**, *137*, 466.

126. Rebouillat, S.; Lyons, M. E. G. Brandon, M. P.; Doyle, R. L. *Int J Electrochem Sci*. 6, 5830.

127. Lyons, M. E. G.; Floquet, S. *Phys Chem Chem Phys*. **2011**, *13*, 5314.

128. Doyle, R. L.; Godwin, I. J.; Brandon, M. P.; Lyons, M. E. G. *Phys Chem Chem Phys*. **2013**, *15*, 13737.

129. Burke, L. D.; Lyons, M. E. G.; Whelan, D. P. J Electroanal Chem. **1982**, 139, 131.

130. Egdell, R. G.; Goodenough, J. B.; Hamnett, A.; Naish, C. J. *J Chem Soc Faraday Trans*. **1983**, *79*, 893.

131. Burke, L. D.; Lyons, M. E. G. *J Electroanal Chem*. **1986**, *198*, 347.

132. Burke, L. D.; Twomey, T. A. M. *J Electroanal Chem*. **1984**, *167*, 285. 270.

133. Lyons, M. E. G. Russell, L. O'Brien, M.; Doyle, R. L.; Godwin, I.; Brandon, M. P. Int J *Electrochem Sci*. **2012**, *7*, 2710.

134. Lyons, M. E. G.; Cakara, A.; O'Brien, P.; Godwin, I.; Doyle, R. L. *Int J Electrochem Sci*. **2012**, *7*, 11768.

135. Burke, L. D.; O'Sullivan, E. J. M. *J Electroanal Chem*. **1978**, *93*, 11.

136. Doyle, R. L.; Lyons, M. E. G. *J Electrochem Soc*. **2013**, *160*, 142.

137. Doyle, R. L.; Lyons, M. E. G. *Phys Chem Chem Phys*. **2013**, *15*, 5224.

138. Burke, L. D.; Whelan, D. P. *J Electroanal Chem*. **1984**, *162*, 121.

139. Lyons, M. E. G.; Floquet, S. *Phys Chem Chem Phys*. **2011**, *13*, 5314.

140. Sato, N. Electrochemistry at metal and semiconductor electrodes. Elsevier, Amsterdam, **1998**, 181.

141. Lyons, M. E. G.; Doyle, R. L.; Fernandez, D.; Godwin, I. J.; Browne, M. P.; Rovetta, A. *Electrochem Commun*. **2014**, *45*, 56.

142. Godwin, I. J.; Doyle, R. L.; Lyons, M. E. G. *J Electrochem Soc*. **2014**, *161*, 906.

143. Lyons, M. E. G.; Brandon, M. P. *J Electroanal Chem*. **2010**, *641*, 119.

144. Doyle, R. L.; Lyons, M. E. G. *J Solid State Electrochem*. **2014**, *18*, 3271.

145. Lyons, M. E. G.; Brandon, M. P. *Phys Chem Chem Phys*. **2009**, *11*, 2203.

146. McDonald, A. R.; Que, L. *Nature*. **2011**, 3, 761.

147. Wang, L. P.; Wu, Q.; Van Voorhis, T. *Inorg Chem*. **2010**, *49*, 4543.

148. Duan, L.; Bozoglian, F.; Mandal, S.; Stewart, B.; Privalov, T.; Llobet, A.; Sun, L. *Nature*. **2012**, *4*, 418.

149. Lodi, G.; Sivieri, E.; De Battisti, A.; Trasatti, S. *J Appl Electrochem*. **1978**, *8*, 135.

150. Kanan, M. W. Nocera, D. G. *Science*. **2008**, *321*, 1072.

151. Surendranath, Y.; Kanan, M. W.; Nocera, D. G. *J Am Chem Soc*. **2010**, *132*, 16501.

152. McAlpin, J. G.; Surendranath, Y.; Dinca, M.; Stich, T. A.; Stoian, S. A.; Casey, W. H.; Nocera, D. G.; Britt, R. D. *J Am Chem Soc*. **2010**, *132*, 6882. 271.

153. Huynh, M.; Bediako, D. K.; Nocera D. G. *J Am Chem Soc*. **2014**, *136*, 6002.

154. Bediako, D.K.; Lassalle-Kaiser, B.; Surendranath, Y.; Yano, J.; Yachandra, V. K. Nocera, D. G. *J Am Chem Soc*. **2012**, *134*, 6801.

155. Bediako, D. K.; Surendranath, Y.; Nocera, D. G. *J Am Chem Soc*. **2013**, *135*, 3662.

156. Surendranath, Y.; Nocera D. G. *Inorganic chemistry*. **2012**, *57*, 505.

157. Lee, S. W.; Carlton, C.; Risch, M.; Surendranath, Y.; Chen, S.; Furutsuki, S.; Yamada, A.; Nocera, D. G.; Shao-Horn, Y. *J Am Chem Soc*. **2012**, *134*, 16959.

158. May, K. J.; Carlton, C. E.; Stoerzinger, K. A.; Risch, M.; Suntivich, J.; Lee, Y.; Grimaud, A.; Shao-Horn, Y. *J Phys Chem Lett*. **2012**, *3*, 3264.

159. Alstrum-Acevedo, J. H.; Brennaman, M. K.; Meyer, T. *J. Inorg. Chem*. **2005**, *44*, 6802.

160. Cox, N.; Pantazis, D. A.; Neese, F.; Lubitz, W. Acc. *Chem. Res*. **2013**, *46*, 1588.

161. Cook, T. R.; Dogutan, D. K.; Reece, S. Y.; Surendranath, Y.; Teets, T. S.; Nocera, D. G. *Chem. Rev*. **2010**, *110*, 6474.

162. Concepcion, J. J.; Jurss, J. W.; Norris, M. R.; Chen, Z.; Templeton, J. L.; Meyer, T. *J. Inorg. Chem*. **2010**, *49*, 1277.

163. Dogutan, D. K.; McGuire, R.; Nocera, D. G. *J. Am. Chem. Soc*. **2011**, *133*, 9178.

164. Mola, J.; Mas-Marza, E.; Sala, X.; Romero, I.; Montserrat, R.; Viñas, C.; Parella, T.; Llobet, A. *Angew. Chem. Int. Ed*. **2008**, *47*, 5830.

165. Geletii, Y. V.; Besson, C.; Hou, Y.; Yin, Q.; Musaev, D. G.; Quinonero, D.; Cao, R.; Hardcastle, K. I.; Proust, A.; K€ogerler, P.; Hill, C. L. *J. Am. Chem. Soc*. **2009**, *131*, 17360.

166. Ellis, W. C.; McDaniel, N. D.; Bernhard, S.; Collins, T. J. *J. Am. Chem. Soc*. **2010**, *132*, 10990.

167. Dau, H.; Limberg, C.; Reier, T.; Risch, M.; Roggan, S.; Strasser, P. *ChemCatChem*. **2010**, *2*, 724.

168. Tarasevich, M. R.; Efremov, B. N. In Electrodes of Conductive Metal Oxides, Part A; Trasatti, S., Ed.; Elsevier: Amsterdam, **1980**; Ch. 5.

169. Trasatti, S. In Electrochemistry of Novel Materials; Lipkowski, J., Ross, P. N., Eds.; VCH: New York, **1994**; Ch. 5. 272.

170. Kinoshita, K. Electrochemical Oxygen Technology; Wiley-Interscience: New York, **1992**; Ch. 2.

171. Miao, Y.; Ouyang, L.; Zhou, S.; Xu, L.; Yang, Z.; Xiao, M.; Ouyang, R. *Biosens. Bioelectron*. **2014**, *53*, 428.

172. Rosen, J.; Hutchings, G. S.; Jiao, F. *J. Am. Chem. Soc*. **2013**, *135*, 4516.

173. Zhuang, Z.; Sheng, W.; Yan, Y. *Adv. Mater*. **2014**, *26*, 3950.

174. Hu, L.; Kim, H. S.; Lee, J.-Y.; Peumans, P.; Cui, Y. *ACS Nano*. **2010,** *4*, 2955.

175. Garnett, E. C.; Cai, W.; Cha, J. J.; Mahmood, F.; Connor, S. T.; Greyson Christoforo, M.; Cui, Y.; McGehee, M. D.; Brongersma, M. L. *Nat. Mater.* **2012,** *11*, 241.

176. Yu, Z.; Zhang, Q.; Li, L.; Chen, Q.; Niu, X.; Liu, J.; Pei, Q. *Adv. Mater.* **2011,** *23*, 664.

177. Song, T. B.; Chen, Y.; Chung, C. H.; Yang, Y.; Bob, B.; Duan, H. S.; Li, G.; Tu, K. N.; Huang, Y. *ACS Nano*. **2014,** *8*, 2804.

178. Lee, P.; Lee, J.; Lee, H.; Yeo, J.; Hong, S.; Nam, K. H.; Lee, D.; Lee, S. S.; Ko, S. H. *Adv. Mater.* **2012,** *24*, 3326.

179. Lee, J. H.; Lee, P.; Lee, D.; Lee, S. S.; Ko, S. H. *Cryst. Growth Des.* **2012,** *12*, 5598.

180. Bob, B.; Song, T.-B.; Chen, C.-C.; Xu, Z.; Yang, Y. *Chem. Mater.* **2013,** *25*, 4725.

181. Frydendal, R.; E. Paoli, A.; Knudsen, B. P.; Wickman, B.; Malacrida, P.; Stephens, L.; Chorkendorff, I. *ChemElectroChem*. **2014**, *1*, 2075.

182. Lee, Y.; Suntivich, J.; May, K. J.; Perry, E. E.; Shao-Horn, Y. *J. Phys. Chem. Lett*. **2012**, *3*, 399.

183. Vukovic, M. *J. Appl. Electrochem*. **1987**, *17*, 737.

184. Cherevko, S.; Geigerm S.; Kasian, O.; Kulyk, N.; Grote, J.-P.; Savan, A.; Shrestha, B. R.; Merzlikin, S.; Breitbach, B.; Ludwig, A; Mayrhofer, K. J. J. *Catal. Today*. **2016**, *262*, 170.

185. Kötz, R.; Lewerenz, H. J.; Stucki, S. *J. Electrochem. Soc*. **1983**, *130*, 825.

186. Kötz, R.; Neff, H.; Stucki, S. *J. Electrochem. Soc*. **1984**, *131*, 72.

187. Marshall, A. T.; Haverkamp, R. G. *Electrochim. Acta*. **2010**, *55*, 1978. 273.

188. Owe, L.-E.; Tsypkin, M.; Wallwork, K. S.; Haverkamp, R. G.; Sunde, S. *Electrochim. Acta*. **2012**, *70*, 158.

189. Mayousse, E.; Maillard, F.; Fouda-Onana, F.; Sicardy, O.; Guillet, N. *Int. J. Hydrogen Energy*, **2011**, *36*, 10474.

190. Mattos-Costa, F. I.; de Lima-Neto, P.; Machado, S. A. S.; Avaca, L. A. *Electrochim. Acta*. **1998**, *44*, 1515.

191. Audichon, T.; Napporn, T.; Canaff, W. C.; Morais, C.; Comminges, C.; Kokoh, K. B. *J. Phys. Chem. C*. **2016**, *120*, 2562.

192. Matsumoto, Y.; Yamada, Nishida, S. T.; Sato, E. *J. Electrochem. Soc*. **1980**, *127*, 2360.

193. Bockris, J. O. M.; Otagawa, T. *J. Electrochem. Soc*. **1984**, *131*, 290.

194. Liu, Y.; Wang, H.; Lin, D.; Liu, C.; Hsu, P. C.; Liu, W.; Chen, W.; Cui, Y. *Energy Environ. Sci*. **2015**, *8*, 1719.

195. Suntivich, J.; May, K. J.; Gasteiger, H. A.; Goodenough, J. B.; Shao-Horn, Y. *Science*. **2011**, *334*, 1383.

196. Lee, J. G.; Hwang, J.; Hwang, H. J; Jeon, O. S.; Jang, J.; Kwon, O.; Lee, Y.; Han, B.; Shul, Y. *J. Am. Chem. Soc*. **2016**, *138*, 3541.

197. Yagi, S.; Yamada, I.; Tsukasaki, H.; Seno, A.; Murakami, M.; Fujii, H.; Chen, H.; Umezawa, N.; Abe, H.; Nishiyama, N.; Mori, S. *Nat. Commun*. **2015**, *6*, 8249.

198. Zhu, Y.; Zhou, W.; Yu, J.; Chen, Y.; Liu, M.; Shao, Z. *Chem. Mater*. **2016**, *28*, 1691.

199. Burns, R. G. Mineralogical applications of crystal field theory, Cambridge University Press, **1993**.

200. Nikolov, I.; Darkaoui, R.; Zhecheva, E.; Stoyanova. R.; Dimitrov, N.; Vitanov, T. *J. Electroanal. Chem*. **1997**, *429*, 157.

201. Li, M.; Xiong, Y.; Liu, X.; Bo, X.; Zhang, Y.; Han, C.; Guom L. *Nanoscale*. **2015**, *7*, 8920.

202. Wang, H.-Y.; Hung, S.-F.; Chen, H.; Chan, T.; Chen, H. M.; Liu, B. *J. Am. Chem. Soc*. **2016**, *138*, 36.

203. Liu, X.; Chang, Z.; Luo, L.; Xu, T.; Lei, X.; Liu, J.; Sun, X. *Chem. Mater*. **2014**, *26*, 1889. 274.

204. Singh, N. K.; Singh, R. N. *Indian J. Chem*. **1999**, *38*, 5.

205. Al-Hoshan, M. S.; Singh, J. P.; Al-Mayouf, A. M.; Al-Suhybani, A. A.; Shaddad, M. N. *Int. J. Electrochem. Sci*. **2012**, *7*, 15.

206. Singh, J. P.; Singh, N. K.; Singh, R. N. *Int. J. Hydrogen Energy*. **1999**, *24*, 433.

207. Hirai, S.; Yagi, S.; Seno, Fujioka, A.; Ohno, M. T.; Matsuda, T. *RSC Adv*. **2016**, *6*, 2019.

208. Koza, J. A.; He, Z. A.; Miller, S.; Switzer, J. A. *Chem. Mater*. **2012**, *24*, 3567.

209. Chen, Z.; Kronawitter, C. X.; Koel, B. E. *Phys. Chem. Chem. Phys*. **2015**, *17*, 29387.

210. Al-Mamun, M.; Su, X.; Zhang, H.; Yin, H.; Liu, P.; Yang, H.; Wang, D.; Tang, Z.; Wang, Y.; Zhao, H. *Small*. **2016**, *12*, 2866.

211. Ma, T. Y.; Dai, S.; Jaroniec, M.; Qiao, S. Z. *J. Am. Chem. Soc*. **2014**, *136*, 13925.

212. Ling, T.; Yan, D.-Y.; Jiao, Y.; Wang, H.; Zheng, Y.; Zheng, X.; Mao J.; Du, X. W.; Hu, Z.; Jaroniec, M.; Qiao, S. Z. *Nat. Commun*. **2016**, *7*, 12876.

213. Ma, T. Y.; Dai, S.; Qiao, S. Z. *Mater. Today*. **2016**, *19*, 265.

214. Tung, C. W.; Hsu, Y. Y.; Shen, Y. P.; Zheng, Y.; Chan, T. S.; Sheu, H. S; Cheng, Y. C.; Chen, H. M. *Nat. Commun*. **2015**, *6*, 8106.

215. Wang, H. Y.; Hsu, Y.; Chen, Y. R.; Chan, T. S.; Chen, H. M.; Liu, B. *Adv. Energy Mater*. **2015**, *5*, 1500091.

216. Subbaraman, R.; Tripkovic, D.; Chang, K. C.; Strmcnik, D.; Paulikas, A. P.; Hirunsit, P.; Chan, M.; Greeley, J.; Stamenkovic, V.; Markovic, N. M. *Nat. Mater*. **2012**, *11*, 550.

217. Corrigan, D. A. *J. Electrochem. Soc*. **1987**, *134*, 377.

218. Trotochaud, L. S.; Young, L.; Ranney, J. K.; Boettcher, S. W. *J. Am. Chem. Soc*. **2014**, *136*, 6744.

219. Klaus, S.; Cai, Y.; Louie, M. W.; Trotochaud, L. A.; Bell, T. *J. Phys. Chem. C*. **2015**, *119*, 7243.

220. Song, F.; Hu, X. *Nat. Commun*. **2014**, *5*, 4477.

221. Luo, J.; Im, J. H.; Mayer, M. T.; Schreier, M.; Nazeeruddin, M. K.; Park, N. G.; Tilley, S. D.; Fan, H. J.; Grätzel, M. *Science*. **2014**, *345*, 1593. 275.

222. Long, X.; Li, J.; Xiao, S.; Yan, K.; Wang, Z.; Chen, H.; Yang, S. *Angew. Chem., Int. Ed*. **2014**, *53*, 7584.

223. Burke, M. S.; Kast, M. G.; Trotochaud, L.; Smith, A. M.; Boettcher, S. W. *J. Am. Chem. Soc*. **2015**, *137*, 3638.

224. Diaz-Morales, O.; Ledezma-Yanez, I.; Koper, M. T. M.; Calle-Vallejo, F. *ACS Catal*. **2015**, *5*, 5380.

225. Zhang, B.; Zheng, X.; Voznyy, O.; Comin, R.; Bajdich, M.; Garcia-Melchor, M.; Han, L.; Xu, J.; Liu, M.; Zheng, L.; Garcia de Arquer, F. P.; Dinh, C. T.; Fan, F.; Yuan, M.; Yassitepe, E.; Chen, N.; Regier, T.; Liu, P.; Li, Y.; De Luna, P.; Janmohamed, A.; Xin, H. L.; Yang, H.; Vojvodic A.; Sargent, E. H. *Science*. **2016**, *352*, 333.

226. Friebel, D.; Louie, M. W.; Bajdich, M.; Sanwald, K. E.; Cai, Y. A.; Wise, M.; Cheng, M. J.; Sokaras, D.; Weng, T. C.; Alonso-Mori, R. R.; Davis, C.; Bargar, J. R.; Norskov, J. K.; Nilsson, A.; Bell, A. T. *J. Am. Chem. Soc.* **2015**, *137*, 1305.

227. Burke, M. S.; Zou, S.; Enman, L. J. J.; Kellon, E. C.; Gabor, A. E.; Boettcher, S. W. *J. Phys. Chem. Lett*. **2015**, *6*, 3737.

228. Zou, S.; Burke, M. S.; Kast, M. G.; Fan, J.; Danilovic, N.; Boettcher, S. W. *Chem. Mater*. **2015**, *27*, 8011.

229. Feng, J. X.; Ye, S. H.; Xu, H.; Tong, Y. X.; Li, G. R. *Adv. Mater*. **2016**, *28*, 4698.

230. Augustyn, V.; Manthiram, A. *J. Phys. Chem. Lett*. **2015**, *6*, 3787.

231. Lu, Z.; Wang, H.; Kong, D.; Yan, K.; Hsu, P. C.; Yao, G. H.; Liang, Z.; Sun, X. Cui, Y. *Nat. Commun*. **2014**, *5*, 4345.

232. Merrill, M. D.; Dougherty, R. C. *J. Phys. Chem. C*. **2008**, *112*, 3655.

233. Smith, R. D. L.; Prevot, M. S.; Fagan, R. D.; Trudel, S. C.; Berlinguette, P. *J. Am. Chem. Soc*. **2013**, *135*, 11580.

234. Kanan, M. W.; Nocera, D. G. *Science*. **2008**, *321*, 1072.

235. Jeong, D.; Jin, K.; Jerng, S. E.; Seo, H.; Kim, D.; Nahm, S. H.; Kim, S. H.; Nam, K. T. *ACS Catal*. **2015**, *5*, 4624.

236. Nie, Z. P.; Ma, D. K.; Fang, G. Y.; Chen W.; Huang, S. M. *J. Mater. Chem. A*. **2016**, *4*, 2438.

237. Huynh, M. D.; Bediako, K.; Nocera, D. G. *J. Am. Chem. Soc*. **2014**, *136*, 6002. 276.

238. 246 154 Dinca, M.; Surendranath, Y.; Nocera, D. G. *Proc. Natl. Acad. Sci. U. S. A*. **2010**, *107*, 10337.

239. Takashima, T.; Hashimoto, K.; Nakamura, R. *J. Am. Chem. Soc*. **2012**, *134*, 1519.

240. Kanan, M. W.; Surendranath, Y.; Nocera, D. G. *Chem. Soc. Rev*. **2009**, *38*, 109.

241. Risch, M.; Khare, V.; Zaharieva, I.; Gerencser, L.; Chernev, P.; Dau, H. *J. Am. Chem. Soc*. **2009**, *131*, 6936.

242. Kanan, M. W.; Yano, J.; Surendranath, Y.; Dinca, M.; Yachandra, V. K.; Nocera, D. G. *J. Am. Chem. Soc*. **2010**, *132*, 13692.

243. Surendranath, Y.; Kanan, M. W.; Nocera, D. G. *J. Am. Chem. Soc*. **2010**, *132*, 16501.

244. Chen, M.; Wu, Y.; Han, Y.; Lin, X.; Sun, J.; Zhang, W.; Cao, R. *ACS Appl. Mater. Interfaces*. **2015**, *7*, 21852.

245. Ahn, H. S.; Tilley, T. D. *Adv. Funct. Mater*. **2013**, *23*, 227.

246. Bediako, D. K.; Surendranath, Y.; Nocera, D. G. *J. Am. Chem. Soc*. **2013**, *135*, 3662.

247. Bediako, D. K.; Lassalle-Kaiser, B.; Surendranath, Y.; Yano, J.; Yachandra, V. K.; Nocera, D. G. *J. Am. Chem. Soc*. **2012**, *134*, 6801.

248. Xu, Y.; Schoonen, M. A. A. *American Mineralogist*. **2000**, *85*, 543.

249. Rasmussen, F. A.; Thygesen, K. S. *J. Phys. Chem. C*. **2015**, *119*, 13169.

250. Lauer, S.; Trautwein, A. X.; Harris, F. E. *Phys. Rev. B*. **1984**, *29*, 6774.

251. Hong, W. T.; Risch, M.; Stoerzinger, K. A.; Grimaud, A.; Sunitvich, J.; Shao-Horn, Y. *Energy Environ. Sci*. **2015**, *8*, 1404.

252. Suntivich, J.; May, K. J.; Gasteiger, H. A.; Goodenough, J. B.; Shao-Horn. Y. *Science*. **2011**, *334*, 1383.

253. Zhou, W.; Wu, X. J.; Cao, X.; Huang, X.; Tan, C.; Tian, J.; Liu, H.; Wang, J.; Zhang, H. *Energy Environ. Sci*. **2013**, *6*, 2921.

254. Gao, M. R.; Lin, Z. Y.; Zhuang, T. T.; Jiang, J.; Xu, Y. F.; Zheng, Y. R.; Yu, S. H. *J. Mater. Chem*. **2012**, *22*, 13662.

255. Pu, Z.; Luo, Y.; Asiri, A. M. & Sun, X. *ACS Appl. Mater. Interfaces.* **2016**, *8*, 4718. 277.

256. Zhu, W.; Yue, X.; Zhang, W.; Yu, S.; Zhang Y.; Wang, J.; Wang J. *Chem. Commun*. **2016**, *52*, 1486.

257. Luo, J.; Im, J. H.; Mayer, M. T.; Schreier, M.; Nazeeruddin, M. K.; Park, N. G.; Tilley, S. D.; Fan, H. J.; Grätzel, M. *Science*. **2014**, *345*, 1593.

258. Xu, X.; Song, F. & Hu, X. *Nat. Commun*. 2016, ***7***, 12324.

259. Swesi, A. T.; Masud, J.; Nath, M. *Energy Environ. Sci*. 2016, ***9***, 1771.

260. Tang, C.; Cheng, N.; Pu, Z.; Xing, W. & Sun, X. *Angew. Chem. Int. Ed*. **2015**, *54*, 9351.

261. Chen, J. S.; Ren J.; Shalom, M.; Fellinger, T.; Antonietti, M. *ACS Appl. Mater. Interfaces*. **2016**, *8*, 5509.

262. Ganesan, P.; Prabu, M.; Sanetuntikul, J.; Shanmugam, S. *ACS Catal*. **2015**, 5, 3625.

263. Zhu, W.; Yue, X.; Zhang, W.; Yu, S.; Zhang, Y.; Wang, J.; Wang, J. *Chem. Commun*. **2016**, *52*, 1486.

264. Dong, B.; Zhao, X.; Han, G. Q.; Li, X.; Shang, X.; Liu, Y. R.; Hu, W. H.; Chai, Y. M.; Zhao H.; Liu, C. G. *J. Mater. Chem. A*. **2016**, *4*, 13499.

265. Xia, C.; Jiang, Q.; Zhao, C.; Hedhili, M. N.; Alshareef, H. N. *Adv. Mater*. **2016**, *28*, 77.

266. Wang; Z.; Li, J.; Tian, X.; Wang, X.; Yu, Y.; Owusu, K. A.; He, L.; Mai, L. *ACS Appl. Mater. Interfaces*. **2016**, *8*, 19386.

267. Gao, M. R.; Xu, Y. F.; Jiang, J.; Zheng, Y. R.; Yu, S. H. *J. Am. Chem. Soc*. **2012**, *134*, 2930.

268. Zheng, Y. R.; Gao, M. R.; Gao, Q.; Li, H. H.; Xu, J.; Wu, Z. Y.; Yu, S. H. *Small*. **2015**, *11*, 182.

269. Liao, M.; Zeng, G.; Luo, T.; Jin, Z.; Wang, Y.; Kou, X.; Xiao, D. *Electrochim. Acta*. **2016**, *194*, 59.

270. Liu, Y.; Cheng, H.; Lyu, M.; Fan, S.; Liu, Q.; Zhang, W.; Zhi, Y.; Wang, C.; Xiao, C.; Wei, S.; Ye, B.; Xie, Y. *J. Am. Chem. Soc*. **2014**, *136*, 15670.

271. Xu, X.; Song, F.; Hu, X. *Nat. Commun*. **2016**, *7*, 12324.

272. Feng, L. L.; Yu, G.; Wu, Y.; Li, G. D.; Li, H.; Sun, Asefa, Y.; Chen, T. W.; Zou, X. *J. Am. Chem. Soc*. **2015**, *137*, 14023. 278.

273. Liu, Y.; Xiao, C.; Lyu, M.; Lin, Y.; Cai, W.; Huang, P.; Tong, W.; Zou, Y.; Xie, Y. *Angew. Chem., Int. Ed*. **2015**, *127*, 11383.

274. Yang, J.; Zhu, G.; Y.; Xia, J.; Ji, Z.; Shen X.; Wu, S. *Adv. Funct. Mater*. **2016**, *26*, 4712.

275. McKendry, I. G.; Thenuwara, A. C.; Sun, J.; Peng, H.; Perdew, J. P.; Strongin D. R.; Zdilla, M. J. *ACS Catal*. **2016**, *6*, 7393.

276. Dou, S.; Tao, L.; Huo, J.; Wang, S.; Dai, L. *Energy Environ. Sci*. **2016**, *9*, 1320.

277. Kwak, I. H.; Im, H. S.; Jang, D. M.; Kim, Y. W.; Kim, Y. W.; Park, K.; Lim, E.; Lim, Y. R.; Cha, E, H.; Park, J. *ACS Appl. Mater. Interfaces*. **2016**, *8*, 5327.

278. Masud, J.; Swesi, A. T.; Liyanage, W. P. R.; & Nath, M. *ACS Appl.Mater. Interfaces*. **2016**, *8*, 17292.

279. Kong, D.; Cha, J. J.; Wang, H.; Lee, H. R.; & Cui, Y. *Energy Environ. Sci*. **2013**, *6*, 3553.

280. Gao, M. R.; Gao, Q.; Jiang, J.; Cui, C. H.; Yao, W. T.; Yu, S. H. *Angew. Chem., Int. Ed*. **2011**, *50*, 4905.

281. Gao, M. R.; Liu, R. S.; Jiang, J.; Cui, C. H.; Yao, W. T.; Yu, S. H. *J. Mater. Chem.* **2010**, *20*, 9355.

282. Sidik, R. A.; Anderson, A. B. *J. Phys. Chem. B*, **2006**, *110*, 936.

283. Zhu, L.; Susac, D.; Teo, M.; Wong, K. C.; Wong, P. C.; Parsons, R. R.; Bizzotto, D.; Mitchell, K. A. R. *J. Catal*. **2008**, *258*, 235.

284. Zhou, Y. X.; Yao, H. B.; Wang, Y.; Liu, H. L.; Gao, M. R.; Shen, P. K. ; Yu, S. H. *Chem. – Eur. J*. **2010**, *16*, 12000.

285. Feng, Y. G.; He, T.; Alonso-Vante, N. *Chem. Mater*. **2008**, *20*, 26.

286. Vayner, E.; Sidik, R. A.; Anderson, A. B.; Popov, B. N. *J. Phys. Chem*. **2007**, *111*, 10508.

287. Feng, Y. J.; He, T.; Alonso-Vante, N. *Electrochim. Acta*, **2009**, *54*, 5252.

288. Wu, G.; Cui, G. F.; Li, D. Y.; Shen, P. K.; Li, N. *J. Mater. Chem*. **2009**, *19*, 6581. 279.

289. Long, X.; Li, G.; Wang, Z.; Zhu, H.; Zhang, T.; Xiao, S.; Guo, W.; Yang, S. *J. Am. Chem. Soc.* **2015**, *137*, 11900.

290. Hinnemann, B. P.; Moses, G.; Bonde, J.; Jorgensen, K. P.; Nielsen, J. H.; Horch, S.; Chorkendorff, I.; Norskov, J. K. *J. Am. Chem. Soc*. **2005**, *127*, 5308.

291. Chen, Z. B.; Cummins, D.; Reinecke, B. N.; Clark,E.; Sunkara, M. K.; Jaramillo, T. F. *Nano Lett*. **2011**, *11*, 4168.

292. Benck, J. D.; Chen, Z. B.; Kuritzky, L. Y.; Forman, A. J.; Jaramillo, T. F. *ACS Catal*. **2012**, *2*, 1916.

293. Li, Y. G.; Wang, H. L.; Xie, L. M.; Liang, Y. Y.; Hong, G. S.; Dai, H. J. *J. Am. Chem. Soc*. **2011**, *133*, 7296.

294. Gao, M. R.; Liang , J. X.; Zheng, Y. R.; Xu,Y. F.; Jiang, J.; Gao, Q.; Li, J.; Yu, S. H. *Nat. Commun.* **2015**, *6*, 5982.

295. Zheng,Y. R.; Gao, M. R.; Gao, Q.; Li, H.; Xu, H. J.; Wu , Z. Y.; Yu, S. H. *Small*. **2015**, *11*, 182.

296. Jiang, J.; Lu, S.; Gao, H.; Zhang, X.; Yu, H. Q. *Nano Energy*. **2016**, *27*, 526.

297. Mabayoje, O.; Shoola, A.; Wygant, B. R.; Mullins, C. B. *ACS Energy Lett*. **2016**, *1*, 195.

298. Safizadeh, F.; Ghali, E.; Houlachi, G. *Int. J. Hydrogen Energy*. **2015**, *40*, 256.

299. Xiao, P.; Chen, W.; Wang, X. *Adv. Energy Mater*. **2015**, *5*, 1500985.

300. Zeng, M.; Li, Y. *J. Mater. Chem. A.* **2015**, *3*, 14942.

301. Chen, P.; Xu, K.; Fang, Z.; Tong, Y.; Wu, J.; Lu, X.; Peng, X.; Ding, H.; Wu, C.; Xie, Y. *Angew. Chem., Int. Ed*. **2015**, *54*, 14710.

302. Zhang,Y.; Ouyang, B.; Xu, J.; Jia, G.; Chen, S.; Rawat, R. S.; Fan, H. *J. Angew. Chem., Int. Ed*. **2016**, *55*, 8670.

303. Liu, M.; Li, J. *ACS Appl. Mater. Interfaces*. **2016**, *8*, 2158.

304. Ryu, J.; Jung, N.; Jang, J. H.; H.; J. Kim S.; Yoo, J. *ACS Catal*. **2015**, *5*, 4066.

305. Stern, L. A.; Feng, L.; Song, F.; Hu, X. *Energy Environ. Sci.* **2015**, *8*, 2347.

306. Chen, P.; Xu, K.; Tong, Y.; Li, X.; Tao, S.; Fang, Z.; Chu, W.; Wu X.; Wu, C. *Inorg. Chem. Front*. **2016**, *3*, 236. 280.

307. Xu, K.; Chen, P.; Li, X.; Tong, Y.; Ding, H.; Wu, X.; Chu, W.; Peng, Z.; Wu, C.; Xie, Y. *J. Am. Chem. Soc*. **2015**, *137*, 4119.

308. Yu, X. Y.; Feng, Y.; Guan, B.; Lou X. W.; Paik, U. *Energy Environ. Sci*. **2016**, *9*, 1246.

309. Read, C. G.; Callejas, J. F.; Holder, C. F.; Schaak, R. E. *ACS Appl. Mater. Interfaces*, **2016**, *8*, 12798.

310. Fu, S.; Zhu, C.; Song, J.; Engelhard, M. H.; Li, X.; Du, D.; Lin, Y. *ACS Energy Lett*. **2016**, *1*, 792.

311. You, B.; Jiang, N.; Sheng, M.; Bhushan M. W.; Sun, Y. *ACS Catal*. **2016**, *6*, 714.

312. Jiao, L.; Zhou Y. X.; Jiang, H. L. *Chem. Sci*. **2016**, *7*, 1690.

313. Li, D. Baydoun, H. C.; Verani, N.; Brock, S. L. *J. Am. Chem. Soc*. **2016**, *138*, 4006.

314. Chang, J.; Xiao, Y.; Xiao, M.; Ge, J.; Liu, Xing, C. W. *ACS Catal*. **2015**, *5*, 6874.

315. Duan, J.; Chen, S.; Vasileff, A.; Qiao, S. Z. *ACS Nano*, **2016**, *10*, 8738.

316. Li, D.; Baydoun, H.; Verani C. N.; Brock, S. L. *J. Am. Chem. Soc*. **2016**, *138*, 4006.

317. Blakemore, J. D.; Crabtree, R. H.; Brudvig, G. W. *Chem. Rev*. **2015**, 115, 12974.

318. Okamura, M.; Kondo, M.; Kuga, R.; Kurashige, Y.; Yanai, T.; Hayami, S.; Praneeth, V. K. K.; Yoshida, M.; Yoneda, K.; Kawata, S.; Masaoka, S. *Nature*. **2016**, *530*, 465.

319. Schulze, M.; Kunz, V.; Frischmann, P. D.; Würthner, F. *Nat. Chem*. **2016**, *8*, 576.

320. Kauffman, D. R.; Alfonso, D. D.; Tafen, N.; Lekse, J.; Wang, C.; Deng, X.; Lee, J.; Jang, H.; Lee, J.; Kumar, S.; Matranga, C. *ACS Catal*. **2016**, *6*, 1225.

321. Schofberger, W.; Faschinger, F.; Chattopadhyay, S.; Bhakta, S.; Mondal, B.; Elemans, J. A. A.; Mullegger, W. S.; Tebi, S.; Koch, R.; Klappenberger, F.; Paszkiewicz, M.; Barth, J. V.; Rauls, E.; Aldahhak, H.; Schmidt, W. G.; Dey, A. *Angew. Chem., Int. Ed*. **2016**, *55*, 2350.

322. Lei, H.; Liu, C.; Wang, Z.; Zhang, Z.; Zhang, M.; Chang, X.; Zhang, W.; Cao, R. *ACS Catal*. **2016**, *6*, 6429.

323. Wurster, B.; Grumelli, D.; Hötger, D.; Gutzler, R.; Kern, K. *J. Am. Chem. Soc*. **2016**, *138*, 3623.

324. Sun, J.; Yin, H.; Liu, P.; Wang, Y.; Yao, X.; Tang, Z.; Zhao, H. *Chem. Sci*. **2016**, *7*, 5640. 281.

325. Sheehan, S. W.; Thomsen, J. M.; Hintermair, U.; Crabtree, R. H.; Brudvig, G. W.; Schmuttenmaer, C. A. *Nat. Commun*. **2015**, *6*, 6469.

326. Ullman, A. M.; Brodsky, C. N.; Li, N.; Zheng, S. L.; Nocera, D. G. *J. Am. Chem. Soc*. **2016**, *138*, 4229.

327. Mirzakulova, E.; Khatmullin, R.; Walpita, J.; Corrigan, T.; Vargas-Barbosa, N. M.; Vyas, S.; Oottikkal, S.; Manzer, S. F.; Hadad, C. M.; Glusac, K. D. *Nat. Chem*. **2012**, *4*, 794.

328. Qu, K.; Zheng, Y.; Dai, S.; Qiao, S. Z. *Nano Energy*. **2016**, *19*, 373.

329. Zhao, Y.; Nakamura, R.; Kamiya, K.; Nakanishi S.; Hashimoto, K. *Nat. Commun*. **2013**, *4*, 2390.

330. Borup, R.; Meyers, J.; Pivovar, B.; Kim, Y. S.; Mukundan, R.; Garland, N.; Myers, D.; Wilson, M.; Garzon, F.; Wood, D.; P.; More, K.; Stroh, K.; Zawodzinski, T.; Boncella, J.; McGrath, J. E.; Inaba, M.; Miyatake, K.; Hori, M.; Ota, K.; Ogumi, Z.; Miyata, S.; Nishikata, A.; Siroma, Z.; Uchimoto, Y.; Yasuda, K.; Kimijima, K.; Iwashita, N. *Chem. Rev*. **2007**, *107*, 3904.

331. Cheng, Y.; Xu, C.; Jia, L.; Gale, J. D.; Zhang, L.; Liu, C.; Shen, P. K.; Jiang, S. P. *Appl. Catal., B*. **2015**, *163*, 96.

332. Lu, X.; Yim, W. L.; Suryanto, B. H. R.; Zhao, C. *J. Am. Chem. Soc*. **2015**, *137*, 2901.

333. Chen, S.; Duan, J.; Jaroniec, M.; Qiao, S. Z. *Adv. Mater*. **2014**, *26*, 2925.

334. Tian, J.; Liu, Q.; Asiri, A. M.; Alamry, K. A.; Sun, X. *ChemSusChem*. **2014**, *7*, 2125.

335. Ma, T. Y.; Dai, S.; Jaroniec, M.; Qiao, S. Z. *Angew. Chem., Int. Ed*. **2014**, *53*, 7281.

336. Ma, T. Y.; Cao, J. L.; Jaroniec, M.; Qiao, S. Z. *Angew. Chem. Int. Ed*. **2016**, *55*, 1138.

337. Jiang, Q.; Xu, L.; Chen, N.; Zhang, H.; Dai, L.; Wang, S. *Angew. Chem., Int. Ed*. **2016**, *55*, 13849.

338. Hong, W. T.; Risch, M.; Stoerzinger, K. A.; Grimaud, A.; Sunitvich, J.; Shao-Horn, Y. *Energy Environ. Sci*. **2015**, *8*, 1404.

339. Swesi, A. T.; Masud, J.; Liyanage, W. P. R.; Umapathi, S.; Bohannan, E.; Medvedeva, J.; Nath, M. *Scientific Reports*. **2017**, *7*, 2401.

VITA

Abdurazag T, Swesi was born in Zawiah, Lybia and received his Bachelor of Science (BSc) degree in Chemistry, from Tripoli University, Tripoli. Upon completion, he had worked as a researcher at Center of Research & Development, Libya. In 2006, he received his Master of Science (MSc) degree from National University of Malysia, Malysis. From 2007 to 2010, he had worked as a teacher at University of Zawia. In August 2014, he joined Missouri University of Science and Technology to pursue a Ph.D in Chemistry under the supervision of Prof. Manashi Nath. During the course of his research journey, he has been able to publish 5 journal articles, submitted 1 article, prepared 3 for submission and presented his research in several (14) meeting conferences including ACS, MRS and ECS national conferences. He also has received the 2016 Pinsheng CS3M Graduate Student Research Award and the 2017 outstanding Graduate Researcher Award. In December, 2017 he received his Ph.D in Chemistry from Missouri University of Science and Technology, USA.